Cyclic multiaxial behavior modeling of Shape Memory Alloys

Dimitrios Chatziathanasiou

To cite this version:

Dimitrios Chatziathanasiou. Cyclic multiaxial behavior modeling of Shape Memory Alloys. Mechanics of materials [physics.class-ph]. Ecole nationale supérieure d'arts et métiers - ENSAM, 2016. English. NNT : 2016ENAM0015 . tel-01344616

HAL Id: tel-01344616
https://pastel.hal.science/tel-01344616v1

Submitted on 12 Jul 2016

2016-ENAM-0015

École doctorale n° 432 : Sciences des Métiers de l'ingénieur

Doctorat ParisTech

THÈSE

pour obtenir le grade de docteur délivré par

l'École Nationale Supérieure d'Arts et Métiers

Spécialité "Mécanique des matériaux"

présentée et soutenue publiquement par

Dimitrios CHATZIATHANASIOU

le 26 avril 2016

Cyclic multiaxial behavior modeling of Shape Memory Alloys

Directeur de thèse : **Fodil MERAGHNI**
Co-encadrement de la thèse : **Yves CHEMISKY et Nadine BOURGEOIS**

Jury

M. Étienne PATOOR, Professeur, Georgia-Tech Lorraine, Georgia Institute of Technology	Président
M. David McDOWELL, Professeur, Institute for Materials, Georgia Institute of Technology	Rapporteur
M. Denis FAVIER, Professeur, UFR Phitem, Université Joseph Fourier	Rapporteur
M. Stefan SEELECKE, Professeur, IMSL, Universität des Saarlandes	Examinateur
M. Björn KIEFER, Professeur, Institut für Mechanik, Technische Universität Dortmund	Examinateur
M. Fodil MERAGHNI, Professeur, LEM3, Arts et Métiers ParisTech - Metz	Examinateur
Mme Nadine BOURGEOIS, Maître de Conférences, LEM3, Université de Lorraine - Metz	Examinateur
M. Yves CHEMISKY, Maître de Conférences, LEM3, Arts et Métiers ParisTech - Metz	Examinateur
M. George CHATZIGEORGIOU, Chargé de Recherche CR1 CNRS, LEM3	Invité

THÈSE

Arts et Métiers ParisTech – Campus de Metz
LEM3 UMR 7239 CNRS

Acknowledgements

The work for this thesis was carried out in LEM3 laboratory between December 2012 and May 2016, under the advising of Fodil Meraghni, professor in Arts et Métiers ParisTech and the co-advising of Yves Chemisky, assistant professor in Arts et Métiers ParisTech and Nadine Bourgeois, assistant professor in Université de Lorraine. It was mainly funded by the project IDEX Paris Nouveaux Mondes / héSam Université, to which I extend my gratitude.

I express my sincere gratitude to Drs. David McDowell, Denis Favier, Stefan Seelecke and Björn Kiefer for taking the time to examine and evaluate this work.

I would like to thank greatly my thesis director Fodil Meraghni for guiding my work and my course through the academic world and for having personally supported me along the way to the end of this thesis. It is as simple as it is truthful to say that without his support, the thesis would have never been completed. I thank wholeheartedly Yves Chemisky, who participated in the most active way possible to the production of the thesis. I feel sincerely lucky and honored for having the chance to do my doctorate under his co-advising. I honestly thank Nadine Bourgeois for having guided and helped me throughout these years. I wish her the best of luck for the accomplishment of her HDR.

A truthful thank you to the members of LEM3 for having contributed to this work. Thanks to Étienne Patoor for his guidance and active participation in my work. Thanks to Laurent Peltier, Patrick Moll and Pierre Charbonnier for having provided me with their expertise in the experimental aspects. Special thanks to Boris Piotrowski and Sylvain Pagura for their support in the IT work and to Dominique Vincent for the secretary support. Thanks to Jean-Sébastien Lecomte for his input regarding my first publication. A special warm thanks to George Chatzigeorgiou for having cared for my work almost like a new co-advisor, for having contributed to publishing articles and for supporting me through hard times over very, or too, long equations.

I extend my gratitude to the colleagues who welcomed me when I arrived at LEM3. Thank you so much Arif, Thomas, Célia, Lotfi, Gaël and Rachid.

My thanks also goes to all the members of LEM3 with whom we have had great times. I wish everyone good luck in the continuation of their professional, as well as personal, plans. Thanks to Nicolas, Akbar, Dimitris, Francis A., Koffi, Clément, Kévin, Pascal, Francis P., Marie, Sebastian, Waffa and Abderrahim.

Thanks to my friends and my family for having helped me since the first all the way to the last moment. A very special thank you to the land of Metz, which quickly made its way to the depths of my heart, and in which I often found comfort.

« One day, we will remember this all and smile. »
Unknown

I

Thesis in English

Contents

Table of Figures

List of Tables

Introduction

Modern day industry has been expressing its interest in replacing commonly used technology with new ideas employing materials that can satisfy at the same time structural and functional purposes. Engineering fields that are driven by the need of innovation, such as aeronautics, automotive and biomedical engineering recognize the capability of unconventional materials to open new horizons in the design of functional structures. These are active materials which couple their mechanical response with other physical aspects, i.e. electrical charges, electric and magnetic fields, temperature and heat flow. This has granted them the general title of smart materials, since their interesting properties help build innovative control techniques and new "intelligent" methods to improve efficiency. They can promote ecological fabrication and lead to new commercial products.

From a point of view of mechanics, active materials exploit their multi-physics properties to alter their behavior with respect to the conditions to which they are subjected. They are mainly classified by the physical aspects of their coupling. Piezoelectric ceramics and piezoresistive carbon-nano-tube reinforced fibers are electroactive materials of which the electric properties depend on an applied mechanical charge. Polymeric organic compounds used in liquid-crystal configurations which alter their polarization properties with respect to temperature are called thermotropic polymers. Magnetostrictive materials convert magnetic energy into mechanical energy and vice versa by adapting their shape to surrounding magnetic fields. Shape memory alloys and composites are materials that recover their original shape when subjected to appropriate temperature variations, thus coupling thermal and mechanical and/or kinetic energy.

Fundamental research of the physical aspects of the relatively newly introduced materials is helpful given the complexity of their properties in comparison with their established mass-used counterparts. Specifically in the domain of designs of products with shape memory alloy (SMA) components, there exist certain challenges in need to be addressed. These include the material thermomechanical response under multiaxial loading, the stability under repeated use, the degradation caused by surrounding components and especially hydrogen embrittlement. Other known challenges are their integration to composite material systems and the enhancing of properties by means of altered chemical compositions and mesoscale precipitates.

Understanding the physical mechanisms in play as smart materials exhibit their multifunctional behavior aids in a proper product design as well as in exploring further potential functions. Phenomenological modeling is actively used in design applications to build tools aimed at predicting overall response and calibrating the design parameters. A phenomenological constitutive model is understood as a set of variables and relations connecting them. It depicts macroscopical observations by a means of a mathematical description, always in the framework of established laws of physics. Modern advanced tools in informatics can then make use of such models to simulate an anticipated material response. In the case of SMAs, the current interest of the scientific and industrial community is the modeling of the properties that present the aforementioned challenges: multiaxial behavior, evolution of material characteristics caused by repeated loading and degradation caused by environmental agents and incorporation to composite structures.

This work deals primarily with the macroscopical modeling of cyclic behavior of SMAs under multiaxial conditions, with emphasis mostly on the commercially successful NiTi alloys. The effort in modeling focuses around a thermodynamically sound system of internal variables and introduces new concepts addressing particular issues of three-dimensional SMA response. The objectives of this work also extend to an experimental study of multiaxial cyclic response of NiTi and the numerical simulation of SMA structures by means of Finite Elements Method.

The first chapter of the manuscript presents the fundamental aspects of the thermomechanical behavior of SMA materials as well as the state of the art regarding its macroscopical modeling. The fundamental concept of martensitic transformation is examined at the micro-scale. It is the basic mechanism which attributes SMAs with their particular characteristics of superelasticity and shape memory, which are thereby reviewed. Three well-established macroscopical models are then analyzed and compared in order to set the basis for the formulation of the new model.

Chapter two focuses on the experimental study of cyclic loading of textured NiTi. The experimental procedures followed include thermomechanical testing of one-dimensional samples and mechanical testing of two-dimensional cross-shaped samples. A complex loading path was followed for both cases involving repeated steps to allow the study of the effect of cyclic activation of transformation to material properties. The degradation of these properties is examined from the point of view of anisotropy as well, since the direction of loading also varies.

The third chapter is meant to address the issue of anisotropic martensitic transformation. Forming conditions are known to affect the crystallographic texture of SMAs and thus to introduce anisotropy in the inelastic mechanical behavior. A new mathematical approach is suggested to capture the dependence of material response to loading direction observed in superelastic tests.

The overall image of the proposed constitutive model is presented in chapter four of the manuscript. The variables chosen to represent the evolution of the internal and observed state of SMA structures are described. Special attention is given to the notion of martensitic reorientation to account for complex response under non-proportional loading. The model is reviewed from its thermodynamical point view to demonstrate its robustness and conformity to the laws of physics. This further allows for the study of the thermomechanics for any case of loading of the material. The result is a strong thermomechanical coupling proving the multi-physics aspect of the model.

The fifth chapter is dedicated to the validation of the proposed model. This is approached on one hand by the effort to simulate complex experiments conducted on SMA structures found in literature. The model parameters are calibrated and the fit of the simulated response is reviewed against the experimental results. On the other hand, numerical simulation of complex SMA structures is carried out in Finite Element Analysis software (Abaqus) to point out the importance of the new considerations input with the proposed model on the multiaxial behavior of the material.

1. SMA thermomechanical behavior and modeling issues

1.1 Shape memory alloys features

Shape memory alloys (SMAs) are metallic materials named after the discovery of their unique capability to retrieve their original shape when their temperature is increased. Significantly large deformation introduced by mechanical loading can be recovered if the temperature increases to specific levels. This deformation would correspond to permanent irrecoverable strain for most common metals. This particular characteristic ranks SMAs in the wider class of shape memory materials. It is the result of the transformation at the crystal level between the two key solid phases that the material can adopt, austenite and martensite. The difference between these two phases lies on the architecture of the crystalline structure, which varies between a cubic-like configuration in austenite and a less symmetric configuration in martensite [Otsuka and Wayman, 1999; Patoor et al., 2006].

The shape memory characteristic is based on the fact that such crystallic transformation can take place in both ways. The direction from austenite to martensite is systematically defined as forward transformation, whereas the inverse procedure is called reverse transformation. This phase transformation can be the result of a change in temperature between critical values, and/or a change in the mechanical state. In the absence of applied stress, forward transformation occurs between martensite start (M_s) and finish (M_f) temperatures and reverse transformation between austenite start (A_s) and finish (A_f) temperatures. The development of appropriate stress levels can also lead to phase transformation. In particular, applying a mechanical loading/unloading cycle above A_f demonstrates the effect of superelasticity in SMAs. During forward transformation, the transformation starts at a critical, temperature-dependent stress. A strain plateau is observed in the uniaxial stress-strain diagram, before the start of the elastic section of martensite. In that case, the large strain that occurs between the two elastic sections on the stress-strain diagram correspond to a transformation strain. This strain is fully recovered after reverse transformation has finished during unloading.

Martensite is the phase that appears at low temperatures/high stress state and consists of zones with different orientation directions found in a single crystal, called variants. Two main forms are observed, with respect to the configuration of variants: twinned martensite, for which the variants appear in multiple directions and form a self-accommodated assembly, and detwinned or oriented martensite, for which a principal direction of variants dominates the martensitic composition [Merzouki et al., 2010]. Contrary to phase transformation, the transition between these two crystallic configurations occurs in one direction, resulting to detwinned martensite only and is called orientation or detwinning. This occurs with the help of mechanical working, when stress is increased between critical levels. Appropriate combination of orientation and phase transformation processes result in the characteristic shape memory effect [Lagoudas, 2008].

The description of the thermomechanical response of shape memory alloys is most commonly associated with a phase diagram in the uniaxial stress-temperature space. Such description had been adopted in the early physically based phenonenological models [Brinson, 1993]. In the phase diagram illustrated in Fig. 1.1, the domains of each phase are clearly annotated. Austenite appears in relatively high temperatures and low stresses. Detwinned martensite is present at relatively low temperatures, as long as the stress is lower than a critical threshold, represented by the term σ^{re}. Once this limit is surpassed, the process of orientation is thought to be initiated, to make the transition to detwinned martensite. On the other hand, the transition from austenite to either twinned or detwinned martensite is induced by moving through the zone designated by the two limits, which mark in the absence of applied stress the temperatures M_s and M_f. These curves usually take the form of straight lines having the same slope C_M. Crossing the line M_s

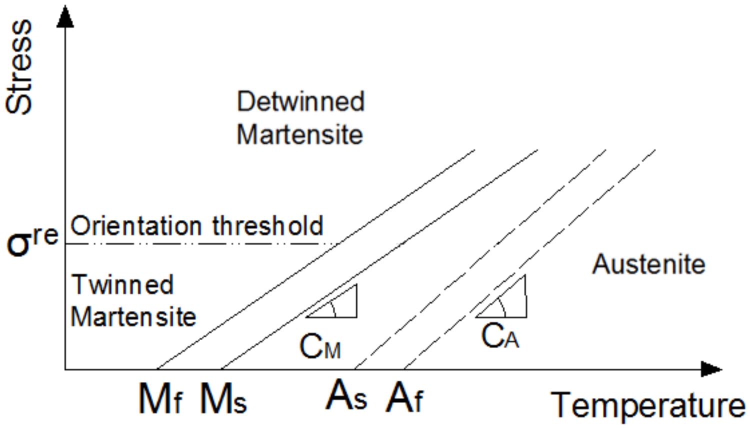

Figure 1.1 – A typical phase diagram for a NiTi alloy.

signals the onset (start) of forward transformation and M_f its saturation (finish). The configuration of resulting martensite depends on the applied stress during transformation: At stresses below σ^{re}, twinned martensite is produced. An example of such transition is present at cooling down at zero stress. At higher stresses, the production of detwinned martensite ensues, as is the case for a superelastic loading at high temperatures. The transition to austenite is achieved by transversing the zone between the limit marking A_s at zero stress, at which reverse transformation starts, and A_f, where it ends. The intersections of the start and finish transition curves with the temperature axis are called effective martensite and austenite start and finish temperatures and are also denoted with the same symbols.

Fig. 1.2 illustrates several aspects of SMA behavior in 1D cases, as well as how the common material parameters affect the resulting response. In case (a), the effective transition temperatures of the fictitious specimen whose properties correspond to the phase diagram on Fig. (1.2a) are evidently different. In case (b) corresponding to Fig. (1.2b), the effective transition temperatures are much closer. In Figures (1.2c) and (1.2d) it becomes evident that the difference between the effective transformation temperatures corrresponds directly to the slope of the stress plateau on the stress-strain diagram and the slope of the strains during

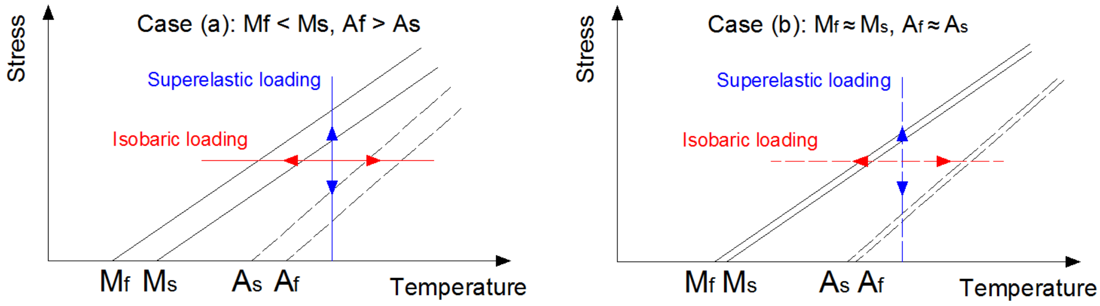

(a) Loading cases on specimen a.

(b) Loading cases on specimen b.

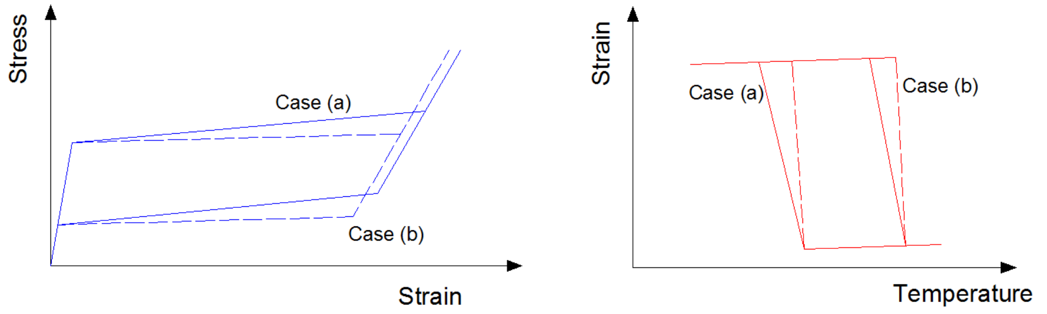

(c) Stress-strain curves for the superelastic loading.

(d) Strain-temperature curves for the isobaric loading.

FIGURE 1.2 – Superelastic and isobaric loading cases and material response in 1D.

transformation on the strain-temperature diagram.

1.2 Issues in the modeling of SMA multiaxial behavior

1.2.1 Anisotropy

Experimental characterization of the superelastic behavior of SMAs has shown that the material exhibits a tension-compression asymmetry [Bouvet et al., 2004; Zhu and Dui, 2010]. Indeed, the critical stress for the onset of transformation is different between tension and compression. A Mises-type criterion is thus not able to accurately predict the transformation surface in the stress space at a given temperature. It has been shown, using a micromechanical model, that the tension-compression asymmetry is linked to the loss of symmetry induced by the appearance of martensitic variants [Patoor et al., 1995]. The tension-compression asymmetry is observable not only on the critical stress to trigger the martensitic transformation, but also on the stress-temperature slopes of the phase diagram and on the magnitude of transformation strains [Šittner and Novák, 2000]. The behavior of processed polycrystal SMAs also shows a strong anisotropic characteristics [Grolleau et al., 2011; Sittner et al., 2009]. Like other metals, the texture of the material and the presence of internal stresses are found to be responsible for such anisotropy. A micromechanical analysis has shown that the transformation of a textured polycrystal is strongly anisotropic [Taillard et al., 2008]. Recent efforts have focused on the development of suitable criteria to take into account the anisotropic behavior of processed SMAs. It is shown that the transformation surfaces could be well predicted but the evolution of transformation strains should be investigated even further [Taillard, 2006].

Some established models make use of the Von Mises criterion to define the constitutive behavior of SMAs [Auricchio et al., 1997; Bodaghi et al., 2014; Boyd and Lagoudas, 1996; Lagoudas et al., 2012; Patoor et al., 2006]. This choice is primarily motivated by the small number of parameters to identify and the specific use of the structures to be designed, mostly linear actuators [Hartl et al., 2010a; Seelecke and Müller, 2004]. Constitutive models that include tension-compression asymmetry have been developped in the last 20 years [Bouvet et al., 2004; Chemisky et al., 2011; Lexcellent et al., 2002a; Peultier et al., 2008; Qidwai and Lagoudas, 2000; Saint-Sulpice et al., 2008]. They rely on a transformation criterion that depends on the invariants of the stress tensor. Following the normality rule for the tranformation strains, associativity to such critrerion is characterized by the invariance of transformation power with respect to loading direction [Gibeau et al., 2010]. At the point of saturation, an analytical expression of the tranformation

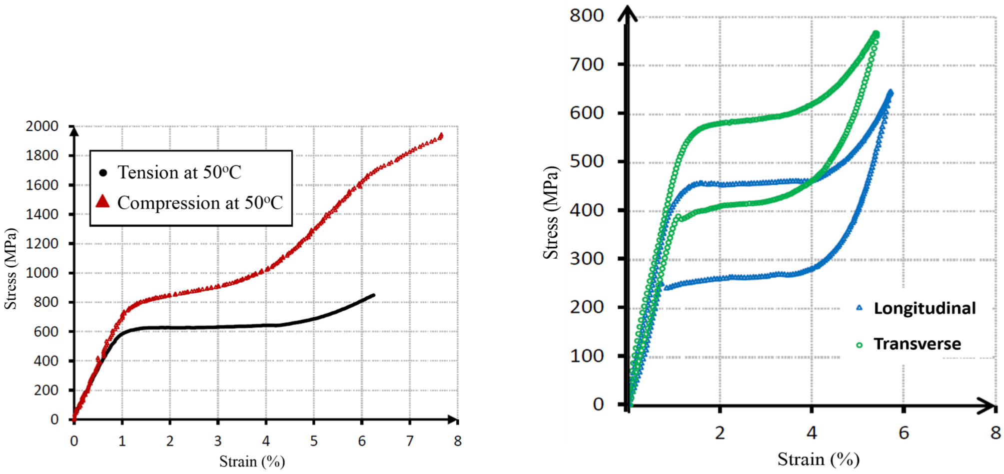

(a) Testing in tension and compression (b) Tension in two directions of rolled samples

Figure 1.3 – Uniaxial testing cases demonstrating tension-compression asymmetry and anisotropy in NiTi samples [Echchorfi, 2013].

strains can thus be expressed. This expression can therefore be utilized as a bound for evolution of transformation strain [Chemisky et al., 2011]. The transformation surface in the stress space can then be derived starting from these physical bounds of the transformation strain. The criterion introduced by Taillard et al. [2008] is able to reproduce the anisotropic transformation, but does not focus on the definition of an evolution equation that could accurately predict the direction of transformation. As for the shape of the transformation surface itself, it appears that quadratic anisotropic yield criteria which are commonly used for a wide variety of materials in numerical computations, such as Hill [Hill, 1948] or its more general form, Tsai-Wu [Tsai and Wu, 1971] do not fit well the data obtained by experiments. In the mentioned models [Gibeau et al., 2010; Taillard et al., 2008; Tsai and Wu, 1971], the particular pear shape of the Prager equation introduced for SMAs by Patoor et al. [Patoor et al., 1995] seems to fit better the experimental observations. The PhD thesis by Echchorfi [2013] provides valuable input concerning tension-compression asymmetry and anisotropy. Fig. 1.3 illustrates pertinent experiments on unidirectional NiTi samples. In (1.3a), it is evident that the plateau associated with transformation is produced at higher stress levels for compression than for tension. Moreover, tension induces higher transformation strains than compression. The difference is similar between tension tests in perpendicular directions in (1.3b): A sample in the direction transverse to rolling undergoes forward and reverse transformation at stresses higher than its longitudinal counterpart. It also develops lower inelastic strains.

1.2.2 Reorientation

Twinned martensite is normally obtained after cooling down the material at the absence of or at considerably low levels of stress. It is a phase of the material where no inelastic strain is apparent, since the martensitic variants are in a self-accommodated state, where no particular direction is dominant. This structure is adopted such that the strain energy is minimized. The resulting self-accommodated microstructure thus does not exhibit any apparent macroscopic strain. Orientation of the variants occurs when self-accommodated martensite is subjected to mechanical loading. Then, the variants comply to the internal stresses by adopting a preferred direction, thus producing a macroscopic inelastic strain. It is important to acknowledge that this is not a two-way process, as is the case for transformation: the notion of reverse orientation does not exist. When the mechanical load is removed, the inelastic strain is not recovered, leading to a plastic-like macroscopic strain response. It is a feature of SMAs exploited in a typical shape memory path, as presented in Fig. 1.4.

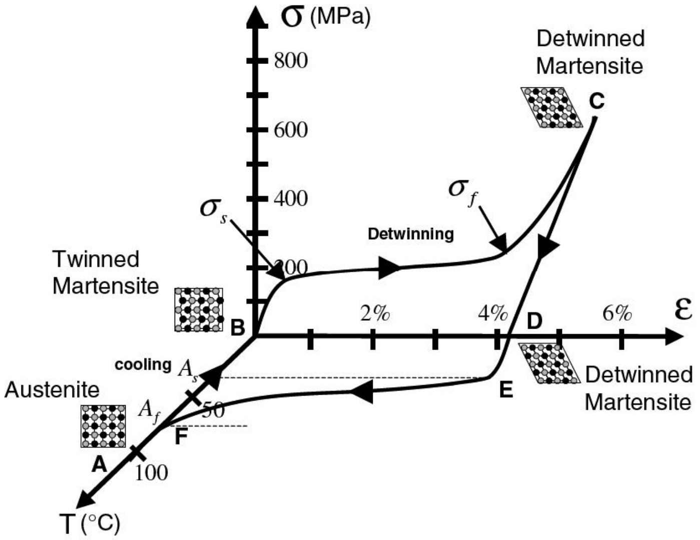

Figure 1.4 – Stress-strain-temperature path for a shape memory loading [Lagoudas, 2008].

Reorientation is the process attributing detwinned variants (variants which have already adopted an orientation) a new preferred direction. It is normally caused by a change in the direction of the applied load. This underlines the importance of macroscopic modeling of reorientation to capturing material response under non-proportional loading. Fig. 1.5 illustrates a strain control loading in multiaxial conditions and the resulting stress response for a NiTi alloy. The points of the arrows on the two graphs correspond to identical moments during the experiment.

The stresses are shown to be affected by the direction of the strain, which implies that the orientation of the total inelastic strain changes during the experiment.

The effect of orientation has been investigated in recent works [Ameduri et al., 2015; Kiefer and Lagoudas, 2007; Saint-Sulpice et al., 2009; Saleeb et al., 2011; Sedlák et al., 2012]. These models add the feature of simulating three-dimensional loading paths to previous simpler models [Boyd and Lagoudas, 1994; Brinson, 1993; Müller and Seelecke, 2001; Saleeb et al., 2001]. Interesting experimental work has been carried out with respect to such loading [Bouvet et al., 2004; Grabe and Bruhns, 2009; Sittner et al., 1995]. The effect of reorientation appears often in these models, too. The procedure of reorientation has a visible effect on the orientation of inelastic strains, whereas detwinning mostly concerns their magnitude [Liu and Favier, 2000; Popov and Lagoudas, 2007]. In certain models [Arghavani et al., 2010; Helm and Haupt, 2003; Panico and Brinson, 2007] and subsequent works, two different volume fractions for martensite are considered as internal variables, one for twinned and one for the detwinned part. This proves a useful consideration, since the evolution of the martensitic strain can be associated to thermally induced and stress induced forward transformation. However, most of these models operate under the assumption that there is a direct relation between the stress induced martensitic fraction and an equivalent transformation strain magnitude, as investigated in [Juhász et al., 2001; Souza et al., 1998; Taillard et al., 2008].

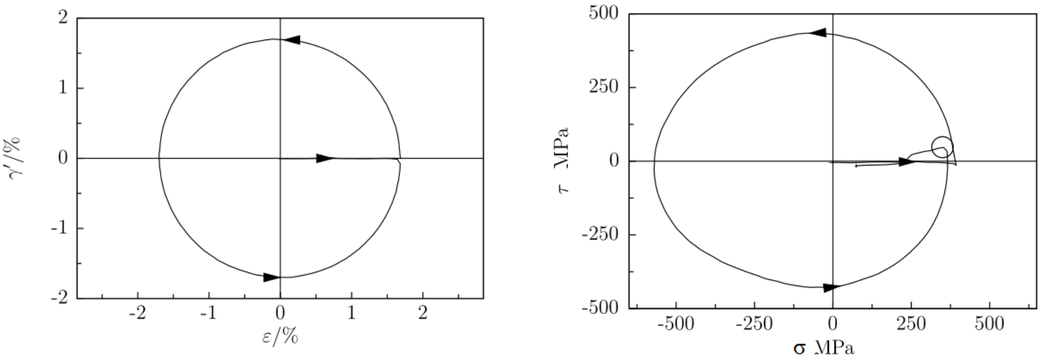

(a) Control path in strains

(b) Material response in stresses

FIGURE 1.5 – Multiaxial experiment and resulting material behavior [Grabe and Bruhns, 2009].

1.2.3 Cyclic effects

It is a recurring problem in SMA applications that the material exhibit a degradation of certain properties when subjected to repeated use. The drop in total transformation strain capacity and the level of hysteresis is the main issue that poses the most concerns when considering to use SMA elements in a mechanical system. It is assumed that the evolution of dislocations resulting from plastic flow interact with the reversible martensitic processes, causing a reduction of the memory strain [Auricchio et al., 1997]. Observations with Transmission Electron Microscopy (TEM) have shown that the absence of dislocation activity leads to a stable cyclic response, whereas stronger dislocation evolution was associated with retained martensite and degrading cycilc behavior [Gall and Maier, 2002]. Authors of recent experimental work [Kang et al., 2009; Olbricht et al., 2008] present relevant macroscopical indications by conducting cyclic tension tests on NiTi wires.

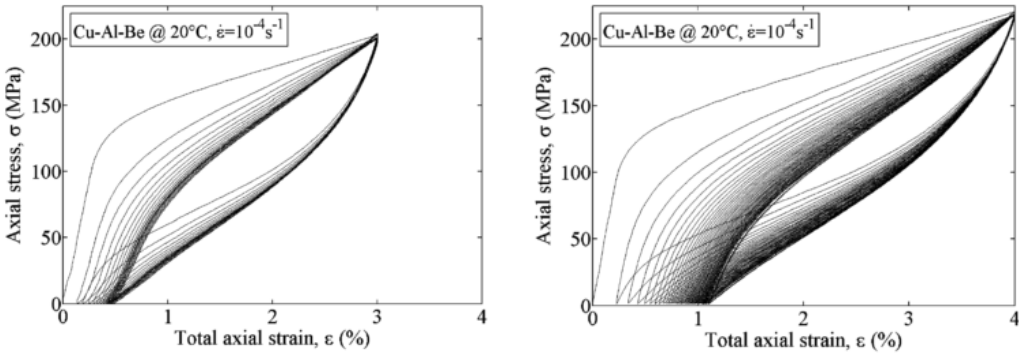

Figure 1.6 – Stress-strain curves for loading (a) in 20 cycles at 3% and (b) in 50 cycles at 4% strain [Saint-Sulpice et al., 2009].

The experiments reported from Saint-Sulpice et al. [2009] in Fig. 1.6 present a residual strain developping with each cycle of loading, along with an apparent reduction of the threshold of the onset of transformation. However, it is also evident that this evolution of material properties is saturated after a certain number of cycles, thus leading to a stable response. This is called training of SMA structures [Hebda and White, 1995; Stalmans et al., 1992a,b] and constitutes a procedure applied to material that is aimed to be utilized in commercial applications [Mohd Jani et al., 2014].

Modern efforts in thermodynamical modeling account for this phenomenon in the scope of transformation induced plasticity. In an extension of the Lagoudas model [Lagoudas and Bo, 1999], the evolution of plastic strains is modelled for the case of stress-assisted thermally induced transformation. In [Lagoudas and Entchev, 2004], an intricate model with many added material parameters is introduced, achieving in capturing residual strain and degradation effects for mechanical loading as well. The evolution of the variables associated to cyclic effects are linked to the accumulated detwinned martensitic volume fraction. Other models include the work by Saint-Sulpice et al. [2009] and Morin et al. [2011].

The change in the material response induced by the application of repeated thermomechanical cycles, including the appearance of resiual strain, is a form of functional fatigue of shape memory alloy devices [Kleinstreuer et al., 2008]. In the case of SMA actuators, the appearance of residual strain leads to a loss of actuation stroke, causing a degradation of the functional properties of the actuator, until the minimal actuation requirement is reached, which corresponds to the functional fatigue limit. Fatigue of SMAs has been investigated experimentally [Bertacchini et al., 2009; Lagoudas et al., 2009]. The introduction of such functional fatigue has also been introduced in phenomenological models recently [Hartl et al., 2014].

1.3 Experimental approaches

There exist several approaches to study the macroscopic behavior of SMAs. One dimensional mechanical and thermomechanical tests are used on thin SMA wires [Shaw and Kyriakides, 1997] and simple one-dimension geometry samples [Brinson et al., 2002] to determine some basic material properties. Other than simple loading-unloading tension tests [Lagoudas et al., 2006; Shaw, 1995], differential scanning calorimetry [Guénin, 1997; Qidwai and Lagoudas, 2000] is used to estimate the transformation temperatures.

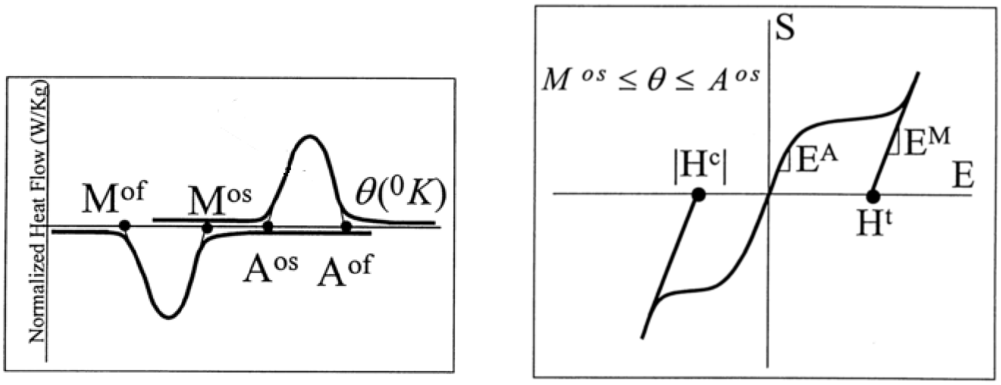

(a) Transformation temperatures on DSC diagram.

(b) Elastic moduli and inelastic strain capacity for tension and compression.

FIGURE 1.7 – Estimation of transformation temperatures based on a DSC test (a) and approximation of elastic moduli and maximum inelastic strains for tension and compression based on mechanical loading from [Qidwai and Lagoudas, 2000].

In Fig. 1.7, indicative experimental diagrams for DSC and mechanical testing are illustrated. DSC measures the energy flow during cooling and heating an

SMA sample to insure steady temperature rates. In (1.7a), the perturbation of the curve during cooling starts and ends at the transformation temperatures for forward transformation, whereas reverse transformation causes the steep slopes of the curve during heating. In (1.7b), loading a sample between the transformation temperatures causes forward but forbids reverse transformation. Thus, all apparent residual strain upon unloading corresponds to the maximum transformation strain.

It should be noted that the forward and reverse transformation limits can significantly vary when being measured to identify the phase diagram parameters using one-dimensional tests and DSC techniques. Such difference renders the identification of material parameters quite challenging. Liu and Favier [2000] and Popov and Lagoudas [2007], among others, have observed that reverse transoformation temperatures are shifted to higher values when martensite is oriented. Piao et al. [1992] have attributed this offset to a diefference in microscopic elastic energy, which would be higher for self-accommodated structure. Liu and Favier [2000] suppose the existence of additional internal friction during reverse transformation of oriented martensite, leading to a higher energy required to trigger it. For practical superelastic devices or actuation purposes, it is therefore recommended to identify the phase diagram using uniaxial tests rather than DSC, since they better match the actual orientation state experienced by the structure.

Most aspects of SMA response can be examined by conducting one-dimensional tests. These include tensile tests under constant temperature, DSC tests under zero stress and isobaric loadings under constant stress levels. Dynamic Mechanical Analysis (DMA) is used to perform temperature sweeps under stress in order to determine dynamic properties as well [Alonso, 2015]. However, because of the complexity of modern SMA models, the material properties cannot be captured with utmost certainty using only 1-D loading [Lagoudas and Bo, 1999]. Modern efforts to investigate experimentally the material behaviors concentrate on

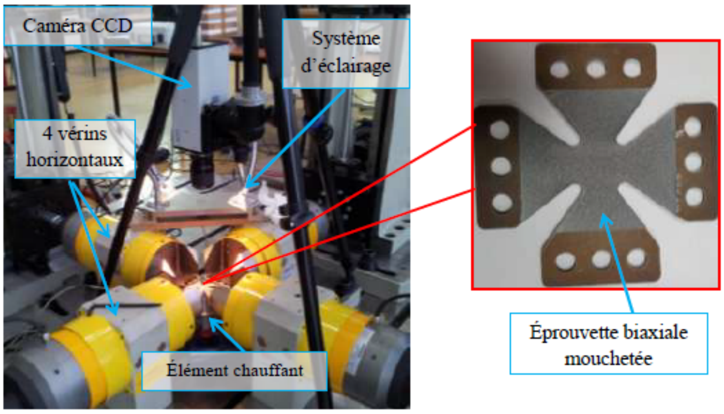

Figure 1.8 – Experimental setup used for biaxial loading in [Echchorfi, 2013].

multi-dimensional loading. A simple technique to induce controlled biaxial stress conditions is employing one-dimensional boundary loading on non-conventional geometries, such as the Meuwissen configuration [Chemisky et al., 2015; Meuwissen et al., 1998]. Tension or compression combined with torsion can be applied on thin-wall tubes, as in [Lexcellent et al., 2002b] or [Grabe and Bruhns, 2008]. Interesting experiments have been conducted on cube shapes made of SMA material in [Bouvet et al., 2004; Rogueda et al., 1996] in the form of biaxial tension. Full control of the mechanical boundary conditions from four sides of a specimen can be achieved with the use of modern technological equipment. In a recent work in LEM3 laboratory [Echchorfi, 2013], NiTi cross-shaped samples have been loaded on a testing device with four load heads independently controlled. This allows for complex non-proportional loading paths of any nature: tension, compression of different force levels can be applied separately for the two directions of the sample. In Fig. 1.8, the experimental setup employed for these tests is illustrated.

1.4 Bibliographic review of existing models

Generally, the macroscopic behavior of SMAs is approached by means of using suitable constitutive equations which involve state variables of the material [Kiefer et al., 2007; Patoor et al., 2006]. Thermodynamic state variables are those that represent all quantities that characterize a material body at a certain state [Coleman and Gurtin, 1967]. If they can be observed, they are called external state variables, otherwise internal state variables [Lagoudas, 2008].

Those constitutive equations are derived through a prescribed thermodynamic potential. This is a function that characterizes a certain thermodynamic state of the body and depends on the state variables. At every state, the thermodynamic potential represents a quantity of energy within the material system. Therefore, it evokes products of the state variables with their thermodynamically conjugant quantities, called the general thermodynamic forces (GTFs). The set of all GTFs will be henceforth denoted as $\boldsymbol{A}$.

It is commonly shown that the transformation strain is thermodynamically conjugant to stress, usually by implementing the procedure first applied by Coleman and Noll [1963] under the conditions described by Lubliner [1972]. All the basic laws of continuum mechanics need to be validated through the implementation of the thermodynamic potential, including the second law of thermodynamics, usually expressed by the local form of the Clausius-Duhem inequality [Lemaitre and Chaboche, 2002].

Two macroscopic models, the first by the team of Lagoudas in Texas A&M University and the second by the team of Brinson in Northwestern University Illinois, that are widely appraised are hereby analytically reviewed. The detail in which they are presented is useful for examining the requirements posed by thermodynamics and the similiarities followed in the architecture of each scheme. Of course, there are a lot more macroscopical models, each presenting its own interest and presenting useful modeling techniques, but reviewing two models would suffice in the scope of this chapter. An exhaustive literature would be redundant. On the contrary, a short critical review from a technical point of view is provided at the end of each subsection.

1.4.1 Lagoudas et al. model

The macroscopic model introduced [Boyd and Lagoudas, 1996] and updated [Bo and Lagoudas, 1999; Hartl and Lagoudas, 2009; Hartl et al., 2010b; Lagoudas et al., 2012; Qidwai and Lagoudas, 2000] by the team of Lagoudas in Texas A&M is a point of reference in most modern modeling works. Presenting the structure of this model for reorientation only, as presented in the [Lagoudas et al., 2012] paper, the bases of macroscopical thermodynamical modeling are also set in this subsection.

The main assumption taken in mind for this model is a direct relation between the evolution of transformation strains and martensitic volume fraction ξ. Although the transformation strain is considered an internal variable, the dissipation linked to transformation is integrally attributed to the evolution of ξ. Another principal assumption is the appearance of “memory variables”, stored as external parameters of the material, every time the loading changes direction. An important limitation of the Lagoudas model is the modeling of reorientation. After the contribution of the work by Popov et al. Popov and Lagoudas [2007], orientation is viewed as a mechanism leading the transition between two martensitic volume fractions, from twinned to detwinned. However, the change of preferred direction, from oriented to reoriented martensite is not addressed.

A Gibbs thermodynamic potential is selected to govern SMA behavior:

$$G(\boldsymbol{\sigma}, T, \boldsymbol{\varepsilon^t}, \xi, g^t) = (1-\xi)G^A(\boldsymbol{\sigma}, T) + \xi G^M(\boldsymbol{\sigma}, T) + G^{mix}(\boldsymbol{\sigma}, \boldsymbol{\varepsilon^t}, g^t) \tag{1.1}$$

where $\boldsymbol{\varepsilon^t}$ is the total transformation strain and ξ the martensitic volume fraction. The total potential is partitioned in the thermoelastic contributions of the two phases, G^A for austenite and G^M for martensite, and of the mixing term G^{mix} corresponding to the inelastic interaction of the two. For each phase $ph = A$, M the thermoelastic parts are:

$$\begin{aligned} G^{ph} = & -\frac{1}{2}\boldsymbol{\sigma} : S^{ph} : \boldsymbol{\sigma} - \boldsymbol{\sigma} : \boldsymbol{\alpha}(T - T_0) + \\ & + c^{ph}\left[(T - T_0) - T\ln\left(\frac{T}{T_0}\right)\right] - s_0^{ph}T + u_0^{ph} \end{aligned} \tag{1.2}$$

S^{ph} is the compliance tensor of the phase ph. c^{ph} is the specific heat, s_0^{ph} the entropy and u_0^{ph} the internal energy. T_0 is a reference temperature at equilibrium. The thermal expansion tensor $\boldsymbol{\alpha}$ is considered equal for the two phases. The energy of mixing is:

$$G^{mix} = -\boldsymbol{\sigma} : \boldsymbol{\varepsilon^t} + g^t$$

where g^t is an energy quantity called here transformation hardening energy and accounts for the shape of the stress-strain-temperature curves during transformation. It is considered, alongside $\boldsymbol{\varepsilon^t}$ and ξ, an internal variable of the model. The GTF for $\boldsymbol{\varepsilon^t}$ is:

$$\boldsymbol{A}_{\boldsymbol{\varepsilon^t}} = -\frac{\partial G}{\partial \boldsymbol{\varepsilon^t}} = \boldsymbol{\sigma} \tag{1.3}$$

For ξ, the GTF is called here p:

$$\begin{aligned} A_\xi = p = -\frac{\partial G}{\partial \xi} &= \frac{1}{2}\boldsymbol{\sigma} : \boldsymbol{\Delta} S : \boldsymbol{\sigma} + \boldsymbol{\sigma} : \boldsymbol{\Delta\alpha}(T - T_0) - \\ &- \Delta c \left[(T - T_0) - Tln\left(\frac{T}{T_0}\right)\right] + \Delta s_0 T - \Delta u_o \end{aligned} \tag{1.4}$$

where the operator Δ denotes the difference of a material constant between the value of the martensitic and the austenitic phase, as in:

$$\boldsymbol{\Delta} S = S^M - S^A$$

For g^t, it is of course: $A_{g^t} = -\dfrac{\partial G}{\partial g^t} = -1$.

The second law of thermodynamics demands for a non-negative dissipation. The Clausius-Planck inequality reduces to the local form of:

$$-(\frac{\partial G}{\partial \boldsymbol{\sigma}} : \boldsymbol{\sigma} + \frac{\partial G}{\partial T}T + \frac{\partial G}{\partial \xi}\dot{\xi} + \frac{\partial G}{\partial \boldsymbol{\varepsilon^t}} : \dot{\boldsymbol{\varepsilon}}^{\boldsymbol{t}} + \frac{\partial G}{\partial g^t}\dot{g}^t) - \dot{\boldsymbol{\sigma}} : \boldsymbol{\varepsilon^t} - s\dot{T} \geq 0$$

Using standard manipulation [Coleman and Gurtin, 1967; Coleman and Noll, 1963], it is deduced that:

$$s = -\frac{\partial G}{\partial T} = s_o + \boldsymbol{\sigma} : \boldsymbol{\alpha} + c_v \ln\left(\frac{T}{T_o}\right) \tag{1.5}$$

and

$$\boldsymbol{\varepsilon} = -\frac{\partial G}{\partial \boldsymbol{\sigma}} = S : \boldsymbol{\sigma} + \boldsymbol{\alpha}\Delta T + \boldsymbol{\varepsilon}^{\mathbf{T}} \tag{1.6}$$

Decoupling the heat flow effects [Lemaitre and Chaboche, 2002], the contribution of mechanical working still needs to be non-negative:

$$-(\frac{\partial G}{\partial \xi}\dot{\xi} + \frac{\partial G}{\partial \boldsymbol{\varepsilon^t}} : \dot{\boldsymbol{\varepsilon}}^{\boldsymbol{t}} + \frac{\partial G}{\partial g^t}\dot{g}^t) \geq 0 \tag{1.7}$$

Before defining the thermoelastic surfaces, the authors present their choice for the evolution rules of the internal variables. $\dot{\boldsymbol{\varepsilon}}^{\boldsymbol{t}}$ and $\dot{g}^t$ are proportionally associated with the evolution of ξ:

$$\dot{\boldsymbol{\varepsilon}}^{\boldsymbol{t}} = \dot{\xi}\boldsymbol{\Lambda}^{\boldsymbol{t}} \tag{1.8}$$

and

$$\dot{g}^t = \dot{\xi} f^t \tag{1.9}$$

Consequently, according to equations (1.3) and (1.4), (1.7) can be written as:

$$(p + \boldsymbol{\sigma} : \boldsymbol{\Lambda}^{\boldsymbol{t}} - f^t)\dot{\xi} \geq 0 \tag{1.10}$$

In (1.8), $\boldsymbol{\Lambda}^{\boldsymbol{t}}$ is the transformation direction tensor. For forward transformation, it is:

$$\boldsymbol{\Lambda}^{\boldsymbol{t}}_{\boldsymbol{fwd}} = \frac{3}{2} H^{cur} \frac{\boldsymbol{\sigma}'}{\bar{\sigma}} \tag{1.11}$$

and for reverse:

$$\boldsymbol{\Lambda}^{\boldsymbol{t}}_{\boldsymbol{rev}} = \frac{\boldsymbol{\varepsilon}^{\boldsymbol{t-r}}}{\xi^r} \tag{1.12}$$

The form of H^{cur} in (1.11) is important for the association of the applied stress to the amplitude of strain caused during transformation [Hartl et al., 2010a]:

$$H^{cur}(\bar{\sigma}) = \begin{cases} H_{\min} & \text{for } \bar{\sigma} \leq \bar{\sigma}_{crit} \\ H_{\min} + (H_{sat} - H_{\min})(1 - e^{-k(\bar{\sigma} - \bar{\sigma}_{crit})}) & \text{for } \bar{\sigma} > \bar{\sigma}_{crit} \end{cases} \tag{1.13}$$

Here, $\bar{\sigma}$ is the Von Mises measure of stress magnitude:

$$\bar{\sigma} = \sqrt{\frac{3}{2} \boldsymbol{\sigma}' : \boldsymbol{\sigma}'}$$

and $\bar{\sigma}_{crit}$ is a critical stress threshold under which transformation strains are considered not to develop. $H_{\min}$, H_{sat} and k are taken as material constants calibrating the relation between strain and stress during isobaric loading at different stress levels, as presented in Fig. (1.9a). This evolution law has a profound effect on the phase diagram, become evident in Fig. (1.9b): the slope of the transition curves is visibly altered for low stresses, which affects strain evolution not only for isobaric loading, but any type of forward transformation.

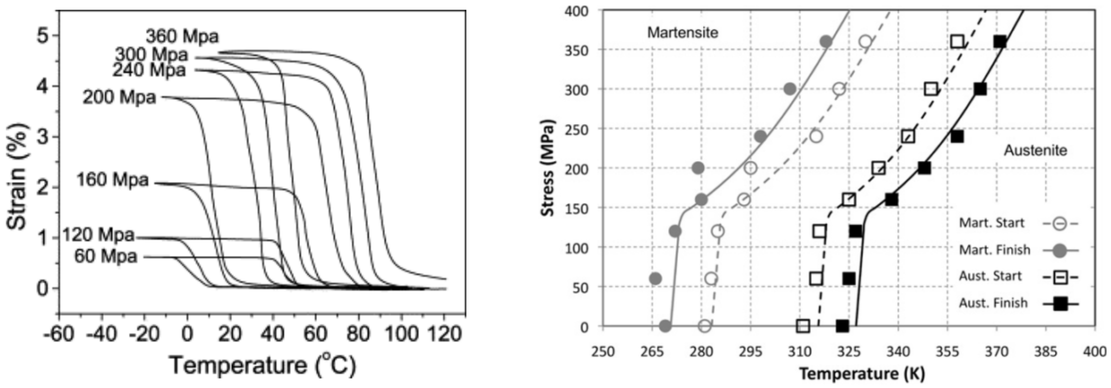

(a) Isobaric loading at different stress levels [Wu et al., 2003]

(b) Modified phase diagram resulting from the implementation of H^{cur} [Lagoudas et al., 2012]

FIGURE 1.9 – Strain-temperature experimental curves for isobaric loading (a) and simulation of the corresponding transformation boundaries considering H^{cur} (b).

The form of equation (1.10) reveals that the whole process of transformation is controlled by one scalar rate, $\dot{\xi}$. This conclusion inspires the definition of a critical thermodynamic force, here the energy quantity π^t, to be used in the expression of the boundary of the thermoelastic region:

$$\pi^t = p + \boldsymbol{\sigma} : \boldsymbol{\Lambda^t} - f^t \tag{1.14}$$

The boundary for forward transformation is:

$$\Phi^t_{fwd} = \pi^t_{fwd} - Y^t_{fwd} \leq 0 \tag{1.15}$$

with

$$\pi^t_{fwd} = p + \boldsymbol{\sigma} : \boldsymbol{\Lambda^t_{fwd}} - f^t_{fwd} \tag{1.16}$$

The boundary for reverse transformation is defined as:

$$\Phi^t_{rev} = \pi^t_{rev} - Y^t_{rev} \leq 0 \tag{1.17}$$

where similarly:

$$\pi^t_{rev} = p + \boldsymbol{\sigma} : \boldsymbol{\Lambda^t_{rev}} - f^t_{rev} \tag{1.18}$$

When the criterion:

$$\pi^t_{fwd} - Y^t_{fwd} = p + \boldsymbol{\sigma} : \boldsymbol{\Lambda^t_{fwd}} - f^t_{fwd} = 0 \tag{1.19}$$

is satisfied, forward transformation is activated. Reverse transformation is under way when:

$$\pi^t_{rev} - Y^t_{rev} = p + \boldsymbol{\sigma} : \boldsymbol{\Lambda^t} - f^t_{rev} = 0 \tag{1.20}$$

The forms of Y^t_{fwd} and Y^t_{rev} are discussed in Appendix A.

Back in equation (1.9), the variable f^t is called in this work hardening function and its form depends on the direction of transformation (forward or reverse):

$$f^t = \begin{cases} f^t_{fwd} \text{ for } \dot{\xi} > 0 \\ f^t_{rev} \text{ for } \dot{\xi} < 0 \end{cases}$$

with

$$\begin{aligned} f^t_{fwd} &= \tfrac{1}{2}a_1(1 + \xi^{n_1} - (1-\xi)^{n_2}) + a_3 \\ f^t_{rev} &= \tfrac{1}{2}a_2(1 + \xi^{n_3} - (1-\xi)^{n_4}) - a_3 \end{aligned} \tag{1.21}$$

In these expressions, the coefficients n_1 to n_4 are introduced to avoid singularity points at the start and end of transformation. The coefficients a_1 to a_3 are calibrated by observations in one-dimensional tension tests.

In equation (1.12), $\boldsymbol{\varepsilon^{t-r}}$ and ξ^r are memory variables, stored as material constants every time the transformation direction changes from forward to reverse. This insures that inelastic strain returns to zero the exact moment in the loading history when ξ is also zero. It is noted that $\boldsymbol{\varepsilon^{t-r}}$ and ξ^r do not have the role of internal variables and therefore do not contribute to dissipation when they evolve. They are only stored as temporary material constants.

The modeling of transformation was discussed in great detail, since it will be the base of the subsequent developped modeling in Chapter 4. Orientation is not present in this paper, but it is discussed in [Popov and Lagoudas, 2007]. In this work, three relative volumetric fractions ξ_1, ξ_2 and ξ_3 are introduced, each representing the history of transformation of material phases:
ξ_1 is the total amount of twinned martensite produced from austenite,
ξ_2 is the total volumetric fraction of detwinned martensite produced from austenite and
ξ_3 is the total amount of detwinned martensite transformed from twinned martensite.
The sum of those is ξ and must satisfy the physical limitation: $0 \leq \xi \leq 1$. $\dot{\xi}_1$ and $\dot{\xi}_2$ may take positive and negative values to represent forward and reverse transformation. $\dot{\xi}_2$ must be non-negative, since there is no notion of reverse orientation. Transformation follows the work already presented, following the evolution of ξ_2:

$$\dot{\boldsymbol{\varepsilon}}^{\boldsymbol{t}} = \dot{\xi}_2 \boldsymbol{\Lambda}^{\boldsymbol{t}} \tag{1.22}$$

The process of orientation is linked to ξ_3 and causes the evolution of a different strain tensor:

$$\dot{\boldsymbol{\varepsilon}}^{\boldsymbol{d}} = \dot{\xi}_3 \boldsymbol{\Lambda}^{\boldsymbol{d}} \tag{1.23}$$

where $\boldsymbol{\Lambda}^{\boldsymbol{d}}$ is called here the flow tensor for detwinning. Its form is:

$$\boldsymbol{\Lambda}^{\boldsymbol{d}} = \sqrt{\frac{3}{2}} H^d \frac{\boldsymbol{\sigma}'}{\bar{\sigma}} \tag{1.24}$$

with H^d being the maximum inelastic strain, considered equal to H_{sat} in (1.13). A new transformation tensor for reverse transformation is also affected to the model:

$$\boldsymbol{\Lambda^t} = \sqrt{\frac{3}{2}} H^t \frac{\boldsymbol{\varepsilon}'^{\boldsymbol{t}}}{\|\boldsymbol{\varepsilon^t}\|} \tag{1.25}$$

This consideration removes the restriction imposed with the memory variables introduced in (1.12). The direction of transformation strains is now decoupled from the direction of stresses, since the history of loading affects the current state of strain. Accordingly, the new resulting evolution law succeeds in insuring recovery of transformation strains upon unloading. The total inelastic strain is:

$$\boldsymbol{\varepsilon^{in}} = \boldsymbol{\varepsilon^t} + \boldsymbol{\varepsilon^d} \tag{1.26}$$

No inelastic strain is caused by the evolution of ξ_1, as imposed by the physical notion of twinned martensite.

In thermodynamics, the energy term G^{mix} is altered to accommodate the new set of volume fractions:

$$G^{mix} = \int_0^t \left[f_1(\{\xi\}; sgn(\dot{\xi}_1))\dot{\xi}_1(\tau) + f_2(\{\xi\}; sgn(\dot{\xi}_2))\dot{\xi}_2(\tau) + f_3(\{\xi\})\dot{\xi}_3(\tau) \right] d\tau \tag{1.27}$$

Here, $\{\xi\}$ is the vector composed of the three new volumetric fractions and $sgn()$ gives the $+$ or $-$ sign of a scalar. t is the relative value of time counting from the start of loading history and $0 \leq \tau \leq t$. f_1 to f_3 are hardening functions, similar to f^t defined in (1.21).

The vector $\{\xi\}$, alongside with $\boldsymbol{\sigma}$ and T are the only internal variables here. The GTFs A_i conjugate to ξ_i are:

$$\begin{cases} A_1 = p - f_1 \\ A_2 = \boldsymbol{\sigma} : \boldsymbol{\Lambda^t} + p - f_2 \\ A_3 = \boldsymbol{\sigma} : \boldsymbol{\Lambda^d} - f_3 \end{cases} \tag{1.28}$$

The Clausius-Duhem inequality is simply:

$$\{A\}\{\xi\} \geq 0 \tag{1.29}$$

The thermoelastic boundaries are separately defined for each phase transition in the form of:

$$\Phi_i = A_i - Y_i \tag{1.30}$$

Especially for the case of reorientation,

$$Y_3 = H^d \sigma_s \tag{1.31}$$

σ_s represents the onset of reorientation and corresponds to σ^{re}. In one-dimensional configurations, this consideration affects the phase diagram at low temperature level. In Fig. 1.10, it is evident that orientation is considered to saturate at a critical stress level σ_f. It is calibrated as:

$$\sigma_f = \sigma_s + \frac{\Delta_3}{H^d}$$

with Δ_3 being an energy parameter, characteristic of the hardening during reorientation. The procedure for calibration conforming to 1D experimental observation is presented in Appendix A.

The Lagoudas model for SMAs has been proven very reliable because of its predictive capabilities. The modeling for phase transformation is a work of reference, cited by practically every new publication concerning theoretical developments. Its values include the thermodynamical robustness, since particular attention has been paid to requirements posed by the physical laws, and the efficiency in which multiple aspects of transformation are captured: the changing slopes of the phase diagram, the influence of stress to the size of transformation strain for isobaric loading and the transition to twinned martensite when cooling down under low stress. Furthermore, the extension brought about by Popov and Lagoudas [2007] attributes the model with a further "degree of freedom" for inelastic strain, adding the process of orientation to the modeling scheme.

However, there still remain some issues concerning modeling of reorientation. The approach followed considering different scalar rates for the different types of

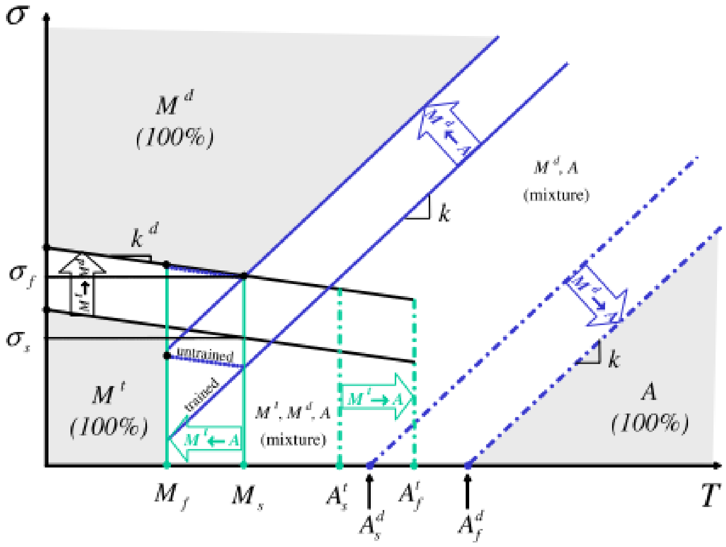

FIGURE 1.10 – Modified phase diagram considering martensite reorientation [Popov and Lagoudas, 2007].

phase transition attributes this model with a scheme of a completely decoupled scheme: there are five different ways to increment the martensitic volumetric fraction, when twinned and detwinned martensite are physically the same phase. The limiting factor of the relation $H^d = H_{sat}$ also deprives a degree of freedom from the model, whereas it is experimentally observed that strain during orientation is lower than during transformation [Auricchio et al., 2014]. Accordingly, the evolution rule for reverse transformation strains should be adapted, seeing that it is only suited for a fixed capacity of strain size. More importantly, this model does not consider reorientation of existing oriented martensite, as it only focues on orientation at low temperature. The complex response of SMAs under non-proportional loadings is therefore not expected to be accurately represented. Finally, even though several transformation criteria have been applied in conjuction with the Lagoudas model [Qidwai and Lagoudas, 2000], there has been no considerable effort capturing anisotropy in phase transformation.

1.4.2 Brinson et al. model

The three-dimensional model proposed in [Panico and Brinson, 2007] is the result of transition of the basic one-dimensional model initially introduced by Brinson [Brinson, 1993]. Throughout these years, there have been several efforts which helped update the model [Bekker and Brinson, 1998; Brinson and Huang, 1996]. The latest variation takes in mind multiaxial behavior under non-proportional loadings and reorientation.

A main assumption of this model is the partition of the total martensitic volume fraction, denoted z in the stress-driven contribution z_σ and the temperature-driven z_T. Detwinned martensite is formed by evolving z_σ, whereas twinned martensite follows the evolution of z_T. Of course, the physical limitation

$$0 \leq z_\sigma + z_T \leq 1 \tag{1.32}$$

must apply.

The cinematics considered in the scope of this work are based on an evident decomposition of strain in the elastic and inelastic parts:

$$\boldsymbol{\varepsilon} = \boldsymbol{\varepsilon}^{\boldsymbol{el}} + \boldsymbol{\varepsilon}^{\boldsymbol{in}} \tag{1.33}$$

in which the increment of the inelastic partition is based on the evolution of two contributions, transformation and reorientation:

$$\dot{\boldsymbol{\varepsilon}}^{\boldsymbol{in}} = \dot{\boldsymbol{\varepsilon}}^{\boldsymbol{tr}} + \dot{\boldsymbol{\varepsilon}}^{\boldsymbol{re}} \tag{1.34}$$

A strong modeling assumption intervenes in the evolution of inelastic strain, since it is considered proportionally associated with detwinned martensite fraction, as in the work by [Juhász et al., 2001]:

$$\left\|\boldsymbol{\varepsilon^{in}}\right\| = \sqrt{\frac{3}{2}}\,\gamma\, z_\sigma \tag{1.35}$$

Here, γ is the magnitude of maximum transformation strain for a uniaxial loading and $\left\|\boldsymbol{\varepsilon^{in}}\right\|$ is measured as $\sqrt{\boldsymbol{\varepsilon^{in}} : \boldsymbol{\varepsilon^{in}}}$. The rate equation resulting from this assumption reads:

$$\boldsymbol{\varepsilon^{in}} : \boldsymbol{\dot{\varepsilon}^{in}} = \sqrt{\frac{3}{2}}\frac{\gamma}{\left\|\boldsymbol{\varepsilon^{in}}\right\|}\dot{z}_\sigma \tag{1.36}$$

The process of reorientation is thought not to affect the martensitic volume. This only evolves in association with $\boldsymbol{\dot{\varepsilon}^{tr}}$. Consequently, reorientation strain is defined such that stress-driven volume z_σ be not influenced by its evolution. Considering a case where $\boldsymbol{\dot{\varepsilon}^{tr}} = \mathbf{0}$, this implies that $\dot{z}_\sigma = 0$ as well. In this case, equation (1.36) reaches by effect of (1.34):

$$\boldsymbol{\varepsilon^{in}} : \boldsymbol{\dot{\varepsilon}^{re}} = 0 \tag{1.37}$$

This obtained condition is a very strong constraining factor on the evolution law chosen for reorientation strain. It actively imposes a perpendicularity condition to the added strain caused by reorientation. More precisely, when reorientation occurs, it must contribute with a strain differential measured by a tensor with a specific relation between its components: they must have zero linear correlation with the components of $\boldsymbol{\varepsilon^{in}}$. If we suppose a change of loading direction resulting in reorientation after a simple uniaxial tension along the axis 1-1, then the differential $\boldsymbol{d\varepsilon^{re}}$ must have, under the assumption of incompressibility, a first component equal to zero:

$$d\varepsilon_{11}^{re} = 0$$

In thermodynamics, the free energy potential is given by a Helmholtz expression in terms of the specific (per unit mass) energy, similar to [Leclercq and Lexcellent, 1996]:

$$\begin{aligned}\Psi(\boldsymbol{\varepsilon^{el}}, T, z_\sigma, z_T) =& \frac{1}{2}\boldsymbol{\varepsilon^{el}} : S : \boldsymbol{\varepsilon^{el}} + u_0^A - T s_0^A - z_T(\Delta u_0 - T\Delta s_0) - \\ & z_\sigma\langle \Delta u_0 - T\Delta s_0\rangle + C_v\left[(T - T_0) - T\ln\left(\frac{T}{T_0}\right)\right] + \Delta\Psi\end{aligned} \tag{1.38}$$

where $\boldsymbol{\varepsilon^{el}}$ and T are considered as control variables and z_σ and z_T are the internal variables. The MacCauley brackets $\langle\rangle$ indicate the positive part of a scalar, returning zero when it is negative. $\Delta\Psi$ is a configurational energy associated to the phase mixture. Its form is:

$$\Delta\Psi = \frac{1}{2}H_\sigma z_\sigma^2 \tag{1.39}$$

The constant H_σ controls the slope of the stress-strain curve during hardening.

The form of the Clausius-Duhem inequality is manipulated to reach:

$$\boldsymbol{A_{tr}} : \dot{\boldsymbol{\varepsilon}}^{\boldsymbol{tr}} + \boldsymbol{A_{re}} : \dot{\boldsymbol{\varepsilon}}^{\boldsymbol{re}} + A_T \dot{z}^T \geq 0 \tag{1.40}$$

The conjugate thermodynamic forces to $\boldsymbol{\varepsilon^{tr}}$, $\boldsymbol{\varepsilon^{re}}$ and z^T are respectively:

$$\boldsymbol{A}_{\varepsilon^{tr}} = \boldsymbol{\sigma}' - (\langle T\Delta s_0 - \Delta u_0 \rangle + H_\sigma z_\sigma) \frac{\boldsymbol{\varepsilon^{in}}}{\sqrt{\frac{3}{2}} \gamma \, \|\boldsymbol{\varepsilon^{in}}\|}$$

$$\boldsymbol{A}_{\varepsilon^{re}} = \boldsymbol{\sigma}'$$

and

$$A_T = -(T\Delta s_0 - \Delta u_0)$$

In these equations the prime ($'$) indicates the deviatoric part of a tensor.

The boundaries of the thermoelastic are in again in this case given separately for phase transition and reorientation.

$$\Phi_{tr} = \|\boldsymbol{A_{tr}}\| - Y_{tr}(z_\sigma) \tag{1.41}$$

$$\Phi_{re} = \frac{1}{2} \boldsymbol{A_{re}} : \hat{\boldsymbol{I}} : \boldsymbol{A_{re}} - Y_{re} \tag{1.42}$$

and

$$\Phi_T = \left\{ \begin{array}{ll} A_T - Y_T^f(z_T) & \\ -A_T - Y_T^r(z_T) & \end{array} \right. \quad for \quad \begin{array}{l} \dot{z}_T > 0 \\ \dot{z}_T < 0 \end{array} \tag{1.43}$$

Here, Y_{tr} is defined as:

$$Y_{tr} = \left\{ \begin{array}{l} A^f z_\sigma - B^f z_\sigma \ln(1 - z_\sigma) + C^f \\ A^r(1 - z_\sigma) - B^r(1 - z_\sigma) \ln(z_\sigma) + C^r \end{array} \right. \quad for \quad \begin{array}{l} \dot{z}_T > 0 \\ \dot{z}_T < 0 \end{array} \tag{1.44}$$

with A, B, C being material constants affecting the hardening slope. Y_{re} is the representation of the orientation threshold. The fourth-order tensor $\hat{\boldsymbol{I}}$ is the "projection tensor" from [Belytschko et al., 2000]. Y_T^f and Y_T^r are respectively:

$$Y_T^f = c_f z_T \tag{1.45}$$

and

$$Y_T^r = Y_{T0}^r + \bar{\sigma} + c_r(1 - z_T) \tag{1.46}$$

where the new variables introduced c_f, c_r and Y_{T0}^r are more material constants.

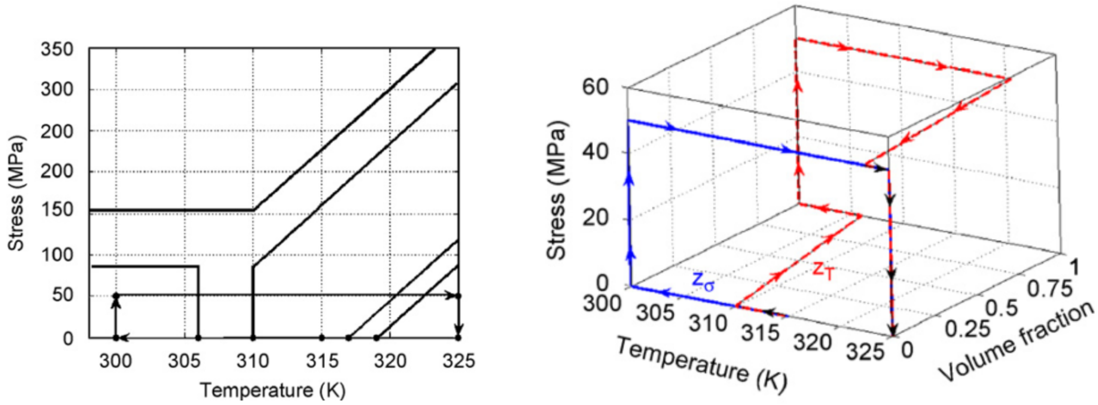

(a) Thermomechanical path on phase diagram. (b) Evolution of martensitic fractions in for the specific loading

FIGURE 1.11 – Thermomechanical loading at low stress illustrated on the modified phase diagram (a) and the associated evolution of martensitic volume fractions z_σ and z_T. [Panico and Brinson, 2007].

The form of the criterion equations in (1.41) through (1.43) modify the phase diagram in a way similar to the Lagoudas model. A simple thermomechanical path is presented in Fig. 1.11 to illustrate the capability of the model to account for forming and recovering self-accommodated martensite. In (1.11a), the stress reached at low temperature is not enought to cause reorientation. When the material is heated back to the initial temperature, all martensite is transformed back to austenite. In (1.11b), it becomes evident that this process is solely captured by the evolution of z_T, whereas z_σ is constantly zero.

The evolution equations are given as expressions of Lagrange multipliers $\dot{\lambda}$.

$$\dot{\boldsymbol{\varepsilon}}^{\boldsymbol{tr}} = \dot{\lambda}^{tr} \boldsymbol{A}_{\boldsymbol{tr}} \tag{1.47}$$

$$\dot{\boldsymbol{\varepsilon}}^{\boldsymbol{re}} = \dot{\lambda}^{tr} \hat{\boldsymbol{I}} : \boldsymbol{A}_{\boldsymbol{re}} \tag{1.48}$$

and

$$\dot{z}_T = \dot{\lambda}_T A_T \tag{1.49}$$

In (1.48), the constraint imposed in equation (1.37) is satisfied by means of implementation of the form of $\hat{\boldsymbol{I}}$:

$$\hat{\boldsymbol{I}} = \boldsymbol{I}' - \frac{\boldsymbol{\varepsilon}^{\boldsymbol{in}}}{\|\boldsymbol{\varepsilon}^{\boldsymbol{in}}\|} \otimes \frac{\boldsymbol{\varepsilon}^{\boldsymbol{in}}}{\|\boldsymbol{\varepsilon}^{\boldsymbol{in}}\|} \tag{1.50}$$

such that

$$\hat{\boldsymbol{I}} : \boldsymbol{\varepsilon}^{\boldsymbol{in}} = \boldsymbol{0} \tag{1.51}$$

This model achieves in overcoming the disadvantage of the Lagoudas model: reorientation and forward transformation are expressed by the evolution of only two scalar variables, z_σ and z_T. When stress is applied to martensite at low temperature, where $z_T > 0$, z_σ increases at the expense of z_T to activate reorientation. In addition to this, $\dot{z}_\sigma$ is the scalar rate which drives the superelastic behavior at constant temperature. z_T, while not completely unaffected by reorientation, as it must reduce in this case, accounts for transformation during cooling down or heating. This simplifies parameter identification, since the constants associated with its evolution can be identified by tests under thermal loading at zero stress.

A critical point of view would focus on the limitation imposed by the evolution law for reorientation. The condition in (1.37) results in a severe restriction of the degree of liberty for strain evolution during reorientation: no matter the direction of applied stress, this equation must be satisfied. Moreover, the history of loading is only imprinted on the inelastic strains. There is no other indication of the history of applied load in any thermodynamic variable. This shortcoming is later addressed in Chapter 4 with the proposed formulation of the new model.

1.5 Concluding remarks

The complex macroscopical behavior of SMAs leads to extensive efforts of thermodynamical modeling. From one hand, inelastic behavior under proportional loading is mainly driven by the phase transformation between the two key crystalline configurations, austenite and martensite, and is an issue addressed in several existing models. Modern works also focus on capturing anisotropy in phase transformation, while there is still the need to express the effect of loading direction to the development of strains. From the other hand, behavior under non-proportional loading is heavily influenced by reorientation of martensitic variants, where modeling can still be improved.

Always in the scope of SMA behavior under multiaxial loading, the effect of retained martensite appears to be influenced by the orientation of the applied load. Evolution of material features, namely residual strain and transformation stress level are direction-dependent during repeated mechanical loading.Thereby, an experimental effort to investigate the effect of direction to cyclic multiaxial behavior of NiTi is conducted in Chapter 2 before the modeling approaches.

Particular focus on the modeling of anisotropy in phase transformation is given in Chapter 3 and, in Chapter 4, modeling efforts concern a new complete model with emphasis on reorientation. This model is primarily based on the Lagoudas model. The validation of this new modeling approach takes place in Chapter 5.

1.6 References

T. Alonso. *Caractérisation par essais DMA et optimisation du comportement thermomécanique de fils de NiTi - Application à une aiguille médicale déformable.* PhD thesis, Université Grenoble Alpes, 2015. 14

S. Ameduri, V. Antonucci, E. Artioli, D. Asprone, F. Auricchio, S. Barbarino, E. Boatti, M. Conti, I. Dimino, G. Faiella, S. Marfia, A. Martone, C. Menna, R. Pecora, E. Sacco, F. Stortiero, A. Vigliotti, and E. Villa. *Shape Memory Alloy Engineering.* Elsevier, 2015. ISBN 9780080999203. doi: 10.1016/B978-0-08-099920-3.01002-0. 11

J. Arghavani, F. Auricchio, R. Naghdabadi, A. Reali, and S. Sohrabpour. A 3-D phenomenological constitutive model for shape memory alloys under multiaxial loadings. *International Journal of Plasticity*, 26(7):976–991, jul 2010. ISSN 07496419. doi: 10.1016/j.ijplas.2009.12.003. 11

F. Auricchio, E. Bonetti, G. Scalet, and F. Ubertini. Theoretical and numerical modeling of shape memory alloys accounting for multiple phase transformations and martensite reorientation. *International Journal of Plasticity*, 59:30–54, aug 2014. ISSN 07496419. doi: 10.1016/j.ijplas.2014.03.008. 23

F. Auricchio, R. L. Taylor, and J. Lubliner. Shape-memory alloys: macromodelling and numerical simulations of the superelastic behavior. *Computer Methods in Applied Mechanics and Engineering*, 146(3-4):281–312, jul 1997. ISSN 00457825. doi: 10.1016/S0045-7825(96)01232-7. 8, 12

A. Bekker and L. Brinson. Phase diagram based description of the hysteresis behavior of shape memory alloys. *Acta Materialia*, 46(10):3649–3665, jun 1998. ISSN 13596454. doi: 10.1016/S1359-6454(97)00490-4. 23

T. Belytschko, W. Liu, and B. Moran. *Nonlinear Finite Elements for Continua and Structures.* Wiley, New York, 2000. 25

O. W. Bertacchini, D. C. Lagoudas, and E. Patoor. Thermomechanical transformation fatigue of TiNiCu SMA actuators under a corrosive environment – Part I: Experimental results. *International Journal of Fatigue*, 31(10):1571–1578, oct 2009. ISSN 01421123. doi: 10.1016/j.ijfatigue.2009.04.012. 13

Z. Bo and D. Lagoudas. Thermomechanical modeling of polycrystalline SMAs under cyclic loading, Part III: evolution of plastic strains and two-way shape memory effect. *International Journal of Engineering Science*, 37(9):1175–1203, jul 1999. ISSN 00207225. doi: 10.1016/S0020-7225(98)00115-3. 16

M. Bodaghi, A. Damanpack, M. Aghdam, and M. Shakeri. A robust three-dimensional phenomenological model for polycrystalline SMAs: Analytical closed-form solutions. *International Journal of Engineering Science*, 82:1–21, sep 2014. ISSN 00207225. doi: 10.1016/j.ijengsci.2014.05.002. 8

C. Bouvet, S. Calloch, and C. Lexcellent. A phenomenological model for pseudoelasticity of shape memory alloys under multiaxial proportional and nonproportional loadings. *European Journal of Mechanics - A/Solids*, 23(1):37–61, jan 2004. ISSN 09977538. doi: 10.1016/j.euromechsol.2003.09.005. 8, 11, 15

J. G. Boyd and D. C. Lagoudas. Thermomechanical Response of Shape Memory Composites. *Journal of Intelligent Material Systems and Structures*, 5(3):333–346, may 1994. ISSN 1045-389X. doi: 10.1177/1045389X9400500306. 11

J. Boyd and D. Lagoudas. A thermodynamical constitutive model for shape memory materials. Part I. The monolithic shape memory alloy. *International Journal of Plasticity*, 12(6):805–842, jan 1996. ISSN 07496419. doi: 10.1016/S0749-6419(96)00030-7. 8, 16

L. C. Brinson and M. S. Huang. Simplifications and Comparisons of Shape Memory Alloy Constitutive Models. *Journal of Intelligent Material Systems and Structures*, 7(1):108–114, jan 1996. ISSN 1045-389X. doi: 10.1177/1045389X9600700112. 23

L. C. Brinson, I. Schmidt, and R. Lammering. Micro and Macromechanical Investigations of CuAlNi Single Crystal and CuAlMnZn Polycrystalline Shape Memory Alloys. *Journal of Intelligent Materials Systems and Structures*, 13(12):761–772, dec 2002. ISSN 00000000. doi: 10.1177/1045389X02013012002. 13

L. Brinson. One-Dimensional Constitutive Behavior of Shape Memory Alloys: Thermomechanical Derivation with Non-Constant Material Functions and Redefined Martensite Internal Variable. *Journal of Intelligent Material Systems and Structures*, 4(2):229–242, apr 1993. ISSN 1045-389X. doi: 10.1177/1045389X9300400213. 6, 11, 23

Y. Chemisky, A. Duval, E. Patoor, and T. Ben Zineb. Constitutive model for shape memory alloys including phase transformation, martensitic reorientation and twins accommodation. *Mechanics of Materials*, 43(7):361–376, jul 2011. ISSN 01676636. doi: 10.1016/j.mechmat.2011.04.003. 8, 9

Y. Chemisky, F. Meraghni, N. Bourgeois, S. Cornell, R. Echchorfi, and E. Patoor. Analysis of the deformation paths and thermomechanical parameter identification of a shape memory alloy using digital image correlation over heterogeneous tests. *International Journal of Mechanical Sciences*, 96-97:13–24, jun 2015. ISSN 00207403. doi: 10.1016/j.ijmecsci.2015.03.007. 15

B. Coleman and M. Gurtin. Thermodynamics with internal variables. *J. Chem. Phys.*, 47(2): 85–98, 1967. 15, 17

B. Coleman and W. Noll. The thermodynamics of elastic materials with heat conduction and viscocity. *Arch. Rational Mech. Anal.*, 13:167, 1963. 15, 17

R. Echchorfi. *Dialogue essais-simulation et identification de lois de comportement d'alliage à mémoire de forme en chargement multiaxial.* PhD thesis, Arts et Métiers ParisTech, 2013. xi, 9, 14, 15

K. Gall and H. Maier. Cyclic deformation mechanisms in precipitated NiTi shape memory alloys. *Acta Materialia*, 50(18):4643–4657, oct 2002. ISSN 13596454. doi: 10.1016/S1359-6454(02)00315-4. 12

E. Gibeau, M. Laydi, and C. Lexcellent. Determination and transport of phase transformation yield surfaces for shape memory alloys. *ZAMM - Journal of Applied Mathematics and Mechanics / Zeitschrift für Angewandte Mathematik und Mechanik*, 90(7-8):595–604, jun 2010. ISSN 00442267. doi: 10.1002/zamm.200900364. 8, 9

C. Grabe and O. Bruhns. Tension/torsion tests of pseudoelastic, polycrystalline NiTi shape memory alloys under temperature control. *Materials Science and Engineering: A*, 481-482: 109–113, may 2008. ISSN 09215093. doi: 10.1016/j.msea.2007.03.117. 15

C. Grabe and O. Bruhns. Path dependence and multiaxial behavior of a polycrystalline NiTi alloy within the pseudoelastic and pseudoplastic temperature regimes. *International Journal of Plasticity*, 25(3):513–545, mar 2009. ISSN 07496419. doi: 10.1016/j.ijplas.2008.03.002. xi, 11

V. Grolleau, H. Louche, V. Delobelle, A. Penin, G. Rio, Y. Liu, and D. Favier. Assessment of tension–compression asymmetry of NiTi using circular bulge testing of thin plates. *Scripta Materialia*, 65(4):347–350, aug 2011. ISSN 13596462. doi: 10.1016/j.scriptamat.2011.05.003. 8

G. Guénin. Shape Memory and Pseudoelastic Properties of Fe-Mn-Si and Ti-Ni Based Alloys. *Le Journal de Physique IV*, 07(C5):C5–467–C5–476, nov 1997. ISSN 1155-4339. doi: 10.1051/jp4:1997574. 13

D. J. Hartl and D. Lagoudas. Constitutive modeling and structural analysis considering simultaneous phase transformation and plastic yield in shape memory alloys. *Smart Materials and Structures*, 18(10):104017, oct 2009. ISSN 0964-1726. doi: 10.1088/0964-1726/18/10/104017. 16

D. J. Hartl, D. C. Lagoudas, F. T. Calkins, J. H. Mabe, J. T. Mooney, D. C. Lagoudas, F. T. Calkins, and J. H. Mabe. Use of a Ni60Ti shape memory alloy for active jet engine chevron application: I. Thermomechanical characterization. *Smart Materials and Structures*, 19(1): 015020, jan 2010a. ISSN 0964-1726. doi: 10.1088/0964-1726/19/1/015020. 8, 18

D. J. Hartl, G. Chatzigeorgiou, and D. C. Lagoudas. Three-dimensional modeling and numerical analysis of rate-dependent irrecoverable deformation in shape memory alloys. *International Journal of Plasticity*, 26(10):1485–1507, oct 2010b. ISSN 07496419. doi: 10.1016/j.ijplas.2010.01.002. 16

D. J. Hartl, Y. Chemisky, and F. Meraghni. Three-dimensional constitutive model considering transformation-induced damage and resulting fatigue failure in shape memory alloys. In N. C. Goulbourne and H. E. Naguib, editors, *SPIE Smart Structures and Materials + Nondestructive Evaluation and Health Monitoring*, page 905805. International Society for Optics and Photonics, mar 2014. doi: 10.1117/12.2046668. 13

D. A. Hebda and S. R. White. Effect of training conditions and extended thermal cycling on nitinol two-way shape memory behavior. *Smart Materials and Structures*, 4(4):298–304, dec 1995. ISSN 0964-1726. doi: 10.1088/0964-1726/4/4/010. 12

D. Helm and P. Haupt. Shape memory behaviour: modelling within continuum thermomechanics. *International Journal of Solids and Structures*, 40(4):827–849, feb 2003. ISSN 00207683. doi: 10.1016/S0020-7683(02)00621-2. 11

R. Hill. A theory of the yielding and plastic flow of anisotropic metals. *Proc. Roy. Soc. London*, (193):281–297, 1948. 9

L. Juhász, H. Andrä, and O. Hesebeck. A Simple Model for Shape Memory Alloys Under Multi-axial Non-Proportional Loading. In *Smart Materials*, pages 51–65. 2001. 11, 24

G. Kang, Q. Kan, L. Qian, and Y. Liu. Ratchetting deformation of super-elastic and shape-memory NiTi alloys. *Mechanics of Materials*, 41(2):139–153, feb 2009. ISSN 01676636. doi: 10.1016/j.mechmat.2008.09.001. 12

B. Kiefer and D. C. Lagoudas. Magnetic field-induced martensitic variant reorientation in magnetic shape memory alloys. *Philosophical Magazine*, feb 2007. 11

B. Kiefer, H. Karaca, D. Lagoudas, and I. Karaman. Characterization and modeling of the magnetic field-induced strain and work output in magnetic shape memory alloys. *Journal of Magnetism and Magnetic Materials*, 312(1):164–175, may 2007. ISSN 03048853. doi: 10.1016/j.jmmm.2006.09.035. 15

C. Kleinstreuer, Z. Li, C. A. Basciano, S. Seelecke, and M. A. Farber. Computational mechanics of Nitinol stent grafts. *Journal of biomechanics*, 41(11):2370–8, aug 2008. ISSN 0021-9290. doi: 10.1016/j.jbiomech.2008.05.032. 13

D. Lagoudas, D. Hartl, Y. Chemisky, L. Machado, and P. Popov. Constitutive model for the numerical analysis of phase transformation in polycrystalline shape memory alloys. *International Journal of Plasticity*, 32-33(null):155–183, may 2012. ISSN 07496419. doi: 10.1016/j.ijplas.2011.10.009. 8, 16, 19

D. C. Lagoudas, D. A. Miller, L. Rong, and P. K. Kumar. Thermomechanical fatigue of shape memory alloys. *Smart Materials and Structures*, 18(8):085021, aug 2009. ISSN 0964-1726. doi: 10.1088/0964-1726/18/8/085021. 13

D. Lagoudas. *Shape Memory Alloys - Modeling and Engineering Applications.* Springer, 2008. xi, 6, 10, 15

D. Lagoudas and Z. Bo. Thermomechanical modeling of polycrystalline SMAs under cyclic loading, Part II: material characterization and experimental results for a stable transformation cycle. *International Journal of Engineering Science*, 37(9):1141–1173, jul 1999. ISSN 00207225. doi: 10.1016/S0020-7225(98)00114-1. 12, 14

D. C. Lagoudas and P. B. Entchev. Modeling of transformation-induced plasticity and its effect on the behavior of porous shape memory alloys. Part I: constitutive model for fully dense SMAs. *Mechanics of Materials*, 36(9):865–892, sep 2004. ISSN 01676636. doi: 10.1016/j.mechmat.2003.08.006. 12

D. C. Lagoudas, P. B. Entchev, P. Popov, E. Patoor, L. C. Brinson, and X. Gao. Shape memory alloys, Part II: Modeling of polycrystals. *Mechanics of Materials*, 38(5-6):430–462, may 2006. ISSN 01676636. doi: 10.1016/j.mechmat.2005.08.003. 13

S. Leclercq and C. Lexcellent. A general macroscopic description of the thermomechanical behavior of shape memory alloys. *Journal of the Mechanics and Physics of Solids*, 44(6): 953–980, jun 1996. ISSN 00225096. doi: 10.1016/0022-5096(96)00013-0. 24

J. Lemaitre and J. L. Chaboche. *Mechanics of Solid Materials.* Cambridge University Press, 2002. ISBN 0521477581. 15, 17

C. Lexcellent, A. Vivet, C. Bouvet, S. Calloch, and P. Blanc. *IUTAM Symposium on Mechanics of Martensitic Phase Transformation in Solids.* Springer, 2002a. ISBN 1402007418. 8

C. Lexcellent, A. Vivet, C. Bouvet, S. Calloch, and P. Blanc. Experimental and numerical determinations of the initial surface of phase transformation under biaxial loading in some polycrystalline shape-memory alloys. *Journal of the Mechanics and Physics of Solids*, 50(12): 2717–2735, dec 2002b. ISSN 00225096. doi: 10.1016/S0022-5096(02)00007-8. 15

Y. Liu and D. Favier. Stabilisation of martensite due to shear deformation via variant reorientation in polycrystalline NiTi. *Acta Materialia*, 48(13):3489–3499, 2000. 11, 14

J. Lubliner. On the thermodynamic foundations of non-linear solid mechanics. *International Journal of Non-linear Mechanics*, 7:237–254, 1972. 15

T. Merzouki, C. Collard, N. Bourgeois, T. Ben Zineb, and F. Meraghni. Coupling between measured kinematic fields and multicrystal SMA finite element calculations. *Mechanics of Materials*, 42(1):72–95, jan 2010. ISSN 01676636. doi: 10.1016/j.mechmat.2009.09.003. 6

M. Meuwissen, C. Oomens, F. Baaijens, R. Petterson, and J. Janssen. Determination of the elasto-plastic properties of aluminium using a mixed numerical–experimental method. *Journal of Materials Processing Technology*, 75(1-3):204–211, mar 1998. ISSN 09240136. doi: 10.1016/S0924-0136(97)00366-X. 15

J. Mohd Jani, M. Leary, A. Subic, and M. A. Gibson. A review of shape memory alloy research, applications and opportunities. *Materials & Design*, 56:1078–1113, apr 2014. ISSN 02613069. doi: 10.1016/j.matdes.2013.11.084. 12

C. Morin, Z. Moumni, and W. Zaki. Thermomechanical coupling in shape memory alloys under cyclic loadings: Experimental analysis and constitutive modeling. *International Journal of Plasticity*, 27(12):1959–1980, dec 2011. ISSN 07496419. doi: 10.1016/j.ijplas.2011.05.005. 13

I. Müller and S. Seelecke. Thermodynamic aspects of shape memory alloys. *Mathematical and Computer Modelling*, 34(12-13):1307–1355, dec 2001. ISSN 08957177. doi: 10.1016/S0895-7177(01)00134-0. 11

J. Olbricht, A. Yawny, A. Condó, F. Lovey, and G. Eggeler. The influence of temperature on the evolution of functional properties during pseudoelastic cycling of ultra fine grained NiTi. *Materials Science and Engineering: A*, 481-482:142–145, may 2008. ISSN 09215093. doi: 10.1016/j.msea.2007.01.182. 12

K. Otsuka and C. M. Wayman. *Shape Memory Materials*. Cambridge University Press, 1999. ISBN 0521663849. 5

M. Panico and L. Brinson. A three-dimensional phenomenological model for martensite reorientation in shape memory alloys. *Journal of the Mechanics and Physics of Solids*, 55(11): 2491–2511, nov 2007. ISSN 00225096. doi: 10.1016/j.jmps.2007.03.010. xi, 11, 23, 26

E. Patoor, M. El Amrani, A. Eberhardt, and M. Berveiller. Determination of the origin for the dissymmetry observed between tensile and compression tests on shape memory alloys. *J. Phys.*, IV(2):495–500, 1995. 8, 9

E. Patoor, D. C. Lagoudas, P. B. Entchev, L. C. Brinson, and X. Gao. Shape memory alloys, Part I: General properties and modeling of single crystals. *Mechanics of Materials*, 38(5-6): 391–429, may 2006. ISSN 01676636. doi: 10.1016/j.mechmat.2005.05.027. 5, 8, 15

B. Peultier, T. Ben Zineb, and E. Patoor. A simplified micromechanical constitutive law adapted to the design of shape memory applications by finite element methods. *Materials Science and Engineering: A*, 481-482(null):384–388, may 2008. ISSN 09215093. doi: 10.1016/j.msea.2007.05.117. 8

M. Piao, S. Miyazaki, and K. Otsuka. Characteristics of Deformation and Transformation in Ti44Ni47Nb9 Shape Memory Alloy. *Materials Transactions, JIM*, 33(4):346–353, jun 1992. ISSN 0916-1821. doi: 10.2320/matertrans1989.33.346. 14

P. Popov and D. C. Lagoudas. A 3-D constitutive model for shape memory alloys incorporating pseudoelasticity and detwinning of self-accommodated martensite. *International Journal of Plasticity*, 23(10-11):1679–1720, oct 2007. ISSN 07496419. doi: 10.1016/j.ijplas.2007.03.011. xi, 11, 14, 16, 20, 22

M. Qidwai and D. Lagoudas. On thermomechanics and transformation surfaces of polycrystalline NiTi shape memory alloy material. *International Journal of Plasticity*, 16(10-11):1309–1343, jan 2000. ISSN 07496419. doi: 10.1016/S0749-6419(00)00012-7. xi, 8, 13, 16, 23

C. Rogueda, C. Lexcellent, and L. Bocher. Experimental study of pseudoelastic behaviour of a Cu Zn AI polycrystalline shape memory alloy under tension-torsion proportional and non-proportional. *Archives of Mechanics*, 1996. 15

L. Saint-Sulpice, S. A. Chirani, and S. Calloch. Super-elastic behavior of shape memory alloys under proportional cyclic loadings. *Materials Science and Engineering: A*, 481-482:174–177, may 2008. ISSN 09215093. doi: 10.1016/j.msea.2007.02.144. 8

L. Saint-Sulpice, S. A. Chirani, and S. Calloch. A 3D super-elastic model for shape memory alloys taking into account progressive strain under cyclic loadings. *Mechanics of Materials*, 41 (1):12–26, jan 2009. ISSN 01676636. doi: 10.1016/j.mechmat.2008.07.004. xi, 11, 12, 13

A. Saleeb, S. Arnold, M. Castelli, T. Wilt, and W. Graf. A general hereditary multimechanism-based deformation model with application to the viscoelastoplastic response of titanium alloys. *International Journal of Plasticity*, 17(10):1305–1350, oct 2001. ISSN 07496419. doi: 10.1016/S0749-6419(00)00086-3. 11

A. Saleeb, S. Padula, and A. Kumar. A multi-axial, multimechanism based constitutive model for the comprehensive representation of the evolutionary response of SMAs under general thermomechanical loading conditions. *International Journal of Plasticity*, 27(5):655–687, may 2011. ISSN 07496419. doi: 10.1016/j.ijplas.2010.08.012. 11

P. Sedlák, M. Frost, B. Benešová, T. Ben Zineb, and P. Šittner. Thermomechanical model for NiTi-based shape memory alloys including R-phase and material anisotropy under multi-axial loadings. *International Journal of Plasticity*, 39(null):132–151, dec 2012. ISSN 07496419. doi: 10.1016/j.ijplas.2012.06.008. 11

S. Seelecke and I. Müller. Shape memory alloy actuators in smart structures: Modeling and simulation. *Applied Mechanics Reviews*, 57(1):23, jan 2004. ISSN 00036900. doi: 10.1115/1.1584064. 8

J. Shaw. Thermomechanical aspects of NiTi. *Journal of the Mechanics and Physics of Solids*, 43(8):1243–1281, aug 1995. ISSN 00225096. doi: 10.1016/0022-5096(95)00024-D. 13

J. Shaw and S. Kyriakides. Initiation and propagation of localized deformation in elasto-plastic strips under uniaxial tension. *International Journal of Plasticity*, 13(10):837–871, dec 1997. ISSN 07496419. doi: 10.1016/S0749-6419(97)00062-4. 13

P. Sittner, Y. Hara, and M. Tokuda. Experimental study on the thermoelastic martensitic transformation in shape memory alloy polycrystal induced by combined external forces. *Metallurgical and Materials Transactions A*, 26(11):2923–2935, nov 1995. ISSN 1073-5623. doi: 10.1007/BF02669649. 11

P. Sittner, L. Heller, J. Pilch, P. Sedlak, M. Frost, Y. Chemisky, A. Duval, B. Piotrowski, T. Ben Zineb, E. Patoor, F. Auricchio, S. Morganti, A. Reali, G. Rio, D. Favier, Y. Liu, E. Gibeau, C. Lexcellent, L. Boubakar, D. Hartl, S. Oehler, D. Lagoudas, and J. V. Humbeeck. Roundrobin SMA modeling. In *ESOMAT 2009 - 8th European Symposium on Martensitic Transformations*, page 08001, Les Ulis, France, sep 2009. EDP Sciences. ISBN 978-2-7598-0480-1. doi: 10.1051/esomat/200908001. 8

P. Šittner and V. Novák. Anisotropy of martensitic transformations in modeling of shape memory alloy polycrystals. *International Journal of Plasticity*, 16(10-11):1243–1268, jan 2000. ISSN 07496419. doi: 10.1016/S0749-6419(00)00009-7. 8

A. Souza, E. Mamiya, and N. Zouain. Three-dimensional model for solids undergoing stress-induced phase transitions. *European Journal of Mechanics - A/Solids1*, 17:789–806, 1998. 11

R. Stalmans, J. Van Humbeeck, and L. Delaey. The two way memory effect in copper-based shape memory alloys — thermodynamics and mechanisms. *Acta Metallurgica et Materialia*, 40 (11):2921–2931, nov 1992a. ISSN 09567151. doi: 10.1016/0956-7151(92)90456-O. 12

R. Stalmans, J. Van Humbeeck, and L. Delaey. Thermomechanical cycling, two way memory and concomitant effects in CuZnAl alloys. *Acta Metallurgica et Materialia*, 40(3):501–511, mar 1992b. ISSN 09567151. doi: 10.1016/0956-7151(92)90399-Y. 12

K. Taillard. *Étude du comportement thermomécanique des alliages à mémoire de forme sous sollicitations multiaxiales complexes.* Phd thesis, École Normale Supérieure de Cachan, 2006. 8

K. Taillard, S. A. Chirani, S. Calloch, and C. Lexcellent. Equivalent transformation strain and its relation with martensite volume fraction for isotropic and anisotropic shape memory alloys. *Mechanics of Materials*, 40(4-5):151–170, apr 2008. ISSN 01676636. doi: 10.1016/j.mechmat.2007.07.005. 8, 9, 11

S. Tsai and E. Wu. A general theory of strength for anisotropic materials. *Journal of Composite Materials*, 5:58–80, 1971. 9

X. Wu, G. Sun, and J. Wu. The nonlinear relationship between transformation strain and applied stress for nitinol. *Materials Letters*, 57(7):1334–1338, jan 2003. ISSN 0167577X. doi: 10.1016/S0167-577X(02)00983-7. 19

Y. Zhu and G. Dui. A macro-constitutive model of polycrystalline NiTi SMAs including tensile–compressive asymmetry and torsion pseudoelastic behaviors. *International Journal of Engineering Science*, 48(12):2099–2106, dec 2010. ISSN 00207225. doi: 10.1016/j.ijengsci.2010.04.002. 8

2. Experimental characterization of cyclic multiaxial thermomechanical behavior of NiTi

2.1 Introduction

The investigation of the evolution of the thermomechanical response of Shape memory Alloys during cyclic loading is an unavoidable step toward the design of structures, as superelasticity and actuation under isobaric conditions are strongly affected by cycling [Lagoudas, 2008; Saint-Sulpice et al., 2009]. In particular, actuation stroke decreases and transformation temperatures shift during actuation cycles. For superelastic loading, recoverable strain is reduced with the appearance of seemingly irrecoverable strain and the transformation stresses threshold for transformation decreases over cycles. Such general behavior under one-dimensional loading conditions depends on the applied temperature and, although certain material parameters degrade with each cycle, the response often reaches a saturated state [Nemat-Nasser and Guo, 2006]. It is a phenomenon commonly associated to transformation-induced plasticity [Hartl and Lagoudas, 2009].

However, the cyclic response of SMAs for multiaxial, non-proportional loading has not been extensively studied. Since SMAs are known to exhibit strong anisotropy for superelastic loading cases [Mehrabi et al., 2014], due to forming conditions inducing texture in the polycrystal [Li et al., 2007], it is expected that the evolution of the thermomechanical response would depend on the loading conditions.

In this chapter, a series of experiments of mechanical cyclic loading on NiTi samples is presented. It aims at investigating the effect of three separate parameters of cyclic loading on the degradation of material properties, namely the residual strains and the transformation threshold in terms of stresses. These three parameters are the number of cycles, the magnitude of reached strain and the loading direction. The first part of this series concerns thermomechanical loading of one-dimensional specimens under different temperatures. A complex cyclic loading path is applied to observe the evolution of material properties, followed by heating to measure the recoverable residual strain. The second part concerns complex mechanical loading of cross-shaped specimens along their two directions. The evolution of the overall kinematic field is tracked through continuous measurements on specific surface points.

2.2 Testing in uniaxial superelastic tension

2.2.1 Experimental methods

The tested samples in all cases, including the cross-shaped geometry presented later, were cut by waterjet from cold-worked rolled plates of NiTi at 50.6% Ni atomic content, provided by Nimesis Technology. The thickness of the plates, and therefore of the specimens, was always 2.5 mm. Their width was 100 mm. A specific heat treatment was applied to obtain annealed material: the samples were thermally treated at 400° for thirty minutes and immediately quenched in cold water. It is a known fact that heat treatment affects material texture in metallic alloys [Miller et al., 2015], thus possibly inducing an influence to anisotropy.

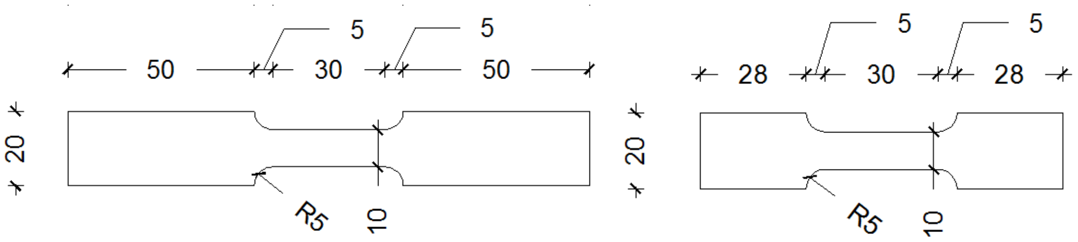

(a) Sample in longitudinal direction (b) Sample in transverse direction

Figure 2.1 – Dogbone geometry for the sample cut along (a) the rolling direction (longitudinal) and (b) the perpendicular direction (transverse).

Unidirectional dogbone specimens were cut by water-jet machining in the two main directions of the plates. Their geometry is given in full detail in Fig. 2.1. The length of the grip section of the specimens in the direction perpendicular, subsequently called transverse, to rolling is limited to 28 mm because of the overall width of the available plates: at only 100 mm, they imposed a considerable constraint to the design of the samples. However, in the longitudinal direction (parallel to rolling), the grip length of 50 mm, along with the width of 20 mm, was deemed sufficient to overcome any possible issues associated to gripping with the tension device clamps. No compromise was allowed in the reduced cross-section: in order for the results in the two directions to be comparable, their respective cross-section had to be the same, at 30 mm long and 10 mm across.

An extensometer was placed approximately on the middle of the specimen and its initial length measurement was at 20 mm. All the tests were performed on an electromechanical Zwick testing machine operating in displacement control. Namely, the relative position between the clamps was controlled. Axial force on the samples was measured by capturing the force on the uniaxial load cell of the machine.

The plan concerning the loading history of the 1-D specimens follows here: Five sequential phases were performed, three of which composed of repeated loading-unloading cycles. All the cycles were conducted under displacement control. The loading step of each cycle was considered completed when a specific predetermined value of strain was reached on the extensometer. Then, it was immediately followed by the unloading step, which was considered completed when a practically zero force was attained. In all experiments, the threshold of 20 N, corresponding to 0.8 MPa of homogeneous stress on the specimen cross-section, marked the finish of unloading steps. Five sequences of mechanical loading cycles, named A to E, were progressively applied. Starting with sequence A, a series of 15 cycles reaching to approximately 3% longitudinal strain was carried out. The following sequence B consisted in a single cycle to the target of 5% strain approximately. Sequence C was identical to A and D identical to B. Finally, sequence E comprised 2 cycles up to 3% strain. It is important to note that the target was not relative to the starting strain value of the cycle, but to the absolute zero of strains. Independently of the strain at which the previous cycle ended, the clamps were programmed to reverse the moving direction when the absolute value 3% (or 5%) was achieved during the next loading step. This decision was chosen to avoid the risk of rupturing the samples. It must be noted that the actual parameter under control was the distance between the clamps. Its speed was always regulated such that the strain rate inside the specimen body never exceeded $10^{-4} sec^{-1}$, in order to avoid effects of latent heat. The plan is presented in Table 2.1 and visualized in Fig. 2.2.

sequence	A	B	C	D	E
Strain target (%)	3	5	3	5	3
Number of cycles	15	1	15	1	2

TABLE 2.1 – Loading path for 1-D experiments.

All experiments took place inside a chamber regulated in temperature with proper isolating conditions. The temperature in the interior was adjusted with the help of a heating system and kept constant throughout the experiments. Vital parts of the installation, such as the clamps, the extensometer and a thermocouple were inside this enclosure during the whole duration of each experiment. The thermocouple was in touch with the body of the specimens, thus measuring the

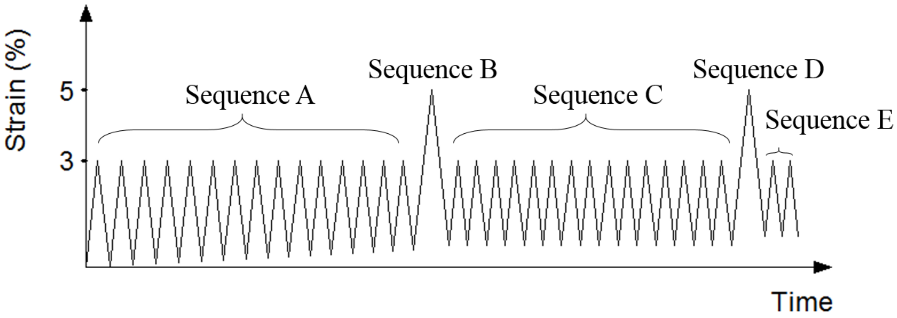

FIGURE 2.2 – Schematic for the loading history of 1-D specimens.

temperature at one point inside the gauge length. The same conditions were maintained for all experiments at temperatures of 30, 40 and 50°C. The strain resulting from the thermal dilation of the extensometer was properly suppressed after gathering the data of the measurements.

At the end of the mechanical loading, the specimens were maintained inside the enclosure, where the ambient temperature was increased to 100°C. During this thermal loading, the force was kept practically zero. Having anticipated the development of residual strains due to cycling, the aim of increasing the temperature is to measure if they can be recovered by thermally induced reverse transformation [Favier and Liu, 2000].

2.2.2 Experimental results

Preliminary remarks concern the difference between the material response in longitudinal and transverse behavior. At the same temperature, the stress threshold for the onset of transformation is higher for transverse loading than for longitudinal loading. In terms of actuation strains, a remark applying to all of the experiments is that the forward transformation cannot be considered completed. Even though the stress curves almost escape the plateau at about 5% strain, we cannot argue that the elastic phase in martensite has been reached. This choice was made to avoid attaining higher stresses or strains and thus to evade the risk of rupturing the available specimens. However, it is also observed that for all temperatures, the response at 5% strain is consistently stiffer for transverse loading compared to longitudinal loading. This indicates that the transformation strain tends to be slightly lower during transverse loading, as observed in previous studies of the same material [Echchorfi, 2013].

Considering now the effect of cycles, the following features are observed for all temperatures and loading directions:

- Seemingly irrecoverable strains are observed for all tests and are slightly

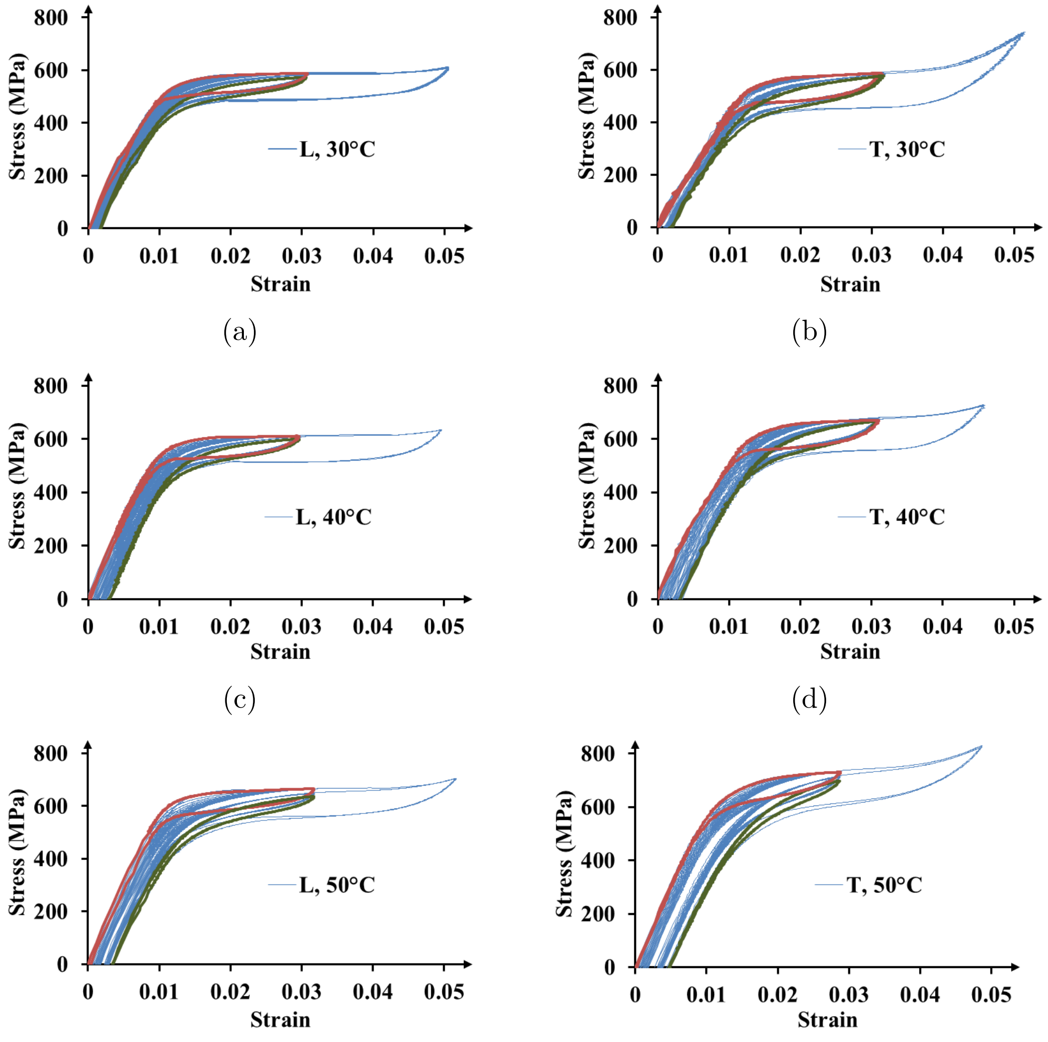

(a) (b)

(c) (d)

(e) (f)

FIGURE 2.3 – Stress-strain diagrams resulting from mechanical cycling under different temperatures for two directions of loading: at 0°(L) and 90°(T) relative to the direction of rolling. The first cycle is designated with red and the last cycle with green color.

more important for transverse loading than longitudinal loading. Larger residual strains are more pronounced at higher temperatures. Note that when such strains are more important, higher values of the transformation plateau average stress appear consistently.

- In all cases, the onset of transformation stress of the 32nd cycle is lower than that of the first cycle.
- The effects of cycles up to 5% strain are more pronounced than those of a

cycle up to 3% for the two previously described effects, i.e. apparition of seemingly irrecoverable strains and reduction of the onset of transformation stress.

- The stress levels reached at the end of the two cycles up to 5% strain are similar for all six tests presented.

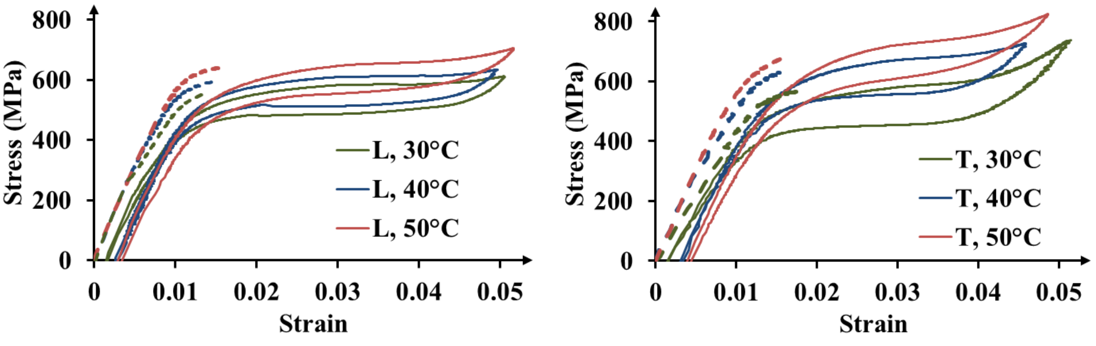

(a) L direction (b) T direction

FIGURE 2.4 – Stress-strain diagrams of the 1st (in dashed lines) and 32nd cycle (in continuous lines) for loading in (a) 0°(L) and (b) 90°(T).

This evolution is more clearly illustrated in the comparative diagrams in Fig. 2.4. The full stress-strain curves of the 32nd cycle, corresponding to sequence D, are drawn in continuous lines for each experiment. Only small parts of the curves, up to the start of transformation, are drawn in dashed lines for the 1st cycle. It becomes clear that the onset of transformation is reduced during cycling. This is combined with a relatively weaker hardening right after the start of the inelastic phase. This is equivalent to a smoother transition to the stress plateau for the 32nd cycle. Furthermore, the tendency of residual strain to increase with higher temperature is evident for loading in both longitudinal and tranverse directions. Finally, the residual strain already looks more important for transverse loading, always comparing at the same temperatures.

The step of the thermal loading followed after the end of Sequence E. Each specimen was practically maintained at zero stress, and the measurement of strains continued without interruption. The strain-temperature diagrams resulting from the heating process are found in Fig. 2.5. The observations are similar for all the specimens: Firstly, the strains started reducing immediately, once the heating was under way. Secondly, the rate of recovery of strains was high at the start of the process, but diminished when strains were also reduced. Virtually the integrity of residual strain was recovered before 80°C. A conclusion drawn from such observation is that the residual strain at the end of the mechanical loading

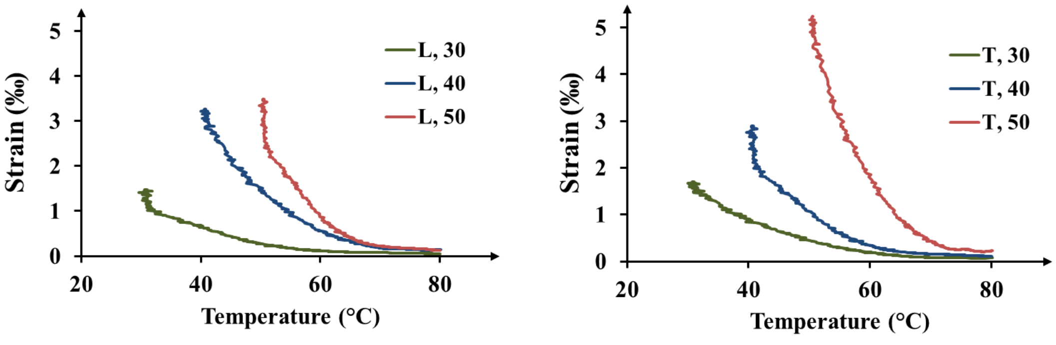

(a) L direction

(b) T direction

FIGURE 2.5 – Temperature-strain diagrams for the stress-free temperature increase of the uniaxial specimens following the mechanical cycling in (a) 0°(L) and (b) 90°(T).

was due to retained martensite. A small fraction of martensite, that was not recovered during unloading to zero force, was eventually transformed back to austenite through heating, causing the disappearance of the associated inelastic strains.

2.2.3 Results analysis and discussion

The actual measurement for residual strain (ε^r) comes from recovering the strain measurement for zero stress at the end of every cycle. In Fig. 2.6, residual strain is plotted against cumulative transformation strain. The measurement of cumulative transformation strain (ε_c) is equal to the sum of transformation strain observed for forward transformation:

$$\varepsilon_c = \int_0^t \varepsilon^{tr} d\tau \tag{2.1}$$

where t is the elapsed time from the start of loading and ε^{tr} is always found as:

$$\varepsilon^{tr} = \varepsilon - \varepsilon^r - \varepsilon^{el} \quad \text{if} \quad \dot{\varepsilon} > 0 \tag{2.2}$$

The elastic component of strain ε^{el} is always calculated from the simple relation $\sigma = E\varepsilon^{el}$. Here, the Young's modulus E for austenite is measured as the mean slope of the stress-strain curve between 50 and 250 MPa for simplicity.

From the analysis of such evolution of residual strains, it is noted that:

- At 30°C: The evolution of residual strains follows a slow and steady increase, regardless of the loading direction or the type of cycle (up to 3% or 5%).

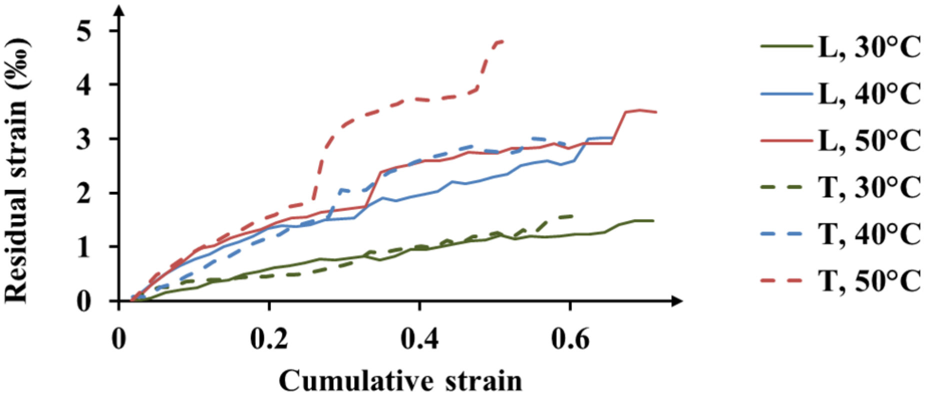

FIGURE 2.6 – Residual - cumulative strain diagram for all conditions of experiments.

- At 40°C: A steady increase is observed for the longitudinal loading direction, while the effect of the cycles up to 5% strain is clearly seen for the case of transverse loading.
- At 50°C: For both longitudinal and transverse loading, the effect of the cycles up to 5% strain is clearly apparent, and even more important for transverse loading.
- It seems that 15 cycles at 3% are not sufficient to stabilize the residual strains. However, their evolution seems saturated at the final cycles of sequence C. In both directions, the second cycle at 5% induces a further increase in residual strains.

It is worth noting that the differences between transverse and longitudinal loading are only significant after a cycle up to large deformation (5%). Also, such representation clearly indicates that the effect of the maximal amount of the seemingly residual strain does not evolve linearly with the evolution of cumulative strain. Indeed, most of the residual strain is generated in the transition from 3% to 5% of deformation. It is worth noting that the stress at these strain levels is not significantly higher than other areas of the transformation plateau.

The method for estimating the transformation threshold is similar to the technique followed in [Lexcellent et al., 2002]. A relative schematic explains the method in Fig. 2.7. After the estimation of the Young's modulus, a line of the same slope is drawn prallel to the linear phase of the stress-strain diagram, at a distance of 1‰along the strain axis. The intersection of that line with the experimental curve is considered as the onset of forward transformation. This conventional estimation represents an effective limit for elasticity for the global structure response. The limit values resulting from such a method do not correspond to a material characteristic, since the geometry of the samples does not allow us to consider fully homogeneous response across their bodies.

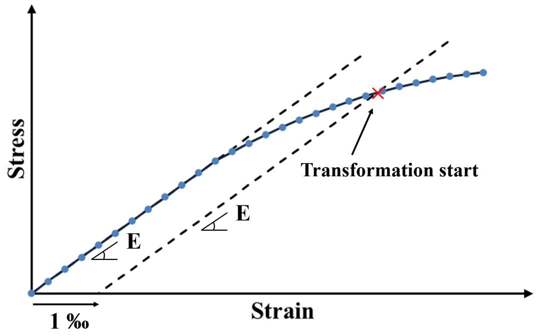

FIGURE 2.7 – Estimation of threshold for forward transformation.

The reduction of the onset of transformation threshold is illustrated in Fig. 2.8. The following conclusions are drawn:

- At 30°C: A rather steady decrease is observed for the longitudinal loading direction, while the effect of the cycles up to 5% strain is apparent for the case of transverse loading.
- At 40°C: A steeper decrease is observed than for the 30°C tests, and the effect of the cycles up to 5% strain is apparent for both longitudinal and transverse loading.
- At 50°C: A steeper decrease is observed than for the 40°C tests. For both longitudinal and transverse loading, the effect of the cycles up to 5% strain is clearly apparent.
- As was the case for the residual strains, 15 cycles at 3% are not sufficient to stabilize the transformation onset. However, its evolution seems saturated at the final cycles of sequence C for longitudinal loading. This point cannot be supported for transverse loading, since the slope of the diagram is still important. In both directions, the second cycle at 5% induces a further drop in transformation threshold.
- It is worth noting that after the 32^{nd} cycle, the stress thresholds difference for the three temperatures is very narrow. Also the threshold order for longitudinal tests has been reversed, and is respectively 50, 40, 30°C in the order of stress increase. For the transverse loading, the order is actually 30,50,40°C. While those results have to be taken with caution due to measurement errors and repeatability issues, they nevertheless raise the point that the transformation diagram in the stress-temperature diagram would

> no longer follow a Clausius-Clapeyron evolution for complex cyclic loading. This indicates that on top of the analysis of martensitic transformation in a perfect crystal, microstructural defects and local fields have to be taken into account. The description of such evolution with TIV (Thermodynamics with Internal Variables) should be well adapted to describe all the aformentioned effects.

The results supporting that transformation would start at lower uniaxial stress levels for 50 than for 40°C confirm that the internal stresses across the geometry of the samples are not homogeneous. These results cannot be used to match the material response to a Clausius-Clapeyron diagram. It is the evolution of the intenal stress state, impacted by the initiation and propagation of transformation, that causes the 1‰ shift from the global linear behavior, tracked in this work. As the stress-strain curves only represent the global response of the samples to the applied boundary conditions, the beginning of the inelastic phase is also representative of the relation between the force and elongation, measured in the scale of the sample geometry. There might also be further possible issues affecting the stress-temperature relationship, such as the activation of R-phase transformation. Austenite to R-phase transformation could also explain the different apparent Young's moduli in the elastic branch of the stress-strain diagrams for the samples loaded in the transverse direction on 2.2b [Favier et al., 2007]. Still, the transformation onset estimation provided here is useful for supplying insight about the influence of anisotropy on the global sample response.

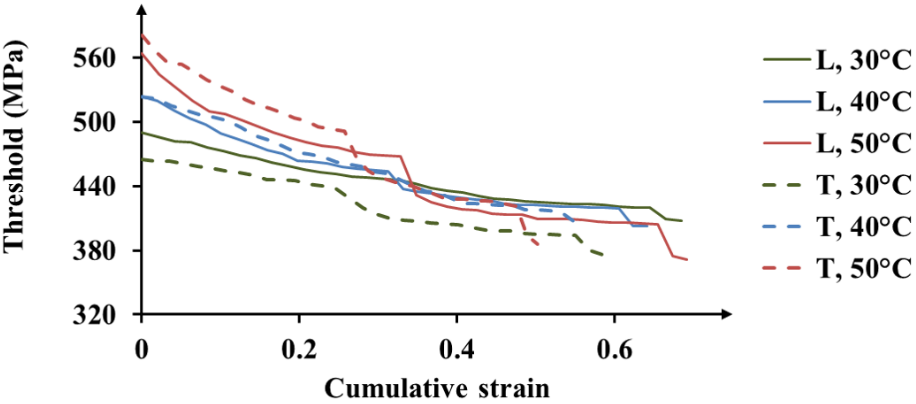

Figure 2.8 – Transformation threshold - cumulative strain diagram for all conditions of experiments.

2.3 Testing in biaxial conditions

2.3.1 Experimental methods

In one of the first series of experiments on SMA under multiaxial loading [Lim and McDowell, 1999], thin-walled NiTi tubes subjected to non-proportional tension-compression cycling in combination with torsion presented strong anisotropy in strains. In particular, it was observed that normal strains in tension were higher than the strains in compression, when combined tension-torsion and compression-torsion proportional tests were conducted. In non-proporitonal configurations, it was shown that the evolution of strain did not follow a normality rule based on the established isotropic asymmetric criterion by Patoor et al. [1995]. This work has shown that the evolution of transformation strains is direction-dependent.

In this section, two cross-shaped specimens were subjected to isothermal cyclic testing at 50°C. The focus is not on anisotropy between normal and shear stresses, but rather between the normal stresses: along the direction of rolling and perpendicular to this direction. The geometry of the sample is presented in Fig. 2.9. This particular geometry was designed to obtain a biaxial stress state at the middle section of the cross, considering the boundary conditions applied from the wide wings. In the following sections, the residual strains of two points of the surface, the geometrical and the point P, will be tracked. The objective of the series of experiments performed under multiaxial conditions is to evaluate the impact of the cyclic loading in one direction on the behavior of a specimen loaded afterwards in a different direction. The definition of a cyclic model could benefit from these experiments, especially if indications arise that the cyclic effect varies during those direction changes. Therefore, appropriate forms of an evolution of the transformation surface (e.g., with the definition of backstress) can be defined and validated from those experiments.

The samples were mounted on an Instron biaxial machine. The wings were fixed on the heads of the machine with the use of three screws in the proper positions of each wing. A cyclic loading of three sequences was applied. Three loading sequences of mechanical cycles were progressively applied. During the loading phase of each cycle, displacement control of the machine heads was held at low speeds. The elongation targets corresponded to the distance between the two heads in the same direction. The control of the heads was performed in such a way that the center of the samples remained stationary. During unloading, force control was applied in order to reach zero force simultaneously in the two directions. It was later measured that the loading speed reached an overall maximum of $\frac{\Delta l/l}{\Delta t} = 2 \cdot 10^{-4}\ \mathrm{sec}^{-1}$ relative to the dimensions of the samples. The experiments took place inside a specially designed enclosure, which covered the samples and

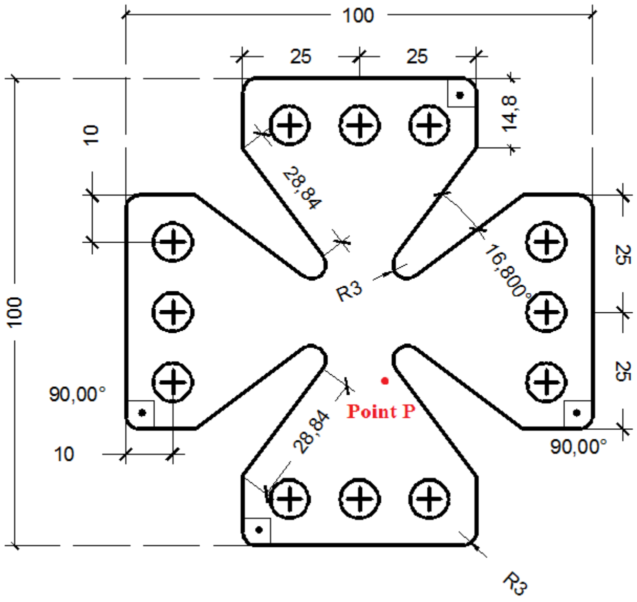

Figure 2.9 – Geometry of cross-shaped sample.

the machine heads. Using an electrical resistance, the temperature in the interior was held constant at the desired 50°C.

The kinematic field of the specimen upper surfaces was tracked with the help of a camera operating in combination with the Digital Image Correlation software Vic2D. The software measured the mean displacement of 0.5x0.5 mm square surfaces, calculating at the same time the mean strain corresponding to the displacement. Because of the long duration of the experiment, only one image per minute was captured. However, the image acquisition at the interesting moments of loading, namely the start and finish of the loading phase, needed to be asserted. For this purpose, an interval of 70 seconds was programmed to interrupt the loading every time the elongation target or the zero force target was attained.

After several trial and error attempts, the final plan for Samples 1 and 2 allowed to recover measurements for residual strain. The plan is illustrated in Fig. 2.10. Starting with sequence A, tension was applied along the direction East-West (E-W), while compression was applied in the perpendicular direction North-South (N-S) in 15 cycles for Sample 1. During sequence B, the axis E-W was maintained free of forces. At the same time, this sample was subjected to 15 cycles of tension in the N-S axis. Finally, during sequence C, 2 of the cycles of sequence A were repeated. For Sample 2, tension and compression direction was reversed. Compression was applied in E-W and Tension in N-S during sequence A. The specimen failed during the first cycle of sequence B, where only tension was applied in E-W. The axis of E-W is parallel to the direction of rolling of the NiTi

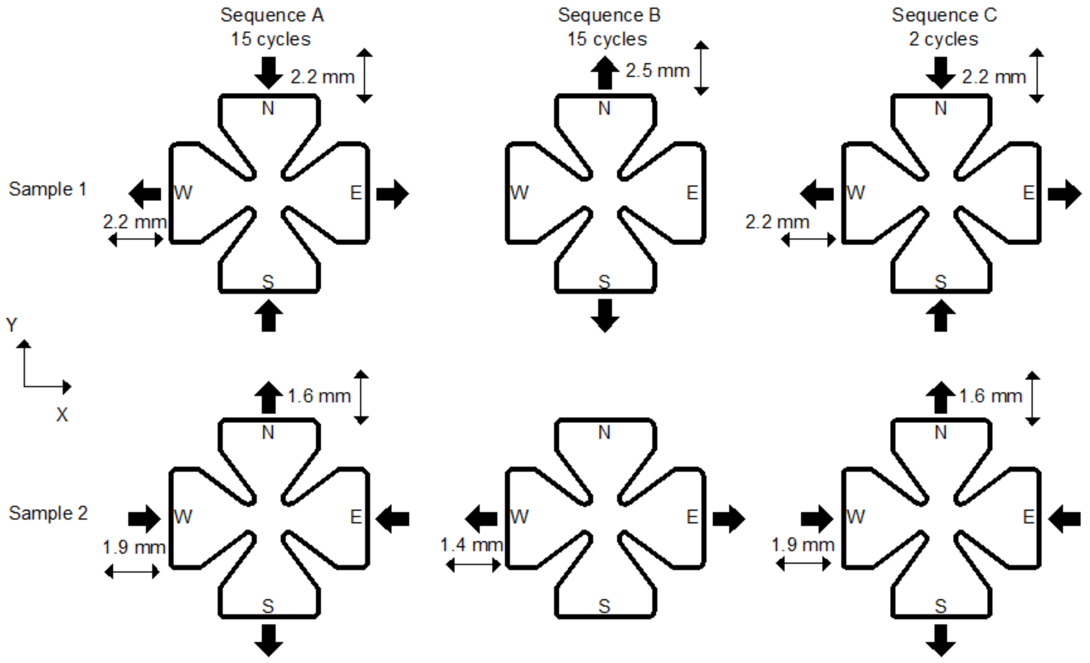

FIGURE 2.10 – Cyclic loading paths for Samples 1 and 2. The axis E-W of the samples is parallel to the rolling direction X.

plates and to the axis X in this figure. The strains in this directions are denoted ε_{xx}, whereas the strains along the direction N-S are called ε_{yy}.

2.3.2 Experimental results

The force-elongation diagrams for the two samples are presented in Figs. 2.11 to 2.13. Only the partial results recovered from the loading of Sample 2 are presented, since this specimen failed shortly after the end of sequence A. Still, it is the only sample which completed sequence A starting with compression along the X axis.

Preliminary remarks concern the form of the global behavior of the samples in terms of their overall force-elongation response. For the axis X of Sample 1 in Fig. 2.11, it is noted:

- A large part of the elongation target is lost after the first cycle. The second cycle of sequence A starts at 0.93 mm of elongation.
- During this first cycle, it seems that a small portion of the sample undergoes transformation starting at around 1 kN of force in the X direction. Then, at appproximately 10 kN, a new linear phase is observed, before further activation of transformation appears in other parts of the sample at 12 kN.

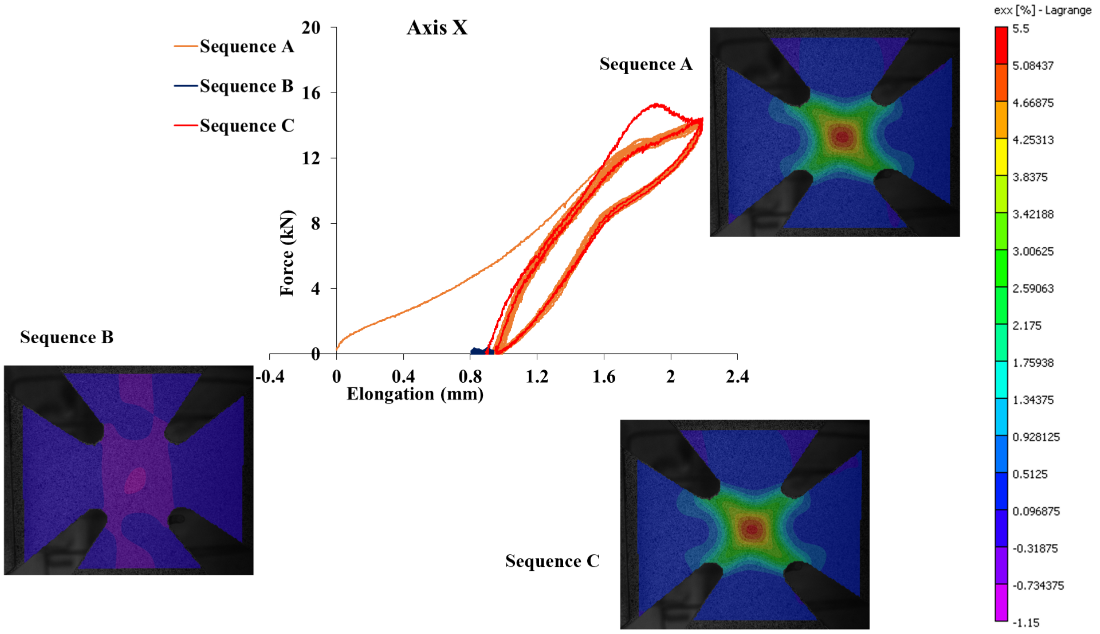

FIGURE 2.11 – Force-elongation diagram of Sample 1 on axis X with the respective strain maps at the end of loading of the last cycle for each sequence.

- The rest of the cycles of sequence A are generally stable, causing negligible residual elongation. The curves of the last 14 cycles show negligible differences.

- During sequence B, the elongation along the X direction appears almost stable, around 0.9 mm. Since no load was applied in that direction during this time, it is caused by the Poisson effect and the transformation strain evolving in all directions following the assumption of isochoric transformation [Hartl et al., 2010; Saleeb et al., 2011]. It is generally accepted that the transformation strain tensor is practically deviatoric, inducing important strain in all normal directions. No measurement apparatus has been utilized to track the off-plane strain during this sequence and thus verify the isochoric nature of transformation, but the strains measured in the Y direction are discussed hereafter.

- Sequence C starts at an elongation level lower than the final elongation of sequence A, meaning that sequence B has nevertheless caused a small amount of residual strain along the X axis.

- During the first step of sequence C, an important irregularity with respect to the rest of the cycles with same loading conditions is observed. In particular, evidently higher forces were developped at approximately 1.8 mm of elongation. However, the force level reached at the end of loading was still the same as previously, causing an apparent hump on the force-elongation curve. At the end of this cycle, the residual strain is comparable on this direction to the one observed at the end of sequence A.

- The strain fields ε_{xx} at the last cycles of sequences A and C are practically identical. This suggests that any observable evolution of the thermomechanical response linked to the sequence A has been annihilated after the first cycle of the sequence C. Note that this is not a statement, and this specific point requires a further particular attention in terms of experimental characterization effort.

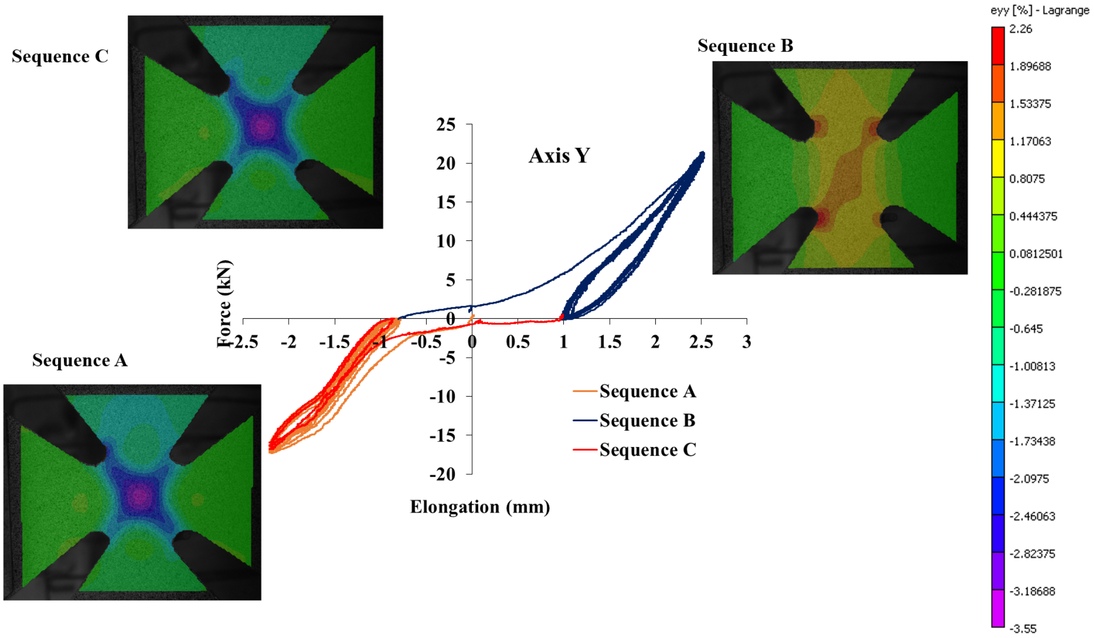

FIGURE 2.12 – Force-elongation diagram of Sample 1 on axis Y with the respective strain maps at the end of loading of the last cycle for each sequence.

For the axis Y of Sample 1 in Fig. 2.12, the following observations can be made:

- Again, residual elongation develops drastically during the first cycle of sequence A. Approximately 0.8 mm of the elongation target are lost. A small portion of the sample seems to cause transformation up to the level of -4 kN and further transformation in the sample is induced after -15 kN.
- The next 14 cycles appear relatively stable.

- The first cycle of sequence B inverts the direction of residual elongation. Its end is found at approximately 1 mm in the direction of loading.

- The remaining 14 cycles of sequence B still exhibit hysteresis, indicating that there are parts of the sample undergoing forward and reverse transformation.

- The irregularity in forces observed in the X axis is not repeated here. The cycles during sequence C are identical to the last cycle of sequence A.

- As expected, the strain fields ε_{yy} at the last cycles of sequences A and C are almost identical.

- The strain field ε_{yy} at the last cycle of sequence B demonstrates values evidently lower in comparison with all other strain measurements at the end of loading phases. Even if transformation appears saturated, the maximum value of 2.26% is suprisingly small, highlighting the anisotropy in transformation strains. It explains the steep slope during transformation in the force-elongation diagram.

- This measurement also explains the relatively small variation of strains strains ε_{xx} during the cycles of sequence B in the previous figure.

In those two fiigures corresponding to Sample 1, the specimen shows a smooth global response in terms of force-elongation in each direction. This effect is linked to a structure response, explained by gradual evolution of transformation throughout the the sample.

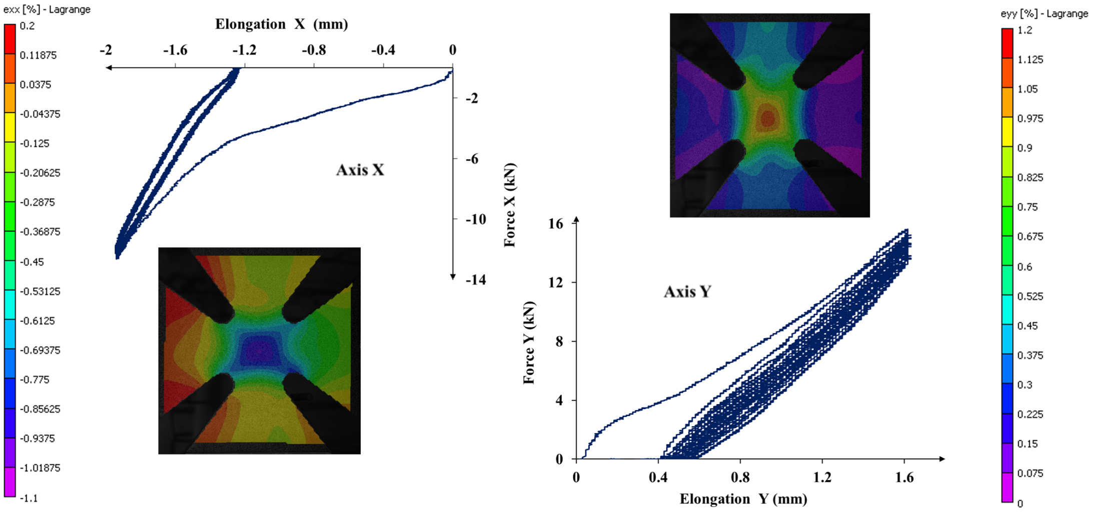

FIGURE 2.13 – Force-elongation diagram of Sample 1 on axes X and Y with the respective strain maps at the end of loading of the last cycle sequence A.

The global response of Sample 2 is depicted in Fig. 2.13. Only the results for the sequence A are extracted. For the response in the directions X and Y, the following can be noted:

- The residual elongation after the first cycle in both axes is approximately 1.205 mm and in axis Y approximately 0.4 mm.
- The transformation starts at comparatively very low forces, at -0.5 kN in direction X and at 1.5 kN in direction Y.
- Similarly gradual activation of transformation is observed in both diagrams.
- Always regarding the first cycle, the elongation caused by transformation in compression seems much more important than for tension, judging from the respective force plateaus.
- Starting from the second cycle, the global response is almost linear in both axes. It appears that the transformed zones which caused already the residual elongation operate in martensitic regime.
- In particular, in the X axis the cycles are stable. The observed hysteresis can be explained by a small fraction of the specimen, not belonging to the part in martensitic regime, undergoing transformation.
- However, the response in the Y axis is different. Even if the hysteresis is not as important, the cycles are not stable. The different levels of force that are reached here might explain the development of 0.18 mm of further residual elongation.
- The ultimate values of strains are much lower in comparison with the respective values in the previous experiment. The maximum value for the strains in the direction of compression was 1.1% and in tension 1.2% .

2.3.3 Results analysis and discussion

In Appendix B, the strain contours corresponding to the end of the first cycle can be found. In the present section, the strain fields captured at the end of sequence A are traced on Fig. 2.14.

- Comparing the axes in tension, it seems that the hardening is more important for tension along the N-W axis (perpendicular to the rolling direction), where less elongation develops linked to transformation strain. The onset of transformation also appears at higher forces, which is consistent to the observation made in the uniaxial testing.
- On the contrary, less residual elongation is developped in the N-W axis, possibly because of the lower reached strain level.

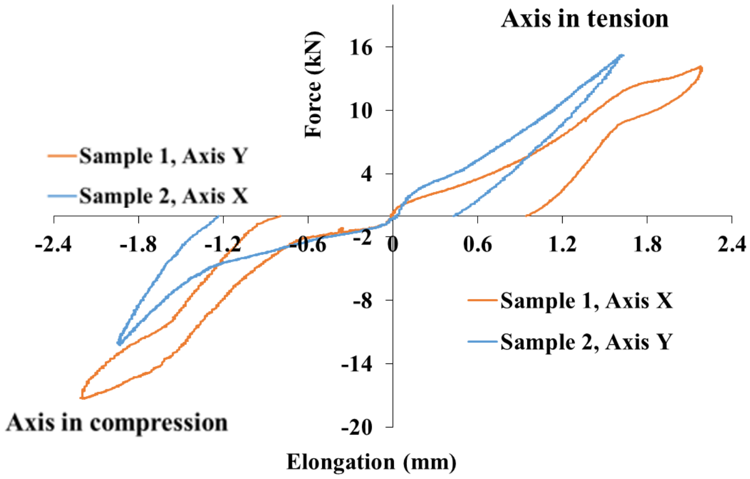

FIGURE 2.14 – Force-elongation diagrams for the first cycle of sequence A for the two samples. At the right-hand side of the force axes, the diagrams corresponding to the directions in tension are traced. Compression at the left-hand side.

- Comparing the axes in compression, the image does not changes considerably regarding all those aspects. Hardening is still more important in the N-W axis and elongation associated to transformation strains is smaller. The residual elongation is also higher along this axis. On the contrary, the force level at the start of transformation seems practically equal.
- For Sample 2, the effect of gradual activation of transformation in the body of the specimen, linked to the multiple slope changes of the diagram, is not observed. This is possibly caused by the smaller reached strain level.
- The only case for which residual elongation evolves importantly after the first cycle is in tension along the N-W axis for Sample 2.

For the irregularity in forces in the force-elongation diagram in the X axis of Sample 1 (see Fig. 2.11), an assumption regarding the appearance of reorientation can be made. It is evident that forward transformation on its own would not be able to produce this softening effect, since this process appears with a subsequent hardening of the whole structure during any other part of the experiment. Although there is no microstructural observation that can support this claim, a gradient activation of a parallel inelastic mechanism, appearing at the same time with transformation, could explain this irregularity. It is assumed here that reorientation is activated in the first cycle of sequence C, caused by the change in the loading direction after the end of sequence B. This activation adds to the loss of the structure stiffness, leading eventually to lower forces as elongation increases after 1.8 mm.

In Fig. 2.15, the residual strain maps are depicted at the end of sequence A. The results from Sample 1 are found on the first row and from Sample 2 on the second row. On the left-hand column are placed the strains corresponding to the direction of tension: ε_{xx} for Sample 1 and ε_{yy} for Sample 2. The strains evolved in the direction of compressive load are on the right-hand column.

Observing the strain maps for Sample 1 (Figs. (a) and (b)), it seems that the residual strains following the loading sense are mostly present around the center. On the contrary, residual strains evolve inversely to loading close to edges of the wings: negative ε_{xx} while tension is applied in that direction and positive ε_{yy} while compression is applied.

The strain maps for Sample 2 (Figs. (c) and (d)) exhibit significantly lower

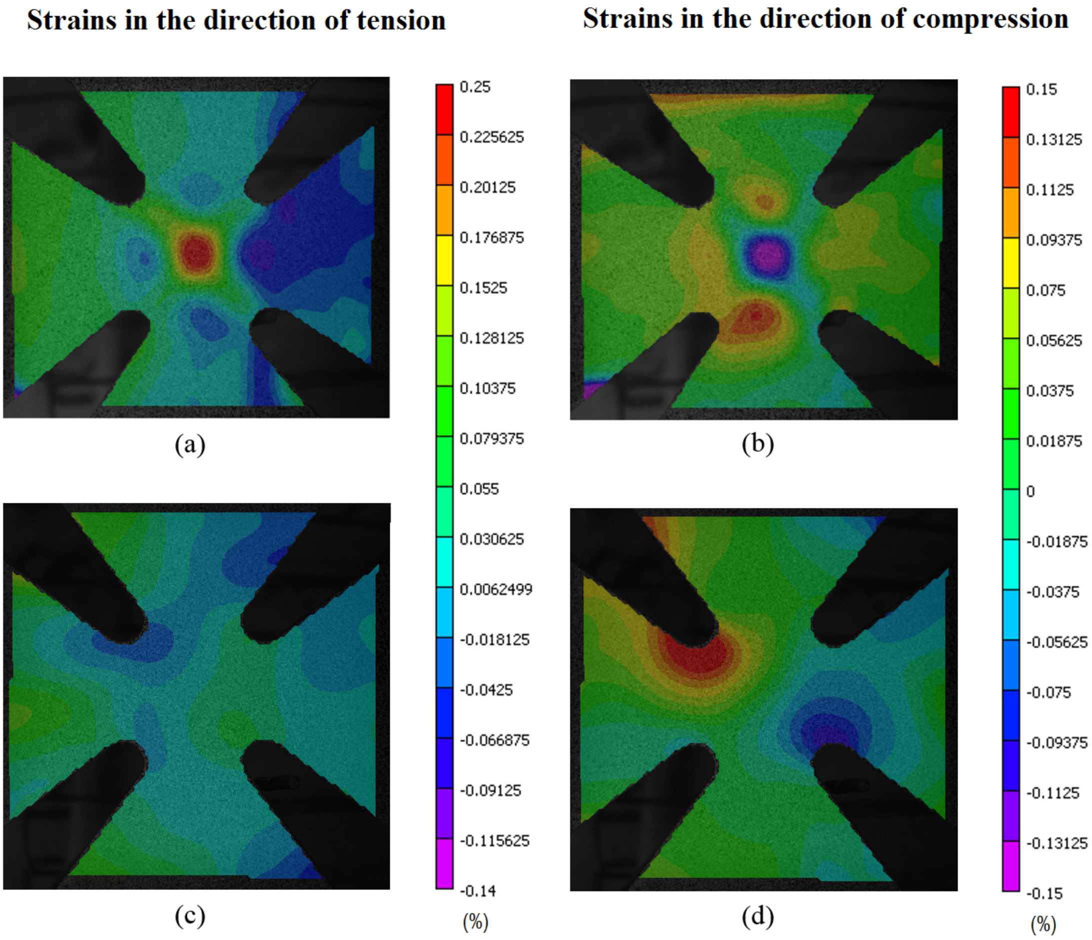

FIGURE 2.15 – Residual strain maps at the end of sequence A. ε_{xx} (a) and ε_{yy} (b) for Sample 1, ε_{yy} (c) and ε_{xx} (d) for Sample 2.

residual strain values in the direction of tension than of compression. This agrees with the higher residual global elongation observed in compression (see Fig. 2.14). The concentration of residual strains appears close to the corners of the middle section here.

Comparing the residual strains in the direction of tension (Figs. (a) and (c)), the strains in Sample 2 are visibly lower. In the direction of compression (Figs. (b) and (d)), the maximum residual strain levels are practically equal, even if the elongation target is lower for Sample 2. This remark further supports the argument that the evolution of residual strains is not only dependent on the total imposed elongation, but also the direction of loading.

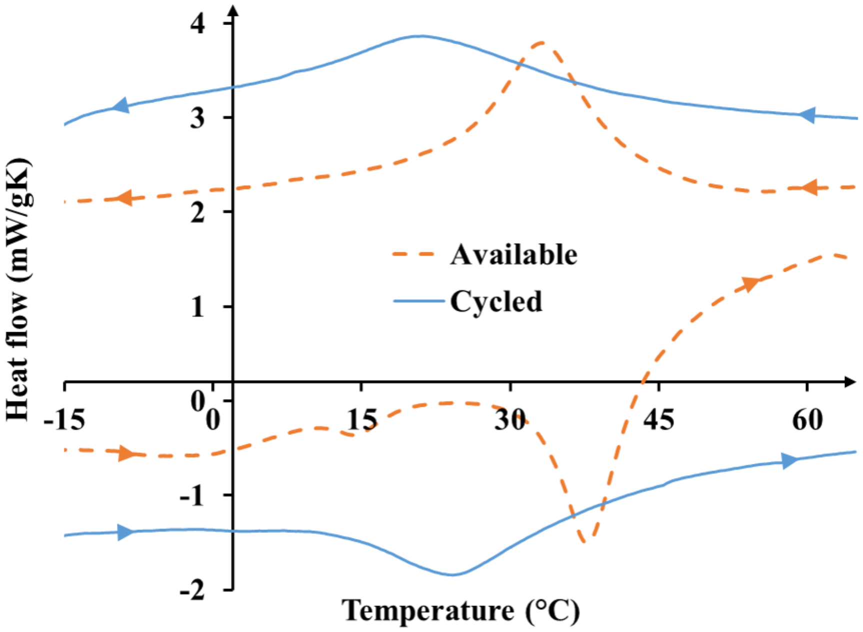

Figure 2.16 – Heat flow measurements from DSC experiments on annealed material not subjected to loading (unloaed) and subjected to biaxial cyclic loading (cycled).

With the intention of acquiring some insight on the effect of mechanical cycling to the evolution of transformation temperatures, DSC experiments were conducted on NiTi fragments and their results are presented in Fig. 2.16. The first fragment was cut from a piece of material subjected to our standard thermal treatment to create specimens available for further testing. The effect of R-phase transformation is visible during heating. At around 15°C, martensite to R-phase transition seems activated. After 45°C, the R-phase to austenite transformation causes an important change in the value of apparent specific heat.

The second fragment was cut from the center of a biaxial Sample 2, after the sample was subjected to the cyclic testing and fractured, while attention has been paid so as not to select a piece close to the fractured zone. Comparing the results with the initial piece, the first conclusion drawn is that the heat flow peaks for martensite and austenite transitions occur at temperatures decreased by about 20°C. Secondly, that the temperature ranges where forward and reverse transformation take place under zero stress have significantly increased. The martensitic and austenitic transformation temperatures have been estimated using the intersecting tangent method and they are presented on Table 2.2. Another important conclusion is that the effect of R-phase transitions is no longer apparent. During heating, the curve after the austenitic transformation is also smoother.

	Unloaded	Cycled
M_s (°C)	42	40
M_f (°C)	26	5
A_s (°C)	30	8
A_f (°C)	45	42

TABLE 2.2 – Transformation temperatures under zero stress for the annealed NiTi (unloaded) and the material subjected to cyclic mechanical loading (cycled).

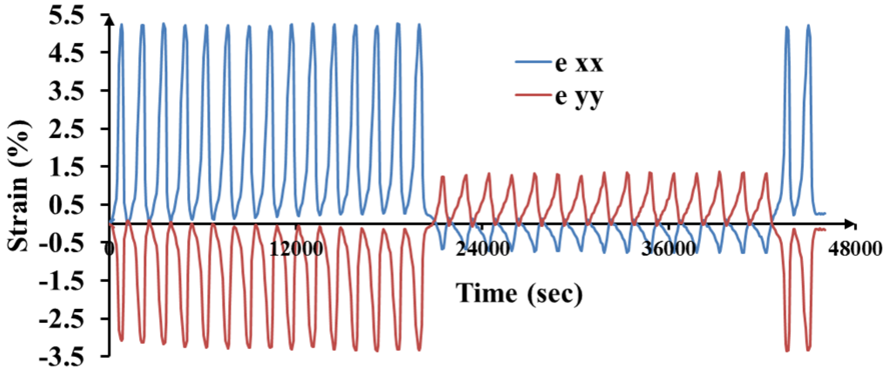

FIGURE 2.17 – History of ε_{xx} and ε_{yy} strain components at the centroid of Sample 1 with respect to time.

In Fig. 2.17, the history of strains for the centroid of Sample 1 is presented. The residual strains evolve gradually during sequence A, reaching 2.7‰ in X direction and -1.4‰ in Y direction. During sequence B, the maximum strains in the centroid are not as important, which possibly explains the lack of residual strains. The loading of sequence C causes residual strains in the level of those in sequence A to appear again.

In Fig. 2.18, the history of strains for the point P of Sample 2 is presented. The first cycle produces 1.1‰in compression and 5.3‰of residual strain. These values

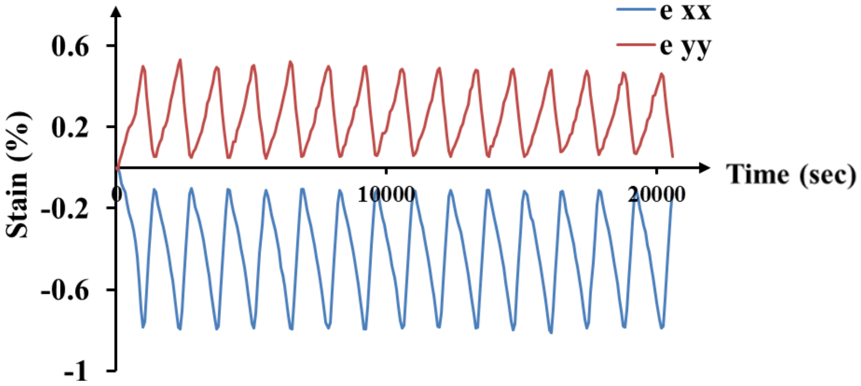

FIGURE 2.18 – History of ε_{xx} and ε_{yy} strain components at point P of Sample 2 with respect to time.

are maintained practically constant in the remaining 14 cycles. The centroid of this sample does not present interest in terms of residual strains. This is evident on Figs. 2.15 (c) and (d), where the strain level is almost zero. The evolution of strains of the point of Sample 1 which is equivalent to P does not show any particular interest either.

2.4 Concluding remarks

In this chapter, the strong effect of loading direction to the behavior of NiTi fabricated by rolling was studied experimentally in terms of cyclic response. In uniaxial experiments, the evolution of residual strains and the reduction of the level of stresses at the transformation start was correlated to cumulative strain. Especially for the transformation onset, the data collected, regarding the loss of linearity on the global response, indicate that the stress heterogeneity is influenced by material anisotropy. In complex cyclic biaxial experiments, important differences in the evolution of transformation strains and the global response of cross-shaped specimens was observed, when the loading directions of these specimens changed. Conclusively, all experimental results support that the cyclic response of rolled NiTi is strongly affected by its inherent anisotropy. All experiments indicate that higher stress levels and lower inelastic strains are consistently expected for loading perpendicular to the direction of rolling.

A setback in terms of results is the lack of data concerning the martensitic volume fraction ξ. Since the modeling work that follows is based on considering ξ as a main internal variable, different methods for investigating anisotropy are used. Still, the results of the experimental work provide a strong inspiration to further investigate the multiaxial behavior in SMAs.

This experimental effort was necessary in order to push further, from the side of cyclic loading, the characterization work which has already been done in the laboratory on plate specimens. The use of the performed experiments in terms of identification will be important to develop a model for cyclic loading of SMAs, that takes properly into account the effect of the loading direction. Some further experiments that will focus on the assumed reorientation effect between the loading sequence should be particularly enlightening. Addressing such modeling aspects, in particular with the further analysis of the complex contribution of transformation induced plasticity and retained martensite besides the phenomena observed in this chapter, remains an open perspective for the team of LEM3. Accordingly, in what follows, the modeling effort emphasizes mostly the aspects of the anisotropy in phase transformation, the reorientation and the strong thermomechanical coupling. This work is the topic of the next chapters of the manuscript.

2.5 References

R. Echchorfi. *Dialogue essais-simulation et identification de lois de comportement d'alliage à mémoire de forme en chargement multiaxial.* PhD thesis, Arts et Métiers ParisTech, 2013. 38

D. Favier, H. Louche, P. Schlosser, L. Orgéas, P. Vacher, and L. Debove. Homogeneous and heterogeneous deformation mechanisms in an austenitic polycrystalline Ti–50.8at.% Ni thin tube under tension. Investigation via temperature and strain fields measurements. *Acta Materialia*, 55(16):5310–5322, sep 2007. ISSN 13596454. doi: 10.1016/j.actamat.2007.05.027. 44

D. Favier and Y. Liu. Restoration by rapid overheating of thermally stabilised martensite of NiTi shape memory alloys. *Journal of Alloys and Compounds*, 297(1-2):114–121, feb 2000. ISSN 09258388. doi: 10.1016/S0925-8388(99)00576-9. 38

D. J. Hartl and D. Lagoudas. Constitutive modeling and structural analysis considering simultaneous phase transformation and plastic yield in shape memory alloys. *Smart Materials and Structures*, 18(10):104017, oct 2009. ISSN 0964-1726. doi: 10.1088/0964-1726/18/10/104017. 35

D. J. Hartl, D. C. Lagoudas, F. T. Calkins, J. H. Mabe, J. T. Mooney, D. C. Lagoudas, F. T. Calkins, and J. H. Mabe. Use of a Ni60Ti shape memory alloy for active jet engine chevron application: I. Thermomechanical characterization. *Smart Materials and Structures*, 19(1): 015020, jan 2010. ISSN 0964-1726. doi: 10.1088/0964-1726/19/1/015020. 48

D. Lagoudas. *Shape Memory Alloys - Modeling and Engineering Applications.* Springer, 2008. 35

C. Lexcellent, A. Vivet, C. Bouvet, S. Calloch, and P. Blanc. Experimental and numerical determinations of the initial surface of phase transformation under biaxial loading in some polycrystalline shape-memory alloys. *Journal of the Mechanics and Physics of Solids*, 50(12): 2717–2735, dec 2002. ISSN 00225096. doi: 10.1016/S0022-5096(02)00007-8. 42

D. Li, H. Garmestani, and S. Ahzi. Processing path optimization to achieve desired texture in polycrystalline materials. *Acta Materialia*, 55(2):647–654, jan 2007. ISSN 13596454. doi: 10.1016/j.actamat.2006.04.041. 35

T. J. Lim and D. L. McDowell. Mechanical Behavior of an Ni-Ti Shape Memory Alloy Under Axial-Torsional Proportional and Nonproportional Loading. *Journal of Engineering Materials and Technology*, 121(1):9, jan 1999. ISSN 00944289. doi: 10.1115/1.2816007. 45

R. Mehrabi, M. T. Andani, M. Elahinia, and M. Kadkhodaei. Anisotropic behavior of superelastic NiTi shape memory alloys ; an experimental investigation and constitutive modeling. *Mechanics of Materials*, 77:110–124, oct 2014. ISSN 01676636. doi: 10.1016/j.mechmat.2014.07.006. 35

M. Miller, T. Chavez, M. Dearborn, E. Tong, E. Devore, R. Marloth, Y.-J. Li, L. Zeng, B. Ramsey, H. Mulazimoglu, J. Guerra, J. Foyos, N. Ula, H. Garmestani, and O. S. Es-Said. Effect of Heat Treatments on the Mechanical Properties of Ti-3Al-2.5V Alloy. *Journal of Materials Engineering and Performance*, 24(9):3277–3290, jul 2015. ISSN 1059-9495. doi: 10.1007/s11665-015-1628-5. 36

S. Nemat-Nasser and W. Guo. Superelastic and cyclic response of NiTi SMA at various strain rates and temperatures. *Mechanics of Materials*, 38(5-6):463–474, may 2006. ISSN 01676636. doi: 10.1016/j.mechmat.2005.07.004. 35

E. Patoor, M. El Amrani, A. Eberhardt, and M. Berveiller. Determination of the origin for the dissymmetry observed between tensile and compression tests on shape memory alloys. *J. Phys.*, IV(2):495–500, 1995. 45

L. Saint-Sulpice, S. A. Chirani, and S. Calloch. A 3D super-elastic model for shape memory alloys taking into account progressive strain under cyclic loadings. *Mechanics of Materials*, 41 (1):12–26, jan 2009. ISSN 01676636. doi: 10.1016/j.mechmat.2008.07.004. 35

A. Saleeb, S. Padula, and A. Kumar. A multi-axial, multimechanism based constitutive model for the comprehensive representation of the evolutionary response of SMAs under general thermomechanical loading conditions. *International Journal of Plasticity*, 27(5):655–687, may 2011. ISSN 07496419. doi: 10.1016/j.ijplas.2010.08.012. 48

3. Contribution to modeling anisotropy in Shape Memory Alloys

3.1 Introduction

Nowadays, SMA applications escape from one-dimensional structures and make use of SMA bodies subjected to complex multi-dimensional loading. In the scope of multi-axial loading, anisotropy has an important influence on material response. An efficient analysis tool thus should be based on a macroscopic continuum model implemented in FEA software that can integrate comprehensive transformation criteria that describe anisotropic effects. Predicting the start and finish of the transformation procedure with as much precision as possible is also of equal importance, since the strains produced during transformation are large in scale and an inaccurate prediction can overthrow the validity of a numerical simulation. The introduction of the effect of processing conditions is also of great importance, since most of the SMA structures are made out of wires or plates. The effect of drawn and rolled processing conditions have to be taken properly into account to obtain an efficient, accurate design tool.

In this chapter, a new suitable transformation criterion for SMAs under isothermal loading is proposed. The purpose is to introduce a criterion that uses the components of the stress tensor and is independent of the transformation strain tensor to form a surface in the space of stresses which determines when transformation in SMAs starts and how it evolves. This criterion proves successful in expressing both asymmetry and anisotropy and also captures multiple results that might come either from experiments or from micromechanical simulations. The second main purpose of the chapter is to develop a formulation that can predict the evolution of transformation strains for textured SMAs.

To calibrate the proposed transformation surface, appropriate experiments are required. Virtual experiments based on micromechanics analysis are used in this chapter. A robust micromechanical model has previously been developed based on the reference work of Patoor et al. [1996]. The input to the micromechanical model is the crystallographic orientation of the grains that forms the SMA polycrystal.

The expected outcome from a polycrystal with random orientation is isotropic yield surface and inelastic strain evolution, whereas textured polycrystal would exhibit anisotropy in transformation [Boehlert et al., 2008; Orgéas and Favier, 1998; Somerday et al., 1997]. By conducting the micromechanics calculations of textured material and then calibrating the proposed equations, the aim is to come up with a consistent scheme which enables the direct connection between the processing conditions and the macroscopic effect on anisotropy that can be implemented in FEA packages for structural design.

The greatest part of the work presented here has been published in the relevant article [Chatziathanasiou et al., 2015]. The present chapter is organized as follows: In the first part, the mathematical configuration of the new transfomation criterion is presented. The convexity and the connection of the formulation with other criteria are investigated. In the second part, two ways of achieving the transition to the space of strains are presented and discussed. The third part is dedicated to the evaluation of the new criterion using results acquired from the micromechanical model and to a discussion about the capability of the present development to capture texture effects of SMAs.

In the terminology of this chapter, experimental results refer either to actual results from experiments, either to results from simulations obtained through the micromechanical model, or both. Furthermore, the following notations are used:

α: representing a scalar.

$\boldsymbol{\alpha}$: representing a second or fourth order tensor.

$\boldsymbol{\alpha}'$: representing the deviatoric part of a second-order tensor.

$tr(\mathbf{A})$: the trace of a second-order tensor denoted $\mathbf{A}$.

$Det(\mathbf{A})$: representing the determinant of a second-order tensor or a matrix denoted $\mathbf{A}$.

$\mathbf{A} : \mathbf{B}$: representing the double contraction product of the tensor $\mathbf{A}$ to the tensor $\mathbf{B}$.

3.2 Anisotropic formulation

The general framework of thermodynamics in which the theoretical work for anisotropy is developped is described in Chapter 1: A prescribed thermodynamic potential involving suitable internal variables dominates the material behavior. The set of all internal variables will be henceforth denoted as $\mathbf{V}$. The set of all general thermodynamic forces (GTFs) will be denoted as $\mathbf{A}$.

It is commonly established that the transformation strain is thermodynamically conjugant to stress, usually by implementing the procedure first applied by Coleman and Gurtin [1967] under the conditions described by Lubliner [1972]. All the basic laws of continuum mechanics need to be validated through the implementation of the thermodynamic potential, including the second law of thermodynamics, usually expressed by the local form of the Clausius-Duhem inequality [Lemaitre and Chaboche, 2002].

SMAs are considered to behave in an elastic manner when transformation does not occur and in a rate-independent, non-linear manner only when transformation occurs. For this reason, the existence of a thermoelastic domain Φ is commonly accepted [Qidwai and Lagoudas, 2000]. It is a closed mathematical hypersurface in the space of selected GTFs, for which the set of GTFs at any given state may only position the material within or on its bounds. In mathematical terms, it is given by:

$$\Phi(\mathbf{A}) \leqslant 0 \quad \text{for all possible sets of } \mathbf{A}. \tag{3.1}$$

When the state of the material lies within the bounds of the thermoelastic region, it behaves elastically and no dissipation is produced. When the state of the material lies on the bounds of the region, the rates $\dot{\boldsymbol{V}}$ of the internal state variables produce dissipation that must comply with the Clausius-Duhem inequality. As a result, the thermoelastic domain is used as the sole criterion to determine whether the material undergoes transformation or not. It is therefore called a transformation criterion and it is comparable to the yield criterion of plasticity for the case of martensitic transformation. It is found as:

$$\Phi(\mathbf{A}) = 0 \tag{3.2}$$

The principle of maximum dissipation has been implemented in some successful models [Lagoudas et al., 2012]. It assumes that the transformation the SMA undergoes is characterized by maximum dissipation. This means that, out of all the admissible sets of rates of the internal variables, the one which leads to the maximum possible dissipation actually occurs. Simo and Hughes [Simo and Hughes, 1998] employed this principle for the case of plasticity to demonstrate the convexity of the yield criterion in stress-internal state variable space, the normality and associativity of the internal variable evolution rules and the presence of Kuhn-Tucker loading conditions. As a direct result of the implementation of the principle, the evolution rule under transformation of all internal state variables is determined by associativity as such:

$$\dot{\mathbf{V}} = \dot{\lambda}\frac{\partial \Phi}{\partial \mathbf{A}}, \ \dot{\lambda} > 0. \tag{3.3}$$

Viewing the transformation strain $\boldsymbol{\varepsilon^t}$ as an internal variable, having established that the stress $\boldsymbol{\sigma}$ is its GTF, it is concluded that:

$$\dot{\boldsymbol{\varepsilon}}^{\boldsymbol{t}} = \dot{\lambda}\frac{\partial \Phi}{\partial \boldsymbol{\sigma}}. \tag{3.4}$$

Similarly, this time avoiding associativity, a transformation potential $Z(\boldsymbol{A})$ can be defined, from which $\dot{\boldsymbol{\varepsilon}}^{\boldsymbol{t}}$ is considered to be derived:

$$\dot{\boldsymbol{\varepsilon}}^{\boldsymbol{t}} = \dot{\lambda}\frac{\partial Z}{\partial \boldsymbol{\sigma}}. \tag{3.5}$$

The notion of the dissipation potential for the case of plasticity is well described in [Lemaitre and Chaboche, 2002]. The difference between (3.4) and (3.5) lies only with the selection of the dissipation potential. In both these equations, the variable $\dot{\lambda}$ is called the transformation multiplier, in equivalence with the plastic multiplier, as found in plasticity.

In the following sections of the current chapter, it will be examined if any of those conditions can hold true for the case of a criterion which is anisotropic in the space of stresses and for the case of a dissipation potential which is isotropic respectively. When relations fitting in (3.4) and (3.5) fail to capture macroscopic observations, then a new evolution rule should be proposed and the whole principle of maximum dissipation does not hold.

3.2.1 Anisotropy in stresses

Introduction of the altered Prager criterion

Patoor et al. [1995] made use of the Prager equation to fit isotropic asymmetric results obtained from their self-consistent micromechanical model. The original form is:

$$h(\boldsymbol{\sigma}) = \sqrt{J_2}\left(1 + b\frac{J_3}{J_2^{3/2}}\right)^{\frac{1}{2}} - k = 0 \tag{3.6}$$

where J_2 and J_3 denote the second and third invariant of the deviatoric part of the stress tensor respectively:

$$J_2 = \frac{1}{2}\sigma'_{ij}\sigma'_{ij}$$

and

$$J_3 = \frac{1}{3}\sigma'_{ij}\sigma'_{jk}\sigma'_{ki},$$

using the Einstein summation for double indices.

In this form (3.6), b corresponds to the actual representation of asymmetry. If $b = 0$, the Prager equation reduces to the classical Von Mises criterion. The value k is the maximum shear stress under pure shear loading, exactly like Von Mises as well. The Prager equation is a valid yield criterion that expresses a convex surface for a specific range of b. Furthermore, it succeeds in expressing an isochoric plastic, or transformation in the case of SMAs, evolution rule, since $tr\left(\frac{\partial h}{\partial \boldsymbol{\sigma}}\right) = 0$ [Bekker and Brinson, 1998].

In this chapter, the notion of the alteration of the stress space axes is used, as in the work of Karafillis and Boyce [1993] to retain the shape of the original transformation surface, but at the same time include anisotropy. On the other hand, the expression is extended to a more general form using a power function. Thus:

$$\hat{\Phi}_\sigma(\boldsymbol{\sigma}) = \sqrt{J_2(\boldsymbol{\sigma}^*)}\left[1 + b\frac{J_3(\boldsymbol{\sigma}^*)}{J_2^{3/2}(\boldsymbol{\sigma}^*)}\right]^{\frac{1}{n}} - k_\sigma = 0 \tag{3.7}$$

where n is a positive real number and:

$$\boldsymbol{\sigma}^* = \boldsymbol{R_\sigma} : \boldsymbol{\sigma} - \boldsymbol{x_\sigma} \tag{3.8}$$

$\boldsymbol{R_\sigma}$ is a fourth order dimensionless tensor which only contains constants and $\boldsymbol{x_\sigma}$ is a second order tensor with dimensions of stress.

In that way, a new space of stresses $\boldsymbol{\sigma}^*$ is created, one that represents a distortion of the space of real stresses and is based on the nature of the tensor $\boldsymbol{R_\sigma}$, the description of which is given below:

1. If the effects that $\boldsymbol{R_\sigma}$ induces on the shear stresses are ignored and a three-dimensional vector $\vec{\sigma}$ consisting in only the normal stresses is considered, then $\boldsymbol{R_\sigma}$ reduces to a matrix expressed as $\boldsymbol{R}$ with the following properties:

    (a) $\boldsymbol{R}$ is expressed as a product of three rotation matrices:

    $$\boldsymbol{R} = \boldsymbol{R_z}\boldsymbol{R_x}\boldsymbol{R_p}. \tag{3.9}$$

    Each of these three matrices represent a simple rotation of the space of normal stresses $\sigma_{11} - \sigma_{22} - \sigma_{33}$ and can be formed out of a single value representing the respective angle:

    $\boldsymbol{R_z}$ represents a rotation around the σ_{33} axis by an angle θ_z.

    $\boldsymbol{R_x}$ represents a rotation around the σ_{11} axis by an angle θ_x.

    $\boldsymbol{R_p}$ represents a rotation around the $\sigma_{11} = \sigma_{22} = \sigma_{33}$ axis by an angle θ_p.

    (b) The result of this expression makes $\boldsymbol{R}$ a rotation matrix itself: It is orthogonal and $Det(\boldsymbol{R}) = 1$.

2. Extending $\boldsymbol{R}$ in order to achieve a transformation of the six-dimensional space of stresses including the shears, results in the fourth-order $\boldsymbol{R_\sigma}$.

Instead of extending the notion of rotation to six dimensions, the transformation of shears is expressed in a simpler way, which is simply the homogeneous anisotropic scaling of the respective axes: in the basic configuration (3.7), $\hat{\Phi}_\sigma$ is expressed by simple scaled functions of the shear stresses:

$$\sigma^*_{ij}{=}l_{ij}\sigma_{ij} \text{ for } i \neq j \text{ where } l_{ij} = l_{ji} > 0. \tag{3.10}$$

The Einstein summation is not used here. The indices i, j denote the dependence of the cofactors l to the position of σ^*_{ij} in the respective tensor.

Eventually, $\boldsymbol{R_\sigma}$ introduces the operation of distortion rather of rotation. More details about the formulation of $\boldsymbol{R_\sigma}$ and its sub-components are found in Appendix C.

On the other hand, $\boldsymbol{x_\sigma}$ represents a translation of the origin of axes by the constant vector $\{\sigma_{o1,}\sigma_{o2}, 0\}$. The analytical expression of the six components of the transformed stress space is finally as follows:

$$\{\sigma^*_{11}, \sigma^*_{22}, \sigma^*_{33}\}^T = \boldsymbol{R_z R_x R_p}\{\sigma_{11}, \sigma_{22}, \sigma_{33}\}^T - \{\sigma_{o1,}\sigma_{o2}, 0\} \tag{3.11}$$

It is worth noting that the operation

$$\boldsymbol{R_\sigma} : \boldsymbol{\sigma}$$

is not equivalent to a rotation of the system coordinates, as in

$$\boldsymbol{\sigma^*} = \boldsymbol{R}.\boldsymbol{\sigma}\boldsymbol{R^T} - \boldsymbol{x_\sigma} \,,$$

except if $\boldsymbol{R}$ is the fourth-order identity tensor. However in that case, the isotropic formulation is reached again. Since the criterion aimed to be utilized depends only on the invariants of the stress deviator, it would be useless to change merely the coordinates, because the value of the invariants would remain the same. Indeed, the choice of introducing rotations around the σ_{11} and σ_{33} axes is purely arbitrary. The case is the same for the choice of introducing the translation of the axes along the direction of the σ_{11} and σ_{22} axes. One could consider rotations and translations with respect to any choice of axes, as long as they induce linearly independent transformations.

A representative 3-D figure illustrating the shape of the criterion is presented in Fig. 3.1. The surface drawn in the space of normal stresses is the locus of the solution of equation (3.7). Its geometrical shape in absolute terms remains unchanged: only its coordinates in the new system are affected. A visible effect of the rotation imposed is that the 3D surface is no longer parallel to the axis $\sigma_{11} = \sigma_{22} = \sigma_{33}$. This means in turn that the proposed criterion is actually pressure-dependent, unlike the isotropic Prager. However, no direction of applied triaxial pressure approaches more favorably the locus of the surface transformation.

In typical pressure-sensitive yield criteria, for example Drucker-Prager [Drucker et al., 1952] or Caddell-Raghava-Atkins [Caddell et al., 1974], tension-compression asymmetry is captured by considering that triaxiality in tension leads to the yield surface at lower levels than in compression. In our case, compressive or tensile triaxiality do not affect differently the stress level for transformation.

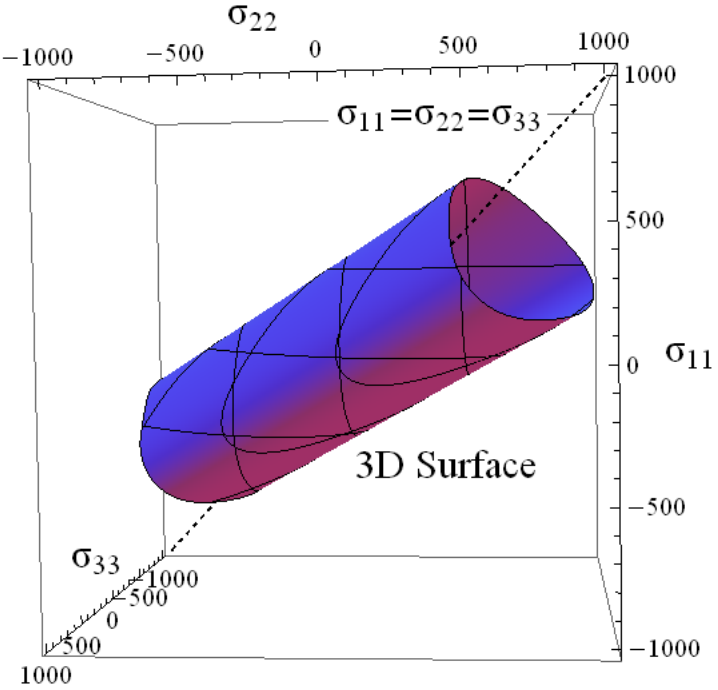

FIGURE 3.1 – Visualization of the 3D shape of the proposed criterion in the space of normal stresses.

One important difference observed between the original and the altered Prager surface is that b is not directly connected to asymmetry. Since the altered Prager equation (3.7) introduces 9 completely independent values:

$$\{\theta_p, \theta_x, \theta_z, \sigma_{o1}, \sigma_{o2}, k_\sigma, l_{12}, l_{23}, l_{13}\}$$

which in turn induce 9 independent transformations, it could capture up to 9 points in the stress space for a choice of b in a wide range. The parameter b is still the main component which controls the shape of the surface.

Convexity analysis and connection with other criteria

The convexity of the new criterion is important in the scope of the present work in order to assist the numerical implementation of the model. Given that the multi-mechanism framework, presented in Chapter 5, is complicated on its own, it is useful to construct equations which can be solved relatively easy. A numerically-friendly convex criterion guarantees a unique minimum during the optimization procedure to approach the solution of the physical problem. When attempting to conduct a convexity analysis, we begin by considering convexity only in the $\sigma_{11} - \sigma_{22} - \sigma_{33}$ space. The shape of the surface in the space of normal stresses is a rotation of the surface described by:

$$\hat{\Phi}^o_\sigma(\boldsymbol{\sigma}) = \sqrt{J_2(\boldsymbol{\sigma})}\left[1 + b\frac{J_3(\boldsymbol{\sigma})}{J_2^{3/2}(\boldsymbol{\sigma})}\right]^{\dfrac{1}{n}} - k_\sigma = 0. \tag{3.12}$$

Therefore, $\hat{\Phi}_\sigma(\boldsymbol{\sigma}) = 0$ is convex as long as $\hat{\Phi}^o_\sigma(\boldsymbol{\sigma}) = 0$ is convex. This realization makes the convexity analysis much simpler. Here, the convexity analysis is straightforward and utilizes simple theorems regarding convexity of surfaces described by an equation of a form such as $\hat{\Phi}^o_\sigma(\boldsymbol{\sigma}) = 0$.
The Hessian:

$$H\left(\hat{\Phi}^o_\sigma\right) = \nabla^2\left(\hat{\Phi}^o_\sigma\left(\boldsymbol{\sigma}\right)\right)$$

is found in the $\sigma_{11} - \sigma_{22} - \sigma_{33}$ space. It is a 3x3 symmetric matrix. The convexity of the surface is guaranteed when H is positive definite, that is when its three leading principal minors are positive for all $\sigma_{11}, \sigma_{22}, \sigma_{33}$. The procedure follows well established methods described in [Boyd and Vandenberghe, 2004; Rockafellar, 1970]. This is a two-way deduction: if the surface is convex, then H must be positive definite. The ending result is a range of values that b can take. For whichever set of $\{\sigma_{11}, \sigma_{22}, \sigma_{33}\}$ H is positive definite as long as b lies within this range. Therefore, the following statement can be made:

$$(\hat{\Phi}_\sigma \text{ and } \hat{\Phi}^o_\sigma \text{ are convex}) \Leftrightarrow |b| < \frac{n\sqrt{27}}{2(9-n)} \leqslant \frac{\sqrt{27}}{2} \quad \text{for} \;\; n < 4.5. \tag{3.13}$$

One conclusion of this is a profound effect for the original isotropic Prager surface (3.6), since b is the physical representation of asymmetry. Indeed, it can be written in the following form:

$$b = \left(\frac{\gamma - 1}{\gamma + 1}\right) a,$$

where $a = \dfrac{3\sqrt{3}}{2} \approx 2.598$ and $\gamma = \left(\dfrac{\sigma_{comp}}{\sigma_{trac}}\right)^n$.

Here, σ_{comp} and σ_{trac} denote the stress level for the start of transformation in unidirectional compression and tension respectively. The limitation of b induces a limitation of the ratio γ as well, in order to ensure convexity:

$$\gamma^{\frac{1}{n}} = \frac{\sigma_{comp}}{\sigma_{trac}} < \left(\frac{9}{9-2n}\right)^{\frac{1}{n}}.$$

This means that the isotropic Prager equation would fail to describe the yield or transformation surface of a material for which the scale of asymmetry exceeds this stress ratio.

As for expanding the convexity analysis to the six-dimensional space which also includes the shear stresses, it proves to be a minor issue to resolve, since $\hat{\Phi}_\sigma(\boldsymbol{\sigma})$ is expressed as a function of a polynomial which is the sum of $l_{ij}^2\sigma_{ij}^2$ components when $i \neq j$. Therefore, convexity ensues.

One may also note how the proposed criterion can reduce to simpler forms. Firstly, considering $\boldsymbol{x_\sigma} = \mathbf{0}$, $\boldsymbol{R_\sigma} = \boldsymbol{I}$ (the fourth order identity tensor) and $n = 2$, the original isotropic Prager equation is yielded. On the other hand, if $\boldsymbol{R_\sigma}$ still represents the said distortion of the stress space, but considering $n \to \infty$, it is shown that the equation is equivalent to a specific case of the Tsai-Wu criterion: Indeed, $\frac{1}{n} \to 0$ and the effect of J_3 vanishes. When $\boldsymbol{R_\sigma} = \boldsymbol{I}$, $\boldsymbol{x_\sigma} = \mathbf{0}$ and $n \to \infty$, the simple Von Mises criterion is reached again. Finally, transversely isotropic behavior for transformation could be given by a suitable combination of the anisotropic constants. The simplest scenario would be a case where σ_{o1} and b are the only non-zero constants. This induces transverse isotropy around the σ_{11} axis, meaning that the transformation for uniaxial tension or compression along the axes 2-2 and 3-3 would evolve in the same manner, manifesting the same deviation from the axis 1-1 in terms of stresses.

3.2.2 Anisotropy in strains

Several constitutive models make use of a scalar ε_{eq}^t called the equivalent transformation strain [Chemisky et al., 2011; Sadjadpour and Bhattacharya, 2007], which is a function of $\boldsymbol{\varepsilon^t}$, to describe at which point the forward transformation is found. In several models [Calloch et al., 2006; Gibeau et al., 2010; Taillard et al., 2008], ε_{eq}^t is considered to be in direct relation with the martensitic volume fraction (MVF) ξ.

The relation between the direction of stress and the rate of transformation strain is called the evolution equation of transformation strain, viewing the strain as the GTF of stress (see Chapter 1). The most general form of this relation is identical to (3.5), choosing a transformation potential $\hat{Z}(\boldsymbol{\sigma})$. Following a direct relation with ξ, a more specific equation is found:

$$\dot{\boldsymbol{\varepsilon}}^{\boldsymbol{t}} = \dot{\xi}\frac{\partial Z}{\partial \boldsymbol{\sigma}}. \tag{3.14}$$

When $\hat{Z}(\boldsymbol{\sigma})$ is chosen to be the transformation surface, the maximum dissipation principle is satisfied [Qidwai and Lagoudas, 2000], and:

$$\dot{\boldsymbol{\varepsilon}}^{\boldsymbol{t}} = \dot{\xi}\frac{\partial\Phi}{\partial\boldsymbol{\sigma}}. \tag{3.15}$$

It is known that in anisotropic SMA, the evolution of strains cannot always be associated with simple J_2-J_3 criteria [Lim and McDowell, 1999]. In this chapter, it is examined how three particular evolution rules for the transformation strain behave with comparison to simulated experimental results. The first rule is consistent with (3.15) and the second with (3.14). In addition to that, a third evolution rule will be introduced, $\dot{\boldsymbol{\varepsilon}}^{\boldsymbol{t}}_{\boldsymbol{r}}$, and compare the total of three options given.

Firstly, we define

$$\dot{\boldsymbol{\varepsilon}}^{\boldsymbol{t}}_{\boldsymbol{as}} = \dot{\xi}H^{cur}\frac{\partial\hat{\Phi}_\sigma}{\partial\boldsymbol{\sigma}} \tag{3.16}$$

This formulation is consistent with the maximum dissipation principle and expresses the rule of associativity. By comparing with (3.4) , it is concluded that the transformation potential is indeed the transformation function. The rate of $\boldsymbol{\varepsilon}^{\boldsymbol{t}}$ is directly linked to $\dot{\xi}$, which is a common practice in various existing works [Boyd and Lagoudas, 1996; Lagoudas et al., 2012]. In a very recent model for anisotropic SMA behavior [Mehrabi et al., 2014], an interesting evolution equation has been proposed, also based on the work of Lagoudas and co-workers. The variable H^{cur} is the scale factor that expresses the magnitude of the rate at which $\boldsymbol{\varepsilon}^{\boldsymbol{t}}$ increases, taken directly from [Hartl et al., 2010] and discussed in Chapter 1.

Secondly, we define

$$\dot{\boldsymbol{\varepsilon}}^{\boldsymbol{t}}_{\boldsymbol{iso}} = \dot{\xi}H^{cur}\frac{\partial\hat{\Phi}^o_\sigma}{\partial\boldsymbol{\sigma}} \tag{3.17}$$

This formulation comes from the consideration of $\hat{\Phi}^o_\sigma$ found in (3.12) as the dissipation potential Z found in (3.5). The derivatives $\frac{\partial\hat{\Phi}^o_\sigma}{\partial\boldsymbol{\sigma}}$ and $\frac{\partial\hat{\Phi}_\sigma}{\partial\boldsymbol{\sigma}}$ found in (3.17) and (3.16) respectively express a tensor which is normal to the respective potentials. The first derivative is called $\boldsymbol{\Lambda_o}$ and it takes the expression that follows:

$$\begin{aligned}\boldsymbol{\Lambda_o}(\boldsymbol{\sigma}) = &\frac{\partial\hat{\Phi}^o_\sigma(\boldsymbol{\sigma})}{\partial\boldsymbol{\sigma}} = \left(1 + b\frac{J_3(\boldsymbol{\sigma})}{J_2^{3/2}(\boldsymbol{\sigma})}\right)^{\frac{1}{n}-1} \\ &\left[\frac{\boldsymbol{\sigma}'}{2\sqrt{J_2(\boldsymbol{\sigma})}} + \frac{b}{6nJ_2^2(\boldsymbol{\sigma})}\left(6J_2(\boldsymbol{\sigma})\boldsymbol{\sigma}'.\boldsymbol{\sigma}' - 4J_2^2(\boldsymbol{\sigma})\boldsymbol{I} + (3n-9)J_3(\boldsymbol{\sigma})\boldsymbol{\sigma}'\right)\right],\end{aligned} \tag{3.18}$$

where $\boldsymbol{I}$ is the identity second-order tensor. On the other hand,

$$\frac{\partial\hat{\Phi}_\sigma}{\partial\boldsymbol{\sigma}} = \frac{\partial\hat{\Phi}^o_\sigma(\boldsymbol{\sigma}^*)}{\partial\boldsymbol{\sigma}} = \frac{\partial\boldsymbol{\sigma}^*}{\partial\boldsymbol{\sigma}} : \frac{\partial\hat{\Phi}^o_\sigma(\boldsymbol{\sigma}^*)}{\partial\boldsymbol{\sigma}^*}, \tag{3.19}$$

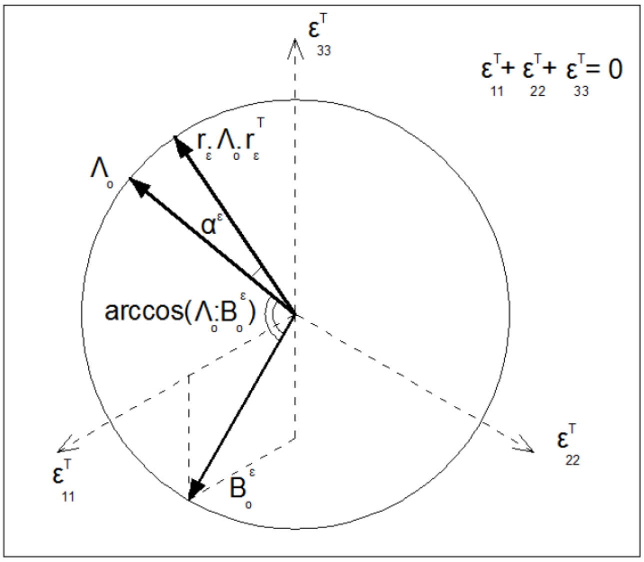

FIGURE 3.2 – The angles involved in the rotation of $\dot{\boldsymbol{\varepsilon}}^{\boldsymbol{t}}_{\boldsymbol{r}}$.

according to the chain rule for derivation.

According to (3.8), it is considered $\dfrac{\partial \boldsymbol{\sigma}^*}{\partial \boldsymbol{\sigma}} = \boldsymbol{R_\sigma}$ and in (3.19) it is found that:

$$\frac{\partial \hat{\Phi}_\sigma}{\partial \boldsymbol{\sigma}} = \boldsymbol{R_\sigma} : \boldsymbol{\Lambda_o}(\boldsymbol{\sigma}^*) \tag{3.20}$$

It is noted that $\boldsymbol{\Lambda_o}(\boldsymbol{\sigma})$ is a deviatoric tensor, as expected from deriving a scalar function of the invariants of the stress deviator.

Finally, we define

$$\dot{\boldsymbol{\varepsilon}}^{\boldsymbol{t}}_{\boldsymbol{r}} = \dot{\xi} H^{cur} \boldsymbol{\Lambda_r} \tag{3.21}$$

Here, a rotation of the normal $\boldsymbol{\Lambda_o}$ of $\dot{\boldsymbol{\varepsilon}}^{\boldsymbol{t}}_2$ is introduced, thus rotating the whole tensor that comes from the expression (3.17):

$$\boldsymbol{\Lambda_r} = \boldsymbol{r_\varepsilon}.\boldsymbol{\Lambda_o}.\boldsymbol{r_\varepsilon^T} \tag{3.22}$$

This rotation comes from an angle a^ε lying on the plane given by $\varepsilon^t_{11}+\varepsilon^t_{22}+\varepsilon^t_{33}=0$. As with $\boldsymbol{R_p}$, the rotation matrix $\boldsymbol{r_\varepsilon}$ is given by:

$$\boldsymbol{r_\varepsilon} = \begin{pmatrix} \cos a^\varepsilon + u^\varepsilon & u^\varepsilon - v^\varepsilon & u^\varepsilon + v^\varepsilon \\ u^\varepsilon + v^\varepsilon & \cos a^\varepsilon + u^\varepsilon & u^\varepsilon - v^\varepsilon \\ u^\varepsilon - v^\varepsilon & u^\varepsilon + v^\varepsilon & \cos a^\varepsilon + u^\varepsilon \end{pmatrix} \tag{3.23}$$

with $u^\varepsilon = \dfrac{\cos a^\varepsilon}{3}$ and $v^\varepsilon = \dfrac{\sin a^\varepsilon}{\sqrt{3}}$. However, unlike θ_p which is considered constant as found in $\boldsymbol{R_p}$, the value of a^ε is a function of $\boldsymbol{\Lambda_o}$:

$$a^\varepsilon = a_o^\varepsilon + 2\sqrt{\frac{F^\varepsilon}{\pi}} Exp\left[-F^\varepsilon\left((\omega-\omega_o^\varepsilon)^2 + (c^\varepsilon)^2\right)\right]\sinh\left[2F^\varepsilon c^\varepsilon(\omega-\omega_o^\varepsilon)\right]. \tag{3.24}$$

In the latter,

$$\omega(\boldsymbol{\Lambda_o} : \boldsymbol{B_o^\varepsilon}) = \begin{cases} \arccos(\boldsymbol{\Lambda_o} : \boldsymbol{B_o^\varepsilon}); & \Lambda_{22} \geqslant 0, \\ 2\pi - \arccos(\boldsymbol{\Lambda_o} : \boldsymbol{B_o^\varepsilon}); & \Lambda_{22} < 0. \end{cases} \tag{3.25}$$

The rest of the variables that appear other than $\boldsymbol{\Lambda_o}$ are constants. The equation (3.24) introduces the rotation necessary to capture the effect of anisotropy to $\boldsymbol{\dot{\varepsilon}^t}$. It is considered that $a_o^\varepsilon = -\theta_p$, whereas $\boldsymbol{B_\varepsilon^o}$ takes the following form:

$$\boldsymbol{B_\varepsilon^o} = \begin{pmatrix} 2^{-1/2} & 0 & 0 \\ 0 & 0 & 0 \\ 0 & 0 & -2^{-1/2} \end{pmatrix}.$$

The choice for the tensor of reference $\boldsymbol{B_o^\varepsilon}$ as the origin for measuring the angles is an arbitrary choice. It represents the intersection of the $\varepsilon_{11}^t + \varepsilon_{22}^t + \varepsilon_{33}^t = 0$ with the plane $\varepsilon_{22}^t = 0$. The criterion $\Lambda_{22} \geqslant 0$ found in (3.25) is a direct result of this choice.

The variables c^ε, F^ε, ω_o^ε should be viewed as material constants and calibrate them according to experimental results. The angles taken in mind for the rotation rule described by (3.21) and (3.24) are demonstrated in the schematic representation of Fig. 3.2. The vectors represent the normal components of the respective tensors and lie on the $\varepsilon_{11}^t + \varepsilon_{22}^t + \varepsilon_{33}^t = 0$ plane.

Another remark for the evolution rule introduced in (3.21) is that it is not given as a direct derivative of a dissipation potential. A surface $\hat{Z}(\boldsymbol{\sigma})$, for which every $\boldsymbol{\dot{\varepsilon}_r^t}$ is normal to, exists but its exact form is unknown.

3.3 Micromechanical model

Trying to comprehend how the microstructure physically affects anisotropy, several interesting works have provided useful insight. Grain boundaries promote inelastic deformations under stress-induced phase transformation. However, it has been shown that, for NiTi systems, they do not affect significantly the macroscopic behavior under mechanical loading. The spread of martensitic transformation to neighboring grains is due to evolution of the local stress field around specific grains where the intergranular constraint inhibits transformation [Gall et al., 2000]. Another aspect is the inherent tension-compression asymmetry at the grain level. In the scope of the work by Patoor et al. [1995], it is found that in the microscopic scale, even the SMA monocrystal is asymmetric in terms of its transformation behavior. Less force is needed to cause direct transformation in tension than in compression and more microscopical strain is produced under tension than under compression. Given the intergranular interaction of crystals with different orientation, and thus with different preferrable directions for transformation under tension, this leads to very strong anisotropy in strains.

Works on crystal plasticity for SMAs have shown that texture is indeed a most important factor determining the recoverable strain [Thamburaja and Anand, 2001]. In the work by Shu and Bhattacharya [1998], the difference between the maximum transformation strains between NiTi and copper-based alloys is explained using a crystal plasticity model, by the different textures these materials develop when subjected to the same forming processes. Finally, crystal plasticity approaches implemented with Finite Element Analysis has allowed the investigation of crystal mechanical problems under complicated internal and external boundary conditions [Merzouki et al., 2010; Roters et al., 2010]. It has lead to the development of multi-scale modeling of anisotropy in polycrystals, as for example in [Van Houtte et al., 2006].

For the purposes of the present work, the numerical simulation of the constitutive response of polycrystalline SMAs is based on a micromechanical model developed by Patoor et al. [1996], implementing the self-consistent scale transition method [Entemeyer, 1996]. It is a method that has been proven robust and been implemented in other micromechanical models as well, e.g. in [Cherkaoui et al., 2000]. The model describes the local thermomechanical behavior inside a single grain from the crystallographic nature of the martensitic transformation and eventually obtains the overall, effective behaviour of the polycrystal. At the local (grain) scale, the thermomechanical constitutive model is derived from a thermodynamical potential. The internal variables are defined as the volume fraction of each of the possible variants according to the crystallographic nature of the crystal. The transformation strain are defined from the Weschler, Liebermann and Read theory, according to the direction of the normal to the habit plane [Siredey et al., 1999; Wechsler et al., 1953]. The evolution of the volume fraction of each of the variant systems is defined from an its associated thermodynamic force. A criterion for forward and for reverse transformation is thus defined, and an adaptative Newton-Raphson algorithm is utilized to determine the volume fraction of each of the variant system accordingly. This method follows the multivariant formulations, where every martensite variant is treated as an inclusion [Patoor et al., 2006]. It allows to escape from the simple consideration that the thermomechanical behavior is driven by one preferred variant according to the loading direction [Gao and Brinson, 2002; Huang and Brinson, 1998]. The operation of estimating the volume fraction of every variant system is conducted for all the grains of the polycrystal at each time increment. Inside a single grain, the martensitic transformation is mainly based on the following assumptions: The lattice vectors of the austenite and martensite possess mutual orientation relationships that depends on the crystallographic nature of the alloy [Bowles and Wayman, 1972]. Martensitic transformation produces predominantly a shear strain along well-defined planes, which is crystallographically reversible [Kaufman and Cohen, 1958].

It is worth mentioning that the choice of this particular micromechanical model was made because it has already been used for the same purpose of assessing other macroscopic models [Taillard et al., 2008]. Its value is furthermore seen to the influence it has on other micromechanical models [Collard and Ben Zineb, 2012]. The thermodynamics involved in the microscopic scale have also influenced the formulation of macroscopic models [Chemisky et al., 2011; Piotrowski et al., 2012] and their application to structural design [Chemisky et al., 2009].

The data input to this model are the crystallographic texture, the transformation temperatures, the material coefficients identified from the state diagram of the SMA, the normal of habit planes and the transformation directions of the 24 variants. An interaction matrix which defines at least two types of interaction (i.e. in the preset case, weak and strong) between the formed martensite variants in a grain is included, following [Entemeyer, 1996]. All these parameters are physical. They do not depend on the past of the material, except for the crystallographic texture.

The crystallographic texture describing the different grains orientation permits to take into account the multiaxial behavior of the polycrystal related to the forming process [Arbab Chirani et al., 2003]. It is well known that the initial crystallographic texture is an important parameter in the behavior of SMA [Bhattacharya and Khon, 1996; Gall and Sehitoglou, 1999]. The use of the micromechanical model permits to follow the microstructure evolution during loading [Calloch et al., 2006].

The evolution equation for the inelastic strain linked with the martensitic transformation ($\dot{\boldsymbol{\varepsilon}}^t$) is written:

$$\dot{\boldsymbol{\varepsilon}}^{\boldsymbol{t}} = \sum_k \dot{\xi}_k \boldsymbol{\varepsilon}^{\boldsymbol{t}}_k, \tag{3.26}$$

where ξ_n is the volume fraction of the k-th variant system and $\boldsymbol{\varepsilon}^t_n$ is the strain associated to such variant, according to the WLR theory [Wechsler et al., 1953]:

$$\boldsymbol{\varepsilon}^{\boldsymbol{t}}_k = g n \otimes m. \tag{3.27}$$

The transformation strain associated to each variant is thus obtain through the knowledge of the shear transformation magnitude g, the unit vector normal to the invariant plane n, and the vector pointing in the direction of the transformation m [Calloch et al., 2006].

The evolution equation for the rate of martensite volume fraction is linked to the thermodynamical force associated to each variant system [Patoor et al., 1995]. The interaction between variants is taken into account through an interaction matrix which differentiate two types of interaction (compatible and incompatible) between the formed martensite variants in a grain. The pair of compatible and incompatible variants are found using the Hill interfacial operators according to [Siredey et al., 1999]. The knowledge of the evolution of each volume fraction of the variant systems allows the computation of the average stress in the grain and the local tangent modulus, according to an imposed increment of total strain. This local increment of strain related to the r-th grain has to be related to the macroscopic boundary conditions, which is achieved using the incremental localisation equation:

$$\dot{\boldsymbol{\varepsilon}}^r = \boldsymbol{A_r}\dot{\boldsymbol{E}} \tag{3.28}$$

where $\dot{\boldsymbol{\varepsilon}}^r$ is the rate of the local total strain tensor, $\dot{\boldsymbol{E}}$ is rate of the macroscopic total strain and $\boldsymbol{A^r}$ is the r-th localization tensor. According to the self-consistent scheme, the localisation tensor is written:

$$\boldsymbol{A_r} = \left[\boldsymbol{I} + \boldsymbol{S}\bar{\boldsymbol{M}}^{\boldsymbol{t}}\left(\boldsymbol{L}^{\boldsymbol{t}}_{\boldsymbol{r}} - \bar{\boldsymbol{L}}^{\boldsymbol{t}}\right)\right]^{-1}, \tag{3.29}$$

where $\boldsymbol{S}$ is the respective Eshelby tensor [Qu and Cherkaoui, 2006], evaluated numerically based on the anisotropic effective modulus description [Lagoudas et al., 1991]. The effective stiffness $\bar{\boldsymbol{L}}^{\boldsymbol{t}}$ (and its inverse, the effective compliance $\bar{\boldsymbol{M}}^{\boldsymbol{t}}$) are computed from

$$\bar{\boldsymbol{L}}^{\boldsymbol{t}} = \sum_r c_r \boldsymbol{A_r}\boldsymbol{L}^{\boldsymbol{t}}_{\boldsymbol{r}} \tag{3.30}$$

3.4 Evaluation of the anisotropic model

The numerical simulations used for assessing the anisotropic model are computed using the microstructural parameters of a Cu-Zn-Al alloy, taken from [Entemeyer, 1996]. These alloys show experimental results matching the simulations carried out by this micromechanical model. The transformation strain amplitude g is 0.23 for all variants. The parameters of the interaction matrix are: 1 MPa describing the weak interaction and 260 MPa for the strong interaction. The elasticity is supposed to be isotropic and the same in the two phases.

In the next two parts, the micromechanical model is used for two purposes:

1. To acquire the necessary experimental results in order to calibrate the criteria. The model provides the set of data used to calculate the target

values of the equation (3.7) for the stress surface and (3.21) for the evolution of transformation strain.

2. To validate the shape and the accuracy of the transformation surfaces. The number of results acquired by the micromechanical model is higher than needed for calibration. Therefore, the remaining data can be used to evaluate how close the transformation surfaces are to the additional predictions of the micromechanical model.

Label of simulation	Loading conditions	Relative angle to 1-1 axis
1	Uniaxial tension in 1	0°
2	Biaxial tension in 1 and 2	45°
3	Uniaxial tension in 2	90°
4	Compression in 1 - tension in 2	135°
5	Uniaxial compression in 1	180°
6	Biaxial compression in 1 and 2	225°
7	Uniaxial compression in 2	270°
8	Tension in 1 - compression in 2	315°

Table 3.1 – Loading paths for the polycrystal specimens. The non-uniaxial cases represent equibiaxial conditions

All the results of that model are obtained after running the simulations of loading of three polycrystal specimens containing 1000 grains each in total. These polycrystals are considered to correspond to an isotropic, rolled or drawn specimen, according to their texture. For the rolled specimen, the rolling direction was set to be along the axis 1-1. For the drawn specimen, the drawing direction was also set along the axis 1-1. Pole figures of these specimens can be found in Appendix D. The results presented hereafter correspond to simulations following eight proportional loading paths assuming plane stress conditions with $\sigma_{33} = \sigma_{12} = 0$ in stress-controlled loading. Normal-shear loading condtions have been the subject of investigations of earlier works. They are not simulated in the present work, because the formulation of anisotropy in the shear directions follows the same principle as existing modeling works, that is a scaling of the shear stress components. The simulated loading paths are presented in Table 3.1. Four of those are uniaxial and the remaining four are biaxial in the directions of the 1-1 and 2-2 axes. In the biaxial cases, the magnitudes of the stress components σ_{11} and σ_{22} are kept equal.

3.4.1 Evaluation of the proposed transformation function

The first set of simulations represent proportional loading of a non-treated polycrystal. The resulting surfaces in the stress and the strain spaces were isotropic. Their shape is found in Figs. 3.3 and 3.5 in dashed lines. The results were similar to those reported in [Bouvet et al., 2004] and [Calloch et al., 2006].

Identified parameter	Value
n	2
b	0.65
θ_p	-0.0953
θ_x	0.0339
θ_z	-0.0373
σ_{o1}	-15.17 MPa
σ_{o2}	-2.93 MPa
k_σ	91.60 MPa

TABLE 3.2 – Calibrated material parameters for rolled specimen

The second set of simulations represents proportional loading of the rolled specimen. The procedure of matching the results of these simulations to fit the criterion described by (3.7) gives the set of target values, presented in Table 3.2.

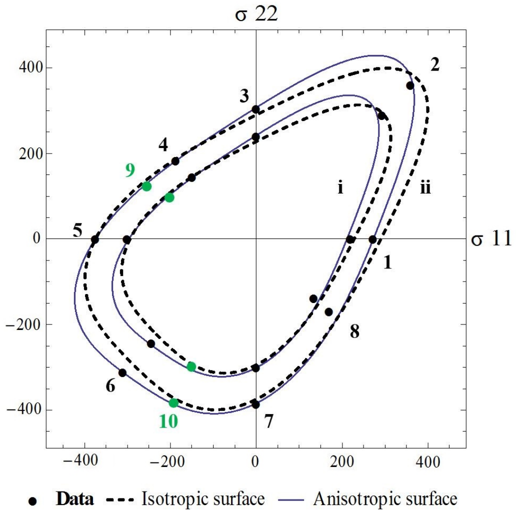

FIGURE 3.3 – Evolution of transformation surface of rolled specimen for (i)$\xi = 20\%$ and (ii)$\xi = 60\%$ and comparison with isotropic surface.

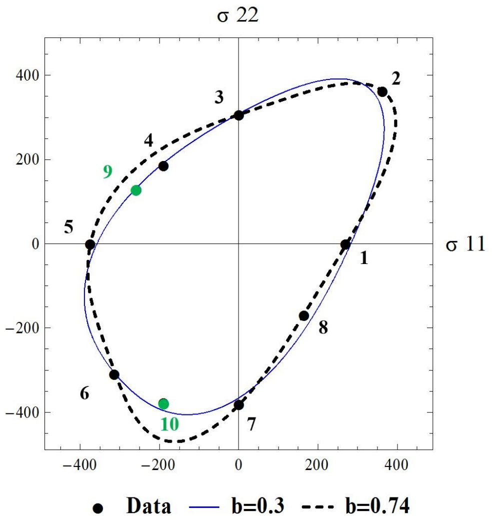

FIGURE 3.4 – Comparison between two anisotropic surfaces for different values of b for the rolled specimen for $\xi = 60\%$.

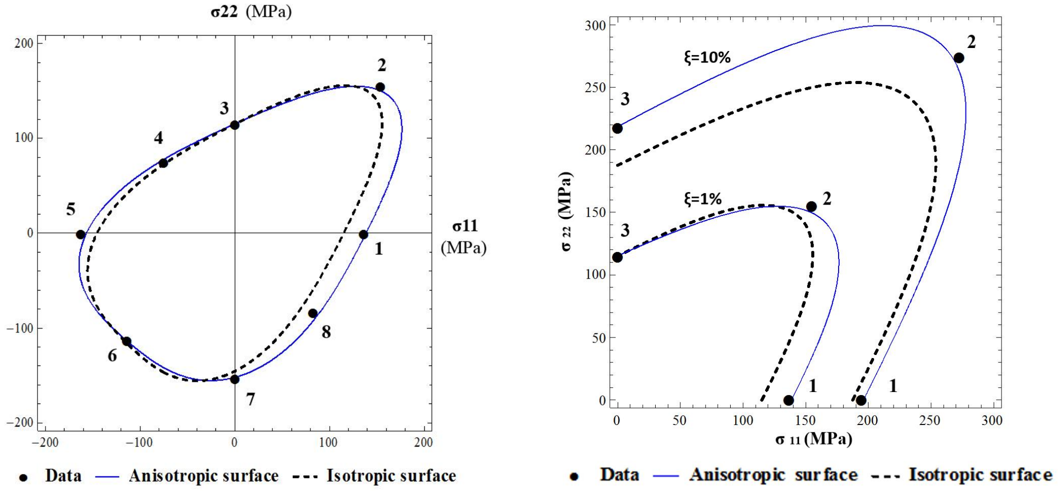

(a) (b)

FIGURE 3.5 – Comparison between isotropic and anisotropic surfaces for the drawn specimen for $\xi = 1\%$ (a) and evolution of transformation surface for $\xi = 1\%$ and $\xi = 10\%$ (b).

Two more anisotropic surfaces were calibrated for a different assumption of the value of the factor b, in order to demonstrate the adaptability of the transformation criterion.

The third set of simulations represents proportional loading of the drawn specimen. Because of the higher level of anisotropy, b was selected here to be a target value and was calibrated at b=0.59.

Figs. 3.3 and 3.5 show a comparison between all the results of the simulations and the criterion in terms of stresses obtained by (3.5), considering n=2. Good agreement is observed. Furthermore, it is shown in Fig. 3.4 that using alternative values for b might result to better surfaces, in the sense that they can capture better the basic material properties, which here are the uniaxial strengths. Given an abundance of data, better calibration is induced by treating b as another target value. To that respect, two more loading paths are considered for the rolled specimen, labelled 9 and 10 in Figs. 3.3 and 3.4. It appears that the extreme in terms of convexity value $b = 0.74$ is not as accurate as the values $b = 0.65$ and $b = 0.3$.

The evolution of the transformation surface as a function of ξ also presents a very interesting effect. The detail of the transformation surfaces corresponding to two different MVFs ξ in Fig. 3.5 reveals that the sense of anisotropy may switch between directions as forward transformation progresses. Indeed, it is clear in Fig. 3.6 that the stress which corresponds to 1% MVF for uniaxial tension in the 1-1 direction is higher than the stress for uniaxial tension in the 2-2 direction ; but this is not the case when $\xi = 10\%$: here, the stress is higher for tension along 2-2. The resulting surfaces accommodating this data are different in shape and not just in size. The size effect would be captured by a direct dependence of k with ξ, and this kind of evolution would be recognized as isotropic hardening [Lemaitre and Chaboche, 2002]. However, in this case, more material parameters have changed between the two MVFs to capture the changing sense of anisotropy. Thus, an evolution of the material parameters is deemed necessary to capture the resulting stress-MVF curves. The proposed anisotropic surfaces in Fig. (3.5b) are calibrated separately according to data points for $\xi = 1\%$ and $\xi = 10\%$ with different sets of σ_{o1}, σ_{o2} and k. For the range of $\xi \in [5\%, 70\%]$, simple linear functions of σ_{o1}, σ_{o2} and k could be considered that fit the evolution. However, more complex functions describing the hardening effect are needed for the implementation with a comprehensive thermodynamic model, such as the ones found in [Lagoudas, 2008].

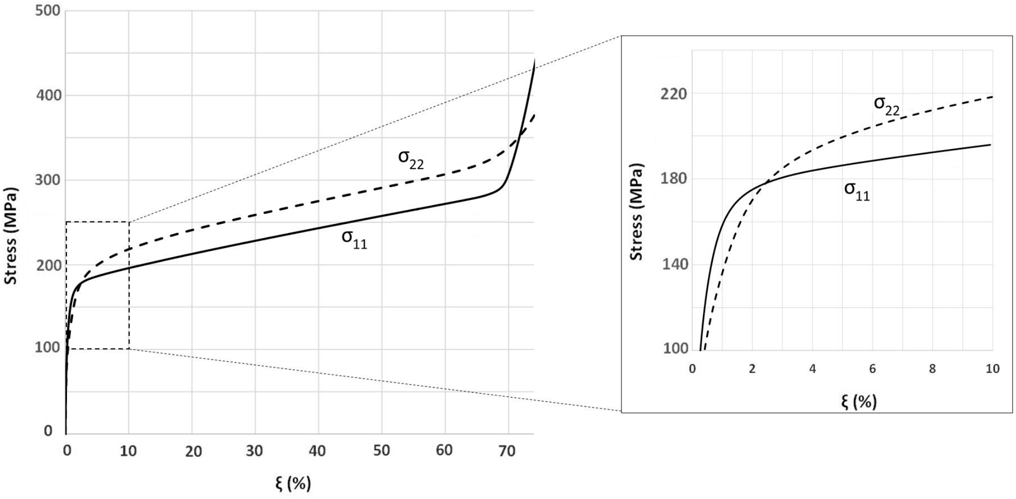

FIGURE 3.6 – Stress-MVF (ξ) diagram for uniaxial tension in directions 1-1 and 2-2 for the drawn specimen.

The importance of calibrating these surfaces extends to compensate for poor abilities to capture the compression-compression strength in a real experiment because of buckling.

3.4.2 Evaluation of evolution equations for the transformation strain

Using the evolution rules (3.16), (3.17) and (3.21), a large number of results regarding transformation strains was gathered. These results correspond to proportional loading under various directions. For every value of ξ, each evolution rule results in a respective locus on which the components of $\boldsymbol{\varepsilon^t}$ lie. In the space of normal transformation strains, the three loci are flat shapes, meaning they all lie on a plane. As demonstrated in Fig. 3.7, the loci S_{iso} and S_r for the normal to the isotropic surface and the proposed evolution rules respectively coincide, whereas the locus S_{as} corresponding to the associative evolution equation lies on a different plane. The results for transformation strain which corresponds to $\xi = 70\%$ for the rolled specimen are also superposed to evaluate the accuracy of the flowrules. The loci S_{iso} and S_r lie on the plane $\varepsilon^t_{11} + \varepsilon^t_{22} + \varepsilon^t_{33} = 0:$ since $\dot{\boldsymbol{\varepsilon}}^{\boldsymbol{t}}_{\boldsymbol{iso}}$ has the same direction as the deviator $\boldsymbol{\Lambda_o}(\boldsymbol{\sigma})$, the resulting $\boldsymbol{\varepsilon}^{\boldsymbol{t}}_{\boldsymbol{2}}$ must be deviatoric. On the other hand, since $\dot{\boldsymbol{\varepsilon}}^{\boldsymbol{t}}_{\boldsymbol{r}}$ represents a rotation of $\dot{\boldsymbol{\varepsilon}}^{\boldsymbol{t}}_{\boldsymbol{iso}}$ around the $\varepsilon^t_{11} = \varepsilon^t_{22} = \varepsilon^t_{33}$ axis, $\dot{\boldsymbol{\varepsilon}}^{\boldsymbol{t}}_{\boldsymbol{r}}$ is still a deviator and the resulting $\boldsymbol{\varepsilon}^{\boldsymbol{t}}_{\boldsymbol{r}}$ is deviatoric as well. That means that the evolution rules (3.17) and (3.21) do succeed in representing transformation as an isochoric process, whereas (3.16) does not.

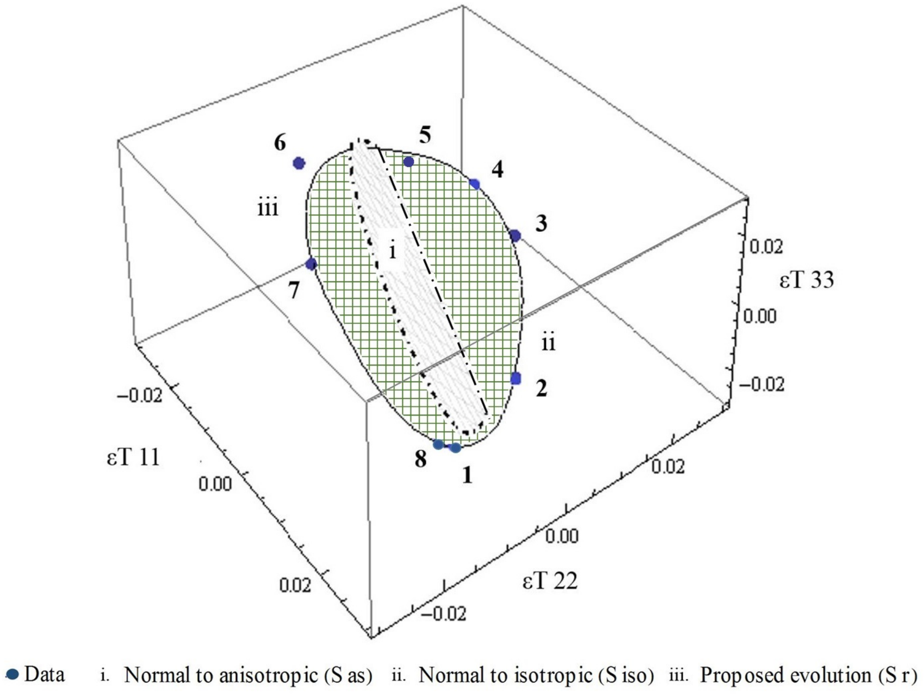

FIGURE 3.7 – 3D map of the normal transformation strains for the rolled specimen at $\xi = 70\%$.

Even though the resulting loci S_{iso} and S_r are identical, the respective evolution rules are not equivalent. While the shape on which they lie is common, the same loading direction corresponds to different positions on the shape. In Figs. (3.8a) and (3.8b), only the strains resulting from proposed criterion are accurate enough to be compared with data points. The results presented are a projection of the points shown in Fig. 3.7 on the $\varepsilon^t_{33} = 0$. For every point on the surfaces corresponding to $\dot{\boldsymbol{\varepsilon}}^t_{\boldsymbol{iso}}$ and $\dot{\boldsymbol{\varepsilon}}^t_{\boldsymbol{r}}$, it is $\varepsilon^t_{33} = -\varepsilon^t_{11} - \varepsilon^t_{22}$.

The fact that the resulting loci coincide for $\dot{\boldsymbol{\varepsilon}}^t_{\boldsymbol{iso}}$ and $\dot{\boldsymbol{\varepsilon}}^t_{\boldsymbol{r}}$ is a direct consequence of the rotation imposed on the direction of $\dot{\boldsymbol{\varepsilon}}^t_{\boldsymbol{iso}}$. This operation simply rearranges the points on the locus: every point is thus reassigned to different loading paths. This is clearly visible on Fig. (3.8a): all the points calculated through the proposed evolution equation still lie on the locus that results from the isotropic prediction. Still, the configuration for $\dot{\boldsymbol{\varepsilon}}^t_{\boldsymbol{r}}$ falls back to $\dot{\boldsymbol{\varepsilon}}^t_{\boldsymbol{iso}}$ if it is assumed that $a^\varepsilon = 0$. Thus, it is shown that $\dot{\boldsymbol{\varepsilon}}^t_{\boldsymbol{r}}$ is a general inclusive form.

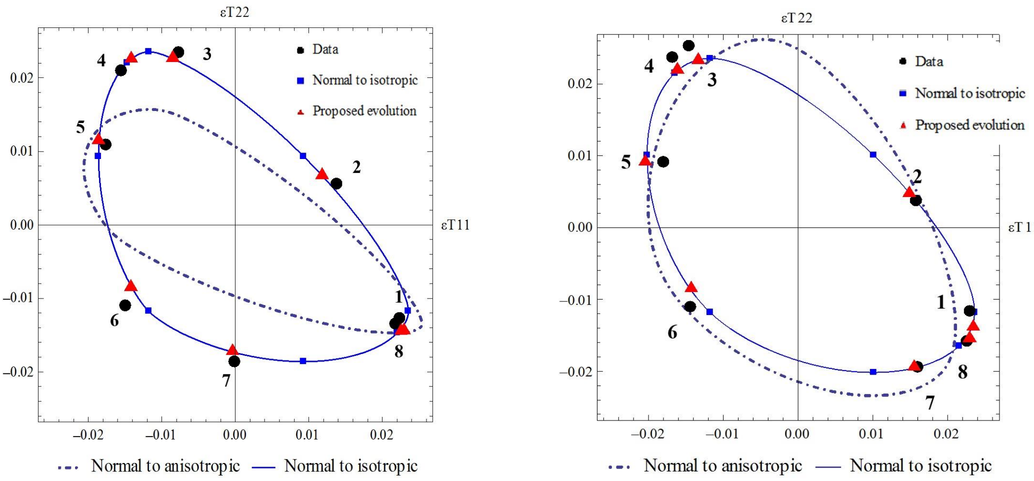

(a) (b)

FIGURE 3.8 – Projection of the resulting transformation strains according to the proposed evolution laws for the rolled (a) and the drawn specimen (b) for $\xi = 70\%$ on the plane $\varepsilon^T_{11} - \varepsilon^T_{22}$.

A notable conclusion drawn from the results of the micromechanics simulations is the strong effect of texture on the anisotropy of transformation strains. The point 7 on Figure (3.8a) corresponds to the response of the rolled specimen under uniaxial compression in the transverse direction of rolling (2-2 axis). Where an isotropic specimen would show a positive strain in the lateral direction (1-1 axis) , this sample shows almost zero strain, and actually negative. The transformation strains corresponding to this point are:
-1.86% in the transverse direction.
-0.05% in the rolling direction.
1.89% in the direction perpendicular to the rolling plane.
On the contrary, the transformation strain values for tension in the transverse direction, respective to the loading case 3, are:
2.34% in the direction of 90°.

-0.77% in the rolling direction.
-1.59% in the direction perpendicular to rolling.
These results are consistent with the observation that in copper-based alloys, martensitic transformation occurs with a small volume change [Bouvet et al., 2004; Lexcellent et al., 2002]. The obtained transformation strains are the result of the activated system of variants, governed by the conjunction of the loading path with the texture effect. A similar anisotropic behavior of transformation strains is apparent on Figure (3.8b) as well. The point 2 corresponds to the response of the drawn specimen under equibiaxial tension. As opposed to the equal evolution of transformation strains for an isotropic material, in this case the material response favors the evolution of strains along the drawing direction. It appears that the effect of texture is much more prominent in the resulting transformation strains of the material than in yield stresses. The proposed evolution law seems able to approach the effect of processing to the end material behavior under proportional loading.

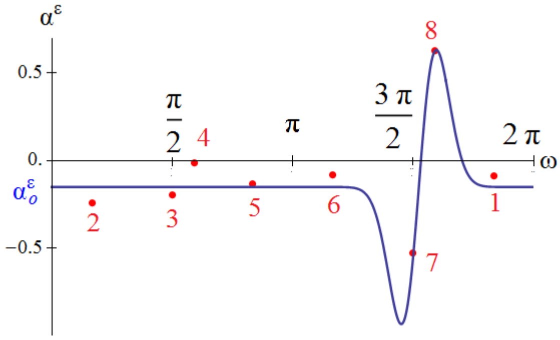

FIGURE 3.9 – Rotation angle α^ε with respect to isotropic prediction ω: representation of equation (3.24)

A schematic representation of the rotation rule conceived in equation (3.24) is given in Fig. 3.9. The direction of strain is rotated by an angle α^ε depending on the equivalent isotropic strain direction ω. This rotation is approximately equivalent to α_o^ε for most loading directions, except in extreme cases. These are captured with the help of the hyperbolic sinus function. The fit of the proposed approach to the loading cases presented on Table 3.1 for the case of the rolled specimen is displayed on the diagram.

It is shown that the expression for $\dot{\boldsymbol{\varepsilon}}_{\boldsymbol{r}}^{\boldsymbol{t}}$ is more accurate to capturing the transformation strain in comparison to $\dot{\boldsymbol{\varepsilon}}_{\boldsymbol{iso}}^{\boldsymbol{t}}$. For the case of the rolled specimen, the values for the material parameters identified are shown in Table 3.3.

Identified parameter	Value
a_o^ε	-0.0953
c^ε	0.0814
F^ε	0.0339
ω_o^ε	-0.0373

Table 3.3 – Calibrated material parameters for the evolution equation (rolled specimen)

3.5 Concluding remarks

A new transformation criterion in terms of stresses and strains suitable for accurately describing the transformation of SMAs has been developed and implemented. The mathematical expressions governing the criterion in terms of stresses are studied with respect to convexity and capturing random anisotropy in SMAs transformation. Furthermore, an accurate evolution rule to govern the evolution of transformation strain has been formulated. It is a non-associated evolution rule which captures incompressibility and still the anisotropy in strains. The equations of the criterion and the evolution rule have been calibrated for a copper based textured SMA (Cu-Zn-Al), using the results from simulations of proportional uniaxial and biaxial plane-stress loading states. These simulations were achieved by utilizing the numerical results from a self-consistent micromechanical model on three polycrystal configurations: isotropic, rolled and drawn. Further results of the model have been used to assess and establish the accuracy of the proposed anisotropic criterion and the related non-associated evolution rule. A good agreement has been obtained by comparing the micromechanical simulations to results provided by the new formulated macroscopic model that can be easily implemented in FE codes. Accordingly, the effects of asymmetry and anisotropy of SMAs behavior can be accounted for structural design of SMA actuators.

A key capability of the procedure used in this chapter to formulate and to calibrate the new transformation criterion and evolution equation is establishing a link between the processing conditions of a material and the final resulting macroscopic anisotropy of the overall behavior. Knowing the texture and the transformation parameters of a SMA polycrystal as a result of processing, and passing through the micromechanical model, the macroscopic behavior is simulated and then the anisotropic effect is captured without the requirement of a large experimental database of multiaxial loadings.

3.6 References

S. Arbab Chirani, D. Aleong, C. Dumont, D. McDowell, and E. Patoor. Superelastic behavior modeling in shape memory alloys. *J. Phys.*, IV(112):205–208, 2003. 72

A. Bekker and L. Brinson. Phase diagram based description of the hysteresis behavior of shape memory alloys. *Acta Materialia*, 46(10):3649–3665, jun 1998. ISSN 13596454. doi: 10.1016/S1359-6454(97)00490-4. 63

K. Bhattacharya and R. Khon. Symmetry, texture and the recoverable strain of shape memory polycrystal. *Acta Materialia*, 44(2):529–542, 1996. 72

C. Boehlert, S. Longanbach, and T. Bieler. Effect of thermomechanical processing on the creep behaviour of Udimet alloy 188. *Philosophical Magazine*, 88(5):641–664, feb 2008. ISSN 1478-6435. doi: 10.1080/14786430801944836. 60

C. Bouvet, S. Calloch, and C. Lexcellent. A phenomenological model for pseudoelasticity of shape memory alloys under multiaxial proportional and nonproportional loadings. *European Journal of Mechanics - A/Solids*, 23(1):37–61, jan 2004. ISSN 09977538. doi: 10.1016/j.euromechsol.2003.09.005. 75, 80

J. S. Bowles and C. M. Wayman. The bain strain, lattice correspondences, and deformations related to martensitic transformations. *Metallurgical Transactions*, 3(5):1113–1121, may 1972. ISSN 0360-2133. doi: 10.1007/BF02642442. 72

J. Boyd and D. Lagoudas. A thermodynamical constitutive model for shape memory materials. Part I. The monolithic shape memory alloy. *International Journal of Plasticity*, 12(6):805–842, jan 1996. ISSN 07496419. doi: 10.1016/S0749-6419(96)00030-7. 68

S. P. Boyd and L. Vandenberghe. *Convex Optimization.* Cambridge University Press, Cambridge, 2004. 66

R. Caddell, R. Raghava, and A. Atkins. Pressure dependent yield criteria for polymers. *Materials Science and Engineering*, 13(2):113–120, 1974. 65

S. Calloch, K. Taillard, S. Arbab Chirani, C. Lexcellent, and E. Patoor. Relation between the martensite volume fraction and the equivalent transformation strain in shape memory alloys. *Materials Science and Engineering: A*, 438-440:441–444, nov 2006. ISSN 09215093. doi: 10.1016/j.msea.2005.12.072. 67, 72, 75

D. Chatziathanasiou, Y. Chemisky, F. Meraghni, G. Chatzigeorgiou, and E. Patoor. Phase Transformation of Anisotropic Shape Memory Alloys: Theory and Validation in Superelasticity. *Shape Memory and Superelasticity*, 1(3):359–374, aug 2015. ISSN 2199-384X. doi: 10.1007/s40830-015-0027-y. 60

Y. Chemisky, A. Duval, B. Piotrowski, T. Ben Zineb, V. Tahiri, and E. Patoor. Numerical tool for SMA material simulation: application to composite structure design. *Smart Materials and Structures*, 18(10):104012, oct 2009. ISSN 0964-1726. doi: 10.1088/0964-1726/18/10/104012. 72

Y. Chemisky, A. Duval, E. Patoor, and T. Ben Zineb. Constitutive model for shape memory alloys including phase transformation, martensitic reorientation and twins accommodation. *Mechanics of Materials*, 43(7):361–376, jul 2011. ISSN 01676636. doi: 10.1016/j.mechmat.2011.04.003. 67, 72

M. Cherkaoui, Q. Sun, and G. Song. Micromechanics modeling of composite with ductile matrix and shape memory alloy reinforcement. *International Journal of Solids and Structures*, 37(11):1577–1594, mar 2000. ISSN 00207683. doi: 10.1016/S0020-7683(98)00332-1. 71

B. Coleman and M. Gurtin. Thermodynamics with internal variables. *J. Chem. Phys.*, 47(2): 85–98, 1967. 60

C. Collard and T. Ben Zineb. Simulation of the effect of elastic precipitates in SMA materials based on a micromechanical model. *Composites Part B: Engineering*, 43(6):2560–2576, sep 2012. ISSN 13598368. doi: 10.1016/j.compositesb.2012.03.015. 72

D. Drucker, W. Prager, and H. Greenberg. Extended limit design theorems for continuous media. *Quarterly of Applied Mathematics*, 9(4):381–389, 1952. 65

D. Entemeyer. *Etude micromécanique du comportement thermomécanique des alliages à mémoire de forme.* Phd, Université de Metz, 1996. 71, 72, 73

K. Gall and H. Sehitoglou. The Role of Texture in Tension-Compression Asymmetry in Polycrystalline NiTi. *International Journal of Plasticity*, 15:69–92, 1999. 72

K. Gall, T. Lim, D. L. McDowell, H. Sehitoglu, and Y. I. Chumlyakov. The role of intergranular constraint on the stress-induced martensitic transformation in textured polycrystalline NiTi. *International Journal of Plasticity*, 16(10-11):1189–1214, jan 2000. ISSN 07496419. doi: 10.1016/S0749-6419(00)00007-3. 70

X. Gao and L. C. Brinson. A Simplified Multivariant SMA Model Based on Invariant Plane Nature of Martensitic Transformation. *Journal of Intelligent Materials Systems and Structures*, 13(12):795–810, dec 2002. ISSN 00000000. doi: 10.1177/1045389X02013012005. 71

E. Gibeau, M. Laydi, and C. Lexcellent. Determination and transport of phase transformation yield surfaces for shape memory alloys. *ZAMM - Journal of Applied Mathematics and Mechanics / Zeitschrift für Angewandte Mathematik und Mechanik*, 90(7-8):595–604, jun 2010. ISSN 00442267. doi: 10.1002/zamm.200900364. 67

D. J. Hartl, D. C. Lagoudas, F. T. Calkins, J. H. Mabe, J. T. Mooney, D. C. Lagoudas, F. T. Calkins, and J. H. Mabe. Use of a Ni60Ti shape memory alloy for active jet engine chevron application: I. Thermomechanical characterization. *Smart Materials and Structures*, 19(1): 015020, jan 2010. ISSN 0964-1726. doi: 10.1088/0964-1726/19/1/015020. 68

M. Huang and L. Brinson. A Multivariant model for single crystal shape memory alloy behavior. *Journal of the Mechanics and Physics of Solids*, 46(8):1379–1409, aug 1998. ISSN 00225096. doi: 10.1016/S0022-5096(97)00080-X. 71

A. Karafillis and M. Boyce. A general anisotropic yield criterion using bounds and a transformation weighting tensor. *J. Mech. Phys. Solids*, 12:1859–1886, 1993. 63

L. Kaufman and M. Cohen. Thermodynamics and kinetics of martensitic transformations. *Progress in Metal Physics*, 7:165–246, jan 1958. ISSN 05028205. doi: 10.1016/0502-8205(58)90005-4. 72

D. Lagoudas, D. Hartl, Y. Chemisky, L. Machado, and P. Popov. Constitutive model for the numerical analysis of phase transformation in polycrystalline shape memory alloys. *International Journal of Plasticity*, 32-33(null):155–183, may 2012. ISSN 07496419. doi: 10.1016/j.ijplas.2011.10.009. 61, 68

D. C. Lagoudas, A. C. Gavazzi, and H. Nigam. Elastoplastic behavior of metal matrix composites based on incremental plasticity and the Mori-Tanaka averaging scheme. *Computational Mechanics*, 8(3):193–203, 1991. ISSN 0178-7675. doi: 10.1007/BF00372689. 73

D. Lagoudas. *Shape Memory Alloys - Modeling and Engineering Applications*. Springer, 2008. 77

J. Lemaitre and J. L. Chaboche. *Mechanics of Solid Materials*. Cambridge University Press, 2002. ISBN 0521477581. 61, 62, 77

C. Lexcellent, A. Vivet, C. Bouvet, S. Calloch, and P. Blanc. *IUTAM Symposium on Mechanics of Martensitic Phase Transformation in Solids*. Springer, 2002. ISBN 1402007418. 80

T. J. Lim and D. L. McDowell. Mechanical Behavior of an Ni-Ti Shape Memory Alloy Under Axial-Torsional Proportional and Nonproportional Loading. *Journal of Engineering Materials and Technology*, 121(1):9, jan 1999. ISSN 00944289. doi: 10.1115/1.2816007. 68

J. Lubliner. On the thermodynamic foundations of non-linear solid mechanics. *International Journal of Non-linear Mechanics*, 7:237–254, 1972. 60

R. Mehrabi, M. T. Andani, M. Elahinia, and M. Kadkhodaei. Anisotropic behavior of superelastic NiTi shape memory alloys ; an experimental investigation and constitutive modeling. *Mechanics of Materials*, 77:110–124, oct 2014. ISSN 01676636. doi: 10.1016/j.mechmat.2014.07.006. 68

T. Merzouki, C. Collard, N. Bourgeois, T. Ben Zineb, and F. Meraghni. Coupling between measured kinematic fields and multicrystal SMA finite element calculations. *Mechanics of Materials*, 42(1):72–95, jan 2010. ISSN 01676636. doi: 10.1016/j.mechmat.2009.09.003. 71

L. Orgéas and D. Favier. Stress-induced martensitic transformation of a NiTi alloy in isothermal shear, tension and compression. *Acta Materialia*, 46(15):5579–5591, sep 1998. ISSN 13596454. doi: 10.1016/S1359-6454(98)00167-0. 60

E. Patoor, M. El Amrani, A. Eberhardt, and M. Berveiller. Determination of the origin for the dissymmetry observed between tensile and compression tests on shape memory alloys. *J. Phys.*, IV(2):495–500, 1995. 62, 70, 73

E. Patoor, A. Eberhardt, and M. Berveiller. Micromechanical Modelling of Superelasticity in Shape Memory Alloys. *Journal de Physique IV*, 6:C1–277, 1996. 59, 71

E. Patoor, D. C. Lagoudas, P. B. Entchev, L. C. Brinson, and X. Gao. Shape memory alloys, Part I: General properties and modeling of single crystals. *Mechanics of Materials*, 38(5-6):391–429, may 2006. ISSN 01676636. doi: 10.1016/j.mechmat.2005.05.027. 71

B. Piotrowski, T. Ben Zineb, E. Patoor, and A. Eberhardt. Modeling of niobium precipitates effect on the Ni47Ti44Nb9 Shape Memory Alloy behavior. *International Journal of Plasticity*, 36:130–147, sep 2012. ISSN 07496419. doi: 10.1016/j.ijplas.2012.03.004. 72

M. Qidwai and D. Lagoudas. On thermomechanics and transformation surfaces of polycrystalline NiTi shape memory alloy material. *International Journal of Plasticity*, 16(10-11):1309–1343, jan 2000. ISSN 07496419. doi: 10.1016/S0749-6419(00)00012-7. 61, 68

J. Qu and M. Cherkaoui. *Fundamentals of Micromechanics of Solids*. John Wiley & Sons, Inc., Hoboken, NJ, USA, aug 2006. ISBN 9780470117835. doi: 10.1002/9780470117835. 73

R. T. Rockafellar. *Convex Analysis*. Princeton University Press, Princeton, 1970. 66

F. Roters, P. Eisenlohr, L. Hantcherli, D. Tjahjanto, T. Bieler, and D. Raabe. Overview of constitutive laws, kinematics, homogenization and multiscale methods in crystal plasticity finite-element modeling: Theory, experiments, applications. *Acta Materialia*, 58(4):1152–1211, feb 2010. ISSN 13596454. doi: 10.1016/j.actamat.2009.10.058. 71

A. Sadjadpour and K. Bhattacharya. A micromechanics inspired constitutive model for shape-memory alloys: the one-dimensional case, feb 2007. 67

Y. Shu and K. Bhattacharya. The influence of texture on the shape-memory effect in polycrystals. *Acta Materialia*, 46(15):5457–5473, sep 1998. ISSN 13596454. doi: 10.1016/S1359-6454(98)00184-0. 71

J. Simo and T. Hughes. *Computational Inelasticity*. 1998. ISBN 0387975209. 61

N. Siredey, E. Patoor, M. Berveiller, and A. Eberhardt. Constitutive equations for polycrystalline thermoelastic shape memory alloys. *International Journal of Solids and Structures*, 36 (28):4289–4315, oct 1999. ISSN 00207683. doi: 10.1016/S0020-7683(98)00196-6. 71, 73

M. Somerday, R. J. Comstock, and J. A. Wert. A systematic analysis of transformation stress anisotropy in shape memory alloys. *Philosophical Magazine A*, 75(5):1193–1207, may 1997. ISSN 0141-8610. doi: 10.1080/01418619708209851. 60

K. Taillard, S. A. Chirani, S. Calloch, and C. Lexcellent. Equivalent transformation strain and its relation with martensite volume fraction for isotropic and anisotropic shape memory alloys. *Mechanics of Materials*, 40(4-5):151–170, apr 2008. ISSN 01676636. doi: 10.1016/j.mechmat.2007.07.005. 67, 72

P. Thamburaja and L. Anand. Polycrystalline shape-memory materials: effect of crystallographic texture. *Journal of the Mechanics and Physics of Solids*, 49(4):709–737, apr 2001. ISSN 00225096. doi: 10.1016/S0022-5096(00)00061-2. 71

P. Van Houtte, A. K. Kanjarla, A. Van Bael, M. Seefeldt, and L. Delannay. Multiscale modelling of the plastic anisotropy and deformation texture of polycrystalline materials. *European Journal of Mechanics - A/Solids*, 25(4):634–648, jul 2006. ISSN 09977538. doi: 10.1016/j.euromechsol.2006.05.003. 71

M. Wechsler, D. Lieberman, and T. Read. On the theory of the formation of martensite. *Trans. AIME J. Metals*, 197:1503–1515, 1953. 71, 72

4. Phenomenological model capturing multiaxial SMA behavior

4.1 Introduction

In this chapter, a physical interpretation of the processes occuring inside a SMA grain is intended to be approached. The notion of mean transformation strain inside the martensitic volume discussed in the article of Chemisky et al. [2011] is examined from a macroscopic point of view to redefine the principles of reorientation, forward and reverse transformation. This leads to the introduction of independent scalar rate variables which drive each of the three strain mechanisms. Accordingly, a robust formalism is presented in terms of thermodynamics which is based on a Gibbs free energy potential. Each internal variable is designed to evolve linearly with respect to those three scalar variables.

In the scope of this chapter, the problem of multiple plasticity-type mechanisms simultaneously activated needs to be addressed. Motivated by the work of Auricchio et al. [2014], each mechanism is thought to have its proper activation criterion. These criteria take the form of yield functions, depending on internal variables. Furthermore, recognizing the strong coupling of thermomechanical effects on SMA behavior [Lim and McDowell, 2002; Morin et al., 2011; Peyroux et al., 1998], the heat caused by mechanical working is calculated under the scope of- multiple mechanisms in play. This investigation is able to cover the issue of latent heat which affects mechanical tests in superelasticity [Brinson et al., 2004; Hartl and Lagoudas, 2008; Heintze and Seelecke, 2008].

A limitation in the present effort of SMA modeling is the absence of a description for R-phase transformations. Especially the austenite to R-phase, followed by R-phase to martensite transitions would add the capability of predicting a dependency of the initial apparent elastic modulus on the temperature [Favier et al., 2007; Sedlák et al., 2012], as observed with the experiments of Chapter 2. Further limitations of the current modeling is the absence of the contribution of even more mechanisms, such as retained marensite, plasticity or viscoplasticity caused by dislocations and other motions inside the SMA polycrystal [Chemisky et al., 2014; Hartl et al., 2010].

In the first part of this chapter, a physical description of the three non-linear mechanisms considered is presented. It is followed by the presentation of the thermodynamic framework which covers the current model. In the second part, certain important remarks allowing the numerical implementation of the model are given, along with a thermomechanical study. In the third part, results deriving from characteristic numerical implementations are given demonstrating the validity of the model.

4.2 Physical description

4.2.1 Strains in the grain scale

In order to give a tangible aspect of the concept behind the current model, a physical representation of the particular behavior of SMAs is attempted to be described. The total continuum of the material is considered divided in a mass of representative volume elements (RVEs). Each of the RVEs has its own continuum for which the proper kinematical relations can be derived. From the work of Chemisky et al. [2011], the notion of the mean transformation strain over the martensitic volume fraction of a RVE is already examined. Since it will be an important variable in the formulation of the model, it is chosen here to be the key element in describing the physical representation of the kinematics.

$$\bar{\boldsymbol{\varepsilon}}^{\boldsymbol{T}} = \frac{1}{V_M} \int\limits_{V_M} \tilde{\boldsymbol{\varepsilon}}^{\boldsymbol{T}}_{\boldsymbol{r}} dV \tag{4.1}$$

In the above expression, $\tilde{\boldsymbol{\varepsilon}}^{\boldsymbol{T}}_{\boldsymbol{r}}$ as the field of transformation strains inside the whole volume V of the RVE for any given point with coordinates $\boldsymbol{r}$, V_M as the martensitic volume in the RVE and $\bar{\boldsymbol{\varepsilon}}^{\boldsymbol{T}}$ is the average value of transformation strain inside V_M. On the other hand, the total transformation strain of the RVE is considered a variable of the material continuum: it is called here $\boldsymbol{\varepsilon}^{\boldsymbol{T}}$:

$$\boldsymbol{\varepsilon}^{\boldsymbol{T}} = \frac{1}{V} \int\limits_{V} \tilde{\boldsymbol{\varepsilon}}^{\boldsymbol{T}}_{\boldsymbol{r}} dV = \frac{1}{V} \left(\int\limits_{V_A} \tilde{\boldsymbol{\varepsilon}}^{\boldsymbol{T}}_{\boldsymbol{r}} dV + \int\limits_{V_M} \tilde{\boldsymbol{\varepsilon}}^{\boldsymbol{T}}_{\boldsymbol{r}} dV \right)$$

where V_A is the austenitic volume inside the RVE. Knowing that the first integral is zero, and by effect of (4.1):

$$\boldsymbol{\varepsilon}^{\boldsymbol{T}} = \frac{V_M}{V} \bar{\boldsymbol{\varepsilon}}^{\boldsymbol{T}} \Leftrightarrow \boldsymbol{\varepsilon}^{\boldsymbol{T}} = \xi \bar{\boldsymbol{\varepsilon}}^{\boldsymbol{T}} \tag{4.2}$$

ξ being the representation of the martensitic volume fraction (MVF).

The variables used so far correspond to different levels of continua. $\tilde{\boldsymbol{\varepsilon}}^{\boldsymbol{T}}_{\boldsymbol{r}}$ is a variable of the RVE continuum. ξ, $\boldsymbol{\varepsilon}^{\boldsymbol{T}}$ and $\bar{\boldsymbol{\varepsilon}}^{\boldsymbol{T}}$ are average values, corresponding to the material continuum. Each RVE is thus treated as a point of the material continuum, achieving the transition to macroscopical considerations. Note that the *macroscopic effective* inelastic strain $\boldsymbol{\varepsilon}^{\boldsymbol{T}}$ is here taken as the volume average of the inelastic strain. This is an assumption that holds only if the average stress in both phases is equal, which is adopted here for such a phenomenological model.

Each particular strain mechanism comes in effect in the evolution of the inelastic strain and the MVF. From (4.2), the time rate formula will be:

$$\dot{\boldsymbol{\varepsilon}}^{\boldsymbol{T}} = \dot{\xi}\bar{\boldsymbol{\varepsilon}}^{\boldsymbol{T}} + \xi\dot{\bar{\boldsymbol{\varepsilon}}}^{\boldsymbol{T}} \tag{4.3}$$

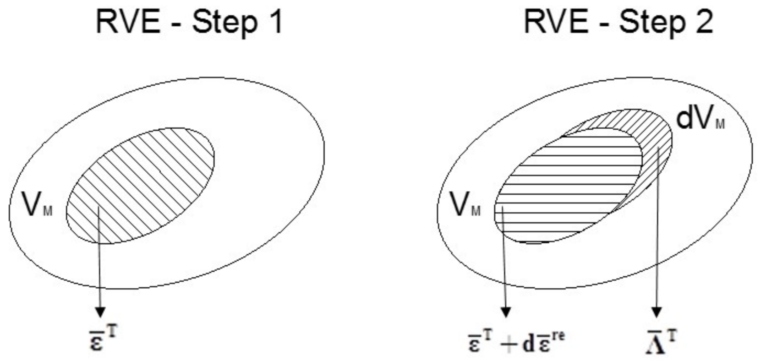

FIGURE 4.1 – Time step representation of a SMA RVE behavior

An incremental scheme of the RVE of a SMA is studied in Fig. 4.1. Two consecutive steps in the loading of a RVE are considered, which are observed with a time difference of dt. Two mechanisms contribute to the change of $\bar{\boldsymbol{\varepsilon}}^{\boldsymbol{T}}$:

a) The transformation strain found in the newly added martensitic volume dV_M, which has a mean value $\bar{\boldsymbol{\Lambda}}^{\boldsymbol{T}}$.

b) The change of transformation strain in the martensitic volume that already exists, causing a change $\boldsymbol{d}\bar{\boldsymbol{\varepsilon}}^{\boldsymbol{re}}$;

Here, it is assumed that these two contributions are the effect of two mechanisms physically separated and independent. The first is the direct effect of the martensitic transformation: in the case of forward transformation, it results to the addition of martensitic volume and, if this volume contains detwinned material, to the addition of the corresponding transformation strain. Accordingly, in the case of reverse transformation, it results to the suppression of martensitic volume and the corresponding transformation strain. Forward and reverse transformation do not affect the transformation strains within the preexisting martensitic volume, and therefore are considered independent of reorientation. The second is the direct effect of reorientation and takes place only inside the pre-existing martensitic volume. It can appear without any change of the martensitic volume fraction, and therefore is considered independent of transformation.

The value of the mean transformation strain in the second step will be a weighted average between the contributions of the two mechanisms, based on the volume in which they occur. The mean transformation strain in the second step is thus considered equal to:

$$\frac{(\bar{\boldsymbol{\varepsilon}}^{\boldsymbol{T}} + \boldsymbol{d\bar{\varepsilon}^{re}})V_M + \bar{\boldsymbol{\Lambda}}^{\boldsymbol{T}} dV_M}{V_M + dV_M}$$

and the respective differential is:

$$\boldsymbol{d\bar{\varepsilon}^{T}} = \frac{(\bar{\boldsymbol{\varepsilon}}^{\boldsymbol{T}} + \boldsymbol{d\bar{\varepsilon}^{re}})V_M + \bar{\boldsymbol{\Lambda}}^{\boldsymbol{T}} dV_M}{V_M + dV_M} - \bar{\boldsymbol{\varepsilon}}^{\boldsymbol{T}} \Rightarrow \boldsymbol{d\bar{\varepsilon}^{T}} = \frac{(\bar{\boldsymbol{\Lambda}}^{\boldsymbol{T}} - \bar{\boldsymbol{\varepsilon}}^{\boldsymbol{T}})dV_M + V_M \boldsymbol{d\bar{\varepsilon}^{re}}}{V_M + dV_M} \tag{4.4}$$

Here, it is assumed that:

$$dV_M \ll V_M \tag{4.5}$$

which is acceptable in the scope of differential calculus. Thus:

$$\boldsymbol{d\bar{\varepsilon}^{T}} = \frac{(\bar{\boldsymbol{\Lambda}}^{\boldsymbol{T}} - \bar{\boldsymbol{\varepsilon}}^{\boldsymbol{T}})dV_M + V_M \boldsymbol{d\bar{\varepsilon}^{re}}}{V_M} = (\bar{\boldsymbol{\Lambda}}^{\boldsymbol{T}} - \bar{\boldsymbol{\varepsilon}}^{\boldsymbol{T}})\frac{dV_M}{V_M} + \boldsymbol{d\bar{\varepsilon}^{re}} \tag{4.6}$$

To simplify the term $\frac{dV_M}{V_M}$, the differential $d\xi$ is considered as:

$$d\xi = d(\frac{V_M}{V}) = \frac{dV_M}{V} - \frac{V_M}{V^2}dV \tag{4.7}$$

The martensitic transformation is considered to be an isochoric process in the sense that

$$tr(\boldsymbol{d\varepsilon^{T}}) = 0$$

[Patoor et al., 1995] and therefore it is recognized that:

$$dV = V\, tr(\boldsymbol{d\varepsilon}) = V\, tr(\boldsymbol{d\varepsilon^{el}} + \boldsymbol{d\varepsilon^{th}}) \tag{4.8}$$

The contribution of the elastic and thermal expansion of the volume of the RVE could be taken in mind to the full extent. However, for the sake of simplicity, these contributions are considered negligible. As a consequence:

$$d\xi = \frac{dV_M}{V} \tag{4.9}$$

which is used to write:

$$d\xi = \frac{dV_M}{V_M}\frac{V_M}{V} = \frac{dV_M}{V_M}\xi \Leftrightarrow \frac{dV_M}{V_M} = \frac{d\xi}{\xi} \tag{4.10}$$

Under the light of (4.10), the equation (4.6) is written:

$$\boldsymbol{d\bar{\varepsilon}^{T}} = (\bar{\boldsymbol{\Lambda}}^{\boldsymbol{T}} - \bar{\boldsymbol{\varepsilon}}^{\boldsymbol{T}})\frac{d\xi}{\xi} + \boldsymbol{d\bar{\varepsilon}^{re}} \tag{4.11}$$

The rate $\dot{\bar{\boldsymbol{\varepsilon}}}^{\boldsymbol{re}}$ is viewed as the foremost effect of reorientation: it is the mean rate of change of transformation strains inside a martensitic volume which is considered constant in time (in two consecutive increments):

$$\dot{\bar{\boldsymbol{\varepsilon}}}^{\boldsymbol{re}} = \frac{1}{V_M}\int\limits_{V_M} \dot{\boldsymbol{\varepsilon}}_{\boldsymbol{r}}^{\boldsymbol{T}}\, dV \tag{4.12}$$

After giving the definitions for transformation and reorientation, it is considered important to clarify the term "transformation strain". In the scope of this chapter, it is used to describe the sum of all inelastic strains in the continuum. All non-thermoelastic strain is included into the term transformation strain. It is stressed that this inelastic strain is not the direct product of only the phase transformation itself ; it is also affected by reorientation. In this sense, both transformation (either forward or reverse) and reorientation contribute in the evolution of transformation strain. Still, this strain is linked to the lattice transformation/orientation in the martensitic, that is "transformed", volume.

4.2.2 Mathematical formulation

Revisiting equation (4.11), a rigorous mathematical formalism is intended to be given. The moving boundaries of the martensite volume, the mathematical representation of which is found in the term $\dot{V}_M$ is shown to be an important aspect to differentiate the two mechanisms. Therefore, it is essential to define the rate of change of the martensitic volume.

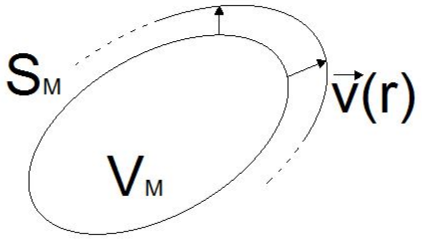

FIGURE 4.2 – Moving boundary of martensitic volume

In Fig. 4.2, S_M is the boundary surface between the martensite and the austenite volumes. The points on this surface have coordinates $\vec{X}(r)$.
$\vec{v}(r) = \dot{\vec{X}}$ is the velocity with which the boundary moves. Here, a flux of martensitic volume is envisioned, basically martensitic volume leaking out of the martensitic volume that is already there. The total difference of it in a step of time should be:

$$dV_M = \int\limits_{V_M} div\left(d\vec{X}(r)\right)dV$$

and in rate form:

$$\dot{V}_M = \int\limits_{V_M} div\dot{\vec{X}}(r)dV = \int\limits_{V_M} div\vec{v}(r)dV \tag{4.13}$$

On the other hand, the rate of the mean transformation strain is given strictly by:

$$\begin{aligned} \dot{\tilde{\boldsymbol{\varepsilon}}}^{\boldsymbol{T}} &= \overset{\bullet}{\left(\frac{1}{V_M}\int\limits_{V_M}\tilde{\boldsymbol{\varepsilon}}_{\boldsymbol{r}}^{\boldsymbol{T}}dV\right)} = -\frac{\dot{V}_M}{V_M^2}\int\limits_{V_M}\tilde{\boldsymbol{\varepsilon}}_{\boldsymbol{r}}^{\boldsymbol{T}}dV + \frac{1}{V_M}\overset{\bullet}{\left(\int\limits_{V_M}\tilde{\boldsymbol{\varepsilon}}_{\boldsymbol{r}}^{\boldsymbol{T}}dV\right)} = \\ &= -\frac{\dot{V}_M}{V_M}\tilde{\boldsymbol{\varepsilon}}^{\boldsymbol{T}} + \frac{1}{V_M}\overset{\bullet}{\left(\int\limits_{V_M}\tilde{\boldsymbol{\varepsilon}}_{\boldsymbol{r}}^{\boldsymbol{T}}dV\right)} \end{aligned} \tag{4.14}$$

According to Leibniz-Reynolds' transport theorem, the rate of the last integral is written:

$$\overset{\bullet}{\left(\int\limits_{V_M}\tilde{\boldsymbol{\varepsilon}}_{\boldsymbol{r}}^{\boldsymbol{T}}dV\right)} = \int\limits_{V_M}(\dot{\tilde{\boldsymbol{\varepsilon}}}_{\boldsymbol{r}}^{\boldsymbol{T}} + \tilde{\boldsymbol{\varepsilon}}_{\boldsymbol{r}}^{\boldsymbol{T}}div\vec{v}(r))dV = \int\limits_{V_M}\dot{\tilde{\boldsymbol{\varepsilon}}}_{\boldsymbol{r}}^{\boldsymbol{T}}dV + \int\limits_{V_M}(\tilde{\boldsymbol{\varepsilon}}_{\boldsymbol{r}}^{\boldsymbol{T}}div\vec{v}(r))dV \tag{4.15}$$

$\vec{v}(r)$ being the vector defined earlier.

In the light of equation (4.12):

$$\overset{\bullet}{\left(\int\limits_{V_M}\tilde{\boldsymbol{\varepsilon}}_{\boldsymbol{r}}^{\boldsymbol{T}}dV\right)} = V_M\dot{\tilde{\boldsymbol{\varepsilon}}}^{\boldsymbol{re}} + \int\limits_{V_M}(\tilde{\boldsymbol{\varepsilon}}_{\boldsymbol{r}}^{\boldsymbol{T}}div\vec{v}(r))dV \tag{4.16}$$

Here, according to the second mean value theorem for integrals, there is a point ψ on the surface S_M for which:

$$\int\limits_{V_M} (\tilde{\boldsymbol{\varepsilon}}^{\boldsymbol{T}}_{\boldsymbol{r}} \, div\vec{v}(r))dV = \tilde{\boldsymbol{\varepsilon}}^{\boldsymbol{T}}_{\psi} \int\limits_{V_M} div\vec{v}(r)dV \tag{4.17}$$

and, by effect of (4.13):

$$\int\limits_{V_M} (\tilde{\boldsymbol{\varepsilon}}^{\boldsymbol{T}}_{\boldsymbol{r}} \, div\vec{v}(r))dV = \boldsymbol{\varepsilon}^{\boldsymbol{T}}(\psi)\dot{V}_M \tag{4.18}$$

The value of $\boldsymbol{\varepsilon}^{\boldsymbol{T}}(\psi)$ is the weighted average of $\tilde{\boldsymbol{\varepsilon}}^{\boldsymbol{T}}_{\boldsymbol{r}}$ based on $div\vec{v}(r)$ in the volume V_M. Here, the definition of $\bar{\boldsymbol{\Lambda}}^{\boldsymbol{T}}$ is updated in order to fit $\boldsymbol{\varepsilon}^{\boldsymbol{T}}(\psi)$. It is the weighted average of $\tilde{\boldsymbol{\varepsilon}}^{\boldsymbol{T}}_{\boldsymbol{r}}$ on the surface S_M based on the divergence of the velocity in V_M:

$$\bar{\boldsymbol{\Lambda}}^{\boldsymbol{T}} = \frac{\int\limits_{V_M} (\tilde{\boldsymbol{\varepsilon}}^{\boldsymbol{T}}_{\boldsymbol{r}} \, div\vec{v})dV}{\int\limits_{V_M} div\vec{v}dV} = \frac{\int\limits_{V_M} (\tilde{\boldsymbol{\varepsilon}}^{\boldsymbol{T}}_{\boldsymbol{r}} \, div\vec{v})dV}{\dot{V}_M} \tag{4.19}$$

Still, in this sense, the product

$$\bar{\boldsymbol{\Lambda}}^{\boldsymbol{T}}\dot{V}_M = \int\limits_{V_M} (\tilde{\boldsymbol{\varepsilon}}^{\boldsymbol{T}}_{\boldsymbol{r}} \, div\vec{v})dV$$

will represent, according to (4.16) the contribution of the transformation strain inside the newly formed martensitic volume to the rate of change of $\tilde{\boldsymbol{\varepsilon}}^{\boldsymbol{T}}$.

Back to the equation (4.15), it will be written, according to (4.16) and (4.18):

$$\dot{\tilde{\boldsymbol{\varepsilon}}}^{\boldsymbol{T}} = -\frac{\dot{V}_M}{V_M}\tilde{\boldsymbol{\varepsilon}}^{\boldsymbol{T}} + \frac{1}{V_M}\left(V_M\dot{\tilde{\boldsymbol{\varepsilon}}}^{\boldsymbol{re}} + \bar{\boldsymbol{\Lambda}}^{\boldsymbol{T}}\dot{V}_M\right) = (\bar{\boldsymbol{\Lambda}}^{\boldsymbol{T}} - \tilde{\boldsymbol{\varepsilon}}^{\boldsymbol{T}})\frac{\dot{V}_M}{V_M} + \dot{\tilde{\boldsymbol{\varepsilon}}}^{\boldsymbol{re}}$$

and by effect of 4.10:

$$\dot{\tilde{\boldsymbol{\varepsilon}}}^{\boldsymbol{T}} = (\bar{\boldsymbol{\Lambda}}^{\boldsymbol{T}} - \tilde{\boldsymbol{\varepsilon}}^{\boldsymbol{T}})\frac{\dot{\xi}}{\xi} + \dot{\tilde{\boldsymbol{\varepsilon}}}^{\boldsymbol{re}} \tag{4.20}$$

which is the rate form of (4.11).

Substituting this in (4.3), it is found that:

$$\dot{\boldsymbol{\varepsilon}}^{\boldsymbol{T}} = \dot{\xi}\bar{\boldsymbol{\Lambda}}^{\boldsymbol{T}} + \xi\dot{\tilde{\boldsymbol{\varepsilon}}}^{\boldsymbol{re}} \tag{4.21}$$

In the incremental scheme described in Fig. 4.1, when an elemental part of martensite dV_M is considered to be removed after the first step, it seems necessary to remove all the transformation strain existing within its volume. This is considered to have a mean value equal to the mean value existing in V_M. Therefore: $\bar{\boldsymbol{\Lambda}}^{\boldsymbol{T}} = \bar{\boldsymbol{\varepsilon}}^{\boldsymbol{T}}$. In the absence of reorientation: $\dot{\boldsymbol{\varepsilon}}^{\boldsymbol{T}} = \dot{\xi}\bar{\boldsymbol{\varepsilon}}^{\boldsymbol{T}}$

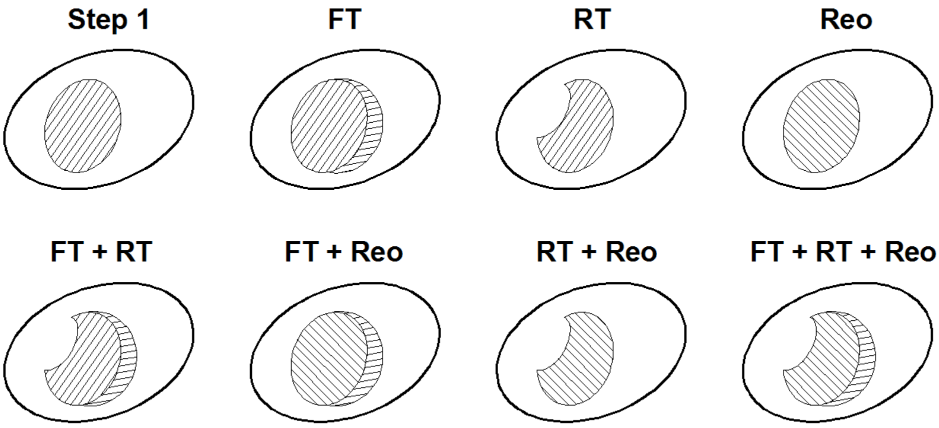

FIGURE 4.3 – Effect of inelastic mechanisms on a SMA RVE

In the next sections, it will become evident that the rate of the total transformation strain is partitioned into three contributors, each driven by the different mechanisms:

$$\dot{\boldsymbol{\varepsilon}}^{\boldsymbol{T}} = \dot{\boldsymbol{\varepsilon}}^{\boldsymbol{F}} + \dot{\boldsymbol{\varepsilon}}^{\boldsymbol{R}} + \dot{\boldsymbol{\varepsilon}}^{\boldsymbol{re}} \tag{4.22}$$

4.3 Phase transformation

The macroscopic effects of the activation of different strain mechanisms on a RVE are visualized in Fig. 4.3. The areas with the filled pattern correspond to martensitic volume, whereas the void areas represent the austenitic volume. All the possible combinations are visualized and compared with the starting configuration of the initial step. The orientation of the filled pattern represents the direction of transformation strains inside the martensitic fraction. When reorientation is activated, this orientation changes. During forward transformation it is visible that the added martensitic volume does not necessarily follow the existing strain orientation. Reverse transformation induces the removal of a piece of martensitic volume and along with it the associated transformation strain.

4.3.1 Forward transformation

The effect of each mechanism in the rate of transformation strain is assumed to follow a linear relation with its respective rate variable. In the macroscopical level, three rate variables are introduced, each of those representing the activation and the magnitude of the effect of their respective mechanisms. For forward transformation, it is:

$$\dot{\xi}^F = \frac{\dot{V}_M^F}{V} \tag{4.23}$$

where $\dot{\xi}^F$ represents the rate of change of the MVF induced by forward transformation is activated.

Furthermore, the effect of each mechanism in the rate of transformation strain is assumed to follow a linear relation with its respective rate variable. The rate of the forward transformation strain is:

$$\dot{\boldsymbol{\varepsilon}}^{\boldsymbol{F}} = \dot{\xi}^F \boldsymbol{\Lambda}_{\boldsymbol{\varepsilon}}^{\boldsymbol{F}} \tag{4.24}$$

where $\boldsymbol{\Lambda}_{\boldsymbol{\varepsilon}}^{\boldsymbol{F}}$ is defined as the forward transformation tensor and gives the relation between $\dot{\xi}^F$ and the magnitude and direction of the induced increment of transformation strain.

4.3.2 Reverse transformation

The macroscopic driving scalar rate for reverse transformation is defined as:

$$\dot{\xi}^R = \frac{\dot{V}_M^R}{V} \tag{4.25}$$

The rate of the reverse transformation strain is:

$$\dot{\boldsymbol{\varepsilon}}^{\boldsymbol{R}} = \dot{\xi}^R \boldsymbol{\Lambda}_{\boldsymbol{\varepsilon}}^{\boldsymbol{R}} \tag{4.26}$$

Here, the definition reverse transformation tensor is presented, which gives the relation between $\dot{\xi}^F$ and the magnitude and direction of the induced increment of transformation strain. As already established at the beginning of the subsection, this should be:

$$\boldsymbol{\Lambda}_{\boldsymbol{\varepsilon}}^{\boldsymbol{R}} = -\bar{\boldsymbol{\varepsilon}}^{\boldsymbol{T}} \tag{4.27}$$

There is the need for a major constraint of SMA behavior to be satisfied: inelastic strains return to zero when there is no martensitic volume. To this end, the following case of loading of a RVE is considered, which induces reverse transformation:

$\dot{\xi} \leq 0$ in a time frame $\Delta t = t - 0$. The reverse transformation is concluded at t, meaning that $\xi(t) = 0$. $\dot{\bar{\boldsymbol{\varepsilon}}}^{\boldsymbol{re}} \neq \mathbf{0}$ for at least one point of Δt, meaning that reorientation is not excluded. Finally, it is assumed that $\bar{\boldsymbol{\Lambda}}^{\boldsymbol{T}} = \bar{\boldsymbol{\varepsilon}}^{\boldsymbol{T}}$, since there is no forward transformation.

It is deduced that:
$\dot{\bar{\boldsymbol{\Lambda}}}^{\boldsymbol{T}} = \dot{\bar{\boldsymbol{\varepsilon}}}^{\boldsymbol{T}}$ and, by effect of (4.20):

$$\dot{\bar{\boldsymbol{\varepsilon}}}^{\boldsymbol{T}} = \dot{\bar{\boldsymbol{\varepsilon}}}^{\boldsymbol{re}} = \dot{\bar{\boldsymbol{\Lambda}}}^{\boldsymbol{T}}$$

The equation (4.3) is now:

$$\dot{\boldsymbol{\varepsilon}}^{\boldsymbol{T}} = \dot{\xi}\bar{\boldsymbol{\Lambda}}^{\boldsymbol{T}} + \xi\dot{\bar{\boldsymbol{\Lambda}}}^{\boldsymbol{T}} = \overset{\bullet}{\left(\xi\bar{\boldsymbol{\Lambda}}^{\boldsymbol{T}}\right)}$$

Looking for $\boldsymbol{\varepsilon}^{\boldsymbol{T}}(t)$, it is found that:

$$\boldsymbol{\varepsilon}^{\boldsymbol{T}}(t) = \boldsymbol{\varepsilon}^{\boldsymbol{T}}(0) + \int_0^t \dot{\boldsymbol{\varepsilon}}^{\boldsymbol{T}}(\tau)d\tau = \boldsymbol{\varepsilon}^{\boldsymbol{T}}(0) + \int_0^t \overset{\bullet}{\left(\xi\bar{\boldsymbol{\Lambda}}^{\boldsymbol{T}}\right)} d\tau = \boldsymbol{\varepsilon}^{\boldsymbol{T}}(0) + \xi(t)\bar{\boldsymbol{\Lambda}}^{\boldsymbol{T}}(t) - \xi(0)\bar{\boldsymbol{\Lambda}}^{\boldsymbol{T}}(0)$$

and

$$\boldsymbol{\varepsilon}^{\boldsymbol{T}}(t) = \boldsymbol{\varepsilon}^{\boldsymbol{T}}(0) + \xi(t)\bar{\boldsymbol{\varepsilon}}^{\boldsymbol{T}}(t) - \xi(0)\bar{\boldsymbol{\varepsilon}}^{\boldsymbol{T}}(0) = \boldsymbol{\varepsilon}^{\boldsymbol{T}}(0) + 0 \cdot \bar{\boldsymbol{\varepsilon}}^{\boldsymbol{T}}(t) - \boldsymbol{\varepsilon}^{\boldsymbol{T}}(0) = \mathbf{0}$$

Conclusively, the finding that $\boldsymbol{\varepsilon}^{\boldsymbol{T}}(t) = \mathbf{0}$ is easily reached. This is an indication that the assumptions made so far satisfy the physical limitations of reverse transformation.

4.3.3 Independence of forward and reverse transformation

The rate of martensitic volume fraction, it is deduced to take the form of:

$$\dot{\xi} = \dot{\xi}^F - \dot{\xi}^R \tag{4.28}$$

Indeed, the expression

$$\dot{\xi} = \frac{\dot{V}_M^F}{V} - \frac{\dot{V}_M^R}{V}$$

complies with the suggestion made in equation (4.9), where dV_M can take positive values for forward and negative values for reverse transformation. It is directly implied that at any given moment,

$$\xi = \int_0^t \dot{\xi}^F d\tau - \int_0^t \dot{\xi}^R d\tau \tag{4.29}$$

These time integrals are denoted as:

$$\xi^F = \int_0^t \dot{\xi}^F d\tau \tag{4.30}$$

and

$$\xi^R = \int_0^t \dot{\xi}^R d\tau \tag{4.31}$$

In order to comply with the physical limitation of the notion of a volume fraction, it is necessary that:

$$0 \leq \xi \leq 1 \Leftrightarrow \xi^R \leq \xi^F \leq 1 + \xi^R \tag{4.32}$$

A simultaneous activation of forward and reverse transformation that may take place during loading presents interesting effects. The increment of forward transformation strain is thought to follow the direction of evolving stress (see Fig. 4.3). The exact relation will be examined later. The evolution of stress is not necessary colinear with previous stress states nor with preexisting strain, thus leading to new average strain direction. An effect of "apparent reorientation" is therefore observed, even if the mechanism of reorientation is activated. A similar phenomenon is proposed in [Saint-Sulpice et al., 2009]. In that work, the term reorientation is used to describe the exact effect of coupled forward and reverse transformation. Careful consideration should be taken when referring to this term in the present chapter. Still, simulations conducted for this work demonstrate that this effect would not be enough to fully capture the change in the direction of inelastic strains and that a full model should be used for complex loading cases.

By using the time integral of equation (4.22), a partition of the total transformation strain in the contribution of forward and reverse transformation and reorientation is proven evident:

$$\boldsymbol{\varepsilon^T} = \boldsymbol{\varepsilon^F} + \boldsymbol{\varepsilon^R} + \boldsymbol{\varepsilon^{re}} \tag{4.33}$$

An important assumption is implied here: Since forward and reverse transformation are considered to appear independently, they may occur simultaneously. In this case, recalling the definition of $\bar{\boldsymbol{\Lambda}}^{\boldsymbol{T}}$ at (4.19), it is deduced that, at any moment:

$$\dot{\xi}^F \boldsymbol{\Lambda}_{\varepsilon}^{\boldsymbol{F}} + \dot{\xi}^R \boldsymbol{\Lambda}_{\varepsilon}^{\boldsymbol{R}} = \dot{\xi} \bar{\boldsymbol{\Lambda}}^{\boldsymbol{T}} \tag{4.34}$$

4.4 Reorientation

The rate variable $\dot{\bar{p}}^{re}$ concerns the evolution of strains inside a grain and represents the rate of change of the magnitude of the mean transformation strain inside a martensitic part of constant volume. It is defined as:

$$\dot{\bar{p}}^{re} = \sqrt{\frac{2}{3}\dot{\bar{\boldsymbol{\varepsilon}}}^{\boldsymbol{re}} : \dot{\bar{\boldsymbol{\varepsilon}}}^{\boldsymbol{re}}} \tag{4.35}$$

Accordingly,

$$\dot{\bar{\boldsymbol{\varepsilon}}}^{\boldsymbol{re}} = \dot{\bar{p}}^{re}\boldsymbol{\Lambda}^{\boldsymbol{re}}_{\boldsymbol{\varepsilon}} \tag{4.36}$$

where $\boldsymbol{\Lambda}^{\boldsymbol{re}}_{\boldsymbol{\varepsilon}}$ is a tensor named reorientation tensor representing the direction for the increment of the mean transformation strain induced by reorientation.

The effect of the rate of increment of mean transformation strain within the martensitic part contributes to the rate of transformation strain in the RVE proportionally to its fraction:

$$\dot{\boldsymbol{\varepsilon}}^{\boldsymbol{re}} = \xi\dot{\bar{\boldsymbol{\varepsilon}}}^{\boldsymbol{re}}$$

and, following equation (4.36):

$$\dot{\boldsymbol{\varepsilon}}^{\boldsymbol{re}} = \xi\dot{\bar{p}}^{re}\boldsymbol{\Lambda}^{\boldsymbol{re}}_{\boldsymbol{\varepsilon}} \tag{4.37}$$

Here, the product $\xi\dot{\bar{p}}^{re}$ is replaced by the new rate variable $\dot{p}^{re}$ to reach:

$$\dot{\boldsymbol{\varepsilon}}^{\boldsymbol{re}} = \dot{p}^{re}\boldsymbol{\Lambda}^{\boldsymbol{re}}_{\boldsymbol{\varepsilon}} \tag{4.38}$$

Thus, equation (4.22) is now rewritten in complete:

$$\dot{\boldsymbol{\varepsilon}}^{\boldsymbol{T}} = \dot{\xi}^{F}\boldsymbol{\Lambda}^{\boldsymbol{F}}_{\boldsymbol{\varepsilon}} + \dot{\xi}^{R}\boldsymbol{\Lambda}^{\boldsymbol{R}}_{\boldsymbol{\varepsilon}} + \dot{p}^{re}\boldsymbol{\Lambda}^{\boldsymbol{re}}_{\boldsymbol{\varepsilon}} \tag{4.39}$$

4.5 Coupling between the mechanisms

4.5.1 Formulation of thermodynamic system

In the thermodynamic framework, it is aimed to incorporate the assumptions made in Section 4.2. A Gibbs free energy potential is chosen to be the base of our model:

$$\begin{aligned} G = &U_o - s_oT + C_v\left[\Delta T - T\ln\left(\frac{T}{T_o}\right)\right] - \frac{1}{2}\boldsymbol{\sigma} : S : \boldsymbol{\sigma} - \boldsymbol{\sigma} : \boldsymbol{\alpha}\Delta T - \boldsymbol{\sigma} : \boldsymbol{\varepsilon}^{\mathbf{T}} + \\ &(1+\lambda^{re})\boldsymbol{X} : \boldsymbol{v}^{\boldsymbol{re}} + H(\xi) \end{aligned} \tag{4.40}$$

where:
$\boldsymbol{\sigma}$ is the Cauchy stress.
S is the elastic compliance tensor.
$\boldsymbol{\alpha}$ is the thermal expansion coefficient.
$\Delta T = T - T_o$ is the difference between the current temperature T and the temperature at the reference state T_o.
U_o is the specific internal energy at the reference state.
s_o is the specific entropy at the reference state.
C_v is the specific heat capacity.
$H(\xi)$ is a function accounting for the isotropic hardening associated with transformation, linked to the martensitic volume fraction [Hartl et al., 2010].
$\boldsymbol{v^{re}}$ is defined as the hardening strain for reorientation.
$\boldsymbol{X}$ is defined as backstress.
Finally, λ^{re} is a limiting cofactor for reorientation.

It is noted that the variables S, $\boldsymbol{\alpha}$, U_o, s_o and C_v are assumed to vary linearly according to the martensitic volume fraction. For example:
$S = S^A + \xi(S^M - S^A)$ for the elastic compliance tensor, where the superscripts A and M stand for the austenitic and martensitic phases respectively. Similar assumption has been adopted in Lagoudas et al. [2012], supported by the analysis of Boyd and Lagoudas. In the case of mechanical elastic properties, it was shown that using either the rule of mixtures on the compliance tensors (which is assumed here) or a micromechanical scheme (Mori-Tanaka) has little impact on the effective response [Boyd and Lagoudas, 1994].

The internal variables are chosen to be: $\boldsymbol{\sigma}, T, \boldsymbol{\varepsilon^F}, \boldsymbol{\varepsilon^R}, \boldsymbol{\varepsilon}^{\boldsymbol{re}}, \boldsymbol{v}^{\boldsymbol{re}}, \xi^F, \xi^R$.
Following the typical Coleman-Noll procedure, the entropy s and the total strain $\boldsymbol{\varepsilon}$ are found as:

$$s = -\frac{\partial G}{\partial T} = s_o + \boldsymbol{\sigma} : \boldsymbol{\alpha} + C_v \ln\left(\frac{T}{T_o}\right) \tag{4.41}$$

and

$$\boldsymbol{\varepsilon} = -\frac{\partial G}{\partial \boldsymbol{\sigma}} = S : \boldsymbol{\sigma} + \boldsymbol{\alpha}\Delta T + \boldsymbol{\varepsilon}^{\mathbf{T}} \tag{4.42}$$

In the latter, a typical decomposition of the total strain is recognized:

$$\boldsymbol{\varepsilon} = \boldsymbol{\varepsilon}^{\mathbf{el}} + \boldsymbol{\varepsilon}^{\mathbf{th}} + \boldsymbol{\varepsilon}^{\mathbf{T}} \tag{4.43}$$

where $\boldsymbol{\varepsilon}^{\mathbf{el}} = S : \boldsymbol{\sigma}$ is the elastic and
$\boldsymbol{\varepsilon}^{\mathbf{th}} = \boldsymbol{\alpha}\Delta T$ is the thermal strain.

The rest of the derived GTFs of the internal variables are found as:

$$\begin{aligned}
\boldsymbol{A}_{\boldsymbol{\varepsilon}^{\boldsymbol{F}}} =& -\frac{\partial G}{\partial \boldsymbol{\varepsilon}^{\boldsymbol{F}}} = -\frac{\partial \boldsymbol{\varepsilon}^{\boldsymbol{T}}}{\partial \boldsymbol{\varepsilon}^{\boldsymbol{F}}} : \frac{\partial G}{\partial \boldsymbol{\varepsilon}^{\boldsymbol{T}}} = \boldsymbol{\sigma} \\
\boldsymbol{A}_{\boldsymbol{\varepsilon}^{\boldsymbol{R}}} =& \boldsymbol{A}_{\boldsymbol{\varepsilon}^{re}} = \boldsymbol{\sigma} \\
\boldsymbol{A}_{\boldsymbol{v}^{re}} =& -\frac{\partial G}{\partial \boldsymbol{v}^{\boldsymbol{re}}} = -(1+\lambda^{re})\boldsymbol{X} \\
A_{\xi^F} =& -\frac{\partial G}{\partial \xi^F} = -\frac{\partial G}{\partial \xi}\frac{\partial \xi}{\partial \xi^F} = -\frac{\partial G}{\partial \xi} = -\tilde{U}_o + \tilde{s}T - \tilde{C}_v\left[\Delta T - T\ln\left(\frac{T}{T_o}\right)\right] + \\
& \frac{1}{2}\boldsymbol{\sigma} : \tilde{\boldsymbol{S}} : \boldsymbol{\sigma} + \boldsymbol{\sigma} : \tilde{\boldsymbol{\alpha}}\Delta T - \frac{\partial \lambda^{re}}{\partial \xi}\boldsymbol{X} : \boldsymbol{v}^{re} - H^F
\end{aligned} \tag{4.44}$$

Here, the variables appearing with a tilde denote the difference of respective constants between the martensitic and austenitic phase. For example:
$\tilde{S} = S^M - S^A$
Likewise,

$$\begin{aligned}
A_{\xi^R} =& -\frac{\partial G}{\partial \xi}\frac{\partial \xi}{\partial \xi^R} = \frac{\partial G}{\partial \xi} = \tilde{U}_o - \tilde{s}T + \tilde{C}_v\left[\Delta T - T\ln\left(\frac{T}{T_o}\right)\right] - \frac{1}{2}\boldsymbol{\sigma} : \tilde{\boldsymbol{S}} : \boldsymbol{\sigma} - \\
& \boldsymbol{\sigma} : \tilde{\boldsymbol{\alpha}}\Delta T + \frac{\partial \lambda^{re}}{\partial \xi}\boldsymbol{X} : \boldsymbol{v}^{re} + H^R
\end{aligned} \tag{4.45}$$

The variables H^F and H^R correspond to the derivative $\dfrac{\partial H}{\partial \xi}$ and can take different forms depending on the sign of $\dot{\xi}$. This is directly equivalent to the form followed by the hardening function f^t in the Lagoudas model, as presented in Subsection 1.4.1.

Following Lemaitre and Chaboche [2002], the second thermodynamic law is reduced to:

$$\boldsymbol{A}_{\boldsymbol{\varepsilon}^{\boldsymbol{F}}} : \dot{\boldsymbol{\varepsilon}}^{\boldsymbol{F}} + A_{\xi^F}\dot{\xi}^F + \boldsymbol{A}_{\boldsymbol{\varepsilon}^{\boldsymbol{R}}} : \dot{\boldsymbol{\varepsilon}}^{\boldsymbol{R}} + A_{\xi^R}\dot{\xi}^R + \boldsymbol{A}_{\boldsymbol{\varepsilon}^{re}} : \dot{\boldsymbol{\varepsilon}}^{\boldsymbol{re}} + \boldsymbol{A}_{\boldsymbol{v}^{re}} : \dot{\boldsymbol{v}}^{\boldsymbol{re}} - \frac{1}{T}\vec{q}\,\overrightarrow{gradT} \geq 0 \tag{4.46}$$

where $\vec{q}$ is the heat flux and $\overrightarrow{gradT}$ the spatial gradient of temperature.

From one hand, the Clausius-Duhem inequality expresses the positive character of these two parts of disspation:

$$\boldsymbol{A}_{\boldsymbol{\varepsilon}^{\boldsymbol{F}}} : \dot{\boldsymbol{\varepsilon}}^{\boldsymbol{F}} + A_{\xi^F}\dot{\xi}^F + \boldsymbol{A}_{\boldsymbol{\varepsilon}^{\boldsymbol{R}}} : \dot{\boldsymbol{\varepsilon}}^{\boldsymbol{R}} + A_{\xi^R}\dot{\xi}^R + \boldsymbol{A}_{\boldsymbol{\varepsilon}^{re}} : \dot{\boldsymbol{\varepsilon}}^{\boldsymbol{re}} + \boldsymbol{A}_{\boldsymbol{v}^{re}} : \dot{\boldsymbol{v}}^{\boldsymbol{re}} \geq 0 \tag{4.47}$$

and

$$-\frac{1}{T}\vec{q}\,\overrightarrow{gradT} \geq 0 \tag{4.48}$$

On the other hand, it is postulated here that the contribution of the internal variables linked to each mechanism to the total dissipation is also non negative:

$$\begin{cases} \gamma^F = \boldsymbol{A}_{\boldsymbol{\varepsilon}^{\boldsymbol{F}}} : \dot{\boldsymbol{\varepsilon}}^{\boldsymbol{F}} + A_{\xi^F}\dot{\xi}^F \geq 0 \\ \gamma^R = \boldsymbol{A}_{\boldsymbol{\varepsilon}^{\boldsymbol{R}}} : \dot{\boldsymbol{\varepsilon}}^{\boldsymbol{R}} + A_{\xi^R}\dot{\xi}^R \geq 0 \\ \gamma^{re} = \boldsymbol{A}_{\boldsymbol{\varepsilon}^{\boldsymbol{re}}} : \dot{\boldsymbol{\varepsilon}}^{\boldsymbol{re}} + \boldsymbol{A}_{\boldsymbol{v}^{\boldsymbol{re}}} : \dot{\boldsymbol{v}}^{\boldsymbol{re}} \geq 0 \end{cases} \tag{4.49}$$

with γ^m being the part of the dissipation induced by the mechanism denoted m.

4.5.1.1 Yield functions

A thermoelastic domain Γ is considered to exist within the coordinates of the free energy potential, in which the dissipation is zero. A hypersurface $\partial\Gamma$ is the boundary of the thermoelastic domain. This hypersurface is defined as the set of solutions of the equation:

$$\Phi(\boldsymbol{A}) = 0$$

where $\boldsymbol{A}$ is the set of all GTFs. For all given coordinates, the following inequality is satisfied:

$$\Phi(\boldsymbol{A}) \leq 0$$

This thermoelastic domain is described by three surfaces corresponding to the three strain mechanisms:

$$\begin{cases} \Phi^F(A_\xi^F, \boldsymbol{A}_{\boldsymbol{\varepsilon}^{\boldsymbol{F}}}) = 0 \\ \Phi^R(A_\xi^R, \boldsymbol{A}_{\boldsymbol{\varepsilon}^{\boldsymbol{R}}}) = 0 \\ \Phi^{re}(A_\xi^{re}, \boldsymbol{A}_{\boldsymbol{\varepsilon}^{\boldsymbol{re}}}) = 0 \end{cases} \tag{4.50}$$

The Φ function for forward transformation is given as:

$$\Phi^F = A_{\xi^F} + \hat{\Phi}^F(\boldsymbol{A}_{\boldsymbol{\varepsilon}^{\boldsymbol{F}}}) - Y^F \tag{4.51}$$

where

$$\hat{\Phi}^F(\boldsymbol{A}_{\boldsymbol{\varepsilon}^{\boldsymbol{F}}}) = \hat{\Phi}^F(\boldsymbol{\sigma})$$

is the function describing the forward transformation function in the space of the stress components. The choice of this function determines which effects relative to anisotropy and asymmetry during forward transformation are taken in mind [Qidwai and Lagoudas, 2000; Sedlák et al., 2012; Taillard et al., 2008]. In the scope of this chapter, a modified Prager function is chosen, as described in Chapter 3. Thus, it is assumed that:

$$\hat{\Phi}^F(\boldsymbol{\sigma}) = H^{cur}(\boldsymbol{\sigma})\sqrt{J_2(\boldsymbol{\sigma})}\left[1 + b\frac{J_3(\boldsymbol{\sigma})}{J_2^{3/2}(\boldsymbol{\sigma})}\right]^{\frac{1}{n}} \tag{4.52}$$

In order to take into account the anisotropy in phase transformation studied in Chapter 3, it suffices to integrate the anisotropic criterion (3.7) in the transformation function (4.51).

For a second-order tensor $\boldsymbol{u}$, the notations $J_2(\boldsymbol{u})$ and $J_3(\boldsymbol{u})$ give the second and third invariants of its deviatoric part $\boldsymbol{u'}$. It is reminded that they are given as:

$$J_2(\boldsymbol{u}) = \frac{1}{2} u'_{ij} u'_{ij} \text{ and}$$

$$J_3(\boldsymbol{u}) = \frac{1}{3} u^{'}_{ij} u^{'}_{jk} u^{'}_{ki}$$

using the Einstein summation for double indices. $H^{cur}(\boldsymbol{\sigma})$ is considered the same as in [Hartl et al., 2010].

The threshold for forward transformation is given as:

$$Y^F = Y_o^F + D\boldsymbol{\sigma} : \boldsymbol{\Lambda_\varepsilon^F} - \frac{\partial \lambda^{re}}{\partial \xi} \boldsymbol{X} : \boldsymbol{v^{re}} \tag{4.53}$$

The variables D and Y_o^F are considered material constants. They are not considered independent, but are calculated with the help of other material constants, see [Hartl et al., 2010]. This approach also guarantees the interaction between stress and temperature states for the activation of transformation.

Likewise, the Φ function for reverse transformation:

$$\Phi^R = A_{\xi^R} + \hat{\Phi}^R(\boldsymbol{A}_{\boldsymbol{\varepsilon^R}}) - Y^R \tag{4.54}$$

where

$$\hat{\Phi}^R(\boldsymbol{A}_{\boldsymbol{\varepsilon^R}}) = \hat{\Phi}^R(\boldsymbol{\sigma}) = -\boldsymbol{\sigma} : \boldsymbol{\bar{\varepsilon}^T} \tag{4.55}$$

and

$$Y^R = Y_o^R + D\boldsymbol{\sigma} : \boldsymbol{\bar{\varepsilon}^T} - \frac{\partial \lambda^{re}}{\partial \xi} \boldsymbol{X} : \boldsymbol{v^{re}} \tag{4.56}$$

with Y_o^R another material constant. In this chapter, it is taken equal to Y_o^F.Their explicit forms are found in Appendix A. The functions for forward and reverse transformation account for isotropic hardening, holding as hardening parameter the martensitic fraction. On the contrary, the function for reorientation is designed to predict kinematic hardening:

$$\Phi^{re} = \hat{\Phi}^{re}(\boldsymbol{A}_{\boldsymbol{\varepsilon^{re}}} + \boldsymbol{A}_{\boldsymbol{v^{re}}}) - Y^{re} \tag{4.57}$$

The choice for the yield function of reorientation is also the modified Prager criterion, in order to account for tension-compression asymmetry during detwinning.

Only this time taking in mind the sum of the thermodynamic forces for $\boldsymbol{\varepsilon^{re}}$ and $\boldsymbol{v^{re}}$:

$$\hat{\Phi}^{re}(\boldsymbol{A}_{\boldsymbol{\varepsilon}^{re}} + \boldsymbol{A}_{\boldsymbol{v}^{re}}) = \sqrt{J_2(\boldsymbol{\Sigma})}\left[1 + b\frac{J_3(\boldsymbol{\Sigma})}{J_2^{3/2}(\boldsymbol{\Sigma})}\right]^{\dfrac{1}{n}} \tag{4.58}$$

Here, the inclusive variable $\boldsymbol{\Sigma}$ is introduced as:

$$\boldsymbol{\Sigma} = \boldsymbol{\sigma} - (1 + \lambda^{re})\boldsymbol{X} \tag{4.59}$$

Finally, the reorientation threshold is considered as a material constant:

$$Y^{re} = Y_o^{re} \tag{4.60}$$

4.5.1.2 Evolution laws

The activation of the evolution of the model variables depends on the satisfaction of the mechanism criteria. This is given by the Kuhn-Tucker loading conditions [Qidwai and Lagoudas, 2000]:

It is aimed to link the evolution of the model variables within linear relation with the rate variables given in Sections 4.3 and 4.4. The forward transformation tensor is expressed as:

$$\boldsymbol{\Lambda}_{\varepsilon}^{\boldsymbol{F}} = H^{cur}\boldsymbol{\eta}_{\boldsymbol{\sigma}} \tag{4.61}$$

where it is recalled that $\boldsymbol{\eta_u}$ for a second-order tensor $\boldsymbol{u}$ is given as (see equation (3.18)):

$$\begin{aligned}\boldsymbol{\eta_u} = \left(1 + b\frac{J_3(\boldsymbol{u})}{J_2^{3/2}(\boldsymbol{u})}\right)^{\frac{1}{n}-1} \Bigg\{ \frac{\boldsymbol{u}'}{2\sqrt{J_2(\boldsymbol{u})}} + \frac{b}{6nJ_2^2(\boldsymbol{u})}\Big[6J_2(\boldsymbol{u})\boldsymbol{u}'.\boldsymbol{u}' - \\ 4J_2^2(\boldsymbol{u})\boldsymbol{I} + (3n-9)J_3(\boldsymbol{u})\boldsymbol{u}'\Big]\Bigg\}\end{aligned} \tag{4.62}$$

This form is chosen to accommodate experimental data demonstrating lower transformation strains under compression than under tension [Bouvet et al., 2004; Chemisky et al., 2015; Grolleau et al., 2011]. Anisotropy in transformation strains can be considered by replacing the evolution rule (4.24) by the proposed equation (3.21) in Chapter 3. The quantity H^{cur} has the role of a proportion factor between the differentials of forward transformation strains and martensitic volume fraction:

$$\left|\mathbf{d}\varepsilon^{\mathbf{F}}\right| = H^{cur}(\sigma)d\xi^F$$

Combined with the hardening rule introduced with the GTF of ξ^F (see H^F in equation (4.44)) found in the yield function (4.51), it accounts for the shape of the stress-strain curve during hardening caused by forward transformation. In simple isothermal tensile loading for instance, it predicts a linear relation between $\left|\mathbf{d}\varepsilon^{\mathbf{T}}\right|$ and $d\xi$, when ξ is in the range typically between 10 and 60%. This relation becomes non linear close to the start or the saturation of transformation.

The reorientation tensor introduced in (4.36) is:

$$\mathbf{\Lambda}_{\varepsilon}^{\boldsymbol{re}} = \boldsymbol{\eta}_{\mathbf{\Sigma}} \tag{4.63}$$

With those definitions, the rates for the partition of transformation strains is now complete:

$$\begin{cases} \dot{\boldsymbol{\varepsilon}}^{\boldsymbol{F}} = \dot{\xi}^{F}\mathbf{\Lambda}_{\varepsilon}^{\boldsymbol{F}} = \dot{\xi}^{F}H^{cur}\boldsymbol{\eta}_{\boldsymbol{\sigma}} \\ \dot{\boldsymbol{\varepsilon}}^{\boldsymbol{F}} = \dot{\xi}^{R}\mathbf{\Lambda}_{\varepsilon}^{\boldsymbol{R}} = -\dot{\xi}^{R}\bar{\boldsymbol{\varepsilon}}^{\boldsymbol{T}} \\ \dot{\boldsymbol{\varepsilon}}^{\boldsymbol{re}} = \dot{p}^{re}\mathbf{\Lambda}_{\varepsilon}^{\boldsymbol{re}} = \dot{p}^{re}\boldsymbol{\eta}_{\mathbf{\Sigma}} \end{cases} \tag{4.64}$$

It is noted that the direction of $\dot{\boldsymbol{\varepsilon}}^{\boldsymbol{re}}$ is normal to the respective yield surface:

$$\boldsymbol{\eta}_{\mathbf{\Sigma}} = \frac{\partial\Phi^{re}}{\partial\mathbf{A}_{\boldsymbol{\varepsilon}^{\boldsymbol{re}}}} = \frac{\partial\Phi^{re}}{\partial\boldsymbol{\sigma}}$$

The evolution of the internal variable $\boldsymbol{v}^{\boldsymbol{re}}$ is also given normal to the reorientation yield surface:

$$\dot{\boldsymbol{v}}^{\boldsymbol{re}} = \dot{p}^{re}\mathbf{\Lambda}_{\boldsymbol{v}}^{\boldsymbol{re}} \tag{4.65}$$

with

$$\mathbf{\Lambda}_{\boldsymbol{v}}^{\boldsymbol{re}} = \frac{\partial\Phi^{re}}{\partial\boldsymbol{A}_{\boldsymbol{v}^{\boldsymbol{re}}}} = \frac{\partial\Phi^{re}}{\partial(-(1+\lambda^{re})\boldsymbol{X})} = \boldsymbol{\eta}_{\mathbf{\Sigma}} \tag{4.66}$$

As for the evolution of backstress, it is decomposed as well in the contributions of the three strain mechanisms:

$$\dot{\boldsymbol{X}} = \dot{\boldsymbol{X}}^{\boldsymbol{F}} + \dot{\boldsymbol{X}}^{\boldsymbol{R}} + \dot{\boldsymbol{X}}^{\boldsymbol{re}} \tag{4.67}$$

The parts of backstress linked to forward and reverse transformation evolve to hinder reorientation from affecting the material behavior when transformation takes place under uniaxial loading. The part linked to reorientation itself is in linear relation with the respective strain part so as to allow for kinematic hardening:

$$\begin{cases} \dot{\boldsymbol{X}}^{\boldsymbol{F}} = \frac{3}{2}\dot{\xi}^{F}\varepsilon_{max}^{re}\boldsymbol{H}^{\boldsymbol{re}} : \frac{\boldsymbol{\sigma'}}{|\boldsymbol{\sigma}|} \\ \dot{\boldsymbol{X}}^{\boldsymbol{R}} = -\frac{\boldsymbol{X}}{\xi} \\ \dot{\boldsymbol{X}}^{\boldsymbol{re}} = \dot{p}^{re}\boldsymbol{H}^{\boldsymbol{re}} : \mathbf{\Lambda}_{\varepsilon}^{\boldsymbol{re}} \end{cases} \tag{4.68}$$

The cofactor $\boldsymbol{H}^{\boldsymbol{re}}$ is a fourth order tensor considered a material constant. In the scope of this chapter, it is given simply by:

$$\boldsymbol{H}^{\boldsymbol{re}} = H^{re}\boldsymbol{I}^{\mathbf{(4)}} \tag{4.69}$$

with $\boldsymbol{I}^{(4)}$ the fourth order symmetric identity tensor. It has the property:

$$\boldsymbol{I}^{(4)} : \boldsymbol{x} = \boldsymbol{x}$$

for any arbitrary symmetric second-order tensor $\boldsymbol{x}$.
ε^{re}_{max} is the maximum inelastic strain allowed to develop during martensite detwinning, usually considered less than the strain caused by phase transformation. H^{re} is a parameter controlling the hardening during reorientation. The stress allowed between start and saturation of detwinning in a uniaxial case is:

$$\Delta\sigma^{reo} = H^{re}\varepsilon^{re}_{max} \tag{4.70}$$

It is apparent that the variable characteristic of backstress affects only the activation of reorientation. The concurrent evolution of backstress with forward and reverse transformation, as implied by (4.68), is introduced to comply with the need to impose a limit for reorientation. Relevant experiments [Lagoudas, 2008] show that, just like transformation, the process of reorientation is limited: after the saturation of detwinning, the elastic part of detwinned martensite is reached. To this aim, when a threshold in the magnitude of backstress is reached, the lagrange multiplier λ^{re} is activated, which leads to an infinitessimal value of $\dot{p}^{re}$ and subsequently to the depending rates of reorientation variables.

The lagrange multiplier is designed as a function of a one-dimensional argument. When it attains values close to 1, the function is activated. For values of the argument between 0 and 1, the function returns 0. The exact form of the function can be found in Appendix E. The argument taken in mind in the case of reorientation is:

$$f^{re} = \frac{|\boldsymbol{X}|}{\xi X_{\max}} \tag{4.71}$$

and thus the respective lagrange multiplier is:

$$\lambda^{re} = \lambda(f^{re}) \tag{4.72}$$

Here, $X_{\max}$ represents a maximum magnitude of backstress when the whole RVE is composed by martensite. According to these assumptions, the maximum magnitude of backstress at any given state is proportional to the MVF. When the value $\xi X_{\max}$ is reached, the lagrange multiplier is activated and forces the variables linked to reorientation to stop evolving, by imposing:

$$\dot{p}^{re} = 0$$

Accordingly, forward and reverse transformation are limited through their respective lagrange multipliers. The following functions:

$$\lambda^{F} = \lambda(\xi) \tag{4.73}$$

and

$$\lambda^R = \lambda(1-\xi) \tag{4.74}$$

are added into the forward and reverse transformation criteria respectively. When activated, they mark the saturation of transformation by imposing $\dot{\xi}^F = 0$ or $\dot{\xi}^R = 0$. The criteria (4.51) and (4.54) are updated:

$$\Phi^F = A_{\xi^F} + \hat{\Phi}^F(\boldsymbol{A}_{\boldsymbol{\varepsilon}^{\boldsymbol{F}}}) + \lambda^F - Y^F \tag{4.75}$$

$$\Phi^R = A_{\xi^R} + \hat{\Phi}^R(\boldsymbol{A}_{\boldsymbol{\varepsilon}^{\boldsymbol{R}}}) + \lambda^R - Y^R \tag{4.76}$$

The exact form of the function λ is described in Appendix A.

4.5.2 Thermomechanical effects

4.5.2.1 First law of thermodynamics

The local form of the first law of thermodynamics is written:

$$\dot{u} = r - \nabla \cdot \boldsymbol{q} + \boldsymbol{\sigma} : \dot{\boldsymbol{\varepsilon}} = \dot{Q} + \boldsymbol{\sigma} : \dot{\boldsymbol{\varepsilon}} \tag{4.77}$$

Here, u is the internal energy, r is the power of the internally generated heat, $\boldsymbol{q}$ is the thermal flux and Q is the total heat exchange due to both internal heat sources and conduction. On the other hand, the Gibbs free energy is given as:

$$G = u - \boldsymbol{\sigma} : \boldsymbol{\varepsilon} - sT \tag{4.78}$$

Its rate form:

$$\dot{u} = \dot{G} + \overset{\cdot}{(\boldsymbol{\sigma} : \boldsymbol{\varepsilon})} + \overset{\cdot}{(sT)} \tag{4.79}$$

is replaced into (4.77) to give:

$$\dot{G} + \dot{\boldsymbol{\sigma}} : \boldsymbol{\varepsilon} + \dot{s}T + s\dot{T} = \dot{Q} \tag{4.80}$$

The framework of multiple activated mechanisms, presented in Chapter 5 is used to derive the relations between the energy quanties and the mechanical input. This framework describes the numerical resolution of a thermodynamical system of an indefinite amount of strain mechanisms governed by similar thermodynFamics as given in this chapter.

Applying the chain rule to derive the rate of the Gibbs free energy potential, it is found:

$$\dot{G} = \frac{\partial G}{\partial \boldsymbol{\sigma}} : \dot{\boldsymbol{\sigma}} + \frac{\partial G}{\partial T}\dot{T} + \sum_j \left[\sum_i \left(\frac{\partial G}{\partial \boldsymbol{V}_i^j} : \dot{\boldsymbol{V}}_i^j \right) \right] \tag{4.81}$$

With the help of equations (4.41), (4.42,) (5.4) and (5.5), this rate is now:

$$\dot{G} = -\boldsymbol{\varepsilon} : \dot{\boldsymbol{\sigma}} - s\dot{T} - \sum_j \left[\dot{p}^j \sum_i \left(\boldsymbol{A}_i^j \boldsymbol{:}\, \boldsymbol{\Lambda}_i^j\right)\right] \tag{4.82}$$

Giving the definition:

$$\pi^j = \sum_i (\boldsymbol{A}_i^j : \boldsymbol{\Lambda}_i^j) \tag{4.83}$$

the equation (4.80) is now:

$$\dot{s}T = \sum_j (\pi^j \dot{p}^j) + \dot{Q} \tag{4.84}$$

in which $\dot{s}$ is found from (4.41):

$$\begin{aligned} \dot{s} &= \frac{\partial s}{\partial \boldsymbol{\sigma}} : \dot{\boldsymbol{\sigma}} + \frac{\partial s}{\partial T}\dot{T} + \sum_j \left(\frac{\partial s}{\partial p^j}\dot{p}^j\right) = \\ &= \dot{\boldsymbol{\sigma}} : \boldsymbol{\alpha} + C_v \frac{\dot{T}}{T} + \sum_j \left\{\dot{p}^j \left[\frac{\partial s_o}{\partial p^j} + \boldsymbol{\sigma} : \frac{\partial \boldsymbol{\alpha}}{\partial p^j} + \frac{\partial C_v}{\partial p^j} \ln\left(\frac{T}{T_o}\right)\right]\right\} \end{aligned} \tag{4.85}$$

Thus, from (4.84):

$$C_v\dot{T} = \sum_j \left\{\dot{p}^j \left[\pi^j - \left[\frac{\partial s_o}{\partial p^j} + \boldsymbol{\sigma} : \frac{\partial \boldsymbol{\alpha}}{\partial p^j} + \frac{\partial C_v}{\partial p^j} \ln\left(\frac{T}{T_o}\right)\right] T\right]\right\} - \dot{\boldsymbol{\sigma}} : \boldsymbol{\alpha} \cdot T + \dot{Q} \tag{4.86}$$

The following notation is adopted:

$$\pi_T^j = \pi^j - \left[\frac{\partial s_o}{\partial p^j} + \boldsymbol{\sigma} : \frac{\partial \boldsymbol{\alpha}}{\partial p^j} + \frac{\partial C_v}{\partial p^j} \ln\left(\frac{T}{T_o}\right)\right] T \tag{4.87}$$

The known forms of $\dot{p}^j$ and $\dot{\boldsymbol{\sigma}}$ from (5.30) and (E.74) are also substituted into (4.86) to acquire:

$$C_v\dot{T} - \dot{Q} = -\left[\sum_j \left(\pi_T^j \boldsymbol{P}_{\varepsilon}^j\right) + \boldsymbol{L} : \boldsymbol{\alpha} \cdot T\right] : \dot{\boldsymbol{\varepsilon}} - \left[\sum_j \left(\pi_T^j P_T^j\right) + \boldsymbol{\Theta} : \boldsymbol{\alpha} \cdot T\right] \dot{T} \tag{4.88}$$

The last equation states that the volumetric heat generation per unit time is not equal to the total heat exchange. The difference between these two quantities arises by effect of mechanical work, as it appears in the right-hand part of the equation. The part of dissipation linked to mechanical reaction of the material, such as the one found in (4.47), is also found in this part.

The quantities

$$\boldsymbol{D}_{,\varepsilon} = -\left[\sum_{j} \left(\pi_T^j \boldsymbol{P}_{\boldsymbol{\varepsilon}}^{\boldsymbol{j}}\right) + \boldsymbol{L} : \boldsymbol{\alpha} \cdot T\right] \tag{4.89}$$

and

$$D_{,T} = -\left[\sum_{j} \left(\pi_T^j P_T^j\right) + \boldsymbol{\Theta} : \boldsymbol{\alpha} \cdot T\right] \tag{4.90}$$

track the linear relation of the power of the heat generated through thermomechanical coupling with the differentials of strain and temperature.

4.5.2.2 Application to SMA model

The scalar quantities p^m whose rates drive the three strain mechanisms are: ξ^F for forward, ξ^R for reverse transformation and p^{re} for reorientation. In Table 4.1, the relation of the rates of the model with the driving scalar rates through their respective evolution tensors $\boldsymbol{\Lambda}_{\boldsymbol{V}\,\boldsymbol{i}}^{\boldsymbol{m}}$.

Strain mechanisms Evolving variables	FT	RT	Re
V_1^m	ξ^F	ξ^R	p^{re}
$\boldsymbol{V}_{\boldsymbol{2}}^{\boldsymbol{m}}$	$\boldsymbol{\varepsilon}^{\boldsymbol{F}}$	$\boldsymbol{\varepsilon}^{\boldsymbol{R}}$	$\boldsymbol{\varepsilon}^{\boldsymbol{re}}$
$\boldsymbol{V}_{\boldsymbol{3}}^{\boldsymbol{m}}$	$\boldsymbol{X}^{\boldsymbol{F}}$	$\boldsymbol{X}^{\boldsymbol{R}}$	$\boldsymbol{X}^{\boldsymbol{re}}$

TABLE 4.1 – Classification of evolving model variables according to the respective mechanisms

Next, the linear relations of the elastic compliance tensor and the thermal expansion coefficient with the driving scalars are reduced to:

$$\begin{aligned} \frac{\partial \boldsymbol{S}}{\partial \xi^F} &= -\frac{\partial \boldsymbol{S}}{\partial \xi^R} = \tilde{\boldsymbol{S}} \quad \text{and} \quad \frac{\partial \boldsymbol{S}}{\partial p^{re}} = \boldsymbol{0} \\ \frac{\partial \boldsymbol{\alpha}}{\partial \xi^F} &= -\frac{\partial \boldsymbol{\alpha}}{\partial \xi^R} = \tilde{\boldsymbol{\alpha}} \quad \text{and} \quad \frac{\partial \boldsymbol{\alpha}}{\partial p^{re}} = \boldsymbol{0} \end{aligned} \tag{4.91}$$

The strain quantities $\boldsymbol{K}^{\boldsymbol{m}}$ are reduced to:

$$\begin{aligned} \boldsymbol{K}^{\boldsymbol{F}} &= \tilde{\boldsymbol{S}} : \boldsymbol{\sigma} + \tilde{\boldsymbol{\alpha}} \Delta T + \boldsymbol{\Lambda}_{\boldsymbol{\varepsilon}}^{\boldsymbol{F}} \\ \boldsymbol{K}^{\boldsymbol{R}} &= -\tilde{\boldsymbol{S}} : \boldsymbol{\sigma} - \tilde{\boldsymbol{\alpha}} \Delta T + \boldsymbol{\Lambda}_{\boldsymbol{\varepsilon}}^{\boldsymbol{R}} \\ \boldsymbol{K}^{\boldsymbol{re}} &= \boldsymbol{\Lambda}_{\boldsymbol{\varepsilon}}^{\boldsymbol{re}} \end{aligned} \tag{4.92}$$

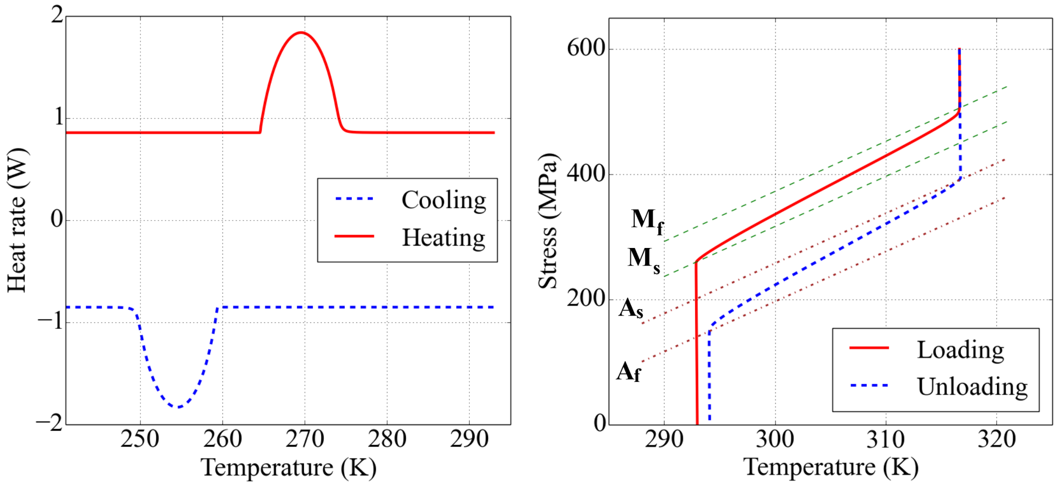

(a) Simulation of DSC measurements

(b) 1-D adiabatic loading

FIGURE 4.4 – Heat rate - temperature diagram of a simulated DSC test (a) and stress-temperature relation on a phase diagram for a simulated 1-D stress-controlled loading under adiabatic conditions (b) for a hypothetical NiTi composition. The starting temperature is 293 K in both cases.

Φ^F	Φ^R	Φ^{re}
$\boldsymbol{\sigma}$, T, ξ	$\boldsymbol{\sigma}$, T, ξ, $\boldsymbol{\varepsilon^F}$, $\boldsymbol{\varepsilon^R}$, $\boldsymbol{\varepsilon^{re}}$	$\boldsymbol{\sigma}$, ξ $\boldsymbol{X^F}$, $\boldsymbol{X^R}$, $\boldsymbol{X^{re}}$

TABLE 4.2 – Variables affecting the yield functions

Furthermore, multiple derivatives and mathematical building components take zero values, since the Φ^m yield equations are not dependent on all the evolving variables. Table 4.2 presents which variables affect the three yield functions.

In simple loading cases, such as stress free temperature variation or 1-D mechanical loading-unloading, reorientation is not activated and the laws applying for transformation are eventually reduced to match the predictions from the Lagoudas model. In Fig. (4.4a), the model response for a cooling-heating cycle under DSC measurements is presented. The implications of the strong thermomechanical coupling for the case of 1-D loading under adiabatic conditions are also illustrated on Fig. (4.4b).

4.6 Concluding remarks

A new phenomenological model to describe the complex behavior of SMAs while experiencing coupled transformation/reorientation during non-proportional thermomechanical loading is proposed. It has been shown that this model is thermodynamically consistent, and the proposed evolution equations correctly describe the evolution of martensitic volumes in a SMA.

The original contribution of this work concerns the independent way in which the physical mechanisms are conceived to take place. The first contribution brought about is the decoupling of forward and reverse transformation. In such a way, it is observed that, in terms of modeling, these two can occur simultaneously inside the material. One more novelty is the simple form for describing the process of reorientation, which is also considered an independent mechanism. Finally, a general framework to resolve the numerical problem of complex non-proportional loading is presented for the case of multiple mechanisms. The thermomechanical effects are fully taken in mind.

At this point, to clear the overall view of the reader, a summarizing table providing the general architecture of the new model is presented. In Table 4.3, the most important equations are classified by the mechanism that they concern.

Forward transformation	Reverse transformation	Reorientation
$\hat{\Phi}^F(\boldsymbol{\sigma}) + A_{\xi^F} - Y^F + \lambda^F \leq 0$	$\hat{\Phi}^R(\boldsymbol{\sigma}, \boldsymbol{\varepsilon^T}) + A_{\xi^R} - Y^R + \lambda^R \leq 0$	$\hat{\Phi}^{re}(\boldsymbol{\Sigma}) - Y^{re} \leq 0$
$\dot{\boldsymbol{\varepsilon}}^{\boldsymbol{F}} = \dot{\xi}^F \boldsymbol{\Lambda}_{\boldsymbol{\varepsilon}}^{\boldsymbol{F}}$	$\dot{\boldsymbol{\varepsilon}}^{\boldsymbol{R}} = \dot{\xi}^R \boldsymbol{\Lambda}_{\boldsymbol{\varepsilon}}^{\boldsymbol{R}}$	$\dot{\boldsymbol{\varepsilon}}^{\boldsymbol{re}} = \dot{p}^{re} \boldsymbol{\Lambda}_{\boldsymbol{\varepsilon}}^{\boldsymbol{re}}$
$\dot{\boldsymbol{X}}^{\boldsymbol{F}} = \dot{\xi}^F \boldsymbol{\Lambda}_{\boldsymbol{X}}^{\boldsymbol{F}}$	$\dot{\boldsymbol{X}}^{\boldsymbol{R}} = \dot{\xi}^R \boldsymbol{\Lambda}_{\boldsymbol{X}}^{\boldsymbol{R}}$	$\dot{\boldsymbol{X}}^{\boldsymbol{re}} = \dot{p}^{re} \boldsymbol{\Lambda}_{\boldsymbol{X}}^{\boldsymbol{re}}$
		$\boldsymbol{\Sigma} = \boldsymbol{\sigma} - (1 + \lambda^{re})\boldsymbol{X}$

Composition
$\xi = \xi^F - \xi^R$
$\boldsymbol{\varepsilon^T} = \boldsymbol{\varepsilon^F} + \boldsymbol{\varepsilon^R} + \boldsymbol{\varepsilon}^{re}$
$\boldsymbol{\varepsilon} = \boldsymbol{\varepsilon^{el}} + \boldsymbol{\varepsilon^{th}} + \boldsymbol{\varepsilon^T}$
$\boldsymbol{\varepsilon^{th}} = \boldsymbol{\alpha}(\xi)\Delta T$
$\boldsymbol{\varepsilon^{el}} = S(\xi) : \boldsymbol{\sigma}$
$\boldsymbol{X} = \boldsymbol{X^F} + \boldsymbol{X^R} + \boldsymbol{X}^{re}$

TABLE 4.3 – Most important relations of the proposed model.

The model response for simple 1-D conditions has been briefly examined. Non-trivial cases will highlight the numerical response in the next chapter. Simulations of simple and complex experiments on SMA structures appearing in the literature will be carried out to demonstrate the practical predictive capabilities of the model. The strong thermomechanical coupling can be assessed by performing appropriate strain rate effect analyses.

4.7 References

F. Auricchio, E. Bonetti, G. Scalet, and F. Ubertini. Theoretical and numerical modeling of shape memory alloys accounting for multiple phase transformations and martensite reorientation.

International Journal of Plasticity, 59:30–54, aug 2014. ISSN 07496419. doi: 10.1016/j.ijplas.2014.03.008. 87

C. Bouvet, S. Calloch, and C. Lexcellent. A phenomenological model for pseudoelasticity of shape memory alloys under multiaxial proportional and nonproportional loadings. *European Journal of Mechanics - A/Solids*, 23(1):37–61, jan 2004. ISSN 09977538. doi: 10.1016/j.euromechsol.2003.09.005. 103

J. G. Boyd and D. C. Lagoudas. Thermomechanical Response of Shape Memory Composites. *Journal of Intelligent Material Systems and Structures*, 5(3):333–346, may 1994. ISSN 1045-389X. doi: 10.1177/1045389X9400500306. 99

L. Brinson, I. Schmidt, and R. Lammering. Stress-induced transformation behavior of a polycrystalline NiTi shape memory alloy: micro and macromechanical investigations via in situ optical microscopy. *Journal of the Mechanics and Physics of Solids*, 52(7):1549–1571, jul 2004. ISSN 00225096. doi: 10.1016/j.jmps.2004.01.001. 87

Y. Chemisky, A. Duval, E. Patoor, and T. Ben Zineb. Constitutive model for shape memory alloys including phase transformation, martensitic reorientation and twins accommodation. *Mechanics of Materials*, 43(7):361–376, jul 2011. ISSN 01676636. doi: 10.1016/j.mechmat.2011.04.003. 87, 88

Y. Chemisky, F. Meraghni, N. Bourgeois, S. Cornell, R. Echchorfi, and E. Patoor. Analysis of the deformation paths and thermomechanical parameter identification of a shape memory alloy using digital image correlation over heterogeneous tests. *International Journal of Mechanical Sciences*, 96-97:13–24, jun 2015. ISSN 00207403. doi: 10.1016/j.ijmecsci.2015.03.007. 103

Y. Chemisky, G. Chatzigeorgiou, P. Kumar, and D. C. Lagoudas. A constitutive model for cyclic actuation of high-temperature shape memory alloys. *Mechanics of Materials*, 68:120–136, jan 2014. ISSN 01676636. doi: 10.1016/j.mechmat.2013.07.020. 87

D. Favier, H. Louche, P. Schlosser, L. Orgéas, P. Vacher, and L. Debove. Homogeneous and heterogeneous deformation mechanisms in an austenitic polycrystalline Ti–50.8at.% Ni thin tube under tension. Investigation via temperature and strain fields measurements. *Acta Materialia*, 55(16):5310–5322, sep 2007. ISSN 13596454. doi: 10.1016/j.actamat.2007.05.027. 87

V. Grolleau, H. Louche, V. Delobelle, A. Penin, G. Rio, Y. Liu, and D. Favier. Assessment of tension–compression asymmetry of NiTi using circular bulge testing of thin plates. *Scripta Materialia*, 65(4):347–350, aug 2011. ISSN 13596462. doi: 10.1016/j.scriptamat.2011.05.003. 103

D. J. Hartl and D. C. Lagoudas. Thermomechanical Characterization of Shape Memory Alloy Materials. In *Shape Memory Alloys*, pages 53–119. Springer US, Boston, MA, 2008. ISBN 978-0-387-47684-1. doi: 10.1007/978-0-387-47685-8. 87

D. J. Hartl, G. Chatzigeorgiou, and D. C. Lagoudas. Three-dimensional modeling and numerical analysis of rate-dependent irrecoverable deformation in shape memory alloys. *International Journal of Plasticity*, 26(10):1485–1507, oct 2010. ISSN 07496419. doi: 10.1016/j.ijplas.2010.01.002. 88, 99, 102

O. Heintze and S. Seelecke. A coupled thermomechanical model for shape memory alloys—From single crystal to polycrystal. *Materials Science and Engineering: A*, 481-482:389–394, may 2008. ISSN 09215093. doi: 10.1016/j.msea.2007.08.028. 87

D. Lagoudas, D. Hartl, Y. Chemisky, L. Machado, and P. Popov. Constitutive model for the numerical analysis of phase transformation in polycrystalline shape memory alloys. *International Journal of Plasticity*, 32-33(null):155–183, may 2012. ISSN 07496419. doi: 10.1016/j.ijplas.2011.10.009. 99

D. Lagoudas. *Shape Memory Alloys - Modeling and Engineering Applications*. Springer, 2008. 105

J. Lemaitre and J. L. Chaboche. *Mechanics of Solid Materials*. Cambridge University Press, 2002. ISBN 0521477581. 100

T. Lim and D. McDowell. Cyclic thermomechanical behavior of a polycrystalline pseudoelastic shape memory alloy. *Journal of the Mechanics and Physics of Solids*, 50(3):651–676, mar 2002. ISSN 00225096. doi: 10.1016/S0022-5096(01)00088-6. 87

C. Morin, Z. Moumni, and W. Zaki. Thermomechanical coupling in shape memory alloys under cyclic loadings: Experimental analysis and constitutive modeling. *International Journal of Plasticity*, 27(12):1959–1980, dec 2011. ISSN 07496419. doi: 10.1016/j.ijplas.2011.05.005. 87

E. Patoor, M. El Amrani, A. Eberhardt, and M. Berveiller. Determination of the origin for the dissymmetry observed between tensile and compression tests on shape memory alloys. *J. Phys.*, IV(2):495–500, 1995. 90

R. Peyroux, A. Chrysochoos, C. Licht, and M. Löbel. Thermomechanical couplings and pseudoelasticity of shape memory alloys. *International Journal of Engineering Science*, 36(4):489–509, mar 1998. ISSN 00207225. doi: 10.1016/S0020-7225(97)00052-9. 87

M. Qidwai and D. Lagoudas. On thermomechanics and transformation surfaces of polycrystalline NiTi shape memory alloy material. *International Journal of Plasticity*, 16(10-11):1309–1343, jan 2000. ISSN 07496419. doi: 10.1016/S0749-6419(00)00012-7. 101, 103

L. Saint-Sulpice, S. A. Chirani, and S. Calloch. A 3D super-elastic model for shape memory alloys taking into account progressive strain under cyclic loadings. *Mechanics of Materials*, 41 (1):12–26, jan 2009. ISSN 01676636. doi: 10.1016/j.mechmat.2008.07.004. 97

P. Sedlák, M. Frost, B. Benešová, T. Ben Zineb, and P. Šittner. Thermomechanical model for NiTi-based shape memory alloys including R-phase and material anisotropy under multi-axial loadings. *International Journal of Plasticity*, 39(null):132–151, dec 2012. ISSN 07496419. doi: 10.1016/j.ijplas.2012.06.008. 87, 101

K. Taillard, S. A. Chirani, S. Calloch, and C. Lexcellent. Equivalent transformation strain and its relation with martensite volume fraction for isotropic and anisotropic shape memory alloys. *Mechanics of Materials*, 40(4-5):151–170, apr 2008. ISSN 01676636. doi: 10.1016/j.mechmat.2007.07.005. 101

5. Simulating SMA structures under complex loading conditions

5.1 Introduction

In this chapter, numerical results proving the value of the theoretical considerations made in Chapter 4 are presented. In order for the model to be implemented in numerical tools and generate results, the implications of the framework of multiple inelastic strain mechanisms are firstly studied. The independence of these mechanisms leads to the incertitude of their activation or absence. The Fischer-Burmeister method for the numerical resolution of Kuhn-Tucker conditions is deployed to overcome this obstacle and appropriate adaptive thermomechanical tangent moduli are developped to allow for fast convergence.

In the second part of the chapter, the SMA model is evaluated in terms of comparing numerical response with results coming from existing experimental databases. Appropriate complex multidimensional loading cases are examined to assess the importance of martensitic reorientation. Finally, the strong thermomechanical coupling is highlighted by conducting numerical simulations of loading under thermal boundary conditions. The influence of adiabatic conditions is briefly examined and a Finite Element simulation of a NiTi structure in environmental conditions is more thoroughly studied under the scope of different imposed loading speeds, inducing strain rate effects. Great parts of this work are the object of an article accepted for publication in IJP [Chatziathanasiou et al., 2016].

5.2 Framework of multiple activation of strain mechanisms

This section aims at providing a framework for addressing the numerical implementation of a model that considers multiple strain mechanisms. Initially, a general solution taking into account a random number of strain mechanisms will be examined. Next, the framework will be reduced to the specific needs of the proposed SMA model.

5.2.1 Framework setup

The evolution of inelastic strains is considered to be caused by several mechanisms which are thought thermodynamically independent. This means that the dissipation associated to each one of them must be non-negative. The total inelastic strain is:

$$\boldsymbol{\varepsilon^T} = \sum_m \boldsymbol{\varepsilon^m} \tag{5.1}$$

where the index m stands for every different mechanism. Each mechanism m is responsible for the evolution of $\boldsymbol{\varepsilon^m}$. Their total number N_m can be indefinite.

Considering each $\boldsymbol{\varepsilon^m}$ as an internal variable, the GTF for each one deriving from the Gibbs free energy potential is:

$$-\frac{\partial G}{\partial \boldsymbol{\varepsilon^m}} = \boldsymbol{\sigma} - \frac{\partial G^v}{\partial \boldsymbol{\varepsilon^m}} \tag{5.2}$$

where G^v is found in the general form of G :

$$G = -\boldsymbol{\sigma} : \boldsymbol{\varepsilon^T} + G^v \tag{5.3}$$

Each mechanism m involves a set of variables $\{\boldsymbol{V_i^m}\}$. Each different $\boldsymbol{V_i^m}$ might be considered an internal variable or not. The first element of every set is defined to be a scalar p^m:

$$p^m = V_1^m$$

The property of every p^j is that the rate of all other variables $\boldsymbol{V_i^j}$ are found by:

$$\dot{\boldsymbol{V}}_{\boldsymbol{i}}^{\boldsymbol{j}} = \dot{p}^j \boldsymbol{\Lambda_i^j} \tag{5.4}$$

with j being an index denoting any mechanism m consistently throughout this section. $\boldsymbol{\Lambda_i^j}$ is a tensor of order which varies according to the nature of $\boldsymbol{V_i^j}$. In the scope of this section, they are given the name evolution tensors. For instance,

$\Lambda_1^j = \Lambda_p^j = 1$ is a zero order tensor equal to the unit so as to comply with (5.4). Likewise,

$\boldsymbol{\Lambda_2^j} = \boldsymbol{\Lambda_\varepsilon^j}$ is a second-order tensor corresponding to $\boldsymbol{\varepsilon^j}$. The second element of every set $\{\boldsymbol{V_i^j}\}$ will consistently be considered $\boldsymbol{\varepsilon^j}$.

In thermodynamics, any element $\boldsymbol{V_i^j}$ which is an internal variable has a conjugate GTF:

$$\boldsymbol{A^m_{V\,i}} = -\frac{\partial G}{\partial \boldsymbol{V_i^m}} \tag{5.5}$$

The thermodynamic criteria which govern the activation of each mechanism have the general form:

$$\Phi^m(\{\boldsymbol{A_V^m}\}) \leq 0 \tag{5.6}$$

where $\{\boldsymbol{A_V^m}\}$ is the whole set of GTFs for the mechanism m.

5.2.2 Fischer-Burmeister technique

The numerical resolution of such a complex non-linear problem must be carefully considered. In all cases, the Convex Cutting Plane (CCP) method [Hartl and Lagoudas, 2009] is used in conjuction with the Newton-Raphson scheme to approximate the solution in the multi-variable space. A particularly interesting method of reinforcing the Newton-Raphson optimization procedure was introduced by Fischer [1992]. This is called the Fischer-Burmeister method and was implemented in recent articles for SMA models [Auricchio et al., 2014; Kiefer et al., 2012].

A mechanism m, activated by satisfying the criterion Φ^m and driven by the rate of the scalar p^m, the Kuhn-Tucker conditions must apply:

$$\begin{aligned} &\Phi^m \leq 0 \\ &\dot{p}^m \geq 0 \\ &\Phi^m \dot{p}^m = 0 \end{aligned} \tag{5.7}$$

The Fischer-Burmeister technique transforms this problem to the resolution of an equivalent set:

$$\sqrt{(\Phi^m)^2 + (\dot{p}^m)^2} + \Phi^m - \dot{p}^m = 0 \tag{5.8}$$

This equation has two sets of roots: either

$$\Phi^m < 0; \;\; \dot{p}^m = 0 \tag{5.9}$$

which means that the mechanism m is not activated, or

$$\Phi^m = 0; \;\; \dot{p}^m > 0 \tag{5.10}$$

for which case m is activated and a solution for $\dot{p}^m$ is searched.

Deploying this method, the need to perform the verification of the inequality $\Phi^m < 0$ is suppressed. Most modern models still make use of a prediction-correction method: a predictive step assuming elastic incrementation of variables is executed first and a temporary value for Φ^m is obtained. If this value is non-negative, the corrective step searches for a solution of equation (5.10). However, in the case of multiple inelastic mechanisms, the prediction step should be applied in layers: even after a criterion is balanced to zero, nothing insures the active or inactive state of the rest of the mechanisms. Thus, a verification process must be repeated as many times as necessary to satisfy the Kuhn-Tucker conditions for all sets of $\{\Phi, \dot{p}\}$.

The application of the Fischer-Burmeister tool, however, eliminates the separation of an increment between predictive and corrective parts. It introduces an elegant approach to the numerical solution, where even elasticity is a possible result: it occurs when all $\dot{p}$ are found zero. In the incremental scheme, a vector $\{F\}$ is introduced, composed of the Fischer-Burmeister components:

$$F^m = \sqrt{(\Phi^m)^2 + (\dot{p}^m)^2} + \Phi^m - \dot{p}^m \tag{5.11}$$

for each mechanism m. The numerical algorithm followed must consistently search for the solution of the system:

$$\{F\} = \{0\} \tag{5.12}$$

Since the system of equations 5.12 is nonlinear, the usual Newton-Raphson approach is utilized to obtain the solution.

5.2.3 Numerical solution algorithm

In the scope of the numerical solution of a structure provided by the Finite Elements Method, the value of every model variable belongs to a set of three repetitive processes, called loops in this subsection. A loading step is partitioned in time increments. The outermost loop solves the balance resulting from the interaction between elements for every one of these increments. It is called here “the n loop”. The Abaqus Finite Element suite is used for the simulation of a SMA structure in a subsequent section 5.4.2 of this chapter. The algorithms regarding the balance in the Finite Element Method framework are not discussed in this work.

The second loop, called “ω loop” is related with iteration process in one element aiming at satisfying the force equilibrium when the stress is updated by the constitutive law.

The third process is the one that loops the algebraic manipulations to find the next admissible set of variable coordinates for a RVE. It is called “the k loop” and it is performed in the level where the constitutive law takes its effect.

When the n loop is carried out, a differential

$$\Delta x^n = x^{n+1} - x^n$$

is approximated to find x^{n+1}. Here, x^n is considered a constant. When the ω loop is carried out, a differential

$$dx^\omega = x^{\omega+1} - x^\omega$$

is approximated to find $x^{\omega+1}$. Here, $x^{n+1(\omega)}$ is considered a constant. When the k loop is carried out, a differential

$$\delta x^k = x^{k+1} - x^k$$

is approximated to find x^{k+1}. Here, $x^{n+1(\omega+1)(k)}$ is considered a constant.

5.2.3.1 Internal loop iterations

During iterative correction in the k loop, the total current strain and temperature are held constant such that:

$$\boldsymbol{\delta\varepsilon}\,{}^{(k)}_{n+1} = \mathbf{0}$$

and

$$\delta T\,{}^{(k)}_{n+1} = 0$$

$\dot{p}^m$ is approximated as $dp^{n+1(k)} = p^{n+1(k)} - p^n$: According to the decomposition of strains:

$$\boldsymbol{\varepsilon} = \boldsymbol{\varepsilon^{el}} + \boldsymbol{\varepsilon^{th}} + \boldsymbol{\varepsilon^{T}} = \boldsymbol{\varepsilon^{el}} + \boldsymbol{\varepsilon^{th}} + \sum_j \boldsymbol{\varepsilon^{j}} \tag{5.13}$$

the constitutive relation for elasticity:

$$\boldsymbol{\varepsilon^{el}} = \boldsymbol{S} : \boldsymbol{\sigma} \tag{5.14}$$

and the null increments of $\boldsymbol{\varepsilon}_{n+1}$ and T_{n+1}, it is deduced that:

$$-\boldsymbol{\delta\varepsilon^{th}}{}^{(k)} - \sum_j \left(\boldsymbol{\delta\varepsilon^{j}}{}^{(k)}\right) = \boldsymbol{\delta S}^{(k)} : \boldsymbol{\sigma}^{(k)} + \boldsymbol{S}^{(k)} : \boldsymbol{\delta\sigma}^{(k)} \tag{5.15}$$

The Fischer-Burmeister method intervenes in this part of the algorithm. The equation (5.11) is solved looking for $F^m(k+1) = 0$ in the iterative process:

$$F^{m(k+1)} - F^{m(k)} = \delta F^{m(k)} \tag{5.16}$$

where

$$\delta F^{m(k)} = \left[\frac{\Phi^{m(k)}}{\sqrt{\left(\Phi^{m(k)}\right)^2 + \left(dp^{m(k)}\right)^2}} + 1\right]\delta\Phi^{m(k)} + \left[\frac{dp^{m(k)}}{\sqrt{\left(\Phi^{m(k)}\right)^2 + \left(dp^{m(k)}\right)^2}} - 1\right]\delta p^{m(k)} \tag{5.17}$$

If $\delta\Phi^m$ can be related proportionally to $\delta p^{m(k)}$, so will $\delta\Phi^m$. Knowing that Φ^m is an expression of $\boldsymbol{\sigma}$, T and all the variables $\boldsymbol{V^j_i}$, it can be written as:

$$\delta\Phi^{m\,(k)} = \frac{\partial\Phi^{m\,(k)}}{\partial\boldsymbol{\sigma}} : \boldsymbol{\delta\sigma}^{(k)} + \sum_j \left[\sum_i \left(\frac{\partial\Phi^{m\,(k)}}{\partial\boldsymbol{V^j_i}} : \boldsymbol{\delta V^{j}_{i}}{}^{(k)}\right)\right] \tag{5.18}$$

Here, $\boldsymbol{\delta\sigma^{(k)}}$ can be replaced with the help of (5.15):

$$\boldsymbol{\delta\sigma}^{(k)} = -\boldsymbol{C}^{(k)} : \sum_{j} \left[\delta p^{j\ (k)} \left(\frac{\partial \boldsymbol{S}^{(k)}}{\partial p^j} : \boldsymbol{\sigma}^{(k)} + \Delta T_{n+1} \frac{\partial \boldsymbol{\alpha}^{(k)}}{\partial p^j} + \boldsymbol{\Lambda}_{\boldsymbol{\varepsilon}}^{\boldsymbol{j}\ (k)} \right) \right] \tag{5.19}$$

According to (5.4), $\boldsymbol{\delta V_i^{j}}^{\ (k)}$ is also an expression of $\delta p^{m(k)}$:

$$\boldsymbol{\delta V_i^{j}}^{\ (k)} = \delta p^{j\ (k)} \boldsymbol{\Lambda_i^{j}}^{\ (k)} \tag{5.20}$$

Now it is evident that $\delta\Phi^{m(k)}$ is a product of $\delta p^{j(k)}$. The vector $\{\delta\Phi^m\}$ will be:

$$\{\delta\Phi^m\} = \boldsymbol{B}^{(k)} \{\delta p^{j\ (k)}\} \tag{5.21}$$

where $\boldsymbol{B}^{(k)}$ is a $N_m \times N_m$ matrix, the components $B_{mj}^{(k)}$ of which are found in Appendix E. Now (5.17) can be expressed as a linear function of $\delta p^{j(k)}$:

$$\delta F^{m(k)} = \sum^{j} (B_{mj}^{f(k)} \delta p^{j(k)}) \tag{5.22}$$

With the help of (5.22), the vector $\{\delta p^{(k)}\}$ is approximated from (5.16):

$$\delta p^{j(k)} = -\sum^{j} \left[(B_{mj}^{f(k)})^{-1} F^{m(k)} \right] \tag{5.23}$$

The form of $B_{mj}^{f(k)}$ is also found in Appendix E. After this operation, the whole set of variables is updated to find $\boldsymbol{V_i^{j(k+1)}}$. If $\{F^{(k+1)}\} = \{0\}$, the k loop is considered closed, and the algorithm proceeds to the ω loop.

5.2.3.2 Thermomechanical tangent moduli and heat exchange

The incremental relation

$$\boldsymbol{d\sigma}^{(\omega)} = \boldsymbol{L}^{(\omega)} : \boldsymbol{d\varepsilon}^{(\omega)} + \boldsymbol{\Theta}^{(\omega)} dT^{(\omega)} \tag{5.24}$$

is utilized during the ω loop, that performs the FE calculation for satisfying the equilibrium equations. In this paragraph, all quantities are evaluated for the current step of the ω loop and therefore the superscript ω will be omitted. $\boldsymbol{L}$ is called the mechanical and $\boldsymbol{\Theta}$ the thermal tangent modulus.

We start by considering:

$$\boldsymbol{d\sigma} = \boldsymbol{d}\{S : \boldsymbol{d\varepsilon^{el}}\} \tag{5.25}$$

and that $d\Phi^m = 0$ for the mechanisms m that were deduced to be activated in the k loop. Similarly to the manipulations followed in the previous paragraph, the vector $\{dp^j\}$ is led to be expressed as a linear expression of other differentials:

$$\hat{\boldsymbol{B}}\{dp^j\} = \left\{-\frac{\partial\Phi^m}{\partial\boldsymbol{\sigma}} : \boldsymbol{C} : \boldsymbol{d\varepsilon} - \left(\frac{\partial\Phi^m}{\partial T} - \frac{\partial\Phi^m}{\partial\boldsymbol{\sigma}} : \boldsymbol{C} : \boldsymbol{\alpha}\right) dT\right\} \tag{5.26}$$

Here, $\hat{\boldsymbol{B}}$ is a $N_m \times N_m$ matrix.

It is worth noting that, contrary to the method followed for the k loop, the Fischer-Burmeister technique cannot be used, since it has already been defined which mechanisms are in play. Consequently, the form of $\hat{\boldsymbol{B}}$ must adapt to their number, even if its dimensions are kept to N_m. To this end, the “precursor” matrix $\bar{\boldsymbol{B}}$ of dimensions $N_m \times N_m$ is firstly built, its components found by:

$$\bar{B}_{mj} = \sum_i \left(\frac{\partial\Phi^m}{\partial\boldsymbol{V}_{\boldsymbol{i}}^{\boldsymbol{j}}} : \boldsymbol{\Lambda}_{\boldsymbol{i}}^{\boldsymbol{j}}\right) - \frac{\partial\Phi^m}{\partial\boldsymbol{\sigma}} : \boldsymbol{C} : \left(\frac{\partial\boldsymbol{S}}{\partial p^j} : \boldsymbol{\sigma} + \frac{\partial\boldsymbol{\alpha}}{\partial p^j}\Delta T + \boldsymbol{\Lambda}_{\varepsilon}^{\boldsymbol{j}}\right) \tag{5.27}$$

The effect of the partial derivatives of yield functions Φ^m which stay negative must be suppressed. Thus, the elements of $\hat{\boldsymbol{B}}$ are found as:

$$\hat{B}_{mj} = U_m U_j \bar{B}_{mj} + (1 - U_m) I_{mj} \tag{5.28}$$

where the index U_m indicates whether a mechanism m (or j) is activated:

$$\begin{cases} U_m = 1 \text{ if } \Phi^m = 0 \\ U_m = 0 \text{ if } \Phi^m < 0 \end{cases} \tag{5.29}$$

Thus, $\hat{B}_{mj} = 0$ for the non-diagonal elements if the mechanism m is not activated, but $\hat{B}_{mm} = 1$ such that $\hat{\boldsymbol{B}}$ stays reversible in (5.27) and also equivalent to a square matrix of reduced dimensions. The corresponding dp^j is then found 0 in the equation:

$$dp^j = -\boldsymbol{P}_{\varepsilon}^{\boldsymbol{j}} : \boldsymbol{d\varepsilon} - P_T^j dT \tag{5.30}$$

where the building components $\boldsymbol{P}_{\varepsilon}^{\boldsymbol{j}}$ and P_T^j are given as:

$$\boldsymbol{P}_{\varepsilon}^{\boldsymbol{j}} = \boldsymbol{C} : \sum_m \left(\hat{B}_{mj}^{-1}\frac{\partial\Phi^m}{\partial\boldsymbol{\sigma}}\right) \tag{5.31}$$

and

$$P_T^j = \sum_m \left[\hat{B}_{mj}^{-1}\left(\frac{\partial\Phi^m}{\partial T} - \frac{\partial\Phi^m}{\partial\boldsymbol{\sigma}} : \boldsymbol{C} : \boldsymbol{\alpha}\right)\right] \tag{5.32}$$

These are used in the expressions of the tangent moduli:

$$\boldsymbol{L} = \boldsymbol{C} : \left[\boldsymbol{I}^{(4)} + \sum_j (\boldsymbol{K}^{\boldsymbol{j}} \otimes \boldsymbol{P}_{\varepsilon}^{\boldsymbol{j}})\right] \tag{5.33}$$

and

$$\boldsymbol{\Theta} = \boldsymbol{C} : \left[\sum_j (P_T^j \boldsymbol{K}^j) - \boldsymbol{\alpha} \right] \tag{5.34}$$

The adaptive nature of the tangent moduli is highlighted by their ability to be evaluated as a function of the activation or absence of the inelastic mechanisms.

During the n loop, a Finite Element Analysis suite, such as Abaqus, performs the task of balancing the influence of thermal fluxes with thermal energy rates. Recalling (4.88), the first law of thermodynamics is expressed in terms of the rate difference between the rise (or reduction) of the thermal energy linked to specific heat and the heat sources. This energy rate is denoted by the variable r^{pl} [Chatzigeorgiou et al., 2016]:

$$r^{pl} = C_v \dot{T} - \dot{Q} = \boldsymbol{D}_{,\boldsymbol{\varepsilon}} : \dot{\boldsymbol{\varepsilon}} + D_{,T} \dot{T} \tag{5.35}$$

Abaqus needs the quantities $\boldsymbol{d}_{\boldsymbol{\varepsilon}}^{\boldsymbol{r}}$ and d_T^r used in the equation

$$dr^{pl} = \boldsymbol{d}_{\boldsymbol{\varepsilon}}^{\boldsymbol{r}} : \boldsymbol{d\varepsilon} + d_T^r dT \tag{5.36}$$

These are found with the help of the thermomechanical tangent moduli and are evaluated at the end of the ω loop. The detailed manipulations to reach their final expressions, as well as the whole procedure leading to the computation of the tangent moduli, are discussed in Appendix E.

5.3 Numerical validation of the SMA model employing experimental databases

The thermomechanical response of the proposed model is compared to several experimentally observed complex, non-proportional thermomechanical responses of SMAs, to the extent of their availability. The selected experimental database includes proportional and non-proportional loading conditions in various thermal and mechanical levels.

A first set of experiments concern the isothermal tension loading of NiTi wires under various temperatures, either above or in-between martensitic transformation temperatures [Sittner et al., 2009]. A second kind of experiment corresponds to non-proportional tension-torsion loading of SMA tube structures [Sittner et al., 1995]. A last experiment is complex tension/torsion and compression/torsion on NiTi tube [Grabe and Bruhns, 2009].

The process of parameter identification is evidently important when trying to fit experimental data to complex models. In a very interesting recent work [Enemark and Santos, 2015], it has been demonstrated that even for simpler

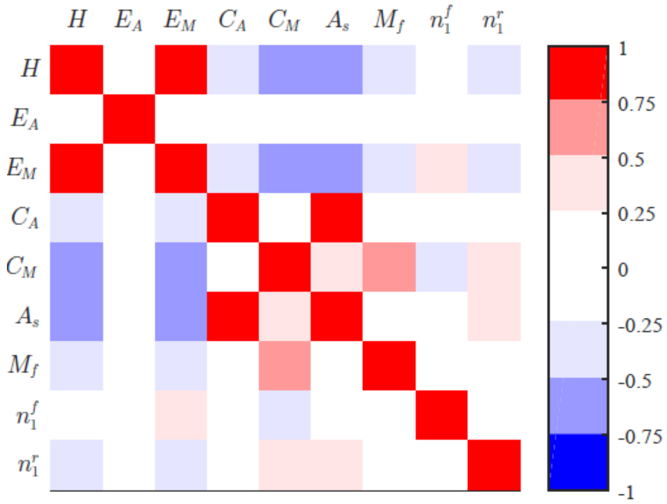

FIGURE 5.1 – Parameter estimate correlation for the SMA model proposed in [Enemark and Santos, 2015].

models not accounting for reorientation, there is a strong correlation between material parameters that are initially assumed independent. In a model built with the purpose to eliminate parameter dependency using a smaller amount of more inclusive constants, there are still certain material constants manifesting important correlation. This means, numerically, that the identification procedure is hindered by the presence of intercorrelation in the Jacobian (sensitivity) matrix. It also means, from a physical point of view, that the number of constants can be even further reduced. The sensitivity matrix presented on Fig. 5.1 reveals strong correlation between the estimations of C_A and A_s or H^{cur} and E_M. These results are collected from a statistical sample of 250 identification runs conducted to calibrate tensile tests on NiTi wires.

With the exception of the constants accounting for anisotropy, all other material parameters represent (or can be related with) important measurements deriving from established characterization of the thermomechanical behavior in SMAs. The three new constants accounting for the behavior led by reorientation (σ^{re}, H^{re}, ε^{re}_{max}) can be identified from a single tensile loading experiment of a specimen in martensitic regime at low temperatures, where it is known that no transformation takes place. However, when experiments under complex non-proportional conditions are exploited to extract the sought parameter values, identification becomes more complex. This is explained by the fact that the experimental response is affected by all possible strain mechanisms, which can also impact each other and therefore cannot be decoupled. As a result, there remain uncertainties regarding the uniqueness of the set of constants provided by identification, as well as for their precision.

In this chapter, parameter identification was carried out using a proven method reliable in identifying complex modeling parameters for SMAs using inverse identification methods developed by Meraghni et al. [2014] and extended for heterogeneous configuration in [Chemisky et al., 2015]. It is a method proven reliable in identifying complex modeling parameters in past works [Echchorfi et al., 2013; Meraghni et al., 2014; Piotrowski et al., 2013]. It has been numerically implemented on the SMART+ digital platform, using C++ coding [SMART+ Development Team, 2012]. Material properties of each individual material are presented in corresponding tables. Not all material parameters are interesting for the modelisation of the inelastic behavior of SMAs, and therefore are not identified, as is the case for the thermal expansion coefficients α. Usual values appearing in relevant literature are considered. Values that are not result of an identification procedure appear in parentheses in the corresponding tables.

5.3.1 Isothermal tension-compression

Three tensile loading tests on NiTi wires of 0.1 mm in diameter and 50 mm in length are simulated in iso-thermal conditions for different temperatures The numerical model corresponds to the experiments in [Sittner et al., 2009]: The displacement control of wires of 0.1 mm in diameter and 50 mm in length is taken as a strain-controlled simulation of a material point in its loading direction, and in stress-free condition in shear in other directions. In these experiments, compression cannot be carried out, since the small diameter of a wire would cause buckling immediately. In the simulations, though, inelastic geometry effects can be ignored.

For the temperature of 333 K , the wire demonstrates a superelastic behavior, since the stress levels cross all the transition thresholds for the start and finish of forward and reverse transformation before returning to zero stress. The behavior is similar for the temperature of 283 K, only with lower stress levels for forward and

E^A (MPa)	E^M (MPa)	v^A	v^M	$\alpha\,(K^{-1})$	H_{min}	H_{sat}
40000	23000	(0.33)	(0.33)	(10^{-5})	0.052	0.052
k	C^A (MPa/K)	C^M (MPa/K)	M_f (K)	M_s (K)	A_s (K)	A_f (K)
–	7.2	4.8	198.5	200	266	270
Y_o^{reo} (MPa)	ε_{max}^{re}	$H^{re}(MPa)$	b	n		
100	0.052	2000	–	–		

Table 5.1 – Material constants for equiatomic NiTi utilized in loading simulations of experiments presented in [Sittner et al., 2009]. Values that are not result of identification appear in parentheses.

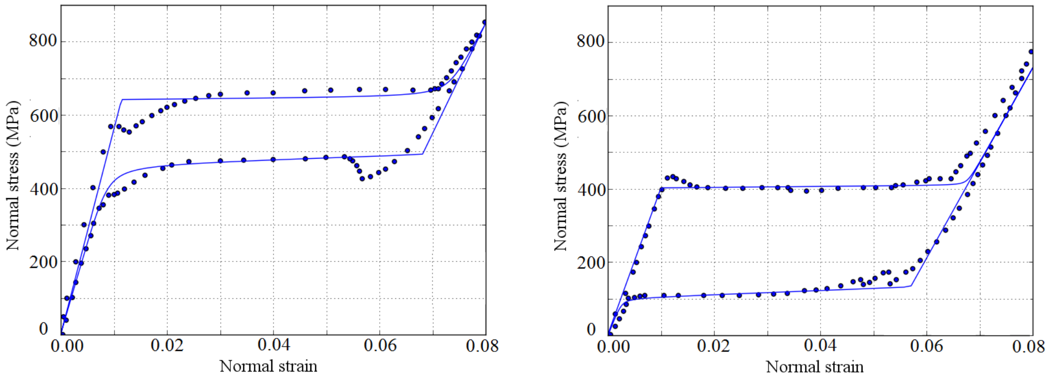

(a) Tension at 333 K (b) Tension at 283 K

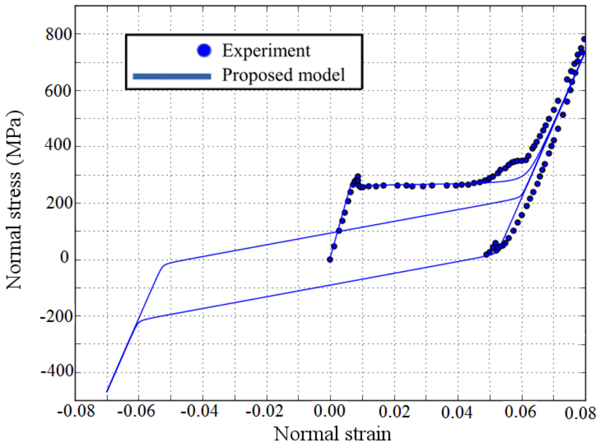

(c) Tension at 253 K

Figure 5.2 – Experimental results (points) and model reponse (continuous line) on stress-strain diagrams for isothermal tension-compression loading of NiTi wires under temperatures of 333, (a) 283 (b) and 253 K (c) taken from [Sittner et al., 2009].

reverse transformation, following a typical SMA phase diagram. At 253 K though, the transformation strain during loading is induced by forward transformation activated alongside reoreintation. This strain cannot be recovered upon unloading: since the temperature is lower than the austenitic transition level, no reverse transformation can take place. Still, the proposed model can predict some level of inelastic strain recovery just before reaching zero stress, associated with reorientation. Continuing further into compression, the material passes in a behavior affected only by reorientation. In the second cycle of loading, no transformation is considered, explaining the difference of shape from the first cycle. Good agrement is observed between the simulation and the experimental findings in tension. It is noted that the value of the elastic modulus is considered different for the test at 333 K, taken at 56000 MPa, since the stress-strain relation clearly indicates so. The current model does not take into account any dependence of the elastic modulus from temperature. However, all other material parameters are considered constant for the three experiments. Figs. 5.2 (a) to (c) present the comparison of the stress-strain diagrams for the isothermal tension-compression loading paths. In Fig. (5.2c), a prediction of the material behavior in compression is also presented. Reverse transformation cannot take place at such temperature. The effect of combined transformation/reorientation leads to a transient response for the first cycle, then to a stable reorientation loop since no reverse transformation occurs. The identified parameters appear in Table 5.1.

5.3.2 Non-proportional tension-torsion

Next, the proposed model is aimed at being further validated by comparing experimental results corresponding to non-proportional loading of thin-walled tube structures [Sittner et al., 1995]. A cylindrical tube made of CuAlZnMn alloy was subjected to a loading path resembling a rectangle in the space of normal (axial) and shear (along the tube walls) stress, with return to zero loading. The path is represented in Fig. (5.3a), while the material properties identified are reported in Table 5.2. The model response is superimposed to experimental data points in diagrams relating shear and normal strain in Fig. (5.3b), normal stress and strain in (5.3c) and shear stress and strain in (5.3d). A comparison with the models proposed by Lagoudas et al. [2012], Arghavani et al. [2010] and Panico and Brinson [2007], who have executed the same simulation is also conducted. The proposed model shows activation of the reorientation mechanism only between points C and D of the loading path, where it is combined with reverse transformation. The normal stress level reached at point A is low enough to allow for even more forward transformation along the shear direction in the

E^A (MPa)	E^M (MPa)	v^A	v^M	$\alpha\,(K^{-1})$	H_{min}	H_{sat}
38000	13000	0.20	0.20	(10^{-5})	(0.007)	0.007
k	C^A (MPa/K)	C^M (MPa/K)	M_f (K)	M_s (K)	A_s (K)	A_f (K)
–	8.7	7.27	215	260	222	275
Y_o^{reo} (MPa)	ε^{re}_{max}	$H^{re}(MPa)$	b	n		
398	0.007	21400	–	–		

Table 5.2 – Material constants for CuAlZnMn tube subjected to non-proportional tension-torsion from [Sittner et al., 1995]. Values that are not result of identification appear in parentheses.

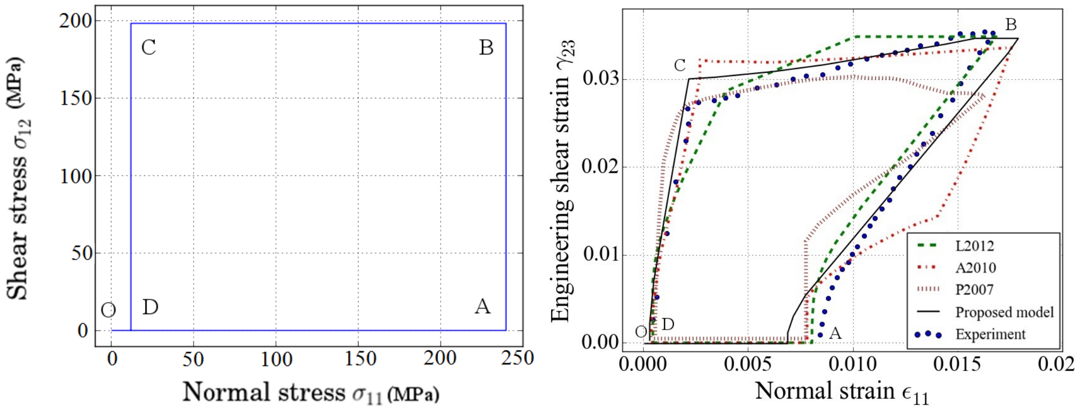

(a) Rectangle path in stresses on SMA tube (b) Material response in normal and shear strains

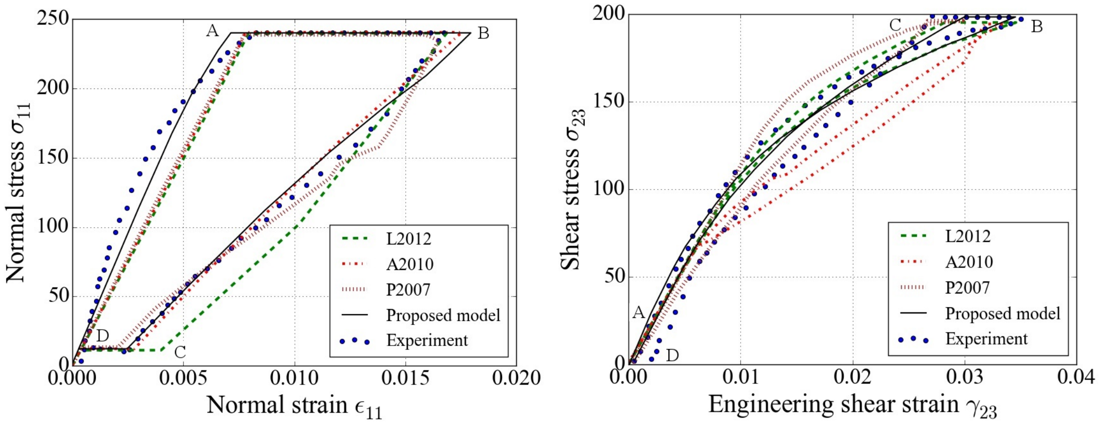

(c) Normal stress-strain diagram (d) Shear stress-strain diagram

FIGURE 5.3 – Experimental results (points) and model reponse (continuous line) on SMA thin-walled tube from [Sittner et al., 1995]. Comparison with model results from [Lagoudas et al., 2012] (L2012), [Arghavani et al., 2010] (A2010) and [Panico and Brinson, 2007] (P2007).

branch A to B, and therefore reorientation is not activated. Sufficient accuracy of the predictive capabilities of the model in this case of non-proportional loading is demonstrated, especially in comparison with the attempts made by previous models. As a final remark, it is added that even the Young's modulus for austenite was captured with higher precision relatively to the other models, as becomes evident at the elastic phase in Fig. (5.3c). This improved approach to such an important material parameter demonstrates the combined adaptive capability of the new model and the implemented identification algorithm.

Comparing the results from simulations between the current model and the model by Lagoudas et al. [2012], it becomes clear that certain aspects of material response are handled better. Specifically, after point B, reorientation is activated alongside reverse transformation when the stress levels are low enough. This has an impact on the two-branch linear response between points B and C in the shear-normal strain curve in Fig. (5.3b). The transition point between the two branches is shifted to lower normal strain values, which is a direct effect of the simultaneous activation of reorientation and reverse activation. This leads to a strong reduction of normal but not shear transformation strains, following the evolution of stress. This could not have been predicted with the previous model. Moreover, in Fig. (5.3d), the crossing of the response curve in the shear stress-shear strain space is reproduced, whereas, with the previous model, the return path C-D never crosses the initial A-B curve. The difference in the predicted capacity for developing transformation strains is also evident. Whereas the previous model presents a value of 3.5% for recoverable strain, the identification of model parameters with the current model reveals that 0.7% would be a better estimate. This implies that the non-linear effects are mostly a result of the change in elastic modulus. As the phase transformation carries through, the fading elastic modulus of martensite takes effect in allowing for more elastic strain to appear at higher values of MVF. The austenitic modulus is recovered during reverse transformation. Note that such parameter identification comes directly out of an optimization process aimed at minimising the square difference between experimental and numerical strains. Also, the proposed model could be reduced here to the Lagoudas et al. [2012] model in the sense that it is a special case of the new model in absence of reorientation mechanism or combined forward/reverse transformation.

5.3.3 Complex thermomechanical loading

A more complicated loading path is chosen to put the new model under test. In [Grabe and Bruhns, 2009], an experiment alternating the stress level of the SMA material between tension and compression, combined with torsion, subjected to a wide range of temperature levels is presented. The full path is presented in

E^A (MPa)	E^M (MPa)	v^A	v^M	$\alpha\,(K^{-1})$	H_{min}	H_{sat}
50120	27000	0.30	0.30	(10^{-5})	(0.056)	0.056
k	C^A (MPa/K)	C^M (MPa/K)	M_f (K)	M_s (K)	A_s (K)	A_f (K)
–	9	9	255	258	264	277
Y_o^{reo} (MPa)	ε^{re}_{max}	$H^{re}(MPa)$	b	n		
132.9	0.046	1546	0.608	2		

Table 5.3 – Material constants for NiTi tube subjected to tension-torsion-thermal loading presented in [Grabe and Bruhns, 2009]. Values that are not result of identification appear in parentheses.

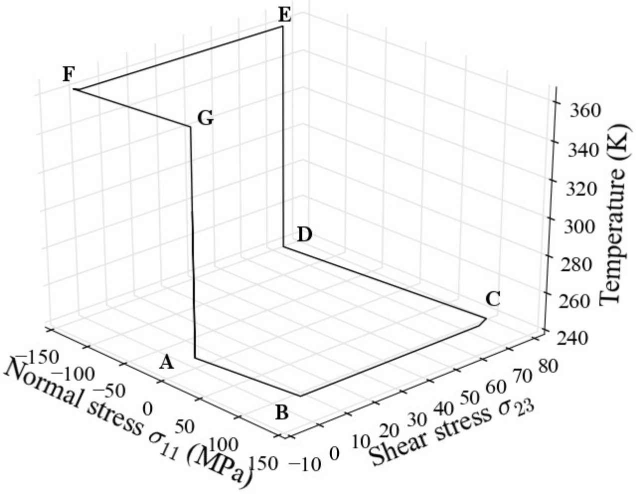

FIGURE 5.4 – Tension-compression loading combined with torsion in varying temperature, taken from [Grabe and Bruhns, 2009].

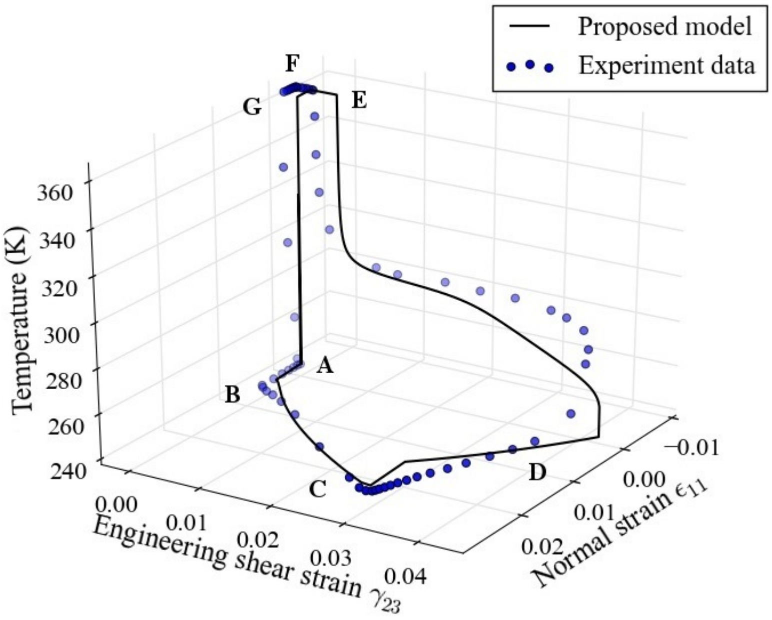

FIGURE 5.5 – Simulated behavior (line) of the complex thermomechanical loading of NiTi tube and comparison with experimental data (points).

Fig. 5.4. A tube specimen made of 50.7 at. % NiTi with a wall thickness of 1.68 mm is heated from 193 to 243 K at a stress-free state. It is then loaded in the axial direction to 120 MPa in tension up to point B, and then to a combined

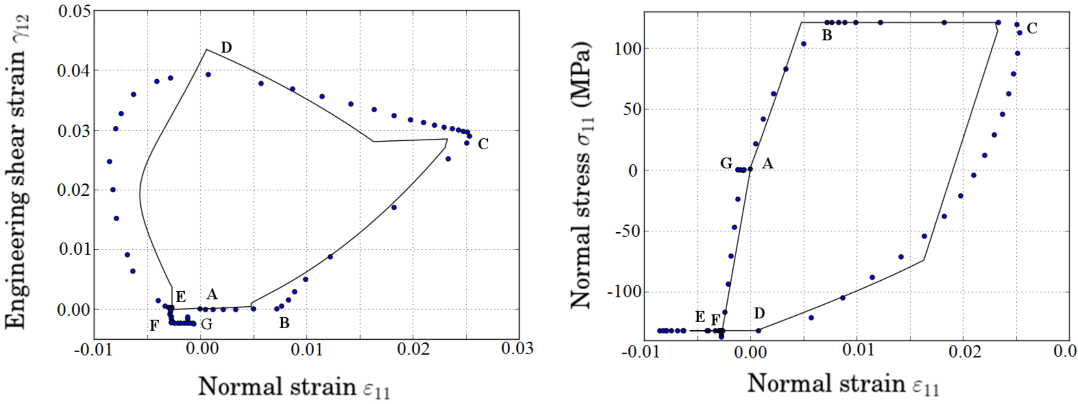

(a) Shear - axial strain relation

(b) Normal stress - strain relation

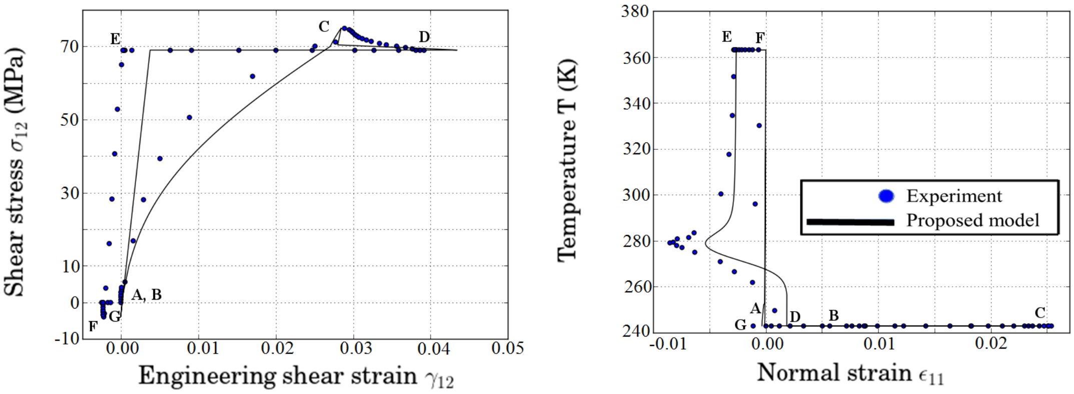

(c) Shear stress - strain relation

(d) Temperature - axial strain relation

Figure 5.6 – Experimental results (points) and model reponse (line) on SMA thin-walled tube from [Grabe and Bruhns, 2009]

tension-torsion state at 120 MPa in torsion to point C. From this point, axial stress is reversed to 132 MPa in compression (D). Then, maintaining the stresses, the tube is heated to 363 K (E), where it is gradually released from torsion first (F) and then compression (G). Finally, the specimen is cooled down to 243 K, returning to the initial point A. The identified material parameters appear in Table 5.3. This time, the model parameters for asymmetry are important, since compression is present in the loading path. The curves resulting from the loading simulation are presented in Figs. 5.5 and 5.6 and compared with the reported experiment results. The material behavior in the space of temperature, axial and shear strain is presented in the 3D graph in Fig. 5.5. In Figs. 5.6 (a) to (d), the relation between the material variables is outlined during the history of the experiment. In the loading history up to point D, all non-linear behavior is due to the orientation mechanism. The temperature is below the martensite transition points and therefore no transformation is allowed. The two-branch response in the C-D path in the normal stress-strain curve confirms the kinematic character of the hardening during reorientation. However, the discrepancies between experiment and simulation imply that a non-linear hardening law would be better suited.

In the part D-E of the loading path, where the tube is heated and submitted to reverse transformation, the current model handles the change in the direction of transformation strains, as revealed in the shear-axial strain curve. The idea of a simple recovery of transformation strains would lead to straight line from point D to E in Fig. 5.6(a) and (d). The form of the selected evolution law of (4.27) however, in combination with the simultaneous activation of reorientation, imposes a more complex strain path resembling the experimental data.

5.4 Analysis of thermomechanical coupling

Interesting work regarding the strain rate effect resulting from thermomechanical coupling in 1-D loading has been published by Maynadier [2012] and in the multiscale framework by Heintze and Seelecke [2008]. In the SMA loading scenarios examined thus far in this chapter, the temperature of the material was constantly controlled. This strict constraint of thermal boundary conditions does not allow to take in mind the strong thermomechanical coupling predicted by the proposed model. Two simple test cases are analyzed in this section to highlight the effect of the heat sources resulting from mechanical working.

5.4.1 Adiabatic conditions

The effect of thermomechanical coupling is particularly set on display when considering adiabatic loading. In equation (4.77), the heat fluxes $\boldsymbol{q}$ are considered zero and all the heat sources are consumed inside the material. The absence of heat exchange with the surroundings means that the temperature is influenced the most heavily possible by the internal heat production. In the case of SMAs, this leads to extreme conditions. A comparison between the responses for a hypothetical isothermal and adiabatic loading of a single NiTi element is given in Figure 5.7. The initial temperature is set at 280 K for both cases, but reaches 340 K under adiabatic conditions, which explains the enhanced hardening effect during transformation [Lagoudas, 2008].

The material parameters taken into account for this demonstration are input to Abaqus for the Finite Element Analysis in the upcoming subsection.

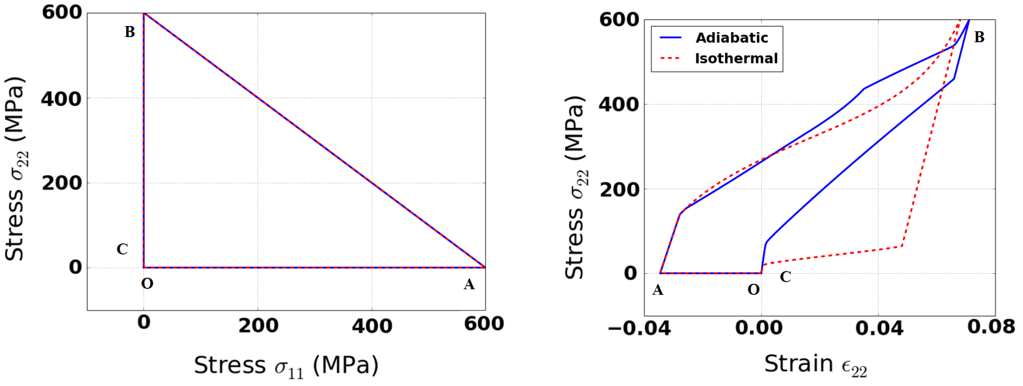

(a) Simulated non-proportional loading path in normal stresses (b) Response under isothermal and adiabatic conditions

FIGURE 5.7 – Non-proportional loading (a) and stress-strain diagrams in the normal direction 2-2 (b) for a NiTi SMA under isothermal and adiabatic conditions.

5.4.2 Finite Element Analysis of the strain rate effect on a NiTi structure

The effect of themomechanical coupling for a SMA structure in environmental conditions becomes evident in cases when the strain rate imposed by external working is so high that regular convection is not sufficient to ensure isothermal conditions. In a simple test-case scenario, a holed plate made of NiTi is subjected to non-proportional mechanical loading. The UMAT subroutine built on the basis of the new model is implemented in the Finite Element package Abaqus to simulate the material response. Convection-type thermal boundary conditions are applied to the surface of the structure.

The plate is considered to be placed in a temperature pool, in which the air has a constant temperature $T_{\infty} = 297K$. A “surface film interaction" with convection parameter $\bar{h} = 0.4\,kW/m^2K$ [Enemark et al., 2015; Pathak et al., 2010] is kept constant throughout the whole analysis to control heat exchanges. Such boundary conditions resemble to that of a real experiment at room temperature. The material properties are reported in Table 5.4. The bottom surface of the plate is considered clamped. In the first step of the loading, tension is applied by controlling the position of the upper surface, gradually increasing to 2.8 mm. Then, in the second step, a "shear-type" loading is applied, consisting of a uniform displacement applied on the same surface in the lateral direction, gradually reaching 3 mm, while longitudinal displacement is maintained at the previous level. In the third step, the two displacements are simultaneously removed until full unloading is reached. The geometry and the history of loading is illustrated in Fig. 5.8. The full geometry has been simulated, since the thermomechanical conditions do not present symmetry in the overall loading history. C3D8T elements were used for the mesh. Two simulations were executed, where the boundary conditions of the top surface were imposed under two different speeds $\dfrac{\Delta l/l}{\Delta t}$: at $1.5 \cdot 10^{-5} sec^{-1}$, considered to correspond to a "static" load, and at $1.5 \cdot 10^{-3} sec^{-1}$, which induces a temperature change actively affecting the mechanical behavior.

On Fig. 5.10, it is clear that the thermomechanical coupling induces a significant change in the temperature field in the case of the high loading rate. The mechanical response of the material should therefore be impacted. Also, reorientation appears in the stress concentration zone around the hole during loading Step 2. It is particularly enlightening to look closer at this location and

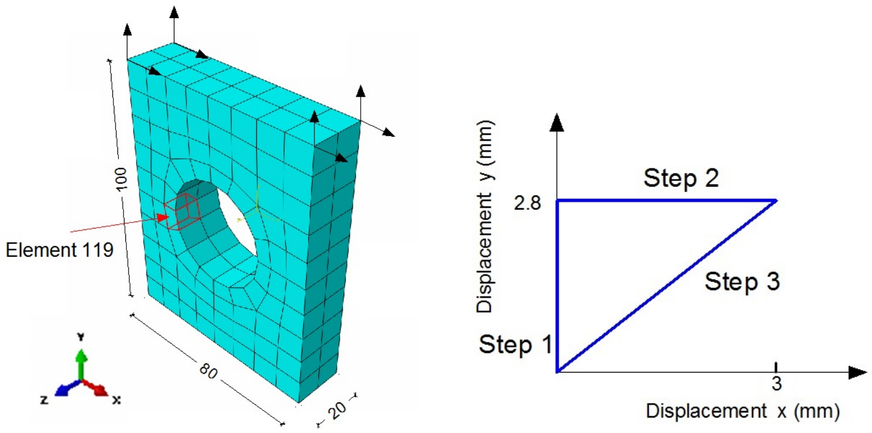

(a) Geometry of the holed plate

(b) Loading path for the top surface

FIGURE 5.8 – Geometry (a) and loading history (b) of the holed plate. Dimensions in mm.

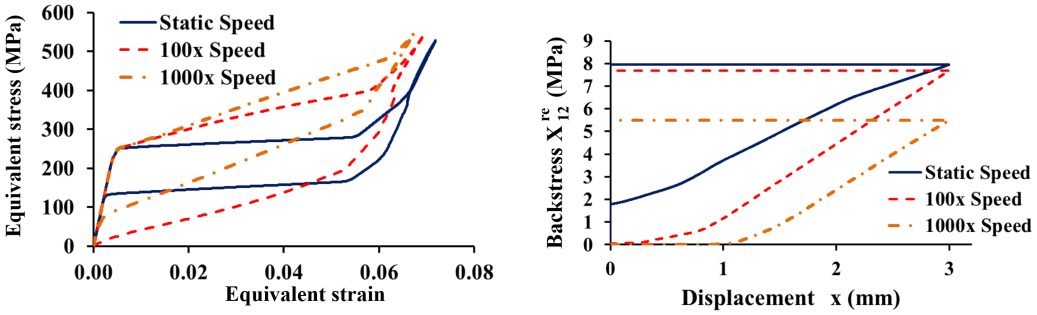

(a) Equivalent (Von Mises) stress-strain diagram

(b) History of X^{re}_{12} in relation to the “shear” loading.

FIGURE 5.9 – The equivalent stress-strain relation (a) and the evolution of the backstress component X^{re}_{12} tracking the history of reorientation (b) for the two loading rates for the element 119 of the mesh.

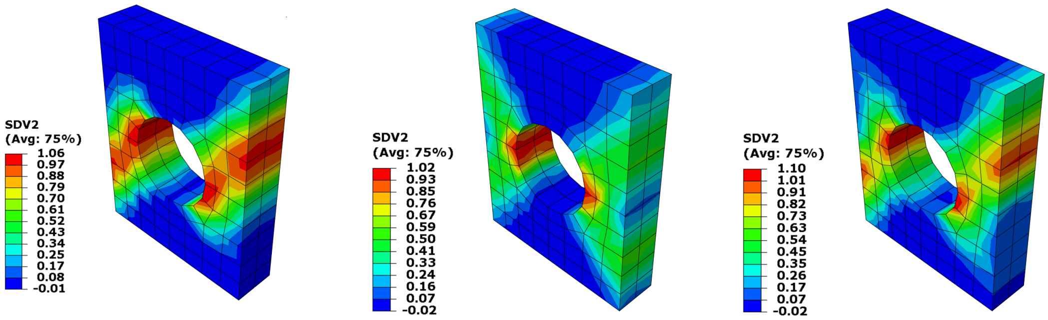

(a) Static speed, ξ at Step 2 (b) Speed 100x, ξ at Step 1 (c) Speed 100x, ξ at Step 2

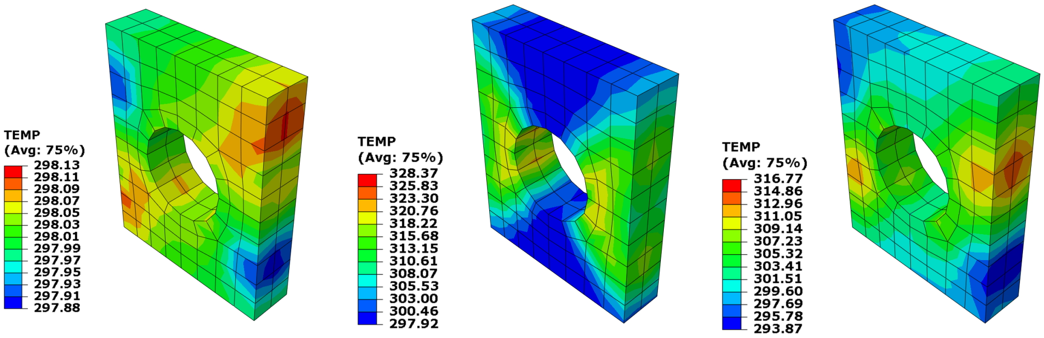

(d) Static speed, temperature at Step 2 (e) Speed 100x, temperature at Step 1 (f) Speed 100x, temperature at Step 2

FIGURE 5.10 – Martensitic volume fraction (ξ) on the first row (a-c) and temperature contour maps on the second (d-f) corresponding to the same time step for the two loading speeds at the end of Step 1 and end of Step 2. [1]

in the centroid of element 119 precisely. Undergoing reorientation, this material point has a particularly complex evolution of stress state, presented in Fig. 5.9. The equivalent Mises stress - Mises strain diagram in (5.9a) provides us a clear view that the heat generation is actually dominated by phase transformation. The crystallographic transition between austenite and martensite corresponds to an

E^A (MPa)	E^M (MPa)	v^A	v^M	$\alpha\,(K^{-1})$	H_{min}	H_{sat}
50120	27000	0.30	0.30	10^{-5}	0.0	0.056
k	C^A (MPa/K)	C^M (MPa/K)	M_f (K)	M_s (K)	A_s (K)	A_f (K)
0.021	6	6	253	258	272	277
Y_o^{reo} (MPa)	ε^{re}_{max}	$H^{re}(MPa)$	b	n	$\rho(kg/m^3)$	$k_{th}(W/mK)$
120	0.05	1000	0	(2)	6450	12

TABLE 5.4 – Material constants for NiTi plate subjected in non-proportional loading modeled in finite element analysis.ρ is the mass density and k_{th} is the thermal conductivity constant.

exothermal (or endothermal for the reverse transformation) reaction and induces latent heat and dissipation. Such phenomena constitute a more important internal heat source compared to reorientation, the latter releasing heat through dissipation only. The increased temperature seems to affect the evolution of reorientation according to (5.9b): before the start of Step 2, reorientation appears blocked for the fast loading, whereas it has appeared during the isothermal loading. The final measurement of X_{12}^{re} at 8 MPa approximately reveals that a strain $\Delta\gamma_{12}^{T} \approx 0.016$ has developped due to reorientation at the end of Step 2, taking in mind the value 1000 MPa given to the parameter H^{re} for this simulation.

The results corresponding to an even higher loading speed, at $1.5 \cdot 10^{-2} sec$ are also available on these two figures. The model response is expected to be similar to adiabatic conditions practically, since there is too little time for heat exchange to take place. Although, at such high loading speeds, dynamic effects (such as damping or influence of inertia) are also expected to appear, this is a demonstration of the limits of the current SMA model.

The temperature maps on Figs. (5.10e) and (5.10f) corresponding to the end of Steps 1 and 2 respectively exhibit a cooling effect deriving from the interaction with the ambient air. The reorientation present in Step 2 does not produce as much energy as forward transformation and therefore the air has the time to absorb a fraction of the excessive heat. In the corresponding volume fraction maps (5.10b) and (5.10c), the difference between the transformed zones is small enough to justify the lack of supplementary heat during Step 2. Still, the difference in temperature at the end of Step 2 between the static loading case (5.10d) and the loading at higher speed is evident, although the MVF contours are practically the same.

5.5 Concluding remarks

In order to perform the practical assessment of the new phenomenological model introduced in Chapter 4, its numerical implementation has firstly been discussed. In the general framework of a rate-independent model taking in mind any number of inelastic mechanisms, the numerical algorithms used for the approximation of the evolution of model variables have been presented. The usefulness of the Fischer-Burmeister technique has mainly been highlighted. It permits an intelligent deduction of the activation of the mechanisms, while at the same time providing with the solution of the internal loop. The thermomechanical tangent moduli are accordingly evaluated in an intelligent adaptive manner.

---

[1] Values of ξ over 1 and below 0 are due to extrapolation from integration points to the element surface.

The new SMA model has been numerically assessed in two principal ways: Firstly, the model parameters have been calibrated against experimental databases. These include simple loadings of NiTi wires, as well as complex loadings in non-proportional thermomechanical conditions for structures of CuAlZnMn and NiTi alloys. The good fit between experimental and numerically generated curves demonstrates the effect of reorientation. Secondly, the strong thermomechanical coupling taken in mind is put to the test by performing test case loading scenarios with thermal boundary conditions. The Finite Element analysis of a NiTi structure in a simulated environment of surrounding air in particular allows to perform a study of the strain rate effect in the case of non-proportional loading and highlights the strength of the model.

5.6 References

J. Arghavani, F. Auricchio, R. Naghdabadi, A. Reali, and S. Sohrabpour. A 3-D phenomenological constitutive model for shape memory alloys under multiaxial loadings. *International Journal of Plasticity*, 26(7):976–991, jul 2010. ISSN 07496419. doi: 10.1016/j.ijplas.2009.12.003. xiii, 124, 125

F. Auricchio, E. Bonetti, G. Scalet, and F. Ubertini. Theoretical and numerical modeling of shape memory alloys accounting for multiple phase transformations and martensite reorientation. *International Journal of Plasticity*, 59:30–54, aug 2014. ISSN 07496419. doi: 10.1016/j.ijplas.2014.03.008. 115

D. Chatziathanasiou, Y. Chemisky, G. Chatzigeorgiou, and F. Meraghni. Modeling of coupled phase transformation and reorientation in shape memory alloys under non-proportional thermomechanical loading. *International Journal of Plasticity*, (IN PRESS), 2016. doi: 10.1016/j.ijplas.2016.03.005. 113

G. Chatzigeorgiou, N. Charalambakis, Y. Chemisky, and F. Meraghni. Periodic homogenization for fully coupled thermomechanical modeling of dissipative generalized standard materials. *International Journal of Plasticity*, 81:18–39, feb 2016. ISSN 07496419. doi: 10.1016/j.ijplas.2016.01.013. 120

Y. Chemisky, F. Meraghni, N. Bourgeois, S. Cornell, R. Echchorfi, and E. Patoor. Analysis of the deformation paths and thermomechanical parameter identification of a shape memory alloy using digital image correlation over heterogeneous tests. *International Journal of Mechanical Sciences*, 96-97:13–24, jun 2015. ISSN 00207403. doi: 10.1016/j.ijmecsci.2015.03.007. 122

R. Echchorfi, Y. Chemisky, N. Bourgeois, F. Meraghni, and E. Patoor. Identification of Model Parameters for the Simulation of SMA Structures Using Full Field Measurements. In I. Karaman, R. Arroyave, and E. Masad, editors, *The International Conference on Shape Memory and Superelastic Technologies (SMST)*. Asm, may 2013. doi: 10.1002/9781119090427.ch19. 122

S. Enemark and I. F. Santos. Quasi-static characterisation of trained pseudoelastic shape memory alloy wire subjected to cyclic loading: transformation kinetics. *Journal of Intelligent Material Systems and Structures*, 27(9):1150–1164, jun 2015. ISSN 1045-389X. doi: 10.1177/1045389X15585900. xiii, 120, 121

S. Enemark, M. A. Savi, and I. F. Santos. Experimental analyses of dynamical systems involving shape memory alloys. *Smart Structures and Systems*, 15(6):1521–1542, jun 2015. ISSN 1738-1584. doi: 10.12989/sss.2015.15.6.1521. 130

A. Fischer. A special newton-type optimization method. *Optimization*, 24(3-4):269–284, jan 1992. ISSN 0233-1934. doi: 10.1080/02331939208843795. 115

C. Grabe and O. Bruhns. Path dependence and multiaxial behavior of a polycrystalline NiTi alloy within the pseudoelastic and pseudoplastic temperature regimes. *International Journal of Plasticity*, 25(3):513–545, mar 2009. ISSN 07496419. doi: 10.1016/j.ijplas.2008.03.002. xiii, xv, 120, 126, 127, 128

D. J. Hartl and D. Lagoudas. Constitutive modeling and structural analysis considering simultaneous phase transformation and plastic yield in shape memory alloys. *Smart Materials and Structures*, 18(10):104017, oct 2009. ISSN 0964-1726. doi: 10.1088/0964-1726/18/10/104017. 115

O. Heintze and S. Seelecke. A coupled thermomechanical model for shape memory alloys—From single crystal to polycrystal. *Materials Science and Engineering: A*, 481-482:389–394, may 2008. ISSN 09215093. doi: 10.1016/j.msea.2007.08.028. 129

B. Kiefer, T. Bartel, and A. Menzel. Implementation of numerical integration schemes for the simulation of magnetic SMA constitutive response. *Smart Materials and Structures*, 21(9): 094007, sep 2012. ISSN 0964-1726. doi: 10.1088/0964-1726/21/9/094007. 115

D. Lagoudas, D. Hartl, Y. Chemisky, L. Machado, and P. Popov. Constitutive model for the numerical analysis of phase transformation in polycrystalline shape memory alloys. *International Journal of Plasticity*, 32-33(null):155–183, may 2012. ISSN 07496419. doi: 10.1016/j.ijplas.2011.10.009. xiii, 124, 125, 126

D. Lagoudas. *Shape Memory Alloys - Modeling and Engineering Applications.* Springer, 2008. 129

A. Maynadier. *Couplages thermomécaniques dans les alliages à mémoire de forme : mesure de champs cinématique et thermique et modélisation multiéchelle.* PhD thesis, nov 2012. 129

F. Meraghni, Y. Chemisky, B. Piotrowski, R. Echchorfi, N. Bourgeois, and E. Patoor. Parameter identification of a thermodynamic model for superelastic shape memory alloys using analytical calculation of the sensitivity matrix. *European Journal of Mechanics - A/Solids*, 45:226–237, may 2014. ISSN 09977538. doi: 10.1016/j.euromechsol.2013.12.010. 122

M. Panico and L. Brinson. A three-dimensional phenomenological model for martensite reorientation in shape memory alloys. *Journal of the Mechanics and Physics of Solids*, 55(11): 2491–2511, nov 2007. ISSN 00225096. doi: 10.1016/j.jmps.2007.03.010. xiii, 124, 125

A. Pathak, D. Brei, and J. Luntz. Transformation strain based method for characterization of convective heat transfer from shape memory alloy wires. *Smart Materials and Structures*, 19 (3):035005, mar 2010. ISSN 0964-1726. doi: 10.1088/0964-1726/19/3/035005. 130

B. Piotrowski, Y. Chemisky, F. Meraghni, R. Echchorfi, N. Bourgeois, and E. Patoor. Identification and Interpretation of Material Parameters of a Shape Memory Alloy (SMA) Model. *Materials Science Forum*, 738-739:276–280, jan 2013. ISSN 1662-9752. doi: 10.4028/www.scientific.net/MSF.738-739.276. 122

P. Sittner, Y. Hara, and M. Tokuda. Experimental study on the thermoelastic martensitic transformation in shape memory alloy polycrystal induced by combined external forces. *Metallurgical and Materials Transactions A*, 26(11):2923–2935, nov 1995. ISSN 1073-5623. doi: 10.1007/BF02669649. xiii, xv, 120, 124, 125

P. Sittner, L. Heller, J. Pilch, P. Sedlak, M. Frost, Y. Chemisky, A. Duval, B. Piotrowski, T. Ben Zineb, E. Patoor, F. Auricchio, S. Morganti, A. Reali, G. Rio, D. Favier, Y. Liu, E. Gibeau, C. Lexcellent, L. Boubakar, D. Hartl, S. Oehler, D. Lagoudas, and J. V. Humbeeck. Roundrobin SMA modeling. In *ESOMAT 2009 - 8th European Symposium on Martensitic Transformations*, page 08001, Les Ulis, France, sep 2009. EDP Sciences. ISBN 978-2-7598-0480-1. doi: 10.1051/esomat/200908001. xiii, xv, 120, 122, 123

SMART+ Development Team. Smart Materials Algorithms and Research Tools SMART+: A Scientific Library for the Analysis of the Thermomechanical Behavior of Heterogeneous Materials, 2012. 122

Conclusion and perspectives

The work presented in this thesis constitutes a contribution in the direction of macroscopic thermodynamic modeling of Shape Memory Alloys. The developments achieved herein are motivated by the need of a reliable predictive numerical tool able to capture the three-dimensional behavior under complex thermomechanical conditions. This kind of digital platform aims at designing products incorporating SMA components, as well as as conceiving new adaptive systems. The techniques approached during this work concern in particular the experimental study and the theoretical modeling of the features that differentiate uniaxial and multiaxial behaviors.

The first challenge of the thesis was to establish an experimental database dedicated to the combined examination of two aspects of SMA structures subjected to multiaxial conditions: anisotropy and cycling effects. Aiming to create a consistent database, a single material was chosen for all the experiments. All the specimens, coming from the same NiTi composition, underwent strictly identical annealing procedures. Having been processed in rolling, the samples exhibit a strong dependence to the direction of loading due to texture effects. Beyond asserting the well-known anisotropy for the stress plateau and the transformation strains, the performed experiments also underline another difference between loading in two separate directions: it is the evolution of behavior related to cycling. Namely, the development of residual strains and the reduction of the stress threshold at the start of transformation differ between two applied loading directions. Additional tests performed on biaxial specimens under non-proportional conditions also confirm the dependence of cyclic behavior to the path of loading direction.

The experimental work is the subject of the second out of a total of five chapters. In its first part, the conducted experiments on dog-bone samples, cut along the longitudinal and the transverse axis of rolling, are presented. These samples underwent a cyclic uniaxial load under three constant temperatures: 30, 40 and 50°C. Even in just one direction, the selected path was quite complex, reaching different strain levels. This allowed to highlight three factors affecting the cyclic behavior of NiTi in total: the number of cycles, the developed stress and, at the same time, the anisotropy. In the second part of the chapter, a repetitive loading path was applied on cross-shaped samples. Two modern experimental tools were utilized for this test: a biaxial testing machine with four independently controled moving heads and a platform of digital image correlation. The obtained results demonstrate here the strong effect of anisotropy on the behavior under repetitive loading in a biaxial case.

Inspired by theses experiments, the first target for the modeling work was to establish a new constitutive law able to capture anisotropy in phase transformation. However, this law had to be part of a general framework which is robust in terms of thermodynamics. For this purpose, a literature review focusing primarily in technical aspects of important thermodynamical models was carried out in the first chapter of this work. The models of Lagoudas and Brinson are acknowledged worldwide for their strength and form a milestone for practically any new theoretical work. Still, a critical point of view was maintained, allowing to build a solid foundation in order to strenghten their ability to capture the complex SMA behavior under multiaxial thermomechanical loading.

The third chapter is dedicated to the development of a constitutive law taking into account anisotropy in forward transformation. A new criterion making use of a transition between the space of real stresses and a space of fictitious stresses is presented. This transition allows for a simple expression of a mathematical surface predicting at the same time the asymmetry between tension and compression and the anisotropy observed in SMAs. A further contribution of this chapter is the introduction of a new evolution rule for transformation strains. It is based on the consideration of martensitic volume fraction as a basic internal variable, as is the case for most of the existing models. The requirement of measuring the martensitic fraction has led to the use of a micromechanical model as a means to evaluate the new criterion. The self-consistent model by Patoor was deployed to simulate proportional loading paths for textured samples. The calibration of the parameters of the new law asserts its adjustive capability and mainly its strength in capturing the important anisotropy in strains caused by forming conditions.

Although the phase transformation dominates the thermomechanical response of SMAs, it is the reorientation of martensitic variants which adds a certain degree of complexity to multiaxial non-proportional loading. With respect to that, the fourth chapter is dedicated to creating a SMA model suitable for any possible thermomechanical loading path. The mechanisms of reorientation and of forward and reverse transformation are described in terms of kinetics and thermodynamics, in order to formulate a system taking into account their simultaneous activation. The reorientation, in particular, is considered as a mechanism of kinematical hardening, introducing a plasticity-type backstress. Moreover, the new anisotropic law is also integrated. The thermomechanical coupling resulting from the first law of thermodynamics is examined and incorporated into the overall scheme. The new model produces the same predictions as the Lagoudas model for simple loading cases, where reorientation is not induced. It allows to detect the absence of reorientation effects for the uniaxial loading cases briefly presented at the end of Chapter 4.

The added value of the new model is assessed in the last chapter. A numerical tool in the form of a UMAT is deployed to execute simulations of SMA structures. The numerical methods necessary for this tool are presented in the beginning. Mainly the framework of multiple inelastic strain mechanisms has great interest for the modeling of different kinds of materials. Then, appropriate experimental databases found in the literature are utilized in order to examine the ability of the model to capture behavior under complex conditions. Thermomechanical loading paths highlighting the influence of reorientation were succesfully simulated. Finally, the model was implemented in the Finite Elements software Abaqus. This implementation emphasized the strength of the model to simulate the strong thermomechanical coupling in multiaxial conditions by examining the strain rate effect on a NiTi structure. Thermal conditions resembling actual experiments highlighted the impact of the loading speed on the variation of the temperature and, consequently, the material response.

The obtained experimental results, as well as the methods developed for creating this simulation tool, generate new topics of discussion for further developments in the study of SMA behavior. These topics are associated with three principal subjects: the experimental examination, the efficient implementation of the model and its application on more extended research fields.

On the experimental topic in particular, the implementation of the image correlation technique is considered very interesting. Even in uniaxial tests, identifying the transformation zones could clarify the dependence of cyclic behavior to the direction of loading. In biaxial experiments, this technique is practically required to evaluate the residual strains in repetitive loading of SMA structures.

It would also be very interesting to repeat the experiments performed here for other NiTi compositions or with other annealing procedures. This would lead to the study of cycling and anisotropy effects for a more extended database. Finally, this development could bring about an effort to optimize annealing with respect to the degradation of NiTi properties caused by cycling.

As far as the implementation of the model is concerned, the most important obstacle confronted during this work was the high number of material parameters. It is a recurring problem in the study of anisotropy that the number of new needed constants renders identification more difficult. Especially in materials as complex as SMAs, which require a modeling with a lot of independent material parameters even in the isotropic case, this proves a serious issue. The thesis by Echchorfi provided a powerful tool for identifying SMA parameters. It is deemed necessary to develop an identification method supplementary to this tool in order to allow for more reliable simulations.

It is also important, in the interest of adding to the work carried out during the thesis, to exploit the experimental results in conjuction with the new model. The framework of multiple activated mechanisms developed here allows for an easy incorporation of transformation induced plasticity as an added process in the global scheme. This might capture the residual strains reported in the uniaxial and biaxial tests. This integration would also lead to the creation of an even more comprehensive model.

The interaction with colleagues during the work of the thesis has highlighted further potential application of the new model. Firstly, the new transformation criterion has already been utilized in a study regarding the initiation of transformation around a fracture inside an anisotropic medium. It was an interesting work done by a student of Professor Patoor, Guillaume Mohara. The coupling of reorientation with transformation opens in general new horizons in fracture mechanics. The high heterogeneous stresses developing in the vicinity of a fracture can indeed cause reorientation with interesting results.

In addition, the strong thermomechanical coupling integrating in the model for generalized loading is worth of a meticulous implementation in order to examine the strain rate effect associated to thermal exchanges with the environment on 3D SMA structures. Even though it is a rate-independent model, it succeeds in explaining the variation in material response with respect to the rate of loading. It would also be interesting to conduct multiaxial experiments with well controled thermal boundary conditions, in order to compare the numerical response with experimental results.

Finally, the field of research of the highest interest related to SMAs for the industrial world is fatigue analysis. It forms a limiting factor against the extensive use of NiTi, since its long term behavior is not yet fully investigated either experimentally or in terms of modeling. It would be important to integrate a model predicting fatigue failure in the existing framework. This would possibly lead to associate the fatigue to the multiaxial state of stresses and to the effect of residual strains in the SMA.

II

Extended summary in French

Table des matières du résumé en français

Introduction

L'industrie contemporaine aspire à faire évoluer et à substituer les technologies utilisées conventionnellement par de nouvelles idées en employant des nouveaux matériaux afin de satisfaire à la fois des exigences structurales et fonctionnelles. Des domaines d'ingénierie menés par le besoin d'innovation, comme l'aéronautique, l'automobile et la biomécanique reconnaissent la compétence des matériaux actifs à explorer de nouveaux horizons pour le design de produits. Ce sont des matériaux dont la réponse mécanique peut être couplée à d'autres aspects physiques, c'est-à-dire la charge électrique, les champs électriques et magnétiques, la température et le flux de chaleur. Les propriétés intéressantes de tels matériaux nommés communément intelligents promeuvent la conception de nouvelles techniques de contrôle de systèmes industriels et même de nouveaux produits à commercialiser.

Du point de vue mécanique, les matériaux actifs exploitent leurs propriétés multi-physiques pour adapter leur comportement selon les conditions qu'ils subissent. Ils sont plutôt triés par rapport aux aspects physiques qu'ils combinent. Les céramiques piézo-électriques et les fibres piézo-résistives renforcées par des nanotubes de carbone sont des matériaux électro-actifs dont les propriétés électriques dépendent de la charge mécanique appliquée. Des substances polymériques organiques utilisées pour des structures de cristaux liquides modifiant leur polarisation optique en fonction de la température sont appelées thermotropiques. Les matériaux magnéto-restrictifs convertissent l'énergie magnétique en énergie cinétique et vice versa en adaptant leur forme aux champs magnétiques proches. Les alliages et composites à mémoire de forme sont des matériaux qui récupèrent leur forme originale quand ils subissent certains changements de températures appropriés et réussissent à coupler l'énergie thermique et cinétique.

La recherche fondamentale sur le comportement et les couplages multi-physiques de ces matériaux constitue un courant fort au sein de la communauté des matériaux adaptatifs. Cet intérêt est motivé par la complexité de leurs propriétés en comparaison avec les matériaux conventionnels utilisés en production industrielle. Spécifiquement dans le domaine de la conception des produits assemblés avec des composants en alliages à mémoire de forme (AMF), ils existent certains challenges à relever. Ils incluent la réponse thermomécanique sous chargement multiaxial, la stabilité en utilisation répétitive, la dégradation causée par les agents environnementaux, en particulier la fragilisation à cause de l'hydrogène, et le renforcement de leurs propriétés à travers des compositions chimiques modifiées et l'ajout de précipités d'échelle moyenne.

La compréhension des mécanismes physiques du comportement multifonctionnel des matériaux intelligents aboutit à un design de produits avancé. Il aide, d'ailleurs, à explorer des fonctions potentielles futures. La modélisation phénoménologique est intensivement utilisée en conception et permet le développement d'outils de simulation permettant la prédiction de la réponse macroscopique et éventuellement la calibration des paramètres de conception. Un modèle phénoménologique constitutif est considéré comme un ensemble de variables et de relations les reliant. Il représente les observations macroscopiques à travers une description mathématique, toujours dans le cadre des lois établies de la physique. Des outils de simulation avancés peuvent ensuite utiliser de tels modèles pour simuler la réponse de matériau. Pour le cas des AMFs, l'intérêt actuel de la communauté scientifique et industrielle est la modélisation de ces propriétés qui correspondent aux challenges spécifiques: le comportement multiaxial, l'évolution des caractéristiques de matériau engendrée par le chargement, la dégradation à cause d'agents environnementaux et l'intégration dans des structures composites.

Ce travail concerne principalement la modélisation macroscopique du comportement cyclique des AMFs sous conditions de chargement multiaxial. La modélisation est principalement dédiée aux alliages NiTi ayant un fort potentiel en termes d'applications industrielles. L'effort de modélisation se base sur le développement d'un système en variables internes thermodynamiquement associées à des forces motrices. Elles permettent d'introduire de nouveaux concepts pour traiter des problèmes particuliers de la réponse des AMFs en trois dimensions. Les objectifs de ce travail s'étendent aussi à une étude expérimentale de la réponse multiaxiale cyclique du NiTi et à la simulation numérique de composants en AMFs à travers la Méthode des Élements Finis.

Le premier chapitre du manuscrit présente les aspects fondamentaux du comportement thermomécanique des AMFs et aussi l'état de l'art concernant la modélisation macroscopique. La notion fondamentale de la transformation martensitique est examinée à l'échelle microscopique. C'est le mécanisme prinicipal des AMFs, responsable de leur caractéristiques, en particulier de la superélasticité et de l'effet de mémoire de forme. Deux modèles macroscopiques éprouvés sont ensuite analysés et comparés pour poser les bases de la formulation d'un nouveau modèle permettant d'intégrer le comportement complexe en chargement multiaxial.

Le deuxième chapitre concerne l'étude expérimentale du chargement cyclique d'un NiTi texturé. Les procédures expérimentales suivies incluent des essais thermomécaniques monoaxiaux et des essais mécaniques biaxiaux sur des éprouvettes cruciformes planes. Un trajet complexe avec des charges répétitives a été appliqué pour les deux cas pour permettre l'étude de l'effet de l'activation cyclique de transformation sur les propriétés du matériau. La dégradation de ces propriétés est également étudiée du point de vue de l'anisotropie aussi, puisque la direction du chargement varie.

Le troisème chapitre a pour but de traiter la problématique de la transformation martensitique anisotrope. Il est connu que les conditions de mise en forme affectent la texture crystallographique des AMFs et par conséquent induisent une certaine anisotropie dans la phase inélastique. Une nouvelle approche mathématique est proposée afin de capturer la dépendance de la réponse du matériau à la direction de chargement, observée lors des essais superélastiques.

La description globale du modèle constitutif proposé est présentée au quatrième chapitre. Les variables choisies pour représenter l'évolution de l'état interne et observable des structures en AMFs y sont décrites. Le mécanisme de la réorientation martensitique engendrant la réponse complexe sous chargement non-proportionnel est traitée avec une attention particulière. Le modèle est examiné du point de vue thermodynamique pour démontrer sa robustesse et sa conformité aux lois physiques. Ceci permet l'étude thermomécanique pour des cas quelconques de chargement du matériau, mettant ainsi en évidence l'aspect multi-physique du modèle.

Le cinquième chapitre est dédié à la validation du modèle proposé. Elle est réalisée d'une part au travers de simulations numériques des expériences complexes effectuées sur des structures en AMFs publiées dans la littérature. Les paramètres du modèle sont calibrés et la conformité de la réponse simulée aux résultats expérimentaux est démontrée. D'autre part, des simulations numériques sont réalisées à l'aide d'un logiciel d'Analyse par Éléments Finis (Abaqus) afin de démontrer l'apport des nouvelles considérations intégrées au modèle proposé sur le comportement multiaxial du matériau.

1. Comportement thermomécanique des AMF et problématique de la modélisation

1.1 Spécificités des alliages à mémoire de forme

Les alliages à mémoire de forme (AMFs) sont des matériaux métalliques dont le nom est dû à la découverte de leur capacité unique de récupérer leur forme originale lors d'une augmentation de température. Des déformations importantes induites par des charges mécaniques peuvent être annihilées si la température atteint des niveaux spécifiques. Dans le cas des métaux ordinaires, ces déformations seraient permanentes et irrécupérables. Ce trait caractéristique classe les AMFs dans la famille générale des matériaux à mémoire de forme. Il résulte d'une transformation à l'échelle cristalline entre les deux phases solides que le matériau peut adopter : l'austénite et la martensite. La différence entre ces deux phases se trouve au niveau de l'architecture de leurs formes cristallines, qui varie entre une configuration cubique dans l'austénite et une configuration moins symétrique dans la martensite [Otsuka and Wayman, 1999; Patoor et al., 2006].

En ce qui concerne la modélisation phénoménologique, la réponse du matériau est surtout associée à un diagramme de phase dans l'espace contrainte-température [Lecce and Concilio, 2014]. Sur le diagramme de phase illustré à la Figure 1.1, les domaines de chaque phase sont clairement mis en évidence. L'austénite apparaît pour des températures relativement élevées et des contraintes basses. La martensite auto-accommodée est présente pour des températures relativement basses, tant que la contrainte est plus basse qu'un seuil critique, représenté par le terme σ^{re}. Une fois ce seuil dépassé, le processus de réorientation est considéré comme initié, menant à la transition vers la martensite orientée. D'ailleurs, la transition vers la martensite à partir de l'austénite, soit orientée soit auto-accommodée, est induite par le passage à travers la zone désignée par les deux courbes M_s et M_f. Ces courbes ont normalement la forme de lignes droites avec la même pente C_M. Traverser la ligne M_s signale le début (start) de la transformation directe et M_f (finish) sa saturation. La transformation inverse s'effectue lors en traversant la zone entre les courbes A_f et A_s. Ces quatres courbes du diagramme de phase expriment la dépendence des températures de transformation avec la contrainte appliquée. La différence entre les températures de transformation explique l'hystérèse des contraintes observée au comportement des AMFs.

1.2 Problématique du comportement multiaxial des AMF

1.2.1 Anisotropie

La caractérisation expérimentale du comportement superélastique des AMFs a montré que le matériau manifeste une dissymétrie traction-compression [Bouvet et al., 2004; Zhu and Dui, 2010]. Concrètement, la contrainte critique de début de transformation est différente entre traction et compression. Par conséquent, un critère du type Von Mises n'est pas capable de prédire avec précision la surface de transformation dans l'espace des contraintes pour une température donnée. Il a été démontré, en utilisant un modèle micromécanique, que la dissymétrie traction-

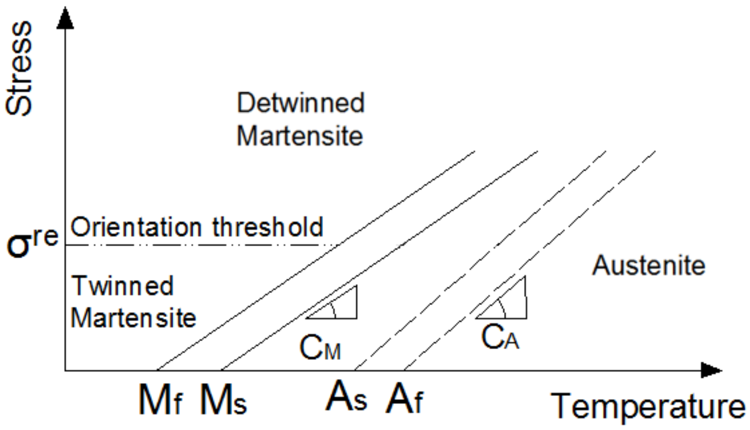

FIGURE 1.1 – Un diagramme de phase typique pour un alliage NiTi.

compression est liée à la perte de symétrie induite par l'apparition des variantes de martensite [Patoor et al., 1995]. La dissymétrie se met en évidence à la fois sur la contrainte critique déclenchant la transformation martensitique, sur les pentes des courbes contrainte-température du diagramme de phase et sur l'amplitude des déformations de transformation [Šittner and Novák, 2000]. Le comportement des AMFs ayant subi des procédés de fabrication manifeste aussi des propriétés anisotropes [Grolleau et al., 2011; Sittner et al., 2009]. Comme dans d'autres métaux, la texture du matériau et la présence de contraintes internes sont les facteurs principaux induisant une telle anisotropie. Une analyse micromécanique a démontré que la transformation d'un polycristal est fortement anisotrope [Taillard et al., 2008].

La thèse d'Echchorfi [2013] a fourni des données expérimentales remarquables concernant la dissymétrie et l'anisotropie. La Figure 1.2 montre des essais pertinents sur des échantillons unidirectionnels en NiTi. Sur (1.2a), il est évident que le plateau associé avec la transformation se produit à des niveaux de contraintes plus hauts en compression qu'en traction. Aussi, la traction induit des déformations de transformation supérieures en comparaison avec la compression. De même, il existe une différence sensible entre les résultats des essais de traction dans les directions de laminage et transverse (perpendiculaire au laminage). Sur (1.2b), un échantillon dans la direction transverse du laminage subit la transformation directe et inverse à des contraintes supérieures que son homologue longitudinal. Il développe par ailleurs des déformations inélastiques inférieures.

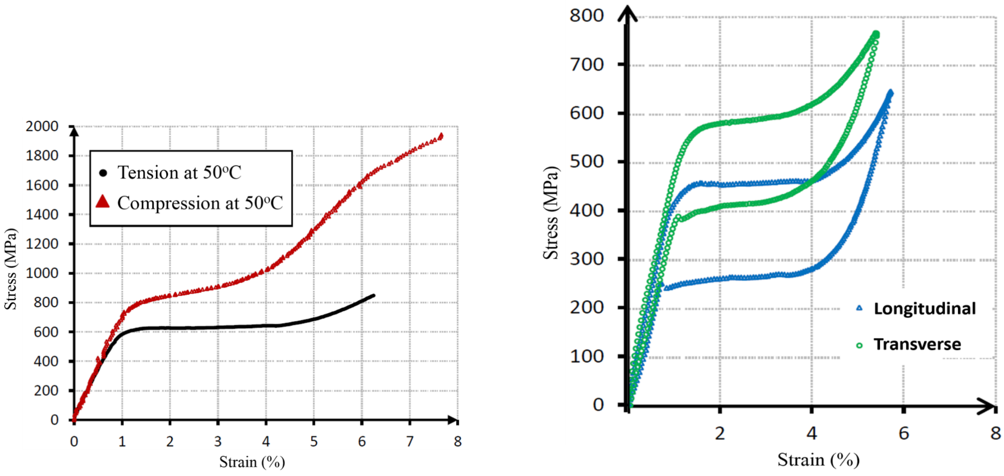

(a) Sollicitation en traction et compression (b) Traction en deux directions

Figure 1.2 – Essais uniaxiaux mettant en évidence la dissymétrie traction-compression et l'anisotropie pour deséprouvettes en NiTi laminé [Echchorfi, 2013].

1.2.2 Réorientation

La martensite auto-accommodée est obtenue normalement lors du refroidissement du matériau sous contrainte nulle ou considérablement basse. C'est une phase du matériau où aucune déformation inélastique n'est présente, car les variantes martensitiques n'adoptent pas une direction dominante. L'orientation des variantes a lieu lorsque la martensite auto-accommodée subit un chargement mécanique. Dans ce cas, les variantes se conforment aux contraintes internes en acquérant une direction préférentielle et, par conséquent, produisent une déformation macroscopique inélastique. Il est important de reconnaître que ceci n'est pas un processus à deux sens, comme c'est le cas pour la transformation : la notion de l'orientation inverse n'existe pas. Quand la charge mécanique est enlevée, la déformation inélastique n'est pas récupérée, menant à une réponse du matériau du type plastique. C'est une particularité des AMFs exploitée dans une sollicitation de mémoire de forme typique, comme celle illustrée sur la Figure 1.3.

Des travaux expérimentaux intéressants ont été réalisés à propos de ce genre de chargement [Bouvet et al., 2004; Grabe and Bruhns, 2009; Sittner et al., 1995]. La Figure 1.4 concerne un essai multiaxial forçant la réorientation martensitique. Elle se manifeste sur la poursuite des contraintes au changement de la direction des déformations imposé par la sollicitation. Les variantes aussi changent de direction pour "accommoder" ce changement. L'effet de l'orientation a été examiné dans des modèles récents [Ameduri et al., 2015; Saleeb et al., 2011; Sedlák et al.,

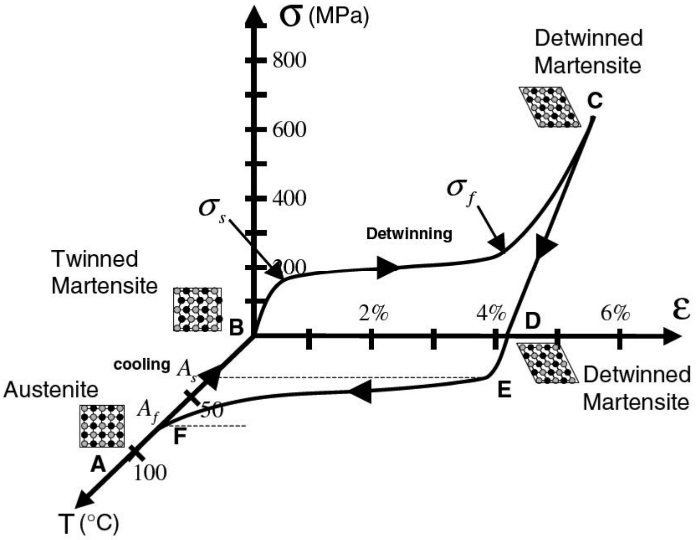

FIGURE 1.3 – Chemin en contrainte-déformation-température suivi lors d'une sollicitation de mémoire de forme [Lagoudas, 2008].

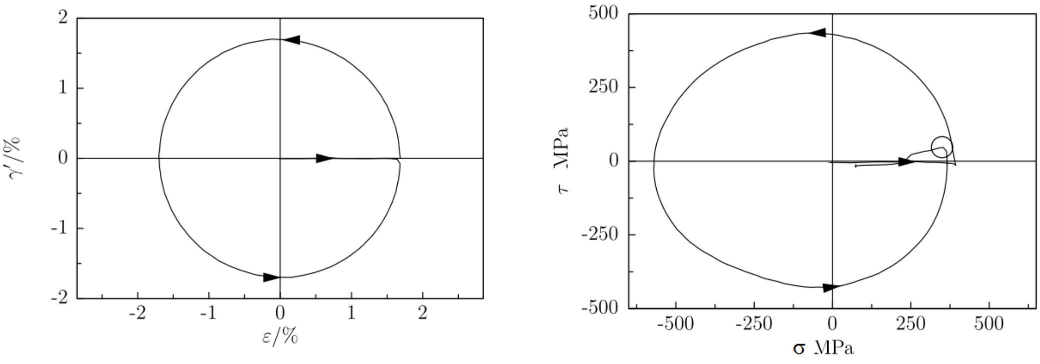

(a) Trajet suivi en déformation (b) Réponse du matériau en contraintes

Figure 1.4 – Essai multiaxial et comportement de matériau obtenu [Grabe and Bruhns, 2009].

2012]. Ces modèles ajoutent la capacité de simuler des trajets de chargement tridimensionnels aux modèles précédents plus simples [Boyd and Lagoudas, 1994; Brinson, 1993; Saleeb et al., 2001]. Dans certains modèles [Arghavani et al., 2010; Helm and Haupt, 2003; Panico and Brinson, 2007], deux fractions volumiques de martensite différentes, une correspondant à la partie auto-accommodée et une à la partie orientée, sont prises en compte en tant que propriétés principales gérant le comportement. Néanmoins, la plupart de ces modèles supposent qu'une relation directe existe entre la fraction martensitique induite par la contrainte et une amplitude de déformation de transformation, comme indiqué dans [Juhász et al., 2001; Souza et al., 1998; Taillard et al., 2008].

1.2.3 Effets cycliques

Un problème récurrent des applications en AMF est que le matériau manifeste une dégradation de certaines propriétés à cause de sa soumission à une sollicitation répétitive. La baisse de la capacité totale en déformation de transformation et en niveau d'hystérèse est le souci principal de l'utilisation des composants de systèmes mécaniques en AMF. Les auteurs des travaux expérimentaux récents [Gall and Maier, 2002; Kang et al., 2009; Olbricht et al., 2008] présentent des preuves pertinentes en réalisant des essais de traction cyclique sur des fils en NiTi.

Les essais publiés par Saint-Sulpice et al. [2009] sur la Figure 1.5 indiquent le développement d'une déformation résiduelle après chaque cycle de chargement, ainsi qu'une réduction apparente du seuil de début de transformation. Ces phénomènes sont surtout associés à un taux de martensite retenue au retour. Toutefois, il est aussi évident que cette évolution des propriétés se sature après un certain nombre de cycles, menant à une réponse stable. Ceci est appelé l'"entraînement" des structures en AMF [Hebda and White, 1995; Stalmans et al., 1992a,b] et constitue une procédure appliquée aux alliages utilisés dans des applications commerciales [Mohd Jani et al., 2014].

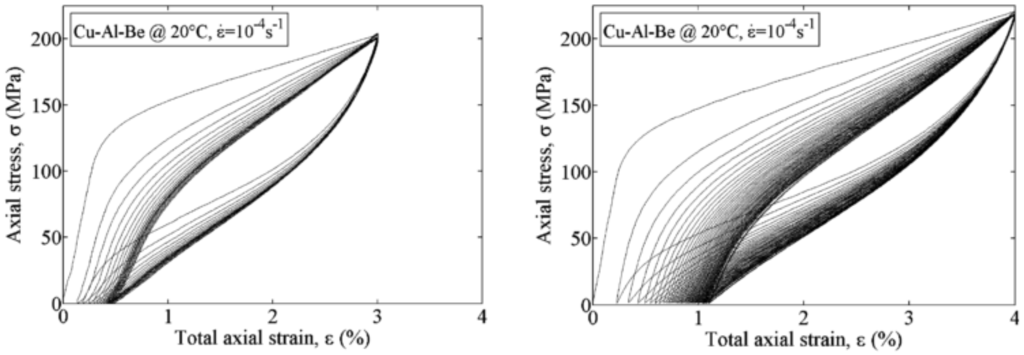

FIGURE 1.5 – Courbes contrainte-déformation concernant une sollicitation de (a) 20 cycles jusqu'à 3% et (b) 50 cycles jusqu'à 4% déformation [Saint-Sulpice et al., 2009].

1.3 Approches expérimentales

Le comportement macroscopique des AMFs est étudié expérimentalement avec plusieurs approches. Des essais mécaniques et thermomécaniques unidirectionnels sont réalisés sur des fils fins en AMF [Shaw and Kyriakides, 1997] et sur des échantillons unidimensionnels de géométrie simple [Brinson et al., 2002] afin de déterminer des propriétés basiques. En outre, la calorimétrie différentielle (DSC) [Guénin, 1997; Qidwai and Lagoudas, 2000] est utilisée pour estimer les températures de transformation.

Une grande partie des efforts modernes étudiant le comportement des AMFs du point de vue expérimentale se focalisent sur les chargements multi-dimensionnels [Bouvet et al., 2004; Chemisky et al., 2015; Grabe and Bruhns, 2008; Lexcellent et al., 2002]. Dans un travail récent [Echchorfi, 2013], des éprouvettes cruciformes en NiTi ont été montées sur une machine d'essais biaxiaux se composant de quatre vérins contrôlés indépendemment. Ceci a permis des chemins de chargement complexes non-proportionnels et l'étude de la réponse du matériau.

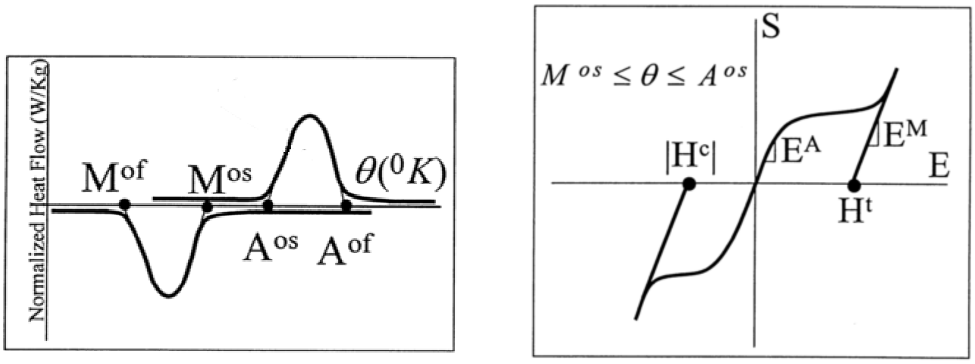

(a) Températures de transformation sur un diagramme DSC.

(b) Modules élastiques et capacité en déformation inélastiques en traction et compression.

FIGURE 1.6 – Estimation des températures de transformation basée sur un essai DSC (a) et approximation des modules élastiques et des déformations inélastiques maximales en traction et compression basée sur un chargement mécanique 1-D mechanical loading [Qidwai and Lagoudas, 2000].

1.4 Revue bibliographique de modèles existants

En général, le comportement macroscopique des AMfs est abordé avec des équations constitutives appropriées basées sur des variables d'état du matériau [Patoor et al., 2006]. Les variables thermodynamiques représentent toutes les quantités physiques caractéristiques d'un corps solide dans un état donné [Coleman and Gurtin, 1967]. Si elles peuvent être observées, elles s'appellent variables externes, sinon variables internes [Lagoudas, 2008].

Deux modèles macroscopiques, le premier développé par l'équipe du Professeur Lagoudas [Bo and Lagoudas, 1999; Boyd and Lagoudas, 1996; Hartl and Lagoudas, 2009; Hartl et al., 2010; Lagoudas et al., 2012; Popov and Lagoudas, 2007; Qidwai and Lagoudas, 2000] et le deuxième par l'équipe de la Professeure Brinson [Bekker and Brinson, 1998; Brinson and Huang, 1996; Brinson, 1993; Panico and Brinson, 2007] sont revus de manière analytique dans le chapitre. La discussion détaillée de la modélisation présentée dans la partie en anglais servira à la construction du nouveau modèle qui sera détaillée dans les prochains chapitres. Cette discussion, étant donné qu'elle est basée sur les aspects techniques, n'est pas répétée ici, mais en revanche, une briève critique est ajoutée pour chaque modèle.

1.4.1 Modèle de Lagoudas et al.

Il a été prouvé que le modèle de Lagoudas est vraiment fiable grâce à ses compétences en modélisation prédictive. Le travail sur la transformation de phase constitue un point de référence, cité par pratiquement toute nouvelle publication concernant les développements théoriques. Sa valeur est surtout mise en évidence par la robustesse thermodynamique : une étude attentive a été réalisée en ce qui concerne les exigences posées par les lois physiques. Aussi, plusieurs particularités de la transformation ont été saisies : le changement de pente des courbes du diagramme de phase, l'influence de la contrainte sur l'amplitude de la déformation de transformation en chargement assisté en température et la transition vers la martensite auto-accommodée lors du refroidissement sous faibles contraintes. En plus, l'extension apportée par Popov and Lagoudas [2007] attribue au modèle un “degré de liberté” supplémentaire pour la déformation inélastique, en rajoutant l'orientation au schéma global.

Néanmoins, quelques soucis concernant la modélisation de la réorientation demeurent. L'approche suivie, prenant en compte des taux scalaires différents pour chaque type de transition de phase, donne au modèle une image complètement découplée : ils existent cinq moyens d'incrémenter la fraction martensitique, alors que la martensite auto-accommodée et orientée sont du point de vue physique la même phase. Aussi, la relation $H^d = H_{sat}$ est un facteur privant le modèle d'un degré de liberté, bien qu'il soit expérimentalement observé que la déformation causée par l'orientation est plus basse que son homologue en transformation [Auricchio et al., 2014]. À ce propos, la loi d'évolution pour la déformation en transformation inverse devrait être adaptée, car pour le moment elle n'est appropriée que pour une capacité fixe en déformation. La remarque la plus importante est que la réorientation de la martensite déjà orientée n'est pas prise en compte, car le modèle se focalise sur l'orientation à basse température. Finalement, même si plusieurs critères de transformation ont été appliqués en combinaison avec le modèle de Lagoudas [Qidwai and Lagoudas, 2000], il n'y a pas eu de travaux considérables pour saisir l'anisotropie en transformation de phase.

1.4.2 Modèle de Brinson et al.

Ce modèle réussit à surmonter un désavantage du modèle de Lagoudas : la réorientation et la transformation directe ne sont exprimées que par l'évolution de deux variables scalaires, z_σ et z_T. Quand une contrainte est appliquée à la martensite à basses températures, où $z_T > 0$, z_σ s'accroît au détriment de z_T pour activer la réorientation. En outre, $\dot{z}_\sigma$ est le scalaire gérant le comportement superélastique à température constante. z_T, étant partiellement affecté par la réorientation, est responsable de la transformation lors du refroidissement ou du rechauffement. Ceci simplifie l'identification des paramètres, car les constantes associées avec ce genre de transformation peuvent être identifiées en réalisant des essais en variation de température sous contrainte nulle.

Un point de vue critique concernerait la limitation imposée par la loi d'évolution pour la réorientation. De la condition (1.37) résulte une restriction sévère du degré de liberté pour l'évolution de la déformation lors de la réorientation : indépendemment de la direction de la contrainte appliquée, cette équation doit être satisfaite. Aussi, l'histoire du chargement n'a d'effet que sur les déformations inélastiques. Il n'y a aucune autre empreinte de l'histoire de la charge appliquée sur une autre variable thermodynamique. Ce désavantage est traité au Chapitre 4, avec la formulation proposée du nouveau modèle.

1.5 Conclusion du chapitre

Le comportement macroscopique complexe des AMF exige des efforts intéressants en modélisation thermodynamique. D'une part, le comportement inélastique est principalement régi par la transformation de phase entre les deux configurations cristallines basiques, l'austénite et la martensite. La transformation est traitée dans plusieurs modèles existants. Des travaux modernes se focalisent aussi sur la saisie l'anisotropie en transformation de phase, alors qu'il existe encore le besoin de capter l'effet de la direction du chargement sur l'évolution des contraintes. D'autre part, le comportement sous chargement non-proportionnel est gravement affecté par la réorientation des variantes martensitiques, point où la modélisation peut toujours s'améliorer.

Toujours au sujet du comportement des AMFs sous chargement multiaxial, l'effet de la martensite retenue semble être impacté par l'orientation de la charge appliquée. L'évolution des propriétés des alliages, à savoir la déformation résiduelle et le niveau de contrainte de transformation dépend de la direction de la charge lors d'une sollicitation mécanique répétitive. Par conséquent, un effort expérimental pour examiner l'effet de la direction sur le comportement multiaxial cyclique du NiTi est réalisé au Chapitre 2, avant les efforts en modélisation.

Des développements, concernant la modélisation de l'anisotropie en transformation de phase, sont réalisés au Chapitre 3 et un nouveau modèle, considérant une manière innovante de prendre en compte la réorientation, est présenté au Chapitre 4. Ce modèle se base surtout sur le modèle de Lagoudas. La validation de cette nouvelle approche de modélisation s'effectue au Chapitre 5.

1.6 Bibliographie

S. Ameduri, V. Antonucci, E. Artioli, D. Asprone, F. Auricchio, S. Barbarino, E. Boatti, M. Conti, I. Dimino, G. Faiella, S. Marfia, A. Martone, C. Menna, R. Pecora, E. Sacco, F. Stortiero, A. Vigliotti, and E. Villa. *Shape Memory Alloy Engineering.* Elsevier, 2015. ISBN 9780080999203. doi: 10.1016/B978-0-08-099920-3.01002-0. 8

J. Arghavani, F. Auricchio, R. Naghdabadi, A. Reali, and S. Sohrabpour. A 3-D phenomenological constitutive model for shape memory alloys under multiaxial loadings. *International Journal of Plasticity*, 26(7):976–991, jul 2010. ISSN 07496419. doi: 10.1016/j.ijplas.2009.12.003. 9

F. Auricchio, E. Bonetti, G. Scalet, and F. Ubertini. Theoretical and numerical modeling of shape memory alloys accounting for multiple phase transformations and martensite reorientation. *International Journal of Plasticity*, 59:30–54, aug 2014. ISSN 07496419. doi: 10.1016/j.ijplas.2014.03.008. 12

A. Bekker and L. Brinson. Phase diagram based description of the hysteresis behavior of shape memory alloys. *Acta Materialia*, 46(10):3649–3665, jun 1998. ISSN 13596454. doi: 10.1016/S1359-6454(97)00490-4. 11

Z. Bo and D. Lagoudas. Thermomechanical modeling of polycrystalline SMAs under cyclic loading, Part III: evolution of plastic strains and two-way shape memory effect. *International Journal of Engineering Science*, 37(9):1175–1203, jul 1999. ISSN 00207225. doi: 10.1016/S0020-7225(98)00115-3. 11

C. Bouvet, S. Calloch, and C. Lexcellent. A phenomenological model for pseudoelasticity of shape memory alloys under multiaxial proportional and nonproportional loadings. *European Journal of Mechanics - A/Solids*, 23(1):37–61, jan 2004. ISSN 09977538. doi: 10.1016/j.euromechsol.2003.09.005. 6, 8, 10

J. G. Boyd and D. C. Lagoudas. Thermomechanical Response of Shape Memory Composites. *Journal of Intelligent Material Systems and Structures*, 5(3):333–346, may 1994. ISSN 1045-389X. doi: 10.1177/1045389X9400500306. 9

J. Boyd and D. Lagoudas. A thermodynamical constitutive model for shape memory materials. Part I. The monolithic shape memory alloy. *International Journal of Plasticity*, 12(6):805–842, jan 1996. ISSN 07496419. doi: 10.1016/S0749-6419(96)00030-7. 11

L. C. Brinson and M. S. Huang. Simplifications and Comparisons of Shape Memory Alloy Constitutive Models. *Journal of Intelligent Material Systems and Structures*, 7(1):108–114, jan 1996. ISSN 1045-389X. doi: 10.1177/1045389X9600700112. 11

L. C. Brinson, I. Schmidt, and R. Lammering. Micro and Macromechanical Investigations of CuAlNi Single Crystal and CuAlMnZn Polycrystalline Shape Memory Alloys. *Journal of Intelligent Materials Systems and Structures*, 13(12):761–772, dec 2002. ISSN 00000000. doi: 10.1177/1045389X02013012002. 10

L. Brinson. One-Dimensional Constitutive Behavior of Shape Memory Alloys: Thermomechanical Derivation with Non-Constant Material Functions and Redefined Martensite Internal Variable. *Journal of Intelligent Material Systems and Structures*, 4(2):229–242, apr 1993. ISSN 1045-389X. doi: 10.1177/1045389X9300400213. 9, 11

Y. Chemisky, F. Meraghni, N. Bourgeois, S. Cornell, R. Echchorfi, and E. Patoor. Analysis of the deformation paths and thermomechanical parameter identification of a shape memory alloy using digital image correlation over heterogeneous tests. *International Journal of Mechanical Sciences*, 96-97:13–24, jun 2015. ISSN 00207403. doi: 10.1016/j.ijmecsci.2015.03.007. 10

B. Coleman and M. Gurtin. Thermodynamics with internal variables. *J. Chem. Phys.*, 47(2): 85–98, 1967. 11

R. Echchorfi. *Dialogue essais-simulation et identification de lois de comportement d'alliage à mémoire de forme en chargement multiaxial.* PhD thesis, Arts et Métiers ParisTech, 2013. 7, 10

K. Gall and H. Maier. Cyclic deformation mechanisms in precipitated NiTi shape memory alloys. *Acta Materialia*, 50(18):4643–4657, oct 2002. ISSN 13596454. doi: 10.1016/S1359-6454(02)00315-4. 9

C. Grabe and O. Bruhns. Tension/torsion tests of pseudoelastic, polycrystalline NiTi shape memory alloys under temperature control. *Materials Science and Engineering: A*, 481-482: 109–113, may 2008. ISSN 09215093. doi: 10.1016/j.msea.2007.03.117. 10

C. Grabe and O. Bruhns. Path dependence and multiaxial behavior of a polycrystalline NiTi alloy within the pseudoelastic and pseudoplastic temperature regimes. *International Journal of Plasticity*, 25(3):513–545, mar 2009. ISSN 07496419. doi: 10.1016/j.ijplas.2008.03.002. 8, 9

V. Grolleau, H. Louche, V. Delobelle, A. Penin, G. Rio, Y. Liu, and D. Favier. Assessment of tension–compression asymmetry of NiTi using circular bulge testing of thin plates. *Scripta Materialia*, 65(4):347–350, aug 2011. ISSN 13596462. doi: 10.1016/j.scriptamat.2011.05.003. 7

G. Guénin. Shape Memory and Pseudoelastic Properties of Fe-Mn-Si and Ti-Ni Based Alloys. *Le Journal de Physique IV*, 07(C5):C5–467–C5–476, nov 1997. ISSN 1155-4339. doi: 10.1051/jp4:1997574. 10

D. J. Hartl and D. Lagoudas. Constitutive modeling and structural analysis considering simultaneous phase transformation and plastic yield in shape memory alloys. *Smart Materials and Structures*, 18(10):104017, oct 2009. ISSN 0964-1726. doi: 10.1088/0964-1726/18/10/104017. 11

D. J. Hartl, G. Chatzigeorgiou, and D. C. Lagoudas. Three-dimensional modeling and numerical analysis of rate-dependent irrecoverable deformation in shape memory alloys. *International Journal of Plasticity*, 26(10):1485–1507, oct 2010. ISSN 07496419. doi: 10.1016/j.ijplas.2010.01.002. 11

D. A. Hebda and S. R. White. Effect of training conditions and extended thermal cycling on nitinol two-way shape memory behavior. *Smart Materials and Structures*, 4(4):298–304, dec 1995. ISSN 0964-1726. doi: 10.1088/0964-1726/4/4/010. 10

D. Helm and P. Haupt. Shape memory behaviour: modelling within continuum thermomechanics. *International Journal of Solids and Structures*, 40(4):827–849, feb 2003. ISSN 00207683. doi: 10.1016/S0020-7683(02)00621-2. 9

L. Juhász, H. Andrä, and O. Hesebeck. A Simple Model for Shape Memory Alloys Under Multi-axial Non-Proportional Loading. In *Smart Materials*, pages 51–65. 2001. 9

G. Kang, Q. Kan, L. Qian, and Y. Liu. Ratchetting deformation of super-elastic and shape-memory NiTi alloys. *Mechanics of Materials*, 41(2):139–153, feb 2009. ISSN 01676636. doi: 10.1016/j.mechmat.2008.09.001. 9

D. Lagoudas, D. Hartl, Y. Chemisky, L. Machado, and P. Popov. Constitutive model for the numerical analysis of phase transformation in polycrystalline shape memory alloys. *International Journal of Plasticity*, 32-33(null):155–183, may 2012. ISSN 07496419. doi: 10.1016/j.ijplas.2011.10.009. 11

D. Lagoudas. *Shape Memory Alloys - Modeling and Engineering Applications.* Springer, 2008. 8, 11

L. Lecce and A. Concilio, editors. *Shape Memory Alloy Engineering: For Aerospace, Structural and Biomedical Applications.* 2014. ISBN 0080999212. 5

C. Lexcellent, A. Vivet, C. Bouvet, S. Calloch, and P. Blanc. Experimental and numerical determinations of the initial surface of phase transformation under biaxial loading in some polycrystalline shape-memory alloys. *Journal of the Mechanics and Physics of Solids*, 50(12):2717–2735, dec 2002. ISSN 00225096. doi: 10.1016/S0022-5096(02)00007-8. 10

J. Mohd Jani, M. Leary, A. Subic, and M. A. Gibson. A review of shape memory alloy research, applications and opportunities. *Materials & Design*, 56:1078–1113, apr 2014. ISSN 02613069. doi: 10.1016/j.matdes.2013.11.084. 10

J. Olbricht, A. Yawny, A. Condó, F. Lovey, and G. Eggeler. The influence of temperature on the evolution of functional properties during pseudoelastic cycling of ultra fine grained NiTi. *Materials Science and Engineering: A*, 481-482:142–145, may 2008. ISSN 09215093. doi: 10.1016/j.msea.2007.01.182. 9

K. Otsuka and C. M. Wayman. *Shape Memory Materials.* Cambridge University Press, 1999. ISBN 0521663849. 5

M. Panico and L. Brinson. A three-dimensional phenomenological model for martensite reorientation in shape memory alloys. *Journal of the Mechanics and Physics of Solids*, 55(11):2491–2511, nov 2007. ISSN 00225096. doi: 10.1016/j.jmps.2007.03.010. 9, 11

E. Patoor, M. El Amrani, A. Eberhardt, and M. Berveiller. Determination of the origin for the dissymmetry observed between tensile and compression tests on shape memory alloys. *J. Phys.*, IV(2):495–500, 1995. 7

E. Patoor, D. C. Lagoudas, P. B. Entchev, L. C. Brinson, and X. Gao. Shape memory alloys, Part I: General properties and modeling of single crystals. *Mechanics of Materials*, 38(5-6):391–429, may 2006. ISSN 01676636. doi: 10.1016/j.mechmat.2005.05.027. 5, 11

P. Popov and D. C. Lagoudas. A 3-D constitutive model for shape memory alloys incorporating pseudoelasticity and detwinning of self-accommodated martensite. *International Journal of Plasticity*, 23(10-11):1679–1720, oct 2007. ISSN 07496419. doi: 10.1016/j.ijplas.2007.03.011. 11, 12

M. Qidwai and D. Lagoudas. On thermomechanics and transformation surfaces of polycrystalline NiTi shape memory alloy material. *International Journal of Plasticity*, 16(10-11):1309–1343, jan 2000. ISSN 07496419. doi: 10.1016/S0749-6419(00)00012-7. 10, 11, 12

L. Saint-Sulpice, S. A. Chirani, and S. Calloch. A 3D super-elastic model for shape memory alloys taking into account progressive strain under cyclic loadings. *Mechanics of Materials*, 41(1):12–26, jan 2009. ISSN 01676636. doi: 10.1016/j.mechmat.2008.07.004. 9, 10

A. Saleeb, S. Arnold, M. Castelli, T. Wilt, and W. Graf. A general hereditary multimechanism-based deformation model with application to the viscoelastoplastic response of titanium alloys. *International Journal of Plasticity*, 17(10):1305–1350, oct 2001. ISSN 07496419. doi: 10.1016/S0749-6419(00)00086-3. 9

A. Saleeb, S. Padula, and A. Kumar. A multi-axial, multimechanism based constitutive model for the comprehensive representation of the evolutionary response of SMAs under general thermomechanical loading conditions. *International Journal of Plasticity*, 27(5):655–687, may 2011. ISSN 07496419. doi: 10.1016/j.ijplas.2010.08.012. 8

P. Sedlák, M. Frost, B. Benešová, T. Ben Zineb, and P. Šittner. Thermomechanical model for NiTi-based shape memory alloys including R-phase and material anisotropy under multi-axial loadings. *International Journal of Plasticity*, 39(null):132–151, dec 2012. ISSN 07496419. doi: 10.1016/j.ijplas.2012.06.008. 8

J. Shaw and S. Kyriakides. Initiation and propagation of localized deformation in elasto-plastic strips under uniaxial tension. *International Journal of Plasticity*, 13(10):837–871, dec 1997. ISSN 07496419. doi: 10.1016/S0749-6419(97)00062-4. 10

P. Sittner, Y. Hara, and M. Tokuda. Experimental study on the thermoelastic martensitic transformation in shape memory alloy polycrystal induced by combined external forces. *Metallurgical and Materials Transactions A*, 26(11):2923–2935, nov 1995. ISSN 1073-5623. doi: 10.1007/BF02669649. 8

P. Sittner, L. Heller, J. Pilch, P. Sedlak, M. Frost, Y. Chemisky, A. Duval, B. Piotrowski, T. Ben Zineb, E. Patoor, F. Auricchio, S. Morganti, A. Reali, G. Rio, D. Favier, Y. Liu, E. Gibeau, C. Lexcellent, L. Boubakar, D. Hartl, S. Oehler, D. Lagoudas, and J. V. Humbeeck. Roundrobin SMA modeling. In *ESOMAT 2009 - 8th European Symposium on Martensitic Transformations*, page 08001, Les Ulis, France, sep 2009. EDP Sciences. ISBN 978-2-7598-0480-1. doi: 10.1051/esomat/200908001. 7

P. Šittner and V. Novák. Anisotropy of martensitic transformations in modeling of shape memory alloy polycrystals. *International Journal of Plasticity*, 16(10-11):1243–1268, jan 2000. ISSN 07496419. doi: 10.1016/S0749-6419(00)00009-7. 7

A. Souza, E. Mamiya, and N. Zouain. Three-dimensional model for solids undergoing stress-induced phase transitions. *European Journal of Mechanics - A/Solids1*, 17:789–806, 1998. 9

R. Stalmans, J. Van Humbeeck, and L. Delaey. The two way memory effect in copper-based shape memory alloys — thermodynamics and mechanisms. *Acta Metallurgica et Materialia*, 40 (11):2921–2931, nov 1992a. ISSN 09567151. doi: 10.1016/0956-7151(92)90456-O. 10

R. Stalmans, J. Van Humbeeck, and L. Delaey. Thermomechanical cycling, two way memory and concomitant effects in CuZnAl alloys. *Acta Metallurgica et Materialia*, 40(3):501–511, mar 1992b. ISSN 09567151. doi: 10.1016/0956-7151(92)90399-Y. 10

K. Taillard, S. A. Chirani, S. Calloch, and C. Lexcellent. Equivalent transformation strain and its relation with martensite volume fraction for isotropic and anisotropic shape memory alloys. *Mechanics of Materials*, 40(4-5):151–170, apr 2008. ISSN 01676636. doi: 10.1016/j.mechmat.2007.07.005. 7, 9

Y. Zhu and G. Dui. A macro-constitutive model of polycrystalline NiTi SMAs including tensile–compressive asymmetry and torsion pseudoelastic behaviors. *International Journal of Engineering Science*, 48(12):2099–2106, dec 2010. ISSN 00207225. doi: 10.1016/j.ijengsci.2010.04.002. 6

2. Caractérisation expérimentale du comportement thermomécanique cyclique multiaxial du NiTi

2.1 Introduction

La sollicitation mécanique cyclique des alliages à mémoire de forme NiTi peut engendrer des effets visibles à la déformation maximale du matériau, ainsi qu'au niveau d'écoulement en transformation directe [Saint-Sulpice et al., 2009]. En conditions monoaxiales, la réponse atteint un niveau de saturation [Nemat-Nasser and Guo, 2006]. Il s'agit là d'un phénomène normalement associé à la plasticité induite par la transformation [Hartl and Lagoudas, 2009]. De plus, les AMF exhibent une forte anisotropie pour des cas de chargement superélastiques [Mehrabi et al., 2014], car les conditions de fabrication induisent une certaine texture dans le polycristal. Ceci a un effet direct sur le comportement en chargement biaxial aussi, comme démontré dans des travaux récents [Chemisky et al., 2015].

Dans ce chapitre, une campagne expérimentale concernant des essais mécaniques sur des échantillons en NiTi est présentée. L'objectif est d'examiner l'effet de trois paramètres différents sur la dégradation des propriétés du matériau, à savoir les déformations résiduelles et le seuil de transformation en contraintes. Ces trois paramètres sont le nombre de cycles, l'amplitude de la déformation atteinte et la direction de chargement. Dans la première partie de la campagne expérimentale, une sollicitation thermomécanique est appliquée sur des échantillons monoaxiaux. La deuxième partie présente les résultats d'essais en chargement cyclique biaxiale non-proportionnel sur des éprouvettes cruciformes. L'évolution spatio-temporelle des champs cinématiques globaux est reportée et analysée.

2.2 Essais en traction uniaxiale en régime super-élastique

2.2.1 Méthodes expérimentales

Les éprouvettes pour les essais uniaxiaiaux ont été découpées à partir d'une plaque en NiTi laminée dans deux orientations : parallèle à la direction du laminage (longitudinale) et perpendiculaire (transverse). Dans un premier temps, un chargement cyclique complexe a été appliquée sur les deux types des éprouvettes en conditions isothermes. Trois niveaux de température ont été choisis : 30, 40 et 50°C. Le plan du chargement est illustré sur la Figure 2.1.

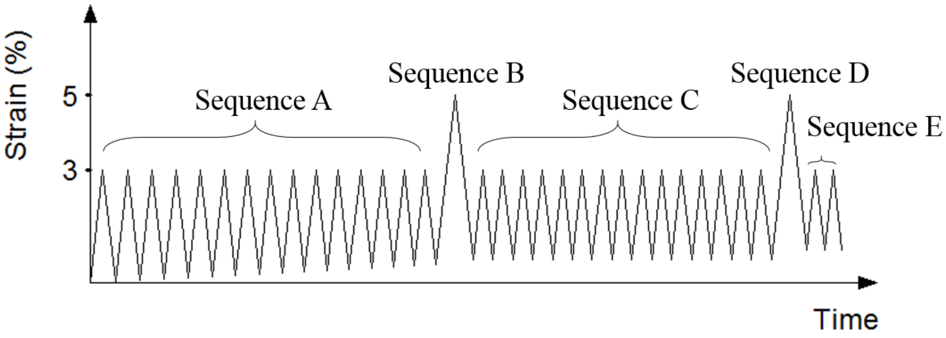

Figure 2.1 – Schéma du chargement mécanique pour les éprouvettes monoaxiales.

Tous les essais présentés dans ce chapitre proviennent d'éprouvettes découpées par jet d'eau dans une plaque laminée de NiTi (50,6% at. Ni) d'épaisseur 2.5mm. Un traitement thermique consistant en un revenu à 400°C pendant 30 minutes, suivi d'une trempe à l'eau, a été appliqué à l'ensemble des éprouvettes.

A la charge comme à la décharge, les essais de traction ont été pilotés en déplacement. La vitesse de traverse imposée assure que la vitesse de déformation ne dépasse pas $10^{-4} sec^{-1}$ à tout moment du cycle et en tout point de l'éprouvette, ce qui évite l'autoéchauffement. L'inversion du chargement au niveau maximal intervient pour une déformation critique atteinte sur l'extensomètre. Le retour est terminé quand la force atteint 20N soit 0.8MPa. Mors, extensomètre et éprouvette sont à l'intérieur d'une enceinte thermique régulée en température. La température de l'éprouvette est mesurée par un thermocouple placé au centre de la partie calibrée de l'éprouvette et entre les couteaux de l'extensomètre.

Dans un second temps, les éprouvettes ont été réchauffées jusqu'à 100°C en maintenant une force quasi-nulle sur l'éprouvette. La déformation résiduelle de fin d'essai est pratiquement totalement recouvrée avant que l'éprouvette n'atteigne 80°C.

2.2.2 Résultats expérimentaux

Les cycles correspondant à la Séquence D sont présentés sur la Figure 2.2. La comparaison des résultats entre les deux directions montre que, à température donnée, la contrainte seuil de transformation est plus élevée dans la direction transversale que dans la direction de laminage. Bien que le plateau de transformation soit dépassé en arrivant aux 5% de déformation imposée, la transformation n'est pas complète ; la phase de comportement élastique de la martensite n'est pas atteinte. Le choix a été fait de ne pas dépasser cette déformation pour éviter toute apparition de la rupture dans les éprouvettes. La pente de la courbe contrainte-déformation aux alentours des 5% est toujours plus élevée dans la direction transverse, la sortie du plateau de transformation est plus nette. En ce qui concerne à proprement parlé des effets du cyclage, les constations sont les suivantes :

- Les déformations résiduelles sont plus importantes dans la direction transverse et elles augmentent avec les températures.
- Le seuil de transformation du 32ème cycle est toujours inférieur à celui du 1er cycle.
- Le niveau de contrainte maximal à la fin des cycles 16 et 32, correspondant aux 5% de déformation, est pratiquement identique pour les deux cycles, pour les six essais présentés.
- La transition entre le début de la courbe et le plateau de transformation s'adoucit au cours du cyclage, elle devient de plus en plus progressive, en même temps que le seuil de transformation s'abaisse.

2.2.3 Analyse des résultats et discussion

La corrélation entre les déformations résiduelles et la déformation cumulée en transformation est présentée sur la Figure 2.3. La déformation cumulée est la somme des déformations de transformation générée au cours du chargement ($\dot{\varepsilon} > 0$), la déformation de transformation étant la déformation totale à laquelle sont retranchées la déformation élastique et la déformation résiduelle en fin de cycle.

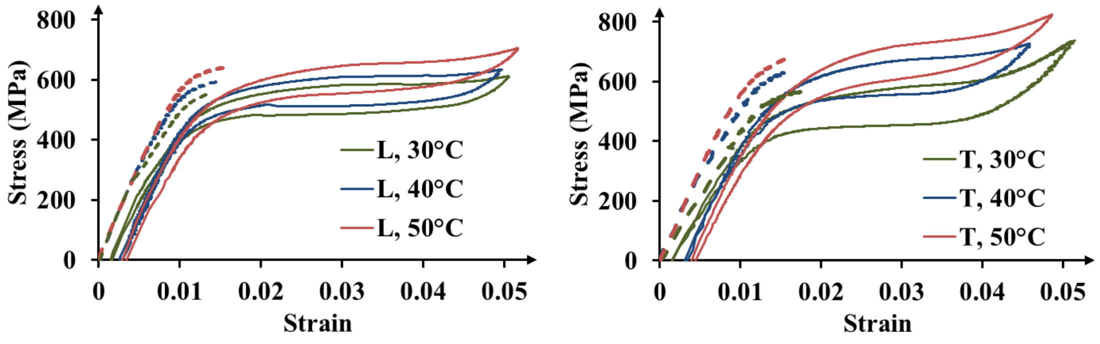

(a) Direction L

(b) Direction T

FIGURE 2.2 – Courbes contrainte-déformation pour le 1er (lignes en pointillés) et le 32ème cycle (lignes conntinues) pour le chargement en directions (a) 0°(L) et (b) 90°(T).

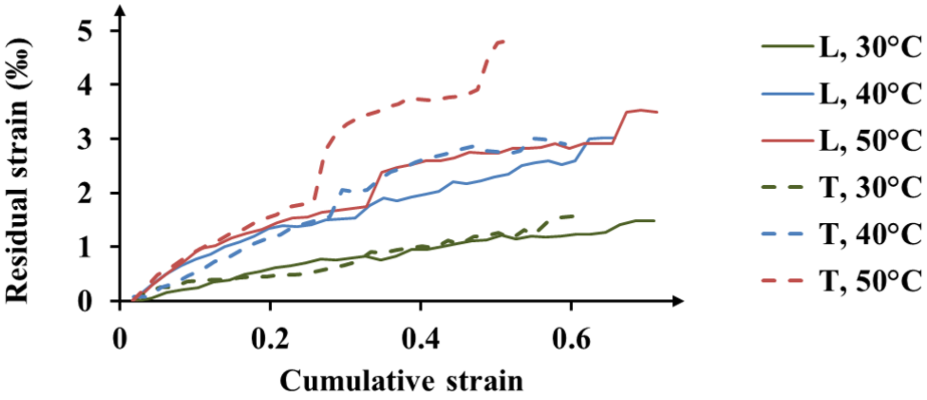

FIGURE 2.3 – Courbes déformation résiduelle - déformation cumulée pour toutes les conditions d'essais.

- À 30°C, la déformation résiduelle croit doucement, et de manière continue. Les cycles à 5% ne perturbent pas la progression. Pas de différence d'évolution entre les deux directions.
- À 40°C, la déformation résiduelle croit un peu plus rapidement. Le cycle à 5% se traduit par une discontinuité de la pente et une évolution plus rapide de la déformation résiduelle pour la direction transversale uniquement.
- À 50°C, l'effet du cycle à 5% est visible dans les directions, mais davantage dans la direction transversale que dans la direction longitudinale. Les 15 premiers cycles ne sont pas suffisants pour stabiliser la déformation résiduelle. Cependant, à la fin du 32ème cycle la déformation semble stabilisée, même si ce cycle engendre une discontinuité visible de l'évolution sur tous les essais.

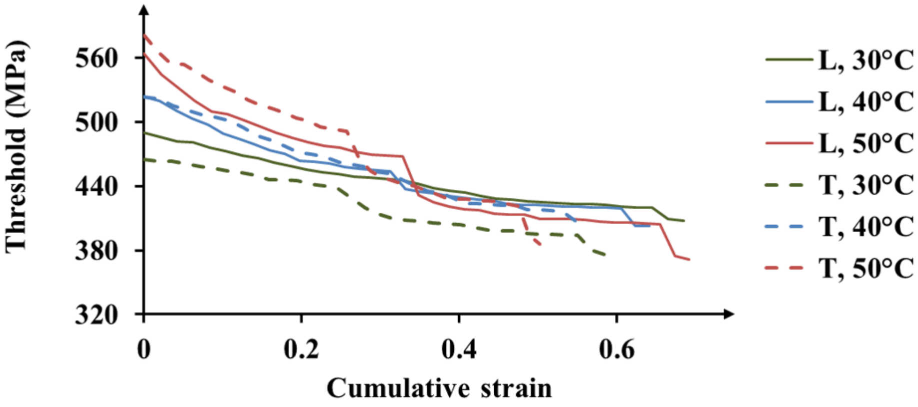

Figure 2.4 – Diagramme seuil de transformation directe - déformation cumulée pour toutes les conditions d'essais.

La diminution, avec la déformation cumulée, de la contrainte seuil de début de transformation, estimée conventionnellement à 0.1% de déformation, respecte les tendances observées sur la déformation résiduelle. Les courbes reliant ce seuil avec la déformation cumulée se trouvent sur la Figure 2.4. L'effet du cycle de déformation à 5% est visible dans la direction T dès 30°C. De plus, les contraintes seuils dans la direction longitudinale, sensiblement différentes en début d'essai, tendent vers une valeur unique. Il est important à noter que ces seuils de transformation correspondent à la réponse globale de l'échantillon et non à un caractéristique du matériau. Le croisement des courbes des échantillons en traction transverse ne peut pas se traduire sur un diagramme du type Clausius-Clapeyron, puisque le seuil de 40°C supérieur à celui de 50°C n'est pas admissible.

2.3 Essais en conditions biaxiales

2.3.1 Méthodes expérimentales

Deux éprouvettes cruciformes issues de la même plaque en NiTi laminée ont été soumises en sollicitation mécanique biaxiale isotherme à 50°C. Les éprouvettes ont été montées sur une machine de sollicitation biaxiale Instron. Leurs têtes ont été fixées aux vérins de la machine avec des vis posées aux endroits appropriées. Le plan du chargement est expliqué sur la Figure 2.5 pour les deux éprouvettes étiquettées “Sample 1” et “Sample 2”. L'axe Est-Ouest (E-W) des éprouvettes est parallèle à la direction de laminage X.

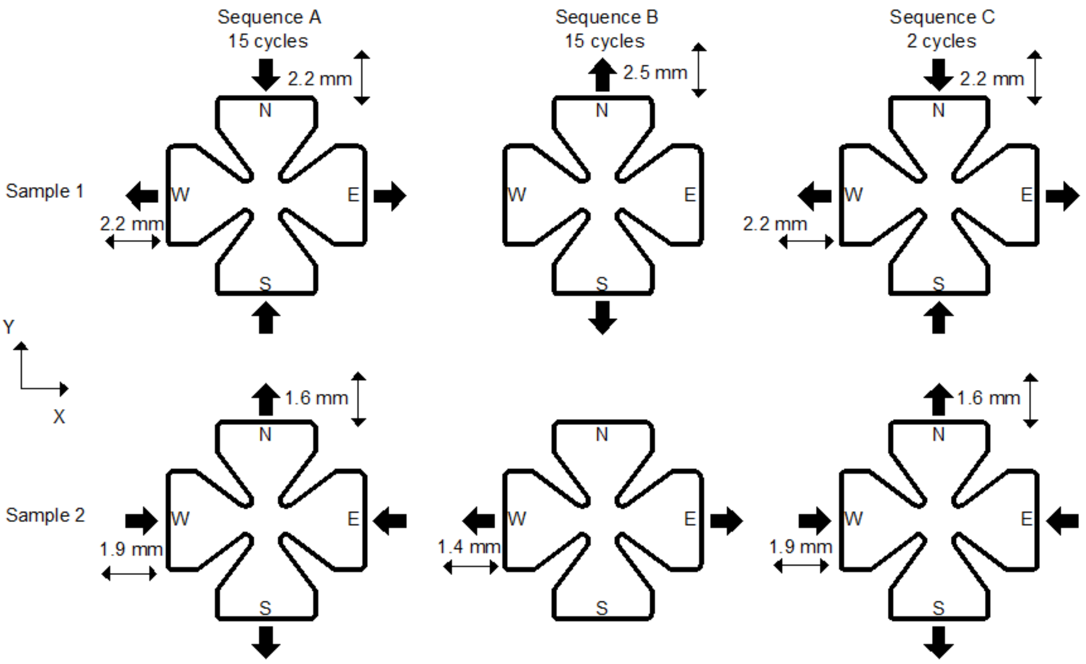

Figure 2.5 – Trajets de chargement cyclique pour les éprouvettes nommées “Sample 1” et “Sample 2”. L’axe Est-Ouest (E-W) des éprouvettes est parallèle à la direction de laminage X.

Trois séquences de chargement cyclique suivant différentes directions de charge ont été appliquées. La charge a été introduite en forme d’élongations imposées aux bords des têtes des éprouvettes en tant que conditions aux limites. Ces élongations ont correspondu aux distances relatives entre les vérins qui se trouvaient face-à-face. Le niveau de température a été assuré à travers un élément chauffant fonctionnant par résistance électrique. Il est à noter que la deuxième éprouvette a été cassée lors du premier cycle de la séquence B.

Le champs cinématique de la surface des éprouvettes a été suivi par une caméra fonctionnant en combinaison avec le logiciel DIC (Corrélation d’Images Numérique) Vic2D. La durée totale des essais étant assez longue, une image toutes les 60 secondes a été capturée. Néanmoins, l’acquisition d’images devait être assurée pour les moments du début et de la fin de la phase de charge pour chaque cycle. Dans ce but, un intervalle de 70 secondes est intervenu chaque fois que la cible en élongation ou la force zéro ont été atteintes.

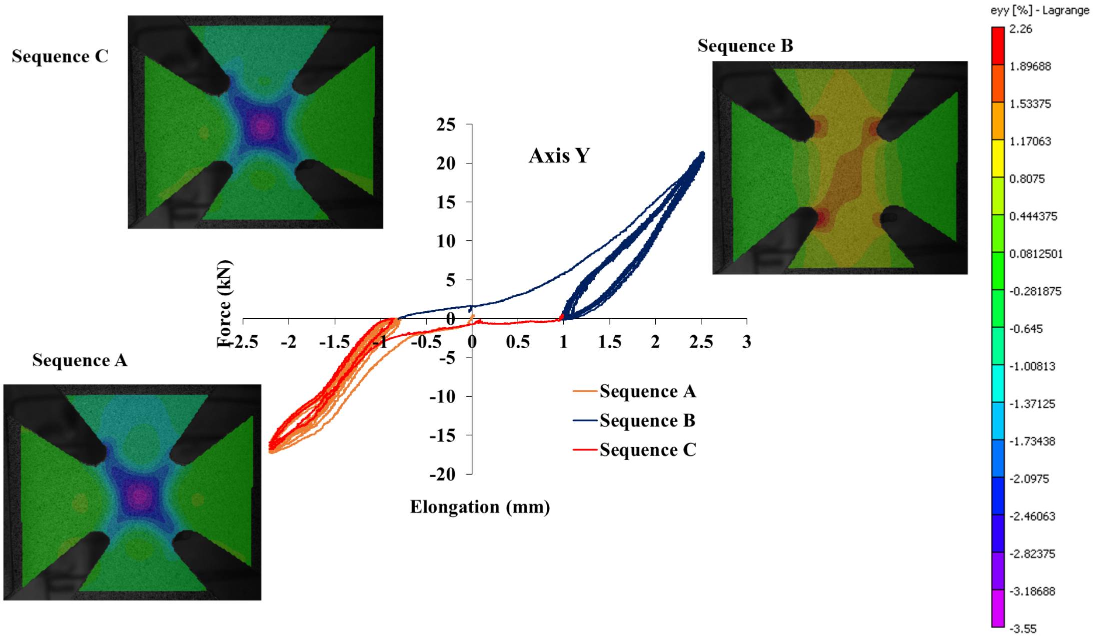

Figure 2.6 – Courbes force-élongation pour Sample 1 sur l'axe Y avec les champs de déformation correspondant à la fin de la charge du dernier cycle de chaque séquence.

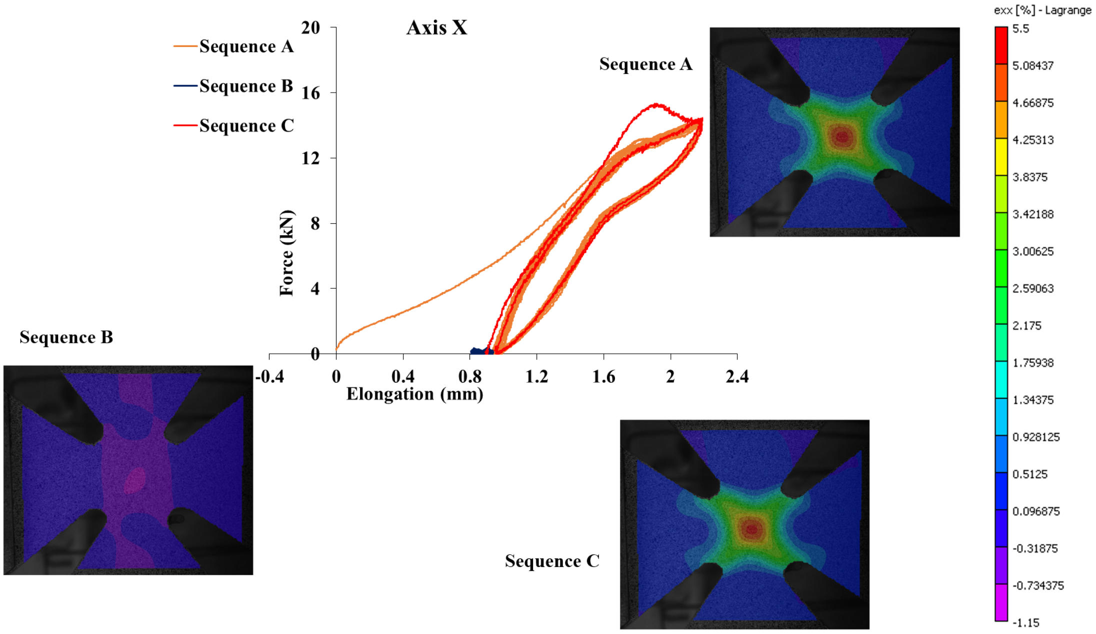

Figure 2.7 – Courbes force-élongation pour Sample 1 sur l'axe X avec les champs de déformation correspondant à la fin de la charge du dernier cycle de chaque séquence.

2.3.2 Résultats expérimentaux

La Figure 2.6 concerne le comportement global et les champs de déformation sur l'axe Y pour le Sample 1. On peut constater que :

- Une élongation résiduelle importante se développe lors du premier cycle de la séquence A. Approximativement 0.8% de la cible en élongation se sont consommées. Une partie de l'échantillon semble être en transformation jusqu'au niveau de -4 kN et de la transformation supplémentaire est induite après -15 kN.
- Les prochains 14 cycles paraissent relativement stables.
- Le premier cycle de la séquence B inverse la direction de l'élongation résiduelle. La fin de ce cycle s'effectue à environ 1 mm dans la direction du chargement.
- Les 14 cycles restants continuent à manifester une hystérésis, indiquant qu'il existe encore des parties de l'éprouvette subissant les transformations directe et inverse.
- Le champs de déformations ε_{yy} lors du dernier cycle de la séquence B montre des valeurs significativement plus basses en comparaison avec les autres mesures. Même si la transformation semble avoir atteint une certaine saturation, la valeur de 2,26% est suprenante, mettant en évidence l'anisotropie en déformations de transformation. Elle explique, d'ailleurs, la pente élevée lors de la transformation sur la courbe force-élongation.

2.3.3 Analyse des résultats et discussion

Sur le diagramme force-élongation correspondant à l'axe X du Sample 1 sur la Figure 2.7, une observation intéressante peut être constatée. Une irrégularité au niveau des forces est présente à environ 1,8 mm d'élongation. En particulier, les forces développées sont clairement plus hautes que celles des cycles précédents. Pourtant, la force à la fin de la charge dans ce cycle retourne au niveau atteint précédemment, induisant la forme d'une bosse sur la courbe. Une hypothèse est faite ici, concernant l'apparition de la réorientation. Alors qu'il n'existe pas d'observations microscopiques pour soutenir cet argument, on peut supposer que l'activation d'un mécanisme inélastique parallèlement à la transformation cause un adoucissement supplémentaire. On peut donc admettre que l'activation de la réorientation induit une perte supplémentaire de la raideur de la structure dans la direction X, expliquant l' abaissement de la force après l'élongation de 1,8 mm.

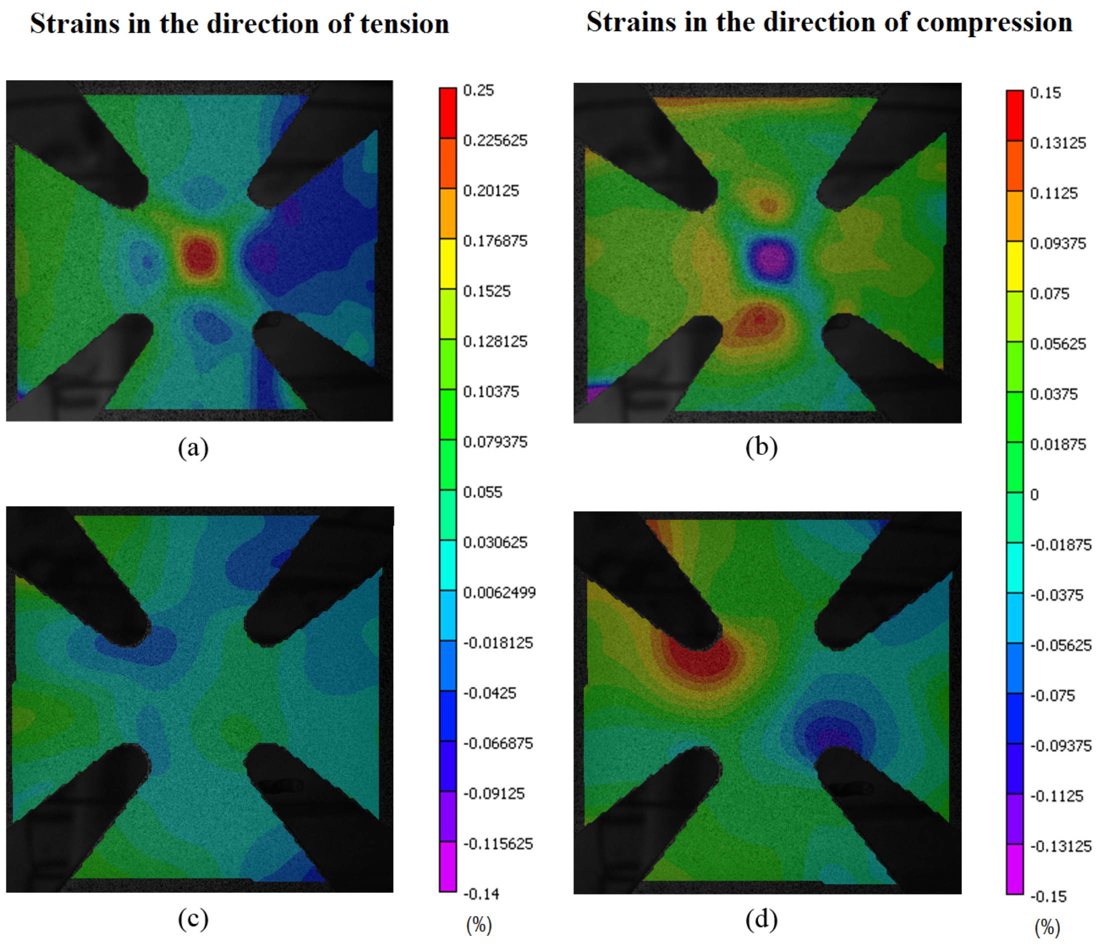

FIGURE 2.8 – Champs de déformations résiduelles à la fin de la séquence A. ε_{xx} (a) et ε_{yy} (b) pour Sample 1, ε_{yy} (c) et ε_{xx} (d) pour Sample 2.

La Figure 2.8 montre les différences entre les déformations résiduelles pour les deux éprouvettes. Les résultats provenant du Sample 1 se trouvent sur la ligne en haut et les résultats du Sample 2 sur la ligne en bas. Sur la colonne gauche sont placés les champs de déformations dans la direction où la traction est appliquée : ε_{xx} pour l'échantillon "Sample 1" et ε_{yy} pour l'échantillon "Sample 2". Les champs de déformations dans la direction de la compression sont placés sur la colonne droite.

La comparaison des déformations résiduelles dans la direction sous traction (Figures (a) et (c)) montre que les déformations de l'échantillon "Sample 2" sont visiblement plus basses. Dans la direction sous compression (Figures (b) et (d)), les niveaux des déformations résiduelles maximales sont pratiquement égaux, alors que la cible d'élongation est plus basse pour l'échantillon “Sample 2”. Cette remarque soutient l'argument que l'évolution des déformations résiduelles dépendent non seulement de l'élongation imposée, mais aussi de la direction de chargement.

2.4 Conclusion du chapitre

Dans ce chapitre, le fort effet de la direction du chargement sur le comportement du NiTi issu de la fabrication par laminage a été expérimentalement étudié dans le cadre de sollicitations cycliques mono et biaxiales. Pour les essais monoaxiaux, l'évolution des déformations résiduelles et la réduction du niveau du début de transformation ont été corrélées à la déformation cumulée. Dans les essais biaxiaux, des différences importantes dans l'évolution des déformations résiduelles et dans la réponse globale des éprouvettes cruci-formes ont été observées sous l'effet d'un chargement complexe.

En termes de résultats expérimentaux obtenus, il serait judicieux de les conforter par des données expérimentales ou des mesures permettant d'accéder à l'évolution du volume de martensite ξ. Le travail sur la modélisation, présenté dans les prochains chapitres, est basé sur le fait que ξ représente une variable interne primordiale permettant de suivre l'évolution du comportement thermomécanique. Par conséquent, différentes méthodes seront implémentées pour examiner prioritairement les effets d'anisotropie du comportement. Néanmoins, les résultats expérimentaux obtenus constituent une excellente base qui alimentera les fondements physiques en vue d'approfondir la compréhension et la modélisation du comportement multiaxial des AMF.

Le travail expérimental présenté dans ce chapitre a été nécessaire pour compléter, en termes des sollicitations cycliques, le travail fait auparavant dans l'équipe. Les efforts mis en modélisation se focalisent sur les aspects de l'anisotropie en transformation de phase, la réorientation et le couplage thermomécanique fort. Ce travail est l'objet des prochains chapitres du manuscrit. L'exploitation des essais permettra d'introduire des phénomènes supplémentaires, telles la plasticité induite par transformation de phase ou la martensite résiduelle, de manière à représenter les phénomènes décrits dans cette partie expérimentale, ce qui est une perspective en termes de modélisation pour l'équipe SMART du LEM3.

2.5 Bibliographie

Y. Chemisky, F. Meraghni, N. Bourgeois, S. Cornell, R. Echchorfi, and E. Patoor. Analysis of the deformation paths and thermomechanical parameter identification of a shape memory alloy using digital image correlation over heterogeneous tests. *International Journal of Mechanical Sciences*, 96-97:13–24, jun 2015. ISSN 00207403. doi: 10.1016/j.ijmecsci.2015.03.007. 19

D. J. Hartl and D. Lagoudas. Constitutive modeling and structural analysis considering simultaneous phase transformation and plastic yield in shape memory alloys. *Smart Materials and Structures*, 18(10):104017, oct 2009. ISSN 0964-1726. doi: 10.1088/0964-1726/18/10/104017. 19

R. Mehrabi, M. T. Andani, M. Elahinia, and M. Kadkhodaei. Anisotropic behavior of superelastic NiTi shape memory alloys ; an experimental investigation and constitutive modeling. *Mechanics of Materials*, 77:110–124, oct 2014. ISSN 01676636. doi: 10.1016/j.mechmat.2014.07.006. 19

S. Nemat-Nasser and W. Guo. Superelastic and cyclic response of NiTi SMA at various strain rates and temperatures. *Mechanics of Materials*, 38(5-6):463–474, may 2006. ISSN 01676636. doi: 10.1016/j.mechmat.2005.07.004. 19

L. Saint-Sulpice, S. A. Chirani, and S. Calloch. A 3D super-elastic model for shape memory alloys taking into account progressive strain under cyclic loadings. *Mechanics of Materials*, 41 (1):12–26, jan 2009. ISSN 01676636. doi: 10.1016/j.mechmat.2008.07.004. 19

3. Contribution à la modélisation de l'anisotropie dans les AMF

3.1 Introduction

Les applications en AMF d'aujourd'hui ont tendance à s'éloigner des structures unidimensionnelles et à utiliser des composants fonctionnels subissant des chargements complexes multidimensionnels. Dans le cadre de ce genre de chargement, l'anisotropie porte un impact important sur la réponse du matériau. Un outil d'analyse efficace devrait être basé sur un modèle macroscopicque qui puisse intégrer des critères de transformation prévoyant les effets de l'anisotrope. La prédiction du début et de la fin du processus de transformation avec une grande précision a aussi une importance capitale, en raison de la grande amplitude des déformations produites lors de la transformation. Une prédiction inexacte peut peut conduire à la perte de la fiabilité d'une simulation numérique. D'un autre côté, la prise en compte de l'effet des conditions de fabrication est primordial pour la plupart des applications actuelles en AMF, car la plupart sont fabriquées sous forme des fils ou des plaques et manifestent une microstructure texturée. L'effet du laminage et du tréfilage devrait être examiné afin d'obtenir un outil de design précis et efficace.

Dans ce chapitre, le développement théorique, aboutissant à la production d'un nouveau critère de transformation des AMFs soumis à un chargement mécanique isotherme, est présenté. Son objectif est d'introduire un critère qui utilise les composants du tenseur des contraintes et qui soit indépendant du tenseur des déformations de transformation, afin de construire une surface dans l'espace des contraintes déterminant le début et le développement de la transformation. Ce critère a permis d'exprimer la dissymétrie traction-compression et l'anisotropie et aussi à saisir plusieurs résultats provenant soit des expériences ou des simulations en micromécanique. Le deuxième but principal est de développer une formulation qui puisse suivre l'évolution des déformations de transformation pour des matériaux texturés.

Afin de déterminer les paramètres de la surface de transformation proposée, des données expérimentales appropriées sont requises. Des expériences numériques basées sur des analyses micromécaniques sont utilisées dans ce chapitre. Un modèle micromécanique robuste a été précédemment construit à partir du travail de Patoor et al. [1996]. Les données d'entrée pour ce modèle sont l'orientation cristallographique des grains composant un polycristal d'AMF. Il est anticipé qu'un polycristal d'orientation aléatoire soit associé avec une surface d'écoulement isotrope, alors qu'un polycristal texturé manifeste de l'anisotropie en transformation [Boehlert et al., 2008; Somerday et al., 1997]. En réalisant les calculs micromécaniques du matériau texturé et ensuite en déterminant les paramètres adéquats, il est visé d'établir un schéma consistant reliant les conditions des procédés à l'expression de l'anisotropie nécessitée par les logiciels d'analyse.

3.2 Formulation anisotrope

Le cadre thermodynamique du travail théorique concernant l'anisotropie est décrit au Chapitre 1. Il existe un domaine thermoélastique où le vecteur des variables internes du matériau ne produisent pas de dissipation. Ce domaine est défini à partir des forces thermodynamiques générales (FTG) $\boldsymbol{A}$ des variables internes $\boldsymbol{V}$. Ses limites prennent la forme d'une surface décrite par :

$$\Phi(\mathbf{A}) = 0 \tag{3.1}$$

La FTG de la déformation de transformation est reconnue comme la contrainte $\boldsymbol{\sigma}$. Son évolution est normalement déduite à partir de la relation :

$$\dot{\boldsymbol{\varepsilon}}^{\boldsymbol{t}} = \dot{\lambda}\frac{\partial Z}{\partial \boldsymbol{\sigma}}. \tag{3.2}$$

où $Z(\boldsymbol{A})$ est un potentiel de transformation et $\dot{\lambda}$ un multiplicateur de dissipation, considéré ici comme $\dot{\xi}$. Dans cette section, au lieu de chercher un potentiel Z, une relation basée sur la direction des contraintes sera introduite.

3.2.1 Anisotropie en contraintes

Inspiré du critère isotrope dissymétrique utilisé par Patoor et al. [1995]

$$h(\boldsymbol{\sigma}) = \sqrt{J_2}\left(1 + b\frac{J_3}{J_2^{3/2}}\right)^{\frac{1}{2}} - k = 0 \tag{3.3}$$

le nouveau critère proposé a la forme générale :

$$\hat{\Phi}_\sigma(\boldsymbol{\sigma}) = \sqrt{J_2(\boldsymbol{\sigma}^*)}\left[1 + b\frac{J_3(\boldsymbol{\sigma}^*)}{J_2^{3/2}(\boldsymbol{\sigma}^*)}\right]^{\frac{1}{n}} - k_\sigma = 0 \tag{3.4}$$

où n est un nombre réel positif et :

$$\boldsymbol{\sigma}^* = \boldsymbol{R_\sigma} : \boldsymbol{\sigma} - \boldsymbol{x_\sigma} \tag{3.5}$$

Cette dernière équation exprime une transformation de l'espace des contraintes. La rotation des axes et la distortion des échelles de cet espace sont gérées par le tenseur de quatrième ordre $\boldsymbol{R_\sigma}$. L'origine des axes est déplacée par effet du tenseur $\boldsymbol{x_\sigma}$. Il y a 8 paramètres indépendants déterminant la forme de la distortion des contraintes apportée. Le coefficient b gère plutôt l'importance de la dissymétrie et k exprime la taille relative de la surface générée. Tous les détails des développements sont donnés dans la partie en anglais et l'Annexe C.

La visualisation dans l'espace des contraintes normales de la surface résultant de cette formule se trouve sur la Figure 3.1. Il est à noter que sa forme reste inchangée en termes de géométrie : seules ses coordonnées dans le nouveau système sont affectées. Un effet visible de la rotation imposée est que la surface 3D n'est plus parallèle à l'axe $\sigma_{11} = \sigma_{22} = \sigma_{33}$. Cela veut dire que, contrairement au critère isotrope, la nouvelle formulation dépend de la pression hydrostatique. Néanmoins, la triaxialité ne favorise pas la transformation au sens de la compression ou de la tension. Ceci est toujours déterminé par les paramètres de l'équation (3.4).

3.2.2 Anisotropie en déformations

Le fait que le critère proposé soit dépendant de la pression entraîne une conséquence par rapport à l'évolution des déformations de transformation associative :

cette considération n'amène pas à une loi prédisant l'incompressibilité observée expérimentalement dans les AMFs [Bekker and Brinson, 1998]. Par conséquent, une nouvelle loi d'évolution est développée ici :

$$\dot{\boldsymbol{\varepsilon}}_{\boldsymbol{r}}^{\boldsymbol{t}} = \dot{\xi} H^{cur} \left(\boldsymbol{r}_{\varepsilon} . \boldsymbol{\Lambda}_{\boldsymbol{o}} . \boldsymbol{r}_{\varepsilon}^{\boldsymbol{T}} \right) \tag{3.6}$$

où H^{cur} est le même que celui de la formule proposée en [Hartl et al., 2010]. $\boldsymbol{r}_{\varepsilon}$ est une matrice de rotation, construite à partir de quatre paramètres supplémentaires. $\boldsymbol{\Lambda}_{\boldsymbol{o}}$ est un tenseur déviateur, défini par l'équation :

$$\boldsymbol{\Lambda}_{\boldsymbol{o}}(\boldsymbol{\sigma}) = \frac{\partial \hat{\Phi}_{\sigma}^{o}(\boldsymbol{\sigma})}{\partial \boldsymbol{\sigma}} \tag{3.7}$$

où $\hat{\Phi}_{\sigma}^{o}(\boldsymbol{\sigma})$ est la fonction en (3.4) pour le cas isotrope :

$$\hat{\Phi}_{\sigma}^{o}(\boldsymbol{\sigma}) = \hat{\Phi}_{\sigma}(\boldsymbol{\sigma}) \text{ quand } \boldsymbol{\sigma}^{*} = \boldsymbol{\sigma} \tag{3.8}$$

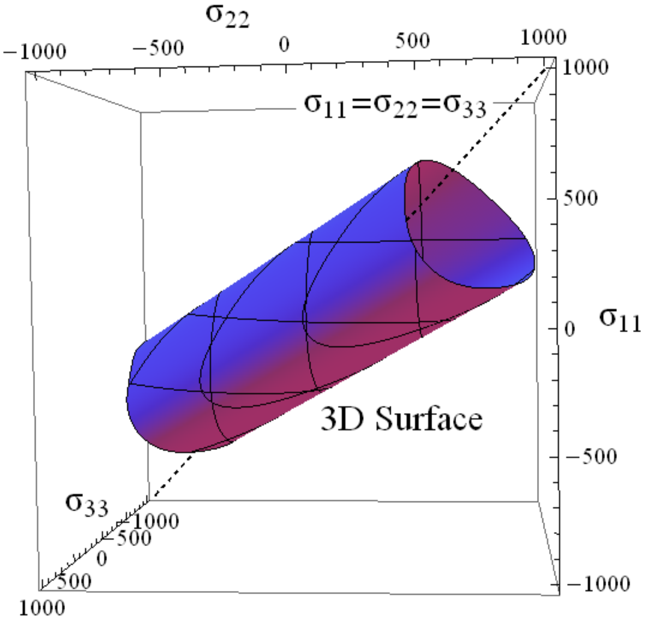

Figure 3.1 – La surface du critère proposé dans l'espace 3D des contraintes normales.

Dans les prochaines sections, cette formulation sera comparée avec l'évolution résultant d'une relation correspondant aux conditions isotropes :

$$\dot{\boldsymbol{\varepsilon}}^{t}_{iso} = \dot{\xi} H \frac{\partial \hat{\Phi}^{o}_{\sigma}}{\partial \boldsymbol{\sigma}} \tag{3.9}$$

La comparaison avec une loi d'évolution associative sera aussi effectuée :

$$\dot{\boldsymbol{\varepsilon}}^{t}_{as} = \dot{\xi} H^{cur} \frac{\partial \hat{\Phi}_{\sigma}}{\partial \boldsymbol{\sigma}} \tag{3.10}$$

Une surface $\hat{Z}(\boldsymbol{\sigma})$ existe, telle quelle tout $\dot{\boldsymbol{\varepsilon}}^{t}_{r}$ suit la loi de normalité. Sa forme exacte reste inconnue.

3.3 Modèle micromécanique

La simulation numérique fournissant les données utilisées pour l'évaluation du nouveau critère est réalisée avec le modèle micromécanique de Patoor et al. [1996], qui implémente la méthode de transition d'échelles auto-cohérente [Entemeyer, 1996]. Les données d'entrée pour l'opération de ce modèle sont les paramètres d'un polycristal en AMF : les températures de transformation, les coefficients relatifs au diagramme de phase, l'orientation des cristaux par l'intermédiaire des vecteurs normaux des plans d'habitat et les directions de 24 variantes pour chaque grain.

3.4 Évaluation du modèle anisotrope

Le modèle micromécanique génère des résultats qui correspondent à 8 essais en chargement proportionnel. Les simulations exécutées approximent la réponse des 3 échantillons en alliage Cu-Zn-Al. Le premier est considéré isotrope, possédant une orientation de grains aléatoire. Les deuxième et troisième correspondent à un échantillon résultant d'un laminage et d'un tréfilage respectivement. Le schéma micromécanique est alimenté avec des tableaux d'orientation de 1000 grains correspondant aux figures de pôles présentées dans l'Annexe D. Les conditions de chargement supposées sont présentées au Tableau 3.1.

Étiquette de simulation	Conditions de chargement	Angle relatif à l'axe 1-1
1	Traction uniaxiale en 1	0°
2	Traction biaxiale en 1 et 2	45°
3	Traction uniaxiale en 2	90°
4	Compression en 1 - traction en 2	135°
5	Compression uniaxiale en 1	180°
6	Compression biaxiale en 1 et 2	225°
7	Compression uniaxiale en 2	270°
8	Traction en 1 - compression en 2	315°

TABLE 3.1 – Trajets de chargement pour les échantillons polycristallins. Les cas non-uniaxiaux sont simulés en conditions équibiaxiales.

3.4.1 Évaluation de la fonction de transformation proposée

Le nouveau critère s'avère suffisamment flexible pour accommoder les 8 points d'entrée et déterminer ses paramètres. L'accord entre les résultats de la simulation de chargement de l'échantillon tréfilé et la surface générée par le critère s'affiche sur la Figure 3.2.

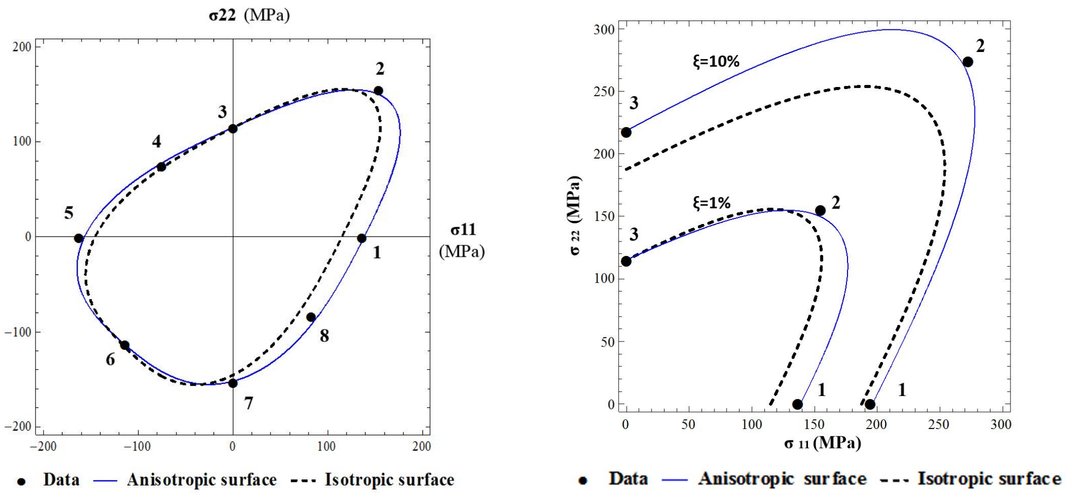

(a) (b)

FIGURE 3.2 – La comparaison entre les surfaces isotropes et anisoropes pour l'échantillon tréfilé (a) et l'évolution de la surface de transformation entre $\xi = 1\%$ et $\xi = 10\%$ (b).

L'évolution de la surface par rapport à la fraction volumique de martensite ξ dévoloppée présente un intérêt particulier. Alors qu'au début de transformation, ici considéré se produisant à $\xi = 1\%$, la contrainte est plus haute lors du chargement sur l'axe 1-1 (cas étiqueté 1) en comparaison avec le chargement en 2-2 (cas 3), ce rapport est inversé dans la suite de la transformation. Cette différence est visualisée à $\xi = 10\%$ sur la Figure (3.2b). Ce changement est bien saisi par le critère de transformation.

3.4.2 Évaluation de la loi d'évolution des déformations de transformation

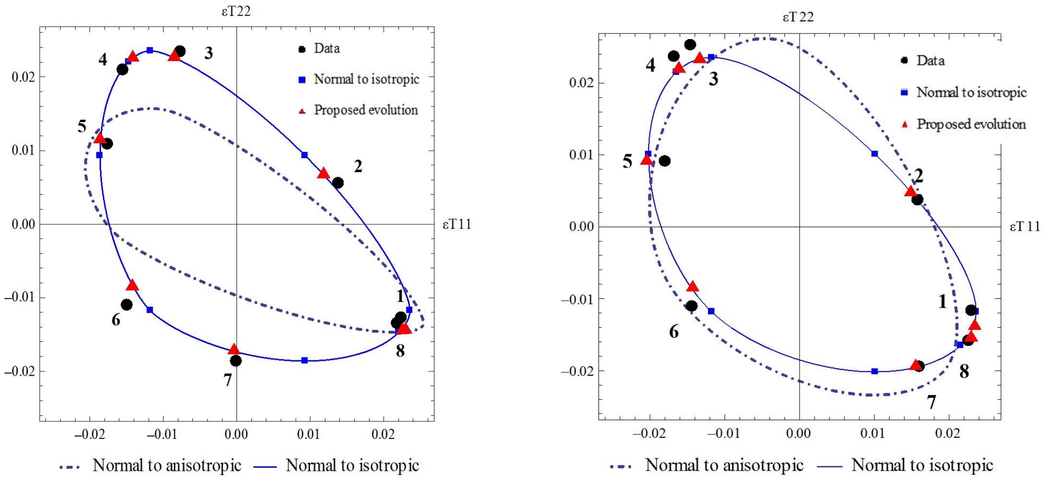

(a) (b)

FIGURE 3.3 – Projection des déformations de transformation générées par les lois d'évolution proposées pour (a) l'échantillon laminé et (b) l'échantillon tréfil sur le plan $\varepsilon^t_{11} - \varepsilon^t_{22}$.

Les lois proposées aux équations (3.6), (3.9) et (3.10) sont utilisées afin de générer des résultats en déformations de transformation $\boldsymbol{\varepsilon^t}$ correspondant aux directions des chargements simulés avec le modèle micromécanique. Les composants des tenseurs $\boldsymbol{\varepsilon^t}$ forment un lieu géométrique pour chaque loi d'évolution. La loi associative $\boldsymbol{\dot{\varepsilon}_{as}}$ produit un lieu prédisant la transformation non-isochore, faisant évoluer le volume du matériau. En revanche, les lois $\boldsymbol{\dot{\varepsilon}_{iso}}$ et $\boldsymbol{\dot{\varepsilon}_{r}}$ produisent le même lieu, alors que la déformation générée pour chaque direction de chargement n'est pas nécessairement identique pour les deux cas. La Figure 3.3 qui met en évidence la différence, représente la projection de ces lieux sur le plan $\varepsilon^t_{11} - \varepsilon^t_{22}$, ainsi que les résultats fournis par la simulation en micromécanique. Un accord satisfaisant entre ces résultats et la loi $\dot{\boldsymbol{\varepsilon}}_{\boldsymbol{r}}$ est constaté.

La forte anisotropie des déformations de transformation, ainsi que la capacité de la nouvelle loi d'évolution à la saisir, est mise en évidence sur la Figure (3.3a). Pour le cas de chargement 7 (traction sur l'axe 1-1 et compression sur l'axe 2-2), la déviation de la prédiction isotrope (point bleu) est si importante qu'elle cause une mise à zéro de la déformation ε^t_{11} (point noir). En même temps, en raison de l'absence de changement de volume, $\varepsilon^t_{33} = -\varepsilon^t_{22}$.

3.5 Conclusion du chapitre

Dans ce chapitre, un nouveau critère de transformation de phase, basé à une distortion maîtrisée de l'espace des contraintes, a été décrit et implémenté. Il saisit l'anisotropie et la dissymétrie traction-compression pour le début et le développement de la transformation dans le cas des alliages à mémoire de forme texturés. Une loi d'évolution a été aussi introduite afin d'exprimer la dépendance des déformations de transformation à la direction du chargement appliqué. Ce travail théorique a été évalué avec l'aide d'un modèle micromécanique, qui a généré des résultats correspondant à des chargements proportionnels d'échantillons en AMF Cu-Zn-Al considérés ayant subi les procédés de laminage et de tréfilage.

3.6 Bibliographie

A. Bekker and L. Brinson. Phase diagram based description of the hysteresis behavior of shape memory alloys. *Acta Materialia*, 46(10):3649–3665, jun 1998. ISSN 13596454. doi: 10.1016/S1359-6454(97)00490-4. 34

C. Boehlert, S. Longanbach, and T. Bieler. Effect of thermomechanical processing on the creep behaviour of Udimet alloy 188. *Philosophical Magazine*, 88(5):641–664, feb 2008. ISSN 1478-6435. doi: 10.1080/14786430801944836. 32

D. Entemeyer. *Etude micromécanique du comportement thermomécanique des alliages à mémoire de forme.* Phd, Université de Metz, 1996. 35

D. J. Hartl, D. C. Lagoudas, F. T. Calkins, J. H. Mabe, J. T. Mooney, D. C. Lagoudas, F. T. Calkins, and J. H. Mabe. Use of a Ni60Ti shape memory alloy for active jet engine chevron application: I. Thermomechanical characterization. *Smart Materials and Structures*, 19(1): 015020, jan 2010. ISSN 0964-1726. doi: 10.1088/0964-1726/19/1/015020. 34

E. Patoor, M. El Amrani, A. Eberhardt, and M. Berveiller. Determination of the origin for the dissymmetry observed between tensile and compression tests on shape memory alloys. *J. Phys.*, IV(2):495–500, 1995. 33

E. Patoor, A. Eberhardt, and M. Berveiller. Micromechanical Modelling of Superelasticity in Shape Memory Alloys. *Journal de Physique IV*, 6:C1–277, 1996. 32, 35

M. Somerday, R. J. Comstock, and J. A. Wert. A systematic analysis of transformation stress anisotropy in shape memory alloys. *Philosophical Magazine A*, 75(5):1193–1207, may 1997. ISSN 0141-8610. doi: 10.1080/01418619708209851. 32

4. Modèle phénoménologique destiné à la saisie du comportement multiaxial des AMF

4.1 Introduction

Dans ce chapitre, une interprétation physique des processus ayant lieu au sein d'un grain d'AMF est tentée. La notion de la déformation de transformation moyenne développée dans l'article de Chemisky et al. [2011] est examiné d'un point de vue macroscopique afin de redéfinir les principes de la réorientation et des transformations de phase directe et inverses. Cette étude amène à l'introduction des variables scalaires indépendantes gérant chacun de trois mécanismes. Dans ce cadre, un formalisme robuste en termes de thermodynamique est présenté, basé sur un potentiel d'énergie libre du type Gibbs. Chaque variable interne est assosiée linéairement avec les trois variables scalaires principales.

La problématique de l'activation simultanée de multiples mécanismes du type de plasticité. Prenant l'inspiration du travail d'Auricchio et al. [2014], chaque mécanisme est considéré être lié à son propre critère d'activation. Ces critères ont la forme des fonctions d'écoulement dépendent des variables internes. En outre, la reconnaissance du couplage fort des effets thermomécaniques sur le comportement des AMFs [Morin et al., 2011; Peyroux et al., 1998], la chaleur générée à cause du travail mécanique est calculée toujours en prenant en compte l'influence des mécanismes multiples. Cette étude concerne, entre autres, le sujet de la chaleur latente impactant les essais mécaniques en superélasticité [Brinson et al., 2004; Hartl and Lagoudas, 2008].

4.2 Description physique

4.2.1 Déformation au niveau des grains

La quantité physique de la déformation de transformation moyenné $\bar{\boldsymbol{\varepsilon}}^{\boldsymbol{T}}$, étudié dans le travail de Chemisky et al. [2011], sera utilisée pour examiner la contribution des mécanismes de transformation et réorientation. Elle est exprimée comme :

$$\bar{\boldsymbol{\varepsilon}}^{\boldsymbol{T}} = \frac{1}{V_M} \int\limits_{V_M} \tilde{\boldsymbol{\varepsilon}}^{\boldsymbol{T}}_{\boldsymbol{r}} dV \tag{4.1}$$

Ici, $\tilde{\boldsymbol{\varepsilon}}^{\boldsymbol{T}}_{\boldsymbol{r}}$ est le champs des déformations de transformation dans le volume entier V d'un Volume Élémentaire Représentatif (VER) pour tout point en coordonnées $\boldsymbol{r}$. V_M est le volume martinsitique dans le VER. La déformation inélastique totale se trouve dans le volume martensitique, ce qui entraîne la relation :

$$\boldsymbol{\varepsilon}^{\boldsymbol{T}} = \frac{V_M}{V} \bar{\boldsymbol{\varepsilon}}^{\boldsymbol{T}} \Leftrightarrow \boldsymbol{\varepsilon}^{\boldsymbol{T}} = \xi \bar{\boldsymbol{\varepsilon}}^{\boldsymbol{T}} \tag{4.2}$$

où ξ est la fraction volumique de martensite. L'évolution de la déformation est étudiée dans le schéma incrémental :

$$\boldsymbol{d\varepsilon}^{\boldsymbol{T}} = d\xi \bar{\boldsymbol{\varepsilon}}^{\boldsymbol{T}} + \xi \boldsymbol{d\bar{\varepsilon}}^{\boldsymbol{T}} \tag{4.3}$$

La valeur de $\boldsymbol{d\bar{\varepsilon}}^{\boldsymbol{T}}$ est approximée avec l'aide de la représentation des incréments temporels sur la Figure 4.1 :

$$\boldsymbol{d\bar{\varepsilon}}^{\boldsymbol{T}} = (\bar{\boldsymbol{\Lambda}}^{\boldsymbol{T}} - \bar{\boldsymbol{\varepsilon}}^{\boldsymbol{T}}) \frac{d\xi}{\xi} + \boldsymbol{d\bar{\varepsilon}}^{\boldsymbol{re}} \tag{4.4}$$

$\bar{\boldsymbol{\Lambda}}^{\boldsymbol{T}}$ correspond à la deformation inélastique moyenne dans le volume martensitique rajouté lors de l'incrément, alors que $\boldsymbol{d\bar{\varepsilon}}^{\boldsymbol{re}}$ est le changement de la déformation

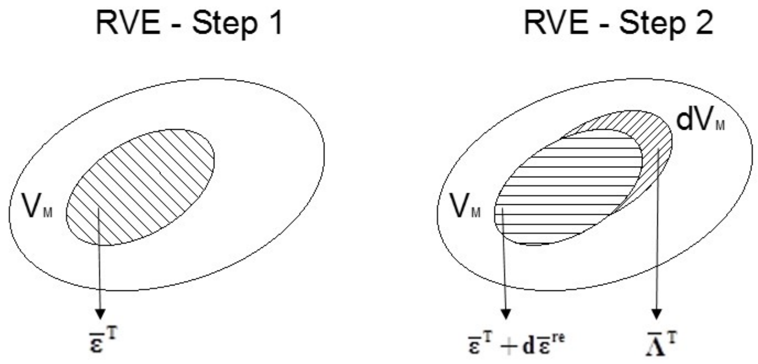

FIGURE 4.1 – Représentation du comportement d'un VER en AMF en incréments temporels.

dans le volume martensitique existant dans le même incrément :

$$\boldsymbol{d\bar{\varepsilon}^{re}} = \frac{1}{V_M}\int\limits_{V_M} \boldsymbol{d\tilde{\varepsilon}_r^T}\, dV \tag{4.5}$$

4.2.2 Formulation mathématique

Le taux de la déformation inélastique totale peut être exprimée comme :

$$\boldsymbol{\dot{\varepsilon}^T} = \dot{\xi}\boldsymbol{\bar{\Lambda}^T} + \xi\boldsymbol{\dot{\bar{\varepsilon}}^{re}} \tag{4.6}$$

Dans les prochaines sections, il deviendra évident que les contributions de la réorientation et les transformations directe et inverse peuvent s'ajouter simultanément :

$$\boldsymbol{\dot{\varepsilon}^T} = \boldsymbol{\dot{\varepsilon}^F} + \boldsymbol{\dot{\varepsilon}^R} + \boldsymbol{\dot{\varepsilon}^{re}} \tag{4.7}$$

Les chiffres en exposant F, R et re correspondent respectivement à la transformation directe (Forward), transformation inverse (Reverse) et la réorientation. L'effet direct de chacun de ces mécanismes est la modification de la déformation dans le volume martensitique. Il est illustré sur la Figure 4.2.

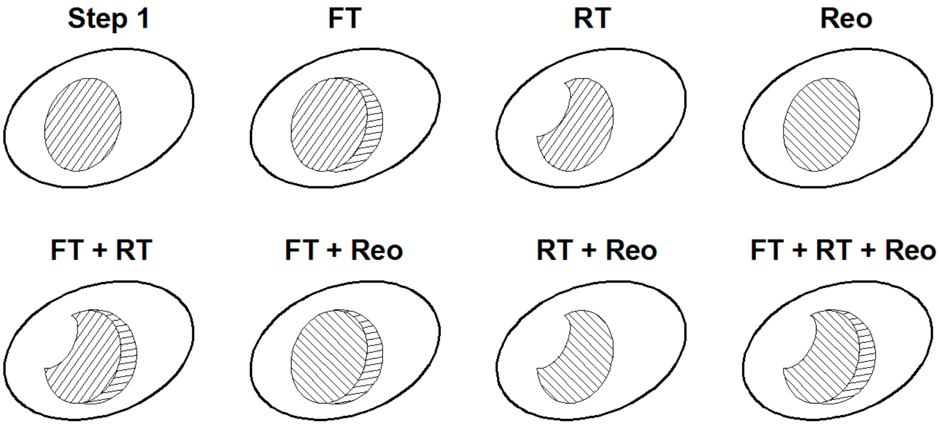

FIGURE 4.2 – L'effet des mécanismes inélastiques sur un VER en AMF.

4.3 Transformation de phase

4.3.1 Transformation directe

Lors de la transformation directe, il est visible sur la Figure 4.2 que le volume martensitique rajouté ne suit pas forcément l'orientation de la déformation existante. Le tenseur $\boldsymbol{\Lambda}_{\varepsilon}^{\boldsymbol{F}}$ est défini comme la relation entre l'incrément de la fraction du volume martensitique $\dot{\xi}^F$ et l'incrément de la déformation en termes d'amplitude et de direction :

$$\dot{\boldsymbol{\varepsilon}}^{\boldsymbol{F}} = \dot{\xi}^F \boldsymbol{\Lambda}_{\varepsilon}^{\boldsymbol{F}} \tag{4.8}$$

4.3.2 Transformation inverse

Ici, la réduction du volume martensitique est exprimée par le taux positif $\dot{\xi}^R$. Le taux des déformations de la transformation inverse est :

$$\dot{\boldsymbol{\varepsilon}}^{\boldsymbol{R}} = \dot{\xi}^R \boldsymbol{\Lambda}_{\varepsilon}^{\boldsymbol{R}} \tag{4.9}$$

Il est prouvé que si la considération :

$$\boldsymbol{\Lambda}_{\varepsilon}^{\boldsymbol{R}} = -\bar{\boldsymbol{\varepsilon}}^{\boldsymbol{T}} \tag{4.10}$$

est implémentée, une condition cruciale du comportement macroscopique des AMFs soit satisfaite : Lors du retour à zéro volume de martensite, au même temps la déformation inélastique doit disparaître.

4.3.3 Indépendance des transformations directe et inverse

Il est déduit que le taux du volume de martensite prenne la forme :

$$\dot{\xi} = \dot{\xi}^F - \dot{\xi}^R \tag{4.11}$$

Les intégrales temporelles ξ^F et ξ^R doivent satsifaire les inégalités :

$$0 \leq \xi \leq 1 \Leftrightarrow \xi^R \leq \xi^F \leq 1 + \xi^R \tag{4.12}$$

Le fait que ξ peut être incrémenté en deux manières indépendantes veut dire que les transformations directe et inverse peuvent avoir lieu, en termes de modélisation, simultanément. En rappelant la définition du tenseur $\bar{\boldsymbol{\Lambda}}^{\boldsymbol{T}}$ en 4.4, ceci est retrouvé comme :

$$\dot{\xi}^F \boldsymbol{\Lambda}^{\boldsymbol{F}}_{\boldsymbol{\varepsilon}} + \dot{\xi}^R \boldsymbol{\Lambda}^{\boldsymbol{R}}_{\boldsymbol{\varepsilon}} = \dot{\xi} \bar{\boldsymbol{\Lambda}}^{\boldsymbol{T}} \tag{4.13}$$

4.4 Réorientation

La variable $\dot{\bar{p}}^{re}$ concerne l'évolution des déformations dans un grain et représente le taux de l'amplitude de la déformation de transformation moyenne dans une partie martensitique de volume constant :

$$\dot{\bar{p}}^{re} = \sqrt{\frac{2}{3} \dot{\bar{\boldsymbol{\varepsilon}}}^{\boldsymbol{re}} : \dot{\bar{\boldsymbol{\varepsilon}}}^{\boldsymbol{re}}} \tag{4.14}$$

où $\dot{\bar{\boldsymbol{\varepsilon}}}^{\boldsymbol{re}}$ est la direction de l'incrément de la déformation concernée. Rapportée dans l'espace du VER, la variable $\dot{\bar{p}}^{re}$ gère le taux des déformations dues à la réorientation :

$$\dot{\boldsymbol{\varepsilon}}^{\boldsymbol{re}} = \xi \dot{\bar{p}}^{re} \boldsymbol{\Lambda}^{\boldsymbol{re}}_{\boldsymbol{\varepsilon}} \tag{4.15}$$

La variable $\dot{p}^{re} = \xi \dot{\bar{p}}^{re}$ est utilisée pour réécrire la relation (4.7) dans la forme de l'équation principale du nouveau modèle :

$$\dot{\boldsymbol{\varepsilon}}^{\boldsymbol{T}} = \dot{\xi}^{F} \boldsymbol{\Lambda}_{\boldsymbol{\varepsilon}}^{\boldsymbol{F}} + \dot{\xi}^{R} \boldsymbol{\Lambda}_{\boldsymbol{\varepsilon}}^{\boldsymbol{R}} + \dot{p}^{re} \boldsymbol{\Lambda}_{\boldsymbol{\varepsilon}}^{\boldsymbol{re}} \tag{4.16}$$

4.5 Couplage entre les mécanismes

4.5.1 Formulation du système thermodynamique

Les considérations proposées sont intégrées dans le cadre thermodynamique basant sur un potentiel d'énergie libre de Gibbs :

$$\begin{aligned} G =& U_o - s_o T + C_v \left[\Delta T - T \ln \left(\frac{T}{T_o} \right) \right] - \frac{1}{2} \boldsymbol{\sigma} : S : \boldsymbol{\sigma} - \boldsymbol{\sigma} : \boldsymbol{\alpha} \Delta T - \boldsymbol{\sigma} : \boldsymbol{\varepsilon}^{\mathbf{T}} + \\ & (1 + \lambda^{re}) \boldsymbol{X} : \boldsymbol{v}^{\boldsymbol{re}} + H(\xi) \end{aligned} \tag{4.17}$$

où :
$\boldsymbol{\sigma}$ is la contrainte de Cauchy.
S est le tenseur de compliance élastique.
$\boldsymbol{\alpha}$ est le coefficient de dilatation thermique.
$\Delta T = T - T_o$ est la différence entre la température actuelle T et la température à l'état de référence T_o.
U_o est l'énergie interne spécifique à à l'état de référence.
s_o est l'entropie spécifique à l'état de référence.
C_v est la capacité thermique spécifique.
$H(\xi)$ est une fonction prenant en compte l'écrouissage isotrope associé à la transformation, lié à la fraction volumique de la martensite [Hartl et al., 2010].
$\boldsymbol{v}^{\boldsymbol{re}}$ est défini comme la déformation d'écrouissage en réorientation.
$\boldsymbol{X}$ est défini comme le backstress.
Finalement, λ^{re} est un coefficient limitant la réorientation.
La discussion concernant la deuxième loi de la thermodynamique se trouve à la partie en anglais.

Un critère d'écoulement est pris en compte séparément pour chaque mécanisme pour garantir leur activation indépendante. Pour la transformation directe, les critères investigués dans la première partie de ce travail sont considérés. Pour la

Transformation directe	Transformation inverse	Réorientation
$\hat{\Phi}^F(\boldsymbol{\sigma}) + A_{\xi^F} - Y^F + \lambda^F \leq 0$	$\hat{\Phi}^R(\boldsymbol{\sigma}, \boldsymbol{\varepsilon^T}) + A_{\xi^R} - Y^R + \lambda^R \leq 0$	$\hat{\Phi}^{re}(\boldsymbol{\Sigma}) - Y^{re} \leq 0$
$\dot{\boldsymbol{\varepsilon}}^{\boldsymbol{F}} = \dot{\xi}^F \boldsymbol{\Lambda}_{\boldsymbol{\varepsilon}}^{\boldsymbol{F}}$	$\dot{\boldsymbol{\varepsilon}}^{\boldsymbol{R}} = \dot{\xi}^R \boldsymbol{\Lambda}_{\boldsymbol{\varepsilon}}^{\boldsymbol{R}}$	$\dot{\boldsymbol{\varepsilon}}^{\boldsymbol{re}} = \dot{p}^{re} \boldsymbol{\Lambda}_{\boldsymbol{\varepsilon}}^{\boldsymbol{re}}$
$\dot{\boldsymbol{X}}^{\boldsymbol{F}} = \dot{\xi}^F \boldsymbol{\Lambda}_{\boldsymbol{X}}^{\boldsymbol{F}}$	$\dot{\boldsymbol{X}}^{\boldsymbol{R}} = \dot{\xi}^R \boldsymbol{\Lambda}_{\boldsymbol{X}}^{\boldsymbol{R}}$	$\dot{\boldsymbol{X}}^{\boldsymbol{re}} = \dot{p}^{re} \boldsymbol{\Lambda}_{\boldsymbol{X}}^{\boldsymbol{re}}$
		$\boldsymbol{\Sigma} = \boldsymbol{\sigma} - (1 + \lambda^{re})\boldsymbol{X}$
Synthèse		
$\xi = \xi^F - \xi^R$		
$\boldsymbol{\varepsilon^T} = \boldsymbol{\varepsilon^F} + \boldsymbol{\varepsilon^R} + \boldsymbol{\varepsilon^{re}}$		
$\boldsymbol{\varepsilon} = \boldsymbol{\varepsilon^{el}} + \boldsymbol{\varepsilon^{th}} + \boldsymbol{\varepsilon^T}$		
$\boldsymbol{\varepsilon^{th}} = \boldsymbol{\alpha}(\xi)\Delta T$		
$\boldsymbol{\varepsilon^{el}} = S(\xi) : \boldsymbol{\sigma}$		
$\boldsymbol{X} = \boldsymbol{X^F} + \boldsymbol{X^R} + \boldsymbol{X}^{re}$		

TABLE 4.1 – Les relations les plus importantes du modèle proposé.

transformation inverse, un critère approprié garantit le retour à déformation nulle quand tout le volume martensitique est récupéré. Un critère imposant l'écrouissage cinématique est appliqué pour le cas de la réorientation. Le backstress X attribue le caractère cinématique au comportement de la réorientation. Les relations les plus importantes sont résumées sur le Tableau 4.1.

4.5.2 Effets thermomécaniques

La forme locale de la première loi de la thermodynamique est écrite comme :

$$\dot{u} = r - \nabla \cdot \boldsymbol{q} + \boldsymbol{\sigma} : \dot{\boldsymbol{\varepsilon}} = \dot{Q} + \boldsymbol{\sigma} : \dot{\boldsymbol{\varepsilon}} \tag{4.18}$$

où u est l'énergie interne, r est la puissance de la chaleur produite à l'intérieur de la masse de l'AMF, $\boldsymbol{q}$ est le flux thermal et Q est l'échange de chaleur totale, due à la fois aux sources de chaleur interne et à la conduction. En développant les relations du nouveau modèle, une équation reliant la génération de la chaleur et le chargement mécanique en résulte :

$$C_v\dot{T} - \dot{Q} = -\left[\sum_j \left(\pi_T^j \boldsymbol{P}_{\boldsymbol{\varepsilon}}^{\boldsymbol{j}}\right) + \boldsymbol{L} : \boldsymbol{\alpha} \cdot T\right] : \dot{\boldsymbol{\varepsilon}} - \left[\sum_j \left(\pi_T^j P_T^j\right) + \boldsymbol{\Theta} : \boldsymbol{\alpha} \cdot T\right] \dot{T} \tag{4.19}$$

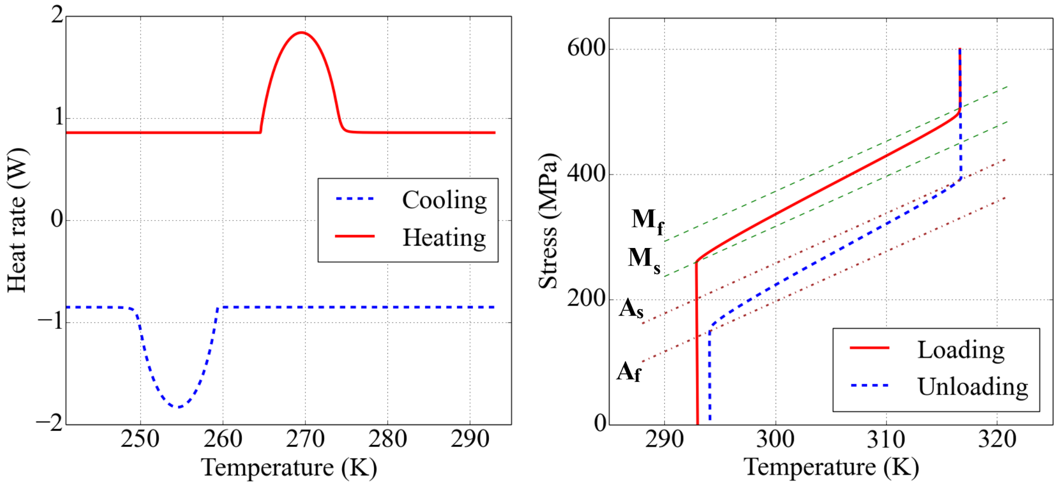

(a) Simulation des mesures DSC (b) Chargement adiabatique 1-D

FIGURE 4.3 – Diagramme puissance de chaleur - température d'un essai DSC simulé (a) et courbes contrainte-température sur un diagramme de phase pour un chargement 1-D simulé en contrôle de contraintes sous conditions adiabatiques (b) pour une composition NiTi hypothétique. La température initiale est 293 K pour les deux cas.

À la partie du côté gauche, la différence entre l'échange de la chaleur et le taux d'énergie absorbé par la masse du matériau doit correspondre à une énergie produite à l'intérieur. Au côté droit, il s'avère que cette énergie est causée par le chargement mécanique et/ou thermique, induisant le changement de la déformation $\dot{\varepsilon}$ et de la température $\dot{T}$. Cette équation est valable pour un nombre de mécanismes inélastiques indéterminé. La procédure suivie pour obtenir les quantités de requises se trouve au Chapitre 5 et l'Annexe D.

Pour des cas de chargement simple, comme une variation en température sous contrainte nulle ou un cycle de charge-décharge en 1-D, la réorientation n'est pas activée et les lois appliquées pour la transformation se réduisent éventuellement à la forme du modèle de Lagoudas. Sur la Figure (4.3a), la réponse du modèle pour un cycle refroidissement-rechauffement sous mesures en DSC est présentée. Les implications du couplage thermomécanique fort pour le cas d'un chargement 1-D sous conditions adiabatiques est aussi illustré sur la Figure (4.3b).

4.6 Conclusion du chapitre

Un nouveau modèle phénoménologique décrivant le comportement complexe des AMFs manifestant la transformation et la réorientation couplées lors du chargement thermodynamique général non-proportionnel est proposé. Il a été démontré que ce modèle soit cohérent aux termes de thermodynamique et que les lois d'évolution des déformations correspondent à l'évolution des volumes martensitiques dans un AMF.

La contribution originale de ce travail concerne la manière indépendante de la prise en compte des mécanismes physiques impactant la déformation. La première contribution est le découplage des transformations directe et inverse, ce qui permet leur activation simultanée. La deuxième originalité est la forme simple décrivant la réorientation des variantes martensitiques. Les effets thermodynamiques sont pris en compte en toute ampleur.

La réponse du modèle pour des conditions simples en une dimension a été brièvement examinée. La mise en évidence de la réponse numérique sera effectuée avec des cas non-triviaux au prochain chapitre. Des simulations des essais simples et complexes sur des structures en AMF trouvés dans la littérature seront réalisées pour examiner les capacités pratiques du modèle. Le couplage thermomécanique fort peut être évalué en mettant en place des analyses d'effet de vitesse appropriées.

4.7 Bibliographie

F. Auricchio, E. Bonetti, G. Scalet, and F. Ubertini. Theoretical and numerical modeling of shape memory alloys accounting for multiple phase transformations and martensite reorientation. *International Journal of Plasticity*, 59:30–54, aug 2014. ISSN 07496419. doi: 10.1016/j.ijplas.2014.03.008. 41

L. Brinson, I. Schmidt, and R. Lammering. Stress-induced transformation behavior of a polycrystalline NiTi shape memory alloy: micro and macromechanical investigations via in situ optical microscopy. *Journal of the Mechanics and Physics of Solids*, 52(7):1549–1571, jul 2004. ISSN 00225096. doi: 10.1016/j.jmps.2004.01.001. 41

Y. Chemisky, A. Duval, E. Patoor, and T. Ben Zineb. Constitutive model for shape memory alloys including phase transformation, martensitic reorientation and twins accommodation. *Mechanics of Materials*, 43(7):361–376, jul 2011. ISSN 01676636. doi: 10.1016/j.mechmat.2011.04.003. 41, 42

D. J. Hartl and D. C. Lagoudas. Thermomechanical Characterization of Shape Memory Alloy Materials. In *Shape Memory Alloys*, pages 53–119. Springer US, Boston, MA, 2008. ISBN 978-0-387-47684-1. doi: 10.1007/978-0-387-47685-8. 41

D. J. Hartl, G. Chatzigeorgiou, and D. C. Lagoudas. Three-dimensional modeling and numerical analysis of rate-dependent irrecoverable deformation in shape memory alloys. *International Journal of Plasticity*, 26(10):1485–1507, oct 2010. ISSN 07496419. doi: 10.1016/j.ijplas.2010.01.002. 46

C. Morin, Z. Moumni, and W. Zaki. Thermomechanical coupling in shape memory alloys under cyclic loadings: Experimental analysis and constitutive modeling. *International Journal of Plasticity*, 27(12):1959–1980, dec 2011. ISSN 07496419. doi: 10.1016/j.ijplas.2011.05.005. 41

R. Peyroux, A. Chrysochoos, C. Licht, and M. Löbel. Thermomechanical couplings and pseudoelasticity of shape memory alloys. *International Journal of Engineering Science*, 36(4): 489–509, mar 1998. ISSN 00207225. doi: 10.1016/S0020-7225(97)00052-9. 41

5. Vers la simulation de structures AMF en conditions de chargement complexe

5.1 Introduction

Dans ce chapitre, des résultats numériques prouvant les capacités prédictives du modèle introduit au Chapitre 4 sont présentés. Afin d'implémenter le modèle dans des outils numériques et générer des résultats simulés, les implications du cadre des multiples mécanismes de déformations inélastiques sont d'abord examinées. L'indépendance de ces mécanismes engendre une incertitude par rapport à leur activation. La méthode Fischer-Burmeister pour la résolution numérique des conditions Kuhn-Tucker est déployée pour lever ce verrou scientifique. En plus, des modules tangents thermomécaniques adaptatifs appropriés sont développés pour permettre la convergence rapide.

Dans la deuxième partie du chapitre, le modèle AMF est évalué en comparant la réponse numérique avec les résultats provenant des bases de données expérimentales issues de la littérature. Des cas de chargement complexes multidimensionnels sont étudiés pour valoriser l'importance de la réorientation martensitique. Finalement, le fort couplage thermomécanique est mis en évidence en réalisant des simulations numériques de chargements sous conditions limites thermiques. L'influence des conditions adiabatiques est présentée et discutée. La simulation par Éléments Finis d'une structure en NiTi est étudiée plus attentivement. Trois cas de vitesses de chargement sont présentés afin d'analyser les effets inhérents à la vitesse de déformation sur le couplage thermomécanique. Une grande partie de ce travail est l'objet d'un article accepté (en attente de publication) dans la revue IJP [Chatziathanasiou et al., 2016].

5.2 Cadre de l'activation multiple des mécanismes de déformation

5.2.1 Configuration de base

Il est considéré que l'évolution de la déformation inélastique est causée par de multiples mécanismes qui sont indépendants aux termes de thermodynamique. Cela veut dire que la dissipation associée à chacun entre eux doit être non-négative. La déformation totale inélastique est :

$$\boldsymbol{\varepsilon^T} = \sum_m \boldsymbol{\varepsilon^m} \tag{5.1}$$

où l'indice m désigne tous les mécanisme différents. Tout mécanisme m est responsable pour l'évolution de $\boldsymbol{\varepsilon^m}$. Il est, au même temps, associé à un set de variables $\{\boldsymbol{V^m_i}\}$. Chaque $\boldsymbol{V^m_i}$ différente peut être considérée une variable interne ou pas. Le premier élément de chaque set est défini comme un scalaire p^m :

$$p^m = V^m_1$$

La propriété basique de tout p^j est que le taux de toute autre variable $\boldsymbol{V^j_i}$ est associé linéairement à $\dot{p}^j$:

$$\dot{\boldsymbol{V}}\boldsymbol{{}^j_i} = \dot{p}^j \boldsymbol{\Lambda}^j_i \tag{5.2}$$

où j est un indice qui peut désigner tout mécanisme m. $\boldsymbol{\Lambda}^j_i$ est un tenseur d'ordre variant par rapport à la nature de $\boldsymbol{V^j_i}$.

En thermodynamique, tout élément $\boldsymbol{V^j_i}$ qui est une variable interne a une force thermodynamique conjuguée (FTC) :

$$\boldsymbol{A^m_{V\ i}} = -\frac{\partial G}{\partial \boldsymbol{V^m_i}} \tag{5.3}$$

où G est le potentiel d'énergie libre de Gibbs régissant le comportement général. Les critères thermodynamiques gérant l'activation de chaque mécanisme ont la forme :

$$\Phi^m(\{\boldsymbol{A_V^m}\}) \leq 0 \tag{5.4}$$

où $\{\boldsymbol{A_V^m}\}$ est le set entier des FTCs du mécanisme m. Le nombre total N_m de tous les mécanismes peut être indéfini.

5.2.2 La méthode Fischer-Burmeister

La résolution numérique de ce problème non-linéaire suit la méthode Convex Cutting Plane (CCP) [Hartl and Lagoudas, 2009] en combinaison avec le schéma Newton-Raphson. Une méthode particulièrement intéressante pour renforcer la procédure de l'optimisation a été introduite par Fischer [1992]. Elle est la méthode appelée Fischer-Burmeister et elle a été récemment implémentée dans des articles concernant des modèles AMF [Auricchio et al., 2014; Kiefer et al., 2012].

Un mécanisme m, activé lors de la satisfaction du critère Φ^m et géré par le taux de la scalaire p^m, les conditions Kuhn-Tucker doivent s'appliquer :

$$\begin{aligned} &\Phi^m \leq 0 \\ &\dot{p}^m \geq 0 \\ &\Phi^m \dot{p}^m = 0 \end{aligned} \tag{5.5}$$

La technique Fischer-Burmeister transforme ce problème en un problème équivalent, dont la solution est obtenue par résolution d'un set d'équations dans la forme :

$$\sqrt{(\Phi^m)^2 + (\dot{p}^m)^2} + \Phi^m - \dot{p}^m = 0 \tag{5.6}$$

L'avantage principal est que l'activation d'un mécanisme ou son absence est décidée par la résolution des équations. Même le cas de l'évolution élastique peut résulter, quand $\dot{p} = 0$ pour tout m.

5.2.3 Algorithme de résolution numérique

Dans le cadre de la résolution numérique des structures réalisée par la Méthode des Éléments Finis (MEF), la valeur de toute variable appartient à un set de trois procédures répétitives, appelées boucles dans cette section. Une étape du chargement est répartie à des incréments de temps. La boucle externe résout la balance associée à l'interaction entre éléments pour chaque incrément. Elle est appelée “la boucle n”. Le logiciel Abqaus est utilisé pour la simulation d'une

structure en AMF dans ce chapitre. Les algorithmes déployés par la MEF ne sont pas examinés dans ce travail.
La deuxième boucle, appelée “boucle ω”, concerne le processus de l’itération dans un élément pour satisfaire la balance des efforts lors de la mise à jour des contraintes par la loi constitutive.
La troisième procédure est celle qui itère les manipulations algébriques aboutissant à trouver le prochain set de coordonnées admissibles des variables dans un VER. Elle est appelée “la boucle k” et elle a lieu à ce niveau où la loi constitutive manifeste ses particularités.

Dans la partie du chapitre en anglais, la procédure suivie pour la résolution de la boucle k est présentée. En plus, les quantités requises par Abaqus, y compris les modules tangents thermomécaniques et l’énergie thermique produite par le chargement.

5.3 Validation numérique exploitant les bases de données expérimentales

La réponse thermomécanique du modèle proposé est comparé avec le comportement thermomécanique complexe non-proportionnel des AMFs observé lors des essais adéquats. La base de données expérimental sélectionnée inclue des essais en conditions de chargement proportionnel et non-proportionnel sous niveaux mécaniques et thermiques différents.

Un premier set d’expériences concerne la traction isotherme des fils en NiTi sous des températures différentes, soit en dessus ou entre les températures de transformation directe [Sittner et al., 2009]. Le deuxième genre d’essais correspond aux conditions non-proportionnelles de traction-torsion combinées sur des tubes en AMF CuAlZnMn [Sittner et al., 1995]. Un dernier essai examiné est un chargement complexe en traction-torsion et compression-torsion combinées avec une variation importante en température [Grabe and Bruhns, 2009]. L’identification des paramètres est faite en utilisant une méthode fiable développée par Meraghni et al. [2014] et étendue en configuration hétérogène dans [Chemisky et al., 2015].

5.3.1 Traction-compression isotherme

Alors qu’il n’y a pas de données expérimentales en compression, la réponse du modèle pour le cas de la température entre M_s et A_f est assez intéressante sur la

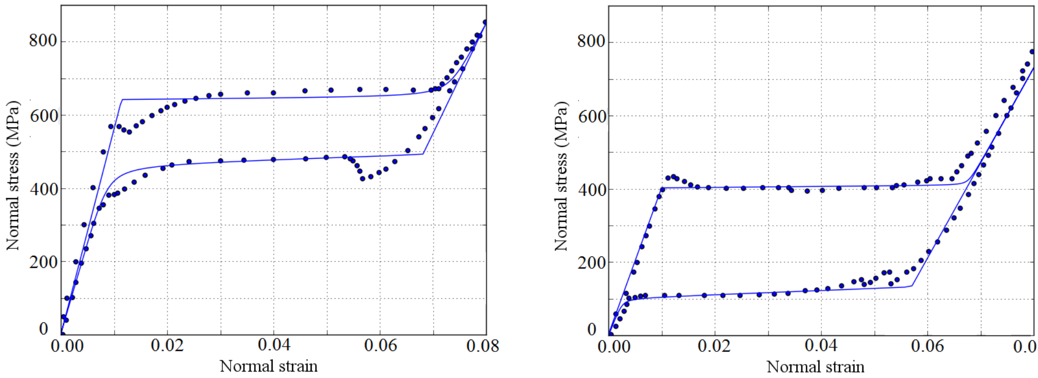

(a) Traction à 333 K

(b) Traction à 283 K

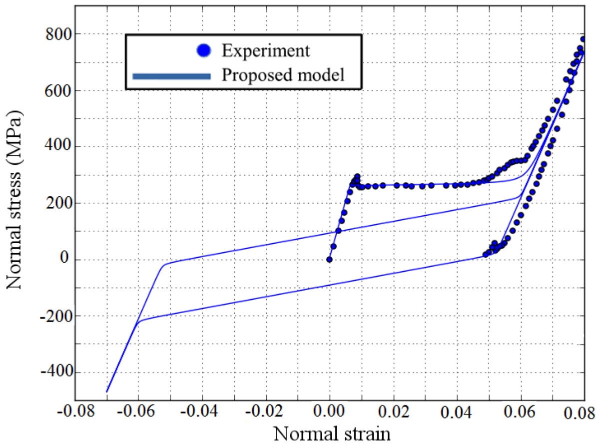

(c) Traction à 253 K

Figure 5.1 – Résultats expérimentaux (points) et réponse du modèle (ligne continue) sur des diagrammes contraintes-déformations pour le chargement en traction-compression de fils en NiTi aux températures de 333, (a) 283 (b) et 253 K (c) pris par [Sittner et al., 2009].

Figure (5.1c). L'absence de la transformation inverse entraîne un comportement dissymétrique entre traction et compression, dû à l'activation de la réorientation.

5.3.2 Traction-torsion non proportionnelle

Ici, la réponse du modèle proposé est aussi comparé avec des modèles existants importants. Les diagrammes associés à cet essai se trouvent sur la Figure 5.2.

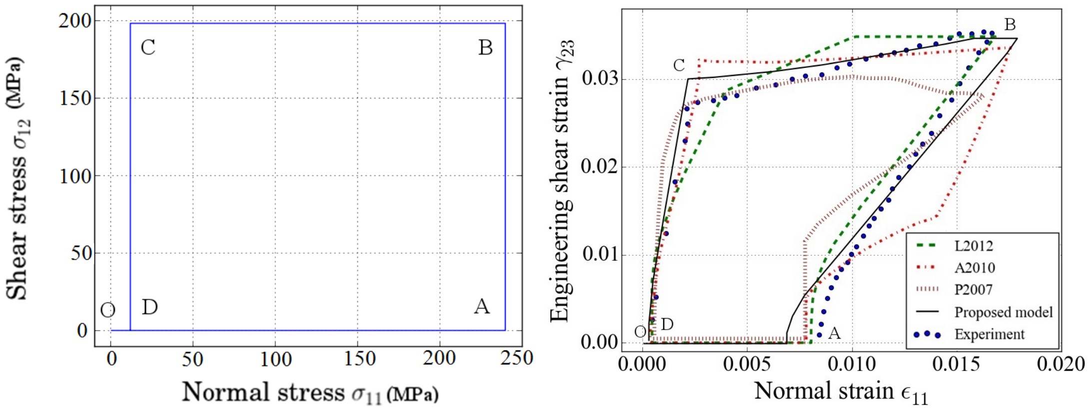

(a) Chargement en contrôle des contraintes sur un tube AMF

(b) Réponse de matériau en déformations normale et en cisaillement

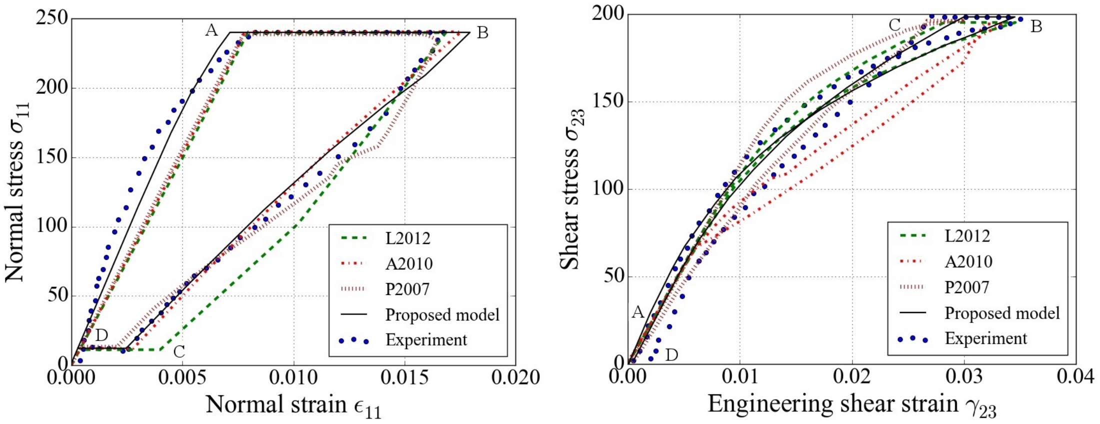

(c) Diagramme contraintes-déformations normales

(d) Diagramme contraintes-déformations de cisaillement

Figure 5.2 – Résultats expérimentaux (points) et réponse du modèle (ligne continue) pour un tube aux parois minces en AMF d'après [Sittner et al., 1995]. Comparaison avec les modèles de [Lagoudas et al., 2012] (L2012), [Arghavani et al., 2010] (A2010), [Panico and Brinson, 2007] (P2007).

5.3.3 Chargement thermomécanique complexe

C'est la première fois que cet essai a été simulé. La comparaison entre la simulation et les résultats expérimentaux s'affiche à la Figure 5.3.

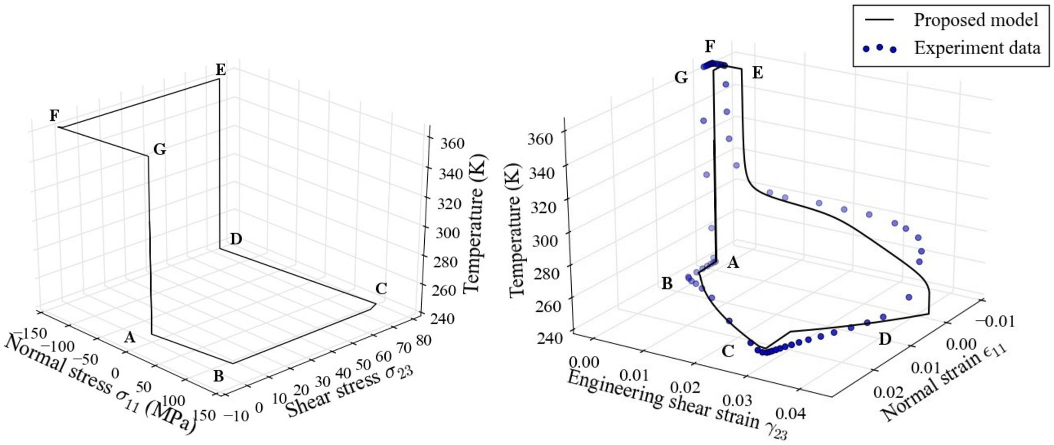

(a) Trajet du chargement suivi en contrôle des contraintes et température

(b) Comportement en température, déformations normales et de cisaillement

Figure 5.3 – Chargement en traction-compression combinées avec torsion en variation de températures, d'après [Grabe and Bruhns, 2009]. Résultats expérimentaux en points, réponse numérique du modèle en ligne continue.

5.4 Analyse du couplage thermomécanique

Du travail intéressant concernant l'effet de vitesse de déformation causé par le couplage thermomécanique en chargement 1-D a été publié par Maynadier [2012] et dans le cadre multi-échelles par Heintze and Seelecke [2008]. Dans les scénarios des chargements d'AMF examinés jusqu'ici, la température du matériau était constamment contrôlée. Cette restriction sévère des des conditions limites thermiques ne permet pas de prendre en compte le fort couplage thermomécanique inclus dans le nouveau modèle. Deux cas d'essais simples sont analysés dans cette section afin de mettre en évidence l'effet des sources de chaleur résultant du travail mécanique.

5.4.1 Conditions adiabatiques

Le chargement adiabatique interdit la fuite de la chaleur générée et cause une variation grave de la température. La différence avec le comportement dans un cas isotherme s'affiche sur la Figure 5.4.

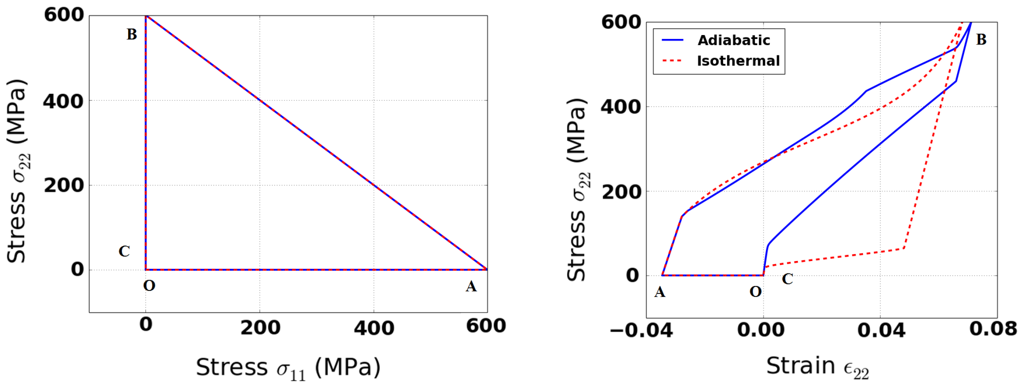

(a) Trajet de chargement non-proportionnel simulé, piloté en contraintes normales

(b) Réponse en conditions isothermes et adiabatiques

FIGURE 5.4 – Chargement non-proportionnel (a) et diagrammes contrainte-déformation dans la direction normale 2-2 (b) pour un AMF NiTi en conditions isothermes et adiabatiques.

5.4.2 Analyse par Éléments Finis de l'effet de la vitesse de déformation sur une structure en NiTi

Une plaque trouée en NiTi est considérée de subir une sollicitation mécanique sous conditions ressemblant la convection avec l'air ambient rencontrée dans un vrai essai. La simulation est exécutée dans le logiciel Abaqus, en implémentant le logiciel UMAT produit à la base du nouveau modèle. La convection permet l'échange d'une partie de la chaleur générée avec l'environnement de la structure. La quantité de la chaleur échangée est relative avec le temps disponible et, par conséquent, la vitesse du chargement.

La charge appliquée induit la transformation et la réorientation sur la masse du NiTi, afin d'employer toute capacité du modèle. La surface en haut est tirée sur l'axe Y dans la première étape (Step 1) du chargement et ensuite sur l'axe X (Step 2). Le contrôle des déplacements est appliqué. Finalement, les deux déplacements sont entièrement supprimés (Step 3). Deux vitesses de déplacement sont appliquées dans deux analyses différentes : d'abord, la vitesse relative $\dfrac{\Delta l/l}{\Delta t}$ est réglée à $1.5 \cdot 10^{-5} sec^{-1}$ est considérée de correspondre à un chargement "statique". Ensuite, la vitesse $1.5 \cdot 10^{-3} sec^{-1}$ vise à induire un changement de température qui puisse activement affecter le comportement mécanique. Les champs de la fraction volumique ξ et de la température pour certains enstantanés représentatifs s'affichent sur la Figure 5.5

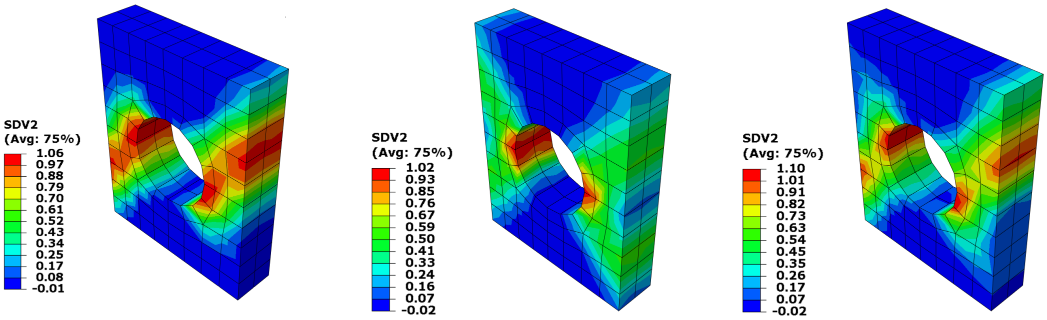

(a) Vitesse statique, ξ à Step 2 (b) Vitesse 100x, ξ à Step 1 (c) Vitess 100x, ξ à Step 2

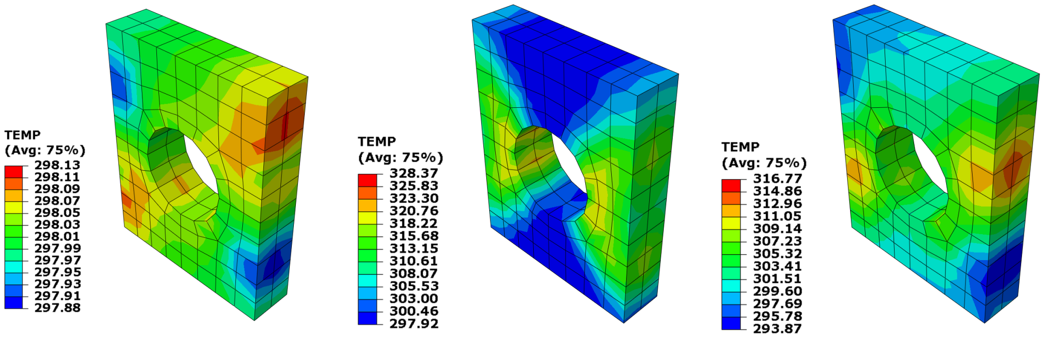

(d) Vitesse 100x, température à Step 2 (e) Vitesse 100x, température à Step 1 (f) Vitesse 100x, température à Step 2

FIGURE 5.5 – Champs de la fraction volumique de martensite (ξ) sur la première ligne (a-c) et de la température sur la deuxième (d-f) correspondant au même moment dans l'histoire de la sollicitation pour les deux vitesses, à la fin du Step 1 et du Step 2.

5.5 Conclusion du chapitre

Afin de mettre en place l'évaluation pratique du nouveau modèle phénoménologique décrit au Chapitre 4, son implémentation numérique a été éprouvée. Dans le cadre général d'un modèle prenant en compte tout nombre de mécanismes inélastiques, les algorithmes numériques utilisés pour la résolution du système sont présentés. La contribution de la technique Fischer-Burmeister est surtout démontrée. Au même temps, les modules tangents thermomécaniques sont aussi calculés avec une méthode adaptative.

Le nouveau modèle AMF a été évalué numériquement en deux façons principales : dans un premier temps, les paramètres du modèle ont été déterminées pour des bases de données expérimentales. Elles incluent des cas de chargements simples pour des fils en NiTi, un chargement non-proportionnel pour un tube en CuAlZnMn et un chargement particulièrement complexe pour un tube en NiTi.

L'accord satisfaisant entre les réponses numériques les courbes expérimentales met en évidence l'effet de la réorientation. Deuxièmement, le fort couplage thermomécanique est examiné en réalisant des simulations en scénarios avec des conditions limites thermiques appropriées. L'analyse par Éléments Finis d'une structure en NiTi dans un environnement d'air ambient (puit thermique) simulé permet d'étudier et de cerner l'effet de la vitesse de déformation pour la sollicitation non-proportionnelle. Elle souligne aussi la puissance du modèle et ses capacités prédictives à capturer de tels effets dans un cadre de couplage thermomécanique fort.

5.6 Bibliographie

J. Arghavani, F. Auricchio, R. Naghdabadi, A. Reali, and S. Sohrabpour. A 3-D phenomenological constitutive model for shape memory alloys under multiaxial loadings. *International Journal of Plasticity*, 26(7):976–991, jul 2010. ISSN 07496419. doi: 10.1016/j.ijplas.2009.12.003. 56

F. Auricchio, E. Bonetti, G. Scalet, and F. Ubertini. Theoretical and numerical modeling of shape memory alloys accounting for multiple phase transformations and martensite reorientation. *International Journal of Plasticity*, 59:30–54, aug 2014. ISSN 07496419. doi: 10.1016/j.ijplas.2014.03.008. 53

D. Chatziathanasiou, Y. Chemisky, G. Chatzigeorgiou, and F. Meraghni. Modeling of coupled phase transformation and reorientation in shape memory alloys under non-proportional thermomechanical loading. *International Journal of Plasticity*, (IN PRESS), 2016. doi: 10.1016/j.ijplas.2016.03.005. 51

Y. Chemisky, F. Meraghni, N. Bourgeois, S. Cornell, R. Echchorfi, and E. Patoor. Analysis of the deformation paths and thermomechanical parameter identification of a shape memory alloy using digital image correlation over heterogeneous tests. *International Journal of Mechanical Sciences*, 96-97:13–24, jun 2015. ISSN 00207403. doi: 10.1016/j.ijmecsci.2015.03.007. 54

A. Fischer. A special newton-type optimization method. *Optimization*, 24(3-4):269–284, jan 1992. ISSN 0233-1934. doi: 10.1080/02331939208843795. 53

C. Grabe and O. Bruhns. Path dependence and multiaxial behavior of a polycrystalline NiTi alloy within the pseudoelastic and pseudoplastic temperature regimes. *International Journal of Plasticity*, 25(3):513–545, mar 2009. ISSN 07496419. doi: 10.1016/j.ijplas.2008.03.002. 54, 57

D. J. Hartl and D. Lagoudas. Constitutive modeling and structural analysis considering simultaneous phase transformation and plastic yield in shape memory alloys. *Smart Materials and Structures*, 18(10):104017, oct 2009. ISSN 0964-1726. doi: 10.1088/0964-1726/18/10/104017. 53

O. Heintze and S. Seelecke. A coupled thermomechanical model for shape memory alloys—From single crystal to polycrystal. *Materials Science and Engineering: A*, 481-482:389–394, may 2008. ISSN 09215093. doi: 10.1016/j.msea.2007.08.028. 57

B. Kiefer, T. Bartel, and A. Menzel. Implementation of numerical integration schemes for the simulation of magnetic SMA constitutive response. *Smart Materials and Structures*, 21(9):094007, sep 2012. ISSN 0964-1726. doi: 10.1088/0964-1726/21/9/094007. 53

D. Lagoudas, D. Hartl, Y. Chemisky, L. Machado, and P. Popov. Constitutive model for the numerical analysis of phase transformation in polycrystalline shape memory alloys. *International Journal of Plasticity*, 32-33(null):155–183, may 2012. ISSN 07496419. doi: 10.1016/j.ijplas.2011.10.009. 56

A. Maynadier. *Couplages thermomécaniques dans les alliages à mémoire de forme : mesure de champs cinématique et thermique et modélisation multiéchelle*. PhD thesis, nov 2012. 57

F. Meraghni, Y. Chemisky, B. Piotrowski, R. Echchorfi, N. Bourgeois, and E. Patoor. Parameter identification of a thermodynamic model for superelastic shape memory alloys using analytical calculation of the sensitivity matrix. *European Journal of Mechanics - A/Solids*, 45:226–237, may 2014. ISSN 09977538. doi: 10.1016/j.euromechsol.2013.12.010. 54

M. Panico and L. Brinson. A three-dimensional phenomenological model for martensite reorientation in shape memory alloys. *Journal of the Mechanics and Physics of Solids*, 55(11): 2491–2511, nov 2007. ISSN 00225096. doi: 10.1016/j.jmps.2007.03.010. 56

P. Sittner, Y. Hara, and M. Tokuda. Experimental study on the thermoelastic martensitic transformation in shape memory alloy polycrystal induced by combined external forces. *Metallurgical and Materials Transactions A*, 26(11):2923–2935, nov 1995. ISSN 1073-5623. doi: 10.1007/BF02669649. 54, 56

P. Sittner, L. Heller, J. Pilch, P. Sedlak, M. Frost, Y. Chemisky, A. Duval, B. Piotrowski, T. Ben Zineb, E. Patoor, F. Auricchio, S. Morganti, A. Reali, G. Rio, D. Favier, Y. Liu, E. Gibeau, C. Lexcellent, L. Boubakar, D. Hartl, S. Oehler, D. Lagoudas, and J. V. Humbeeck. Roundrobin SMA modeling. In *ESOMAT 2009 - 8th European Symposium on Martensitic Transformations*, page 08001, Les Ulis, France, sep 2009. EDP Sciences. ISBN 978-2-7598-0480-1. doi: 10.1051/esomat/200908001. 54, 55

Conclusion et perspectives

Les travaux présentés dans cette thèse constituent une avancée en direction du développement de la modélisation thermodynamique macroscopique des Alliages à Mémoire de Forme. Ces développements sont motivés par la nécessité de disposer d'un outil numérique fiable en vue de la prédiction du comportement en trois dimensions de ces matériaux adaptatifs sous chargement thermomécanique. Un tel outil prédictif contribue au dimensionnement des produits utilisant les AMF et à la conception de nouveaux produits. Les points abordés au cours de ce travail concernent notamment l'étude expérimentale et la modélisation théorique des particularités inhérentes aux différences entre les comportements uniaxial et multiaxial.

Le premier challenge de la thèse était de constituer une base de données expérimentales dédiée à l'étude de deux aspects des structures en AMF sollicitées en conditions multiaxiales : l'anisotropie et le cyclage. Pour que la base de données soit unifiée, un seul matériau a été utilisé pour toutes les expériences. Tous les échantillons provenant d'un même lot de NiTi ont subi un traitement thermique strictement identique. Provenant d'une tôle laminée, les éprouvettes manifestent une forte dépendance à la direction de leur sollicitation à cause des effets de texture. Au-delà de la confirmation de l'anisotropie connue pour le plateau des contraintes et la déformation de transformation, les essais réalisés soulignent aussi une autre différence entre les deux directions de chargement : celle des évolutions du comportement liées au cyclage. En particulier, le développement des déformations résiduelles et la réduction de la contrainte de début de transformation sont clairement différentes entre les deux directions de chargement testées. Les essais sur éprouvettes biaxiales chargées en conditions non-proportionnelles confirment également la dépendance du comportement cyclique à la direction de chargement.

Le travail expérimental a été l'objet du deuxième des cinq chapitres de ce manuscrit. Dans sa première partie, les expériences effectuées sur des éprouvettes haltères découpés dans les directions parallèle et perpendiculaire à la direction du laminage sont présentées. Ces éprouvettes ont subi un chargement uniaxial cyclique à trois températures constantes, respectivement à 30, 40 et 50°C. Même dans ce cas, le trajet suivi est assez complexe, atteignant différents niveaux de déformation maximale. Les résultats expérimentaux ont permis de mettre en évidence trois facteurs affectant le comportement cyclique du NiTi : le nombre de cycles, les contraintes développées et en même temps l'anisotropie. Dans la deuxième partie du chapitre, une sollicitation répétitive a été appliquée sur des éprouvettes cruciformes. Deux dispositifs expérimentaux avancés ont été exploités pour réaliser ces expériences originales : une machine d'essais biaxiaux à quatre vérins contrôlés indépendamment et un dispositif de mesure de déformations par corrélation d'images numériques. Ici, les résultats obtenus démontrent, dans un cas biaxial, le fort impact de l'anisotropie sur le comportement en sollicitation répétée.

Prenant motivation sur ces expériences, le premier objectif posé pour les efforts en modélisation était d'établir une nouvelle loi de comportement saisissant l'anisotropie en transformation de phase. Cette loi devait cependant respecter le cadre général de la thermodynamique, afin d'assurer sa robustesse. Dans ce but, une revue bibliographique, qui se focalise particulièrement sur les aspects techniques des modèles thermodynamiques importants, a été réalisée au premier chapitre de ce manuscrit. Les modèles de Lagoudas et Brinson sont reconnus pour leur robustesse et constituent un point de référence pour pratiquement tous les travaux théoriques. Le regard critique porté sur ces deux modèles permet d'envisager certaines voies d'amélioration de leur capacité à saisir le comportement complexe des AMF sous sollicitation thermomécanique multiaxiale.

Le troisième chapitre concerne le développement de la loi prenant en compte l'anisotropie de la transformation directe. Un nouveau critère, exploitant une transition entre l'espace des contraintes réelles et un espace des contraintes fictives, est présenté. Cette transition permet une expression simple d'une surface d'écoulement prédisant à la fois la dissymétrie entre traction et compression et l'anisotropie observées dans les AMF. Une contribution supplémentaire de ce chapitre est l'introduction d'une nouvelle loi d'évolution anisotrope des déformations de transformation. Elle considère la fraction volumique de martensite en tant que variable interne de base, comme c'est le cas pour la plupart des modèles existants. La nécessité de mesurer la fraction martensitique a entraîné l'utilisation d'un modèle micromécanique comme moyen d'évaluer le nouveau critère. Le modèle auto-cohérent de Patoor, développé au sein de l'équipe, a été employé pour simuler des trajets de chargement proportionnels sur des échantillons texturés. La calibration des paramètres de la nouvelle loi confirme son adaptabilité et surtout sa capacité à saisir la forte anisotropie en déformations engendrée par les conditions de fabrication.

Alors que la transformation de phase domine la réponse thermomécanique des AMF, c'est la réorientation des variantes de martensite qui ajoute un degré de complexité supplémentaire aux sollicitations multiaxiales non-proportionnelles. À ce propos, le quatrième chapitre est dédié à la formulation d'un modèle pour les AMF visant à prédire une réponse du matériau adaptée à tous les trajets de chargement thermomécanique possibles. Les mécanismes de réorientation et de transformations directe et inverse sont décrits en termes de cinétique et de thermodynamique, afin de formuler un système mécanique prenant en compte leur activation simultanée. La nouvelle loi anisotrope est bien intégrée. La réorientation est considérée comme un mécanisme d'écrouissage cinématique, introduisant un backstress de type plastique. Le couplage thermomécanique résultant de la première loi de la thermodynamique est étudié et intégré dans le schéma global. Le nouveau modèle produit les même prédictions que celui de Lagoudas pour des cas de chargement simples n'induisant pas la réorientation. Le modèle développé permet de détecter l'absence d'effet de réorientation sur le comportement global dans les cas de chargements monoaxiaux présentés brièvement à la fin du Chapitre 4.

La valeur ajoutée du nouveau modèle est évaluée dans le cinquième et dernier chapitre. Un nouvel outil numérique sous forme d'une UMAT a été codé pour exécuter des simulations de structures en AMF. Tout d'abord, les méthodes numériques nécessaires pour cet outil sont présentées. La prise en compte des mécanismes multiples de déformations inélastiques peut en particulier avoir un fort intérêt pour la modélisation de différents matériaux. Ensuite, des bases de données expérimentales appropriées, parues dans la littérature, ont été exploitées afin d'examiner la capacité du modèle à saisir le comportement en conditions complexes. Des trajets thermomécaniques non-proportionnels, mettant en évidence la réorientation, ont bien été simulés avec succès. Finalement, le modèle a été implémenté dans le logiciel de simulation par Éléments Finis Abaqus. Cette implémentation a souligné la puissance du modèle à modéliser et capturer le fort couplage thermomécanique en conditions multiaxiales à travers l'examen de l'effet de la vitesse de déformation sur une structure en NiTi. Des conditions thermiques, ressemblant à celles des essais réels, ont illustré l'impact de la vitesse de chargement sur la variation de température et, par conséquent, sur la réponse du matériau.

Les résultats expérimentaux obtenus, ainsi que les méthodes développées pour la création de cet outil de simulation, génèrent de nouvelles problématiques pour des développements supplémentaires concernant l'étude du comportement des AMF. Ces problématiques sont associées à trois axes principaux : la caractérisation expérimentale, l'implémentation efficace du modèle et son application à des domaines de recherche plus étendus.

Concrètement, sur l'axe expérimental, l'implémentation de la technique de corrélation d'images pour mesurer les champs de déformation est jugée très intéressante. Même dans le cas des essais uniaxiaux, l'identification des zones de déformations résiduelles pourrait apporter de nouvelles pistes pour la compréhension de la dépendance du comportement cyclique à la direction de chargement.

Dans le cas des essais biaxiaux, cette technique est pratiquement indispensable pour évaluer les déformations résiduelles lors des chargements répétés sur des structures adaptatives en AMF.

Il serait aussi très intéressant de répéter les expériences réalisées ici pour d'autres compositions de NiTi ou pour d'autres traitements thermiques. Ceci permettrait l'examen de l'effet du cyclage et de l'anisotropie sur une base de données plus étendue. Finalement, ces développements pourraient être utilisés comme un outil d'optimisation de la composition du NiTi par rapport à la tenue en service.

En ce qui concerne l'implémentation du modèle, l'obstacle le plus important rencontré pendant ce travail fut le nombre requis de paramètres matériau. C'est un problème récurrent dans l'étude de l'anisotropie, les nouvelles constantes sont plus nombreuses que ce qui serait souhaitable. Pour des matériaux aussi complexes que les AMF, dont le comportement requiert déjà une modélisation avec beaucoup de paramètres indépendants dans le cas isotrope, ceci s'avère un point dur. La thèse d'Echchorfi a fourni un outil puissant pour l'identification des paramètres des AMF. Il est cependant jugé nécessaire de développer une méthode d'identification supplémentaire à cet outil, afin de rendre les simulations plus fiables.

Il est aussi important, pour enrichir le travail réalisé pendant cette thèse, d'exploiter les résultats expérimentaux en combinaison avec le nouveau modèle mis à la disposition du LEM3. Le cadre de mécanismes multiples développé permet une insertion facile de la plasticité dans le schéma global comme processus supplémentaire. Les déformations résiduelles observées dans les expériences uniaxiales et biaxiales pourraient ainsi être capturées. Cette intégration produirait aussi un modèle encore plus complet.

Les interactions avec les collègues pendant la réalisation de cette thèse ont mis en évidence des applications potentielles supplémentaires du nouveau modèle. D'abord, le nouveau critère de transformation de phase a déjà été utilisé dans une étude concernant l'initiation de la transformation autour d'une fissure dans un milieu anisotrope. Ce travail intéressant a été réalisé par un étudiant du Professeur Patoor, Guillaume Mohara. En outre, la réorientation couplée avec la transformation ouvre de nouveaux horizons dans le domaine de la mécanique de la rupture. Les fortes contraintes hétérogènes développées à proximité d'une fissure peuvent entraîner la réorientation, avec des effets intéressants.

De plus, le fort couplage thermomécanique intégré pour les sollicitations généralisées mérite une utilisation attentive pour examiner, sur des structures 3D en AMF, l'effet de vitesse causé par des échanges thermiques avec l'environnement. Bien que le modèle soit indépendant du taux de déformations, il réussit à expliquer la variation de la réponse du matériau par rapport à la vitesse de chargement. Il serait également très intéressant de réaliser des expériences multiaxiales avec des conditions aux limites thermiques bien contrôlées, afin de comparer la réponse du modèle avec les résultats expérimentaux.

Finalement, le domaine de recherche lié aux AMF qui porte le plus fort intérêt pour le monde industriel est l'analyse de la fatigue. Elle constitue un facteur limitant l'utilisation intensive du NiTi, car son comportement à long terme n'est pas encore complètement fiable. Il serait important d'intégrer un modèle prédisant la durabilité fonctionnelle (fatigue) dans le cadre existant. Les critères de fatigue du type Crossland ou Dang-Van, peuvent y être appliqués. Du travail pertinent sur les alliages légers d'aluminium a déjà été réalisé au sein de l'équipe. L'association de la fatigue à l'état de contraintes multiaxial et à l'effet des déformations résiduelles dans les AMF serait rendue possible.

III

Appendices

Appendix A : Model parameters of the SMA constitutive law

In the scope of this appendix, several aspects of the SMA models presented in Chapter 1 are reviewed. The 1D calibration of the model, leading to the determination of important material parameters, is mainly discussed. The material parameters of the new proposed model in Chapter 4 are also connected wih the parameters from the Lagoudas model.

1D calibration of the Lagoudas model

The main reasoning behind the 1D reduction and calibration in the Lagoudas model is retrieving the initial value of the Gibbs free energy potential at a full loading-unloading cycle. The material is thought to start from austenitic phase, at $\xi = 0$, and reach the fully martensitic phase, at $\xi = 1$, due to thermomechanical loading, where its stress state is always limited to a single component of the stress tensor. Then, the stress tensor is reduced to an equivalent scalar σ and the strain tensor to an equivalent ε. Subsequently, the strain partitions are equivalent to their proper scalars :

$$\varepsilon^{el} = S\sigma \tag{A.1}$$

$$\varepsilon^{th} = \alpha(T - T_0) \tag{A.2}$$

and

$$\varepsilon^{t} = \varepsilon^{el} - \varepsilon^{el} - \varepsilon^{el} \tag{A.3}$$

where the elastic compliance and the thermal expansion coefficient are represented by their equivalent scalars as well.

The return of the Gibbs potential to its inital state after a full cycle is assured when the hardening energy g^t takes back its initial value. Given the form of its evolution :

$$\dot{g}^t = \begin{cases} \dot{\xi} f^t_{fwd} \text{ for } \dot{\xi} > 0 \\ \dot{\xi} f^t_{rev} \text{ for } \dot{\xi} < 0 \end{cases} \tag{A.4}$$

satisfying the following relation assures the balance of the Gibbs potential upon return to martensite :

$$\int\limits_0^1 f^t_{fwd} d\xi + \int\limits_1^0 f^t_{rev} d\xi = 0 \tag{A.5}$$

The hardening functions f^t take the form :

$$\begin{aligned} f^t_{fwd} &= \tfrac{1}{2} a_1 (1 + \xi^{n_1} - (1-\xi)^{n_2}) + a_3 \\ f^t_{rev} &= \tfrac{1}{2} a_2 (1 + \xi^{n_3} - (1-\xi)^{n_4}) - a_3 \end{aligned} \tag{A.6}$$

From (A.1) :

$$\sigma = E(\xi)[\varepsilon - \alpha(T - T_0) - \varepsilon^t] \tag{A.7}$$

in which the current elastic modulus E can be found as :

$$E(\xi) = \left[\frac{1}{E^A} + \xi\left(\frac{1}{E^M} - \frac{1}{E^A}\right)\right]^{-1} \tag{A.8}$$

At the same time, the evolution of transformation strains is reduced to :

$$\dot{\varepsilon}^t = \begin{cases} \dot{\xi} H^{cur} sgn(\sigma) \text{ for } \dot{\xi} > 0 \\ \dot{\xi} \dfrac{\varepsilon^{t-r}}{\xi^r} \quad \text{for } \dot{\xi} < 0 \end{cases} \tag{A.9}$$

The function $sgn(\sigma)$ returns $\dfrac{|\sigma|}{\sigma}$ or 0 if $\sigma = 0$.

The boundary for forward transformation is written :

$$\Phi^t_{fwd} = \pi^t_{fwd} - Y^t_{fwd} \leq 0 \tag{A.10}$$

where

$$Y^t_{fwd} = Y^t_0 + D\sigma : \mathbf{\Lambda^t_{fwd}} \tag{A.11}$$

For reverse transformation :

$$\Phi^t_{rev} = \pi^t_{rev} - Y^t_{rev} \leq 0 \tag{A.12}$$

with

$$\Phi^t_{rev} = Y^t_0 + D\sigma : \mathbf{\Lambda^t_{rev}} \tag{A.13}$$

D is dimensionless variable taking into account the dependence of the yield functions to temperature. The slope of the transition zones, as well as the values for transformation temperatures on the phase diagram are eventually correlated with D.

It necessary to expand the yield functions in order to solve analytically the 1D problem. Recalling the form of the General Thermodynamic Forces, and neglecting the differences ΔC and $\Delta\alpha$ this leads to :

$$\Phi^t_{fwd}(\sigma, T, \xi) = (1-D)\left|\sigma\right| H^{cur} + \frac{1}{2}\left(\frac{1}{E^M} - \frac{1}{E^A}\right)\sigma^2 + \Delta s_0 T - \rho\Delta u_0 - f^t_{fwd} - Y^t_0 \tag{A.14}$$

and

$$\Phi^t_{rev}(\sigma, T, \xi) = -(1+D)\sigma\frac{\varepsilon^{t-r}}{\xi^r} - \frac{1}{2}\left(\frac{1}{E^M} - \frac{1}{E^A}\right)\sigma^2 - \Delta s_0 T + \rho\Delta u_0 + f^t_{fwd} - Y^t_0 \tag{A.15}$$

Two boundary conditions can be established for each direction of transformation in a thermal loading under zero stress, knowing that the yield functions take zero values to correspond to activation :

1. $\Phi^t_{fwd}(0, M_s, 0) = 0$ at the start of forward,
2. $\Phi^t_{fwd}(0, M_f, 1) = 0$ at the end,
3. $\Phi^t_{rev}(0, A_s, 1) = 0$ at the start of reverse transformation
4. $\Phi^t_{rev}(0, A_f, 0) = 0$ at the end.

Taking also into account the relation (A.5), a set of 5 independent equations is created, resulting to associating the model parameters Δu_0, Δs_0, Y^t_0 and the characteristic transition temperatures.

$$\Delta u_0 = \frac{\Delta s_0}{2}(M_s + A_f) \tag{A.16}$$

and

$$Y_0^t = \frac{\Delta s_0}{2}(M_s - A_f) - a_3 \tag{A.17}$$

Here, a_3 is a variable resulting from algebraic manipulations :

$$a_3 = -\frac{a_1}{4}\left(1 + \frac{1}{n_1+1} - \frac{1}{n_2+1}\right) + \frac{a_2}{4}\left(1 + \frac{1}{n_3+1} - \frac{1}{n_4+1}\right) \tag{A.18}$$

with

$$a_1 = \Delta s_0(M_f - M_s), \quad a_2 = \Delta s_0(A_s - A_f) \tag{A.19}$$

To move forward, another type of 1-D material state is considered : at stress $\sigma = \sigma^*$ and $\xi = 0$, the material is considered to only slightly start transforming. This leads to two conclusions : Firstly, the state variable coordinates are located on the M_s curve. Secondly, we can accept that $d\xi = 0$. This hypothesis allows to reduce the general rule

$$d\Phi^t = \partial_\sigma \Phi^t d\sigma + \partial_T \Phi^t dT + \partial_\xi \Phi^t d\xi = 0 \tag{A.20}$$

to only :

$$\frac{d\sigma}{dT} = \frac{-\partial_T \Phi^t}{\partial_\sigma \Phi^t} \tag{A.21}$$

Knowing that at the start of forward transformation, the derivative $\left.\frac{d\sigma}{dT}\right|_{\sigma=\sigma^*, \dot{\xi}>0}$ corresponds to the slope C^M of the M_s curve, it is deduced that :

$$C^M = \left.\frac{-\Delta s_0}{H^{cur} + \sigma\partial_\sigma H^{cur} + \sigma\left(\frac{1}{E^M} - \frac{1}{E^A}\right) - \partial_\sigma Y^t_{fwd}}\right|_{\sigma=\sigma^*} \tag{A.22}$$

Similarly, at stress $\sigma = \sigma^*$ and $\xi = 1$, when the material enters reverse transformation :

$$C^A = \left.\frac{-\Delta s_0}{\varepsilon^{t-r} + \sigma\left(\frac{1}{E^M} - \frac{1}{E^A}\right) + \partial_\sigma Y^t_{rev}}\right|_{\sigma=\sigma^*} \tag{A.23}$$

Recognizing that $\varepsilon^{t-r} = H^{cur}$ for a full loading-unloading cycle and evaluating the derivatives for the transformation thresholds, it is obtained :

$$\Delta s_0 = \left. \frac{-2(C^M C^A)\left[H^{cur} + \sigma\partial_\sigma H^{cur} + \sigma\left(\frac{1}{E^M} - \frac{1}{E^A}\right)\right]}{C^M + C^A} \right|_{\sigma=\sigma^*} \tag{A.24}$$

and

$$D = \left. \frac{(C^M - C^A)\left[H^{cur} + \sigma\partial_\sigma H^{cur} + \sigma\left(\frac{1}{E^M} - \frac{1}{E^A}\right)\right]}{(C^M + C^A)\left[H^{cur} + \sigma\partial_\sigma H^{cur}\right]} \right|_{\sigma=\sigma^*} \tag{A.25}$$

Now the key parameters of the phase diagram have been integrated in the mathematical modeling. Conclusively, the transitiion temperatures M_s, M_f, A_s, A_f and the C^M, C^A slopes intervene in the Δu_0 parameter of the thermodynamic forces π^t and in the Y^t energy thresholds.

Connection with the new model

The hardening functions f^t are conserved intact in the formulation of the new model. Specifically :

$$-\frac{\partial H}{\partial \xi} = \begin{cases} H^F = \frac{1}{2}a_1(1 + \xi^{n_1} - (1-\xi)^{n_2}) + a_3 \\ H^R = \frac{1}{2}a_2(1 + \xi^{n_3} - (1-\xi)^{n_4}) - a_3 \end{cases} \tag{A.26}$$

These are important variables for the general thermodynamic forces of ξ^F and ξ^R :

$$\begin{aligned} A_{\xi^F} =& -\tilde{U}_o + \tilde{s}T - \tilde{C}_v\left[\Delta T - T\ln\left(\frac{T}{T_o}\right)\right] + \\ & \frac{1}{2}\boldsymbol{\sigma} : \tilde{\boldsymbol{S}} : \boldsymbol{\sigma} + \boldsymbol{\sigma} : \tilde{\boldsymbol{\alpha}}\Delta T - \frac{\partial \lambda^{re}}{\partial \xi}\boldsymbol{X} : \boldsymbol{v}^{re} - H^F \end{aligned} \tag{A.27}$$

and

$$\begin{aligned}A_{\xi^R} =&\tilde{U}_o - \tilde{s}T + \tilde{C}_v \left[\Delta T - T \ln\left(\frac{T}{T_o}\right)\right] - \frac{1}{2}\boldsymbol{\sigma} : \tilde{\boldsymbol{S}} : \boldsymbol{\sigma} - \\ &\boldsymbol{\sigma} : \tilde{\boldsymbol{\alpha}}\Delta T + \frac{\partial \lambda^{re}}{\partial \xi}\boldsymbol{X} : \boldsymbol{v}^{\boldsymbol{re}} + H^R\end{aligned} \tag{A.28}$$

The thresholds Y^F and Y^R appearing in the yield functions :

$$\Phi^F = A_{\xi^F} + \hat{\Phi}^F(\boldsymbol{A}_{\boldsymbol{\varepsilon^F}}) - Y^F \tag{A.29}$$

and

$$\Phi^R = A_{\xi^R} + \hat{\Phi}^R(\boldsymbol{A}_{\boldsymbol{\varepsilon^R}}) - Y^R \tag{A.30}$$

are also expressed in a form similar to the model by Lagoudas, in order to take into account the values of the slopes C^M and C^A with the help of the variable D :

$$Y^F = Y_o^F + D\boldsymbol{\sigma} : \boldsymbol{\Lambda}_{\boldsymbol{\varepsilon}}^{\boldsymbol{F}} - \frac{\partial \lambda^{re}}{\partial \xi}\boldsymbol{X} : \boldsymbol{v}^{\boldsymbol{re}} \tag{A.31}$$

and

$$Y^R = Y_o^R + D\boldsymbol{\sigma} : \bar{\boldsymbol{\varepsilon}}^{\boldsymbol{T}} - \frac{\partial \lambda^{re}}{\partial \xi}\boldsymbol{X} : \boldsymbol{v}^{\boldsymbol{re}} \tag{A.32}$$

The value of the constants Y_o^F and Y_o^R could vary, but it is chosen to correspond to Y_0^t for simplicity. The transformation temperatures and the slopes of the respective transition curves take their effect on the calibration of the following variables, as discussed in the previous section :

$$\begin{aligned}\tilde{U}_o &= \Delta u \\ \tilde{s} &= \Delta s \\ D & \\ Y_o^F &= Y_o^R = Y_0^t\end{aligned}$$

Now the full form for the yield function for forward transformation is :

$$
\begin{aligned}
\Phi^F = & - \tilde{U}_o + \tilde{s}T - \tilde{C}_v \left[\Delta T - T \ln\left(\frac{T}{T_o}\right)\right] + \frac{1}{2}\boldsymbol{\sigma} : \tilde{\boldsymbol{S}} : \boldsymbol{\sigma} + \boldsymbol{\sigma} : \tilde{\boldsymbol{\alpha}}\Delta T \\
& - H^F + \sqrt{J_2(\boldsymbol{\sigma})}\left[1 + b\frac{J_3(\boldsymbol{\sigma})}{J_2^{3/2}(\boldsymbol{\sigma})}\right]^{\frac{1}{n}} - D\boldsymbol{\sigma} : \boldsymbol{\Lambda}^{\boldsymbol{F}}_{\boldsymbol{\varepsilon}} - Y^F_o - \lambda^F \leq 0
\end{aligned}
\tag{A.33}
$$

For reverse transformation :

$$
\begin{aligned}
\Phi^F = & \tilde{U}_o - \tilde{s}T + \tilde{C}_v \left[\Delta T - T \ln\left(\frac{T}{T_o}\right)\right] - \frac{1}{2}\boldsymbol{\sigma} : \tilde{\boldsymbol{S}} : \boldsymbol{\sigma} - \boldsymbol{\sigma} : \tilde{\boldsymbol{\alpha}}\Delta T \\
& + H^R - (1 + D)\boldsymbol{\sigma} : \bar{\boldsymbol{\varepsilon}}^{\boldsymbol{T}} - Y^R_o - \lambda^R \leq 0
\end{aligned}
\tag{A.34}
$$

λ limit functions

The variables λ^F, λ^R and λ^{re} aim in expressing the saturation of (forward and reverse) transformation and reorientation respectively. They are based on the function $\lambda(r)$ which takes the form :

$$
\lambda(r) = \begin{cases} P_o r(1-r)^{-\kappa} & \text{for } 0 \leq r < c \\ P_o[(1-c)^{-\kappa} + \kappa c(1-c)^{-\kappa-1}](x-c) + c(1-c)^{-\kappa} + \mathrm{a}(r-c)^2 & \\ \qquad\qquad\qquad\qquad\qquad\qquad\qquad\qquad \text{for } c < r < 1 & \end{cases}
\tag{A.35}
$$

It is a function defined for a scalar argument $r \in [0, 1)$ and returns positive values. It needs four positive independent parameters P_o, κ, c, a as additional input. When appropriate values are chosen, the function λ returns values which are positive, but practically zero relatively to the size of the yield functions Φ when $r < 1$. However, when $r \approx 1$, λ executes a continuous jump to significant values, forcing to Φ to approach 0.

In the case of forward transformation, $r = \xi$. When $\xi \approx 1$, the function Φ^F takes the value 0 for an insignificant size of increment $d\xi^F$. Thus, forward transformation is activated, but all the associated internal variables remain stable. Likewise, for reverse transformation, $r = 1 - \xi$, limiting the increment $d\xi^R$ when $\xi \approx 0$.

For reorientation, $r = \dfrac{|\boldsymbol{X}|}{\xi X_{max}}$. Here, dp^{re} takes practically 0 value and the variables evolving in association with reorientation stop evolving, even if this mechanism is technically considered activated.

Appendix B : Additional experimental data

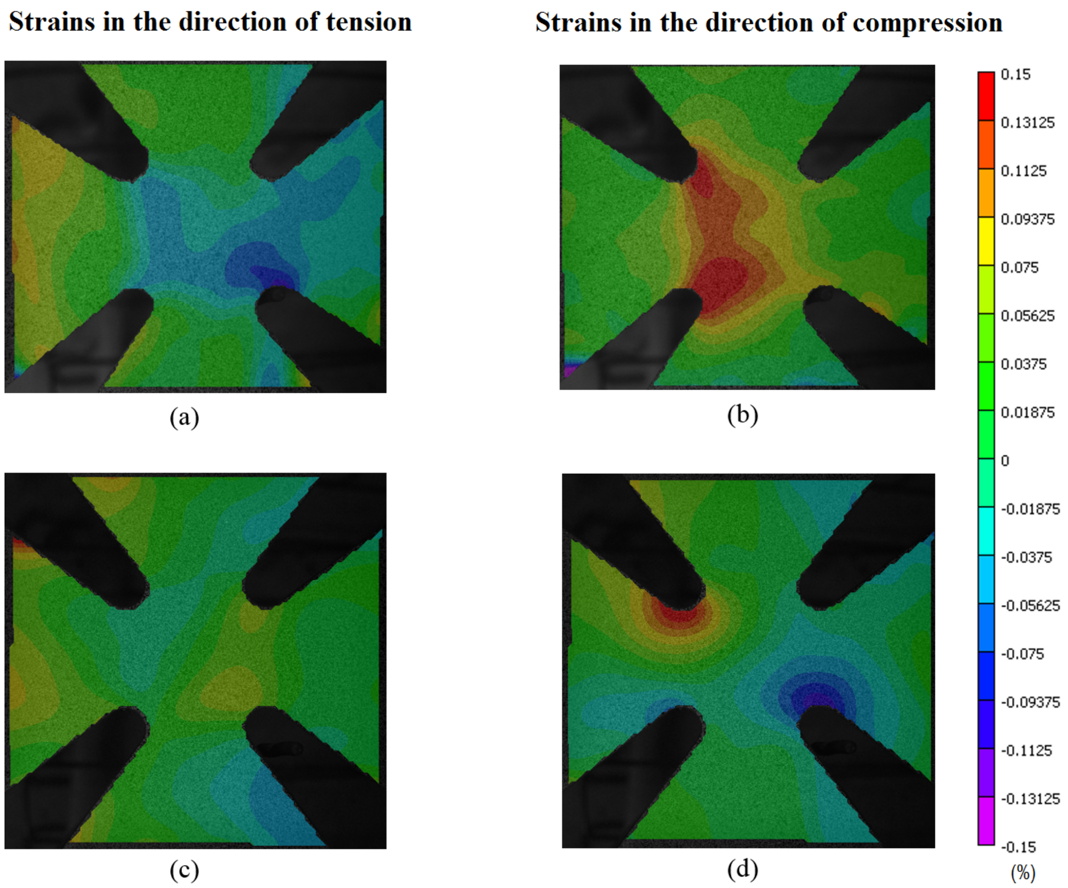

FIGURE B-1 – Residual strain fields at the end of the first cycle of loading at the end of the first cycle of loading. ε_{xx} (a) and ε_{yy} (b) for Sample 1. ε_{yy} (c) and ε_{yy} (d) for Sample 2.

Appendix C : Transformation rule for the stress space

The rotation matrices $\boldsymbol{R_z},\ \boldsymbol{R_x},\ \boldsymbol{R_p}$ appearing in (3.11) are found as such :

$$\boldsymbol{R_z} = \begin{pmatrix} \cos\theta_z & -\sin\theta_z & 0 \\ \sin\theta_z & \cos\theta_z & 0 \\ 0 & 0 & 1 \end{pmatrix},\ \boldsymbol{R_x} = \begin{pmatrix} 1 & 0 & 0 \\ 0 & \cos\theta_x & -\sin\theta_x \\ 0 & \sin\theta_x & \cos\theta_x \end{pmatrix} \text{ and}$$

$$\boldsymbol{R_p} = \begin{pmatrix} \cos\theta_p + u_1 & u_1 - v_1 & u_1 + v_1 \\ u_1 + v_1 & \cos\theta_p + u_1 & u_1 - v_1 \\ u_1 - v_1 & u_1 + v_1 & \cos\theta_p + u_1 \end{pmatrix},$$

where $u_1 = \dfrac{1-\cos\theta_p}{3}$ and $v_1 = \dfrac{\sin\theta_p}{\sqrt{3}}$.

The tensor $\boldsymbol{R_\sigma}$ is found finally as :

$$\boldsymbol{R_\sigma} = \begin{pmatrix} \begin{pmatrix} R_{11} & 0 & 0 \\ 0 & R_{21} & 0 \\ 0 & 0 & R_{31} \end{pmatrix} & \begin{pmatrix} 0 & l_{12} & 0 \\ 0 & 0 & 0 \\ 0 & 0 & 0 \end{pmatrix} & \begin{pmatrix} 0 & 0 & l_{13} \\ 0 & 0 & 0 \\ 0 & 0 & 0 \end{pmatrix} \\ \begin{pmatrix} 0 & 0 & 0 \\ l_{12} & 0 & 0 \\ 0 & 0 & 0 \end{pmatrix} & \begin{pmatrix} R_{12} & 0 & 0 \\ 0 & R_{22} & 0 \\ 0 & 0 & R_{32} \end{pmatrix} & \begin{pmatrix} 0 & 0 & 0 \\ 0 & 0 & l_{23} \\ 0 & 0 & 0 \end{pmatrix} \\ \begin{pmatrix} 0 & 0 & 0 \\ 0 & 0 & 0 \\ l_{13} & 0 & 0 \end{pmatrix} & \begin{pmatrix} 0 & 0 & 0 \\ 0 & 0 & 0 \\ 0 & l_{23} & 0 \end{pmatrix} & \begin{pmatrix} R_{13} & 0 & 0 \\ 0 & R_{23} & 0 \\ 0 & 0 & R_{33} \end{pmatrix} \end{pmatrix},$$

where R_{ij} are found in (3.9)

Appendix D : Data for the micromechanical model

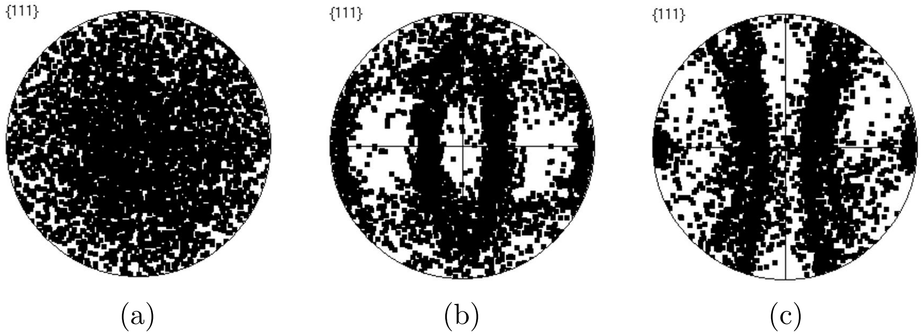

(a) (b) (c)

FIGURE D-1 – Pole figures corresponding to : (a) Isotropic specimen (b) Rolled specimen (c) Drawn specimen.

Appendix E : Numerical resolution of multiple strain mechanisms framework

The aim of this appendix is to provide a framework for addressing the numerical implementation of a model that considers multiple strain mechanisms. Some concepts introduced in sections 4.5 and 5.2 are revisited and the procedures leading to the calculation of necessary components of the numerical algorithm are explained in full detail. The components of an algorithm built for a general solution taking in mind a random number of rate-independent strain mechanisms will be examined.

Implicit formulation for fully coupled problem

The evolution of inelastic strains is due to several mechanisms which are considered thermodynamically independent. This means that the dissipation caused by each one of them must be non-negative. The total inelastic strain is:

$$\boldsymbol{\varepsilon^T} = \sum_m \boldsymbol{\varepsilon^m} \tag{E.36}$$

where the index m stands for every different mechanism. Each mechanism m is responsible for the evolution of $\boldsymbol{\varepsilon^m}$.

A Gibbs free energy potential G governs the thermodynamics of modeling. It is given intially in a general form:

$$G = -\boldsymbol{\sigma} : \boldsymbol{\varepsilon^T} + G^v \tag{E.37}$$

Here, G^v is considered a part of the free energy potential disassociated with inelastic strain. Now, viewing each $\boldsymbol{\varepsilon^m}$ as an internal variable, the GTF for each one deriving from this potential is:

$$-\frac{\partial G}{\partial \boldsymbol{\varepsilon^m}} = \boldsymbol{\sigma} \tag{E.38}$$

Each mechanism m involves a set of variables $\{\boldsymbol{V_i^m}\}$. Each different $\boldsymbol{V_i^m}$ might be considered an internal variable or not. The first element of every set is defined to be a scalar p^m:

$$p^m = V_1^m$$

The property of every p^j is that the rate of all other variables $\boldsymbol{V_i^j}$ are found by:

$$\dot{\boldsymbol{V}}_{\boldsymbol{i}}^{\boldsymbol{j}} = \dot{p}^j \boldsymbol{\Lambda_i^j} \tag{E.39}$$

with j being an index denoting any mechanism m consistently throughout this section. The order of the tensor $\boldsymbol{\Lambda_i^j}$ varies according to the nature of $\boldsymbol{V_i^j}$. In the scope of this section, they are given the name evolution tensors. For instance,

$\Lambda_1^j = \Lambda_p^j = 1$ is a zero order tensor equal to the unit so as to comply with (E.39). Likewise,

$\boldsymbol{\Lambda_2^j} = \boldsymbol{\Lambda_\varepsilon^j}$ is a second-order tensor corresponding to $\boldsymbol{\varepsilon^j}$. The second element of every set $\{\boldsymbol{V_i^j}\}$ will consistently be considered $\boldsymbol{\varepsilon^j}$.

In thermodynamics, any element $\boldsymbol{V_i^m}$ which is an internal variable, has a conjugant GTF:

$$\boldsymbol{A_{V\,i}^m} = -\frac{\partial G}{\partial \boldsymbol{V_i^m}} \tag{E.40}$$

The thermodynamic criteria which govern the activation of each mechanism have the general form:

$$\Phi^m(\{\boldsymbol{A_V^m}\}) \leq 0 \tag{E.41}$$

where $\{\boldsymbol{A_V^m}\}$ is the whole set of GTFs for the mechanism m.

For a given loading case, the convex cutting plane (CCP) [Hartl and Lagoudas, 2009] algorithm is implemented. For every iteration k within a loading step $n \to n+1$, it is considered that:

$$\boldsymbol{\delta V}_{\boldsymbol{i}\;n+1}^{\boldsymbol{m}\;(k)} = \delta p_{n+1}^{m\;(k)} \boldsymbol{\Lambda}_{\boldsymbol{i}\;n+1}^{\boldsymbol{m}\;(k)} \tag{E.42}$$

The symbol δ denotes the difference in a value of a variable between two consecutive iterations in the CCP scheme.

During iterative correction, the total current strain and temperature are held constant such that:

$$\boldsymbol{\delta\varepsilon}\,{}^{(k)}_{n+1} = \mathbf{0}$$

and

$$\delta T\,{}^{(k)}_{n+1} = 0$$

According to the decomposition of strains:

$$\boldsymbol{\varepsilon} = \boldsymbol{\varepsilon^{el}} + \boldsymbol{\varepsilon^{th}} + \boldsymbol{\varepsilon^{T}} = \boldsymbol{\varepsilon^{el}} + \boldsymbol{\varepsilon^{th}} + \sum_j \boldsymbol{\varepsilon^{j}} \tag{E.43}$$

the constitutive relation for elasticity:

$$\boldsymbol{\varepsilon^{el}} = \boldsymbol{S} : \boldsymbol{\sigma} \tag{E.44}$$

and the null increments of $\boldsymbol{\varepsilon}_{n+1}$ and T_{n+1} (as the return mapping algorithm requires), it is deduced that:

$$-\boldsymbol{\delta\varepsilon}^{\boldsymbol{th}\,(k)}_{n+1} - \sum_j \left(\boldsymbol{\delta\varepsilon}^{\boldsymbol{j}\,(k)}_{n+1}\right) = \boldsymbol{\delta S}^{(k)}_{n+1} : \boldsymbol{\sigma}^{(k)}_{n+1} + \boldsymbol{S}^{(k)}_{n+1} : \boldsymbol{\delta\sigma}^{(k)}_{n+1} \tag{E.45}$$

According to (E.42),

$$\boldsymbol{\delta\varepsilon}^{\boldsymbol{j}\,(k)}_{n+1} = \delta p^{j\,(k)}_{n+1} \boldsymbol{\Lambda}^{\boldsymbol{j}\,(k)}_{\varepsilon\;n+1} \tag{E.46}$$

If the elastic compliance tensor and the thermal expansion coefficient are considered a direct function of the variables p^j, it also evident that:

$$\boldsymbol{\delta S}^{(k)}_{n+1} = \sum_j \left(\delta p^{j\,(k)}_{n+1} \frac{\partial \boldsymbol{S}^{(k)}_{n+1}}{\partial p^j}\right) \tag{E.47}$$

and

$$\boldsymbol{\delta\alpha}^{(k)}_{n+1} = \sum_j \left(\delta p^{j\,(k)}_{n+1} \frac{\partial \boldsymbol{\alpha}^{(k)}_{n+1}}{\partial p^j}\right) \tag{E.48}$$

With the help of (E.46), (E.47) and (E.48), the equation (E.45) is now written:

$$\begin{aligned}-\Delta T_{n+1}\sum_j\left(\delta p_{n+1}^{j\ (k)}\frac{\partial\boldsymbol{\alpha}_{n+1}^{(k)}}{\partial p^j}\right)-\sum_j\left(\delta p_{n+1}^{j\ (k)}\boldsymbol{\Lambda}_{\boldsymbol{\varepsilon}\ n+1}^{\boldsymbol{j}\ (k)}\right)&=\\ =\sum_j\left(\delta p_{n+1}^{j\ (k)}\frac{\partial\boldsymbol{S}_{n+1}^{(k)}}{\partial p^j}\right):\boldsymbol{\sigma}_{n+1}^{(k)}&+\boldsymbol{S}_{n+1}^{(k)}:\boldsymbol{\delta\sigma}_{n+1}^{(k)}\end{aligned}$$

$$\Leftrightarrow \boldsymbol{\delta\sigma}_{n+1}^{(k)}=-\boldsymbol{C}_{n+1}^{(k)}:\sum_j\left[\delta p_{n+1}^{j\ (k)}\left(\frac{\partial\boldsymbol{S}_{n+1}^{(k)}}{\partial p^j}:\boldsymbol{\sigma}_{n+1}^{(k)}+\Delta T_{n+1}\frac{\partial\boldsymbol{\alpha}_{n+1}^{(k)}}{\partial p^j}+\boldsymbol{\Lambda}_{\boldsymbol{\varepsilon}\ n+1}^{\boldsymbol{j}\ (k)}\right)\right]$$

The following notation is accepted:

$$\boldsymbol{K}_{n+1}^{\boldsymbol{j}\ (k)}=\frac{\partial\boldsymbol{S}_{n+1}^{(k)}}{\partial p^j}:\boldsymbol{\sigma}_{n+1}^{(k)}+\Delta T_{n+1}\frac{\partial\boldsymbol{\alpha}_{n+1}^{(k)}}{\partial p^j}+\boldsymbol{\Lambda}_{\boldsymbol{\varepsilon}\ n+1}^{\boldsymbol{j}\ (k)}$$

to reach:

$$\boldsymbol{\delta\sigma}_{n+1}^{(k)}=-\boldsymbol{C}_{n+1}^{(k)}:\sum_j(\delta p_{n+1}^{j\ (k)}\boldsymbol{K}_{n+1}^{\boldsymbol{j}\ (k)}) \tag{E.49}$$

On the other hand, the consistency condition of the Φ^m criteria dictates that:

$$\Phi_{n+1}^{m\ (k)}+\delta\Phi_{n+1}^{m\ (k)}=\Phi_{n+1}^{m\ (k+1)}\approx 0 \tag{E.50}$$

From (E.41), taking into account the form of $\boldsymbol{A}_{\boldsymbol{V}}^{\boldsymbol{m}}$, the following general condition is deduceds:

$$\Phi^m(\boldsymbol{\sigma},T,\{\boldsymbol{V}_{\boldsymbol{i}}^{\boldsymbol{j}}\})\leq 0 \tag{E.51}$$

In the latter, applying the chain rule it is derived:

$$\delta\Phi_{n+1}^{m\ (k)}=\frac{\partial\Phi_{n+1}^{m\ (k)}}{\partial\boldsymbol{\sigma}}:\boldsymbol{\delta\sigma}_{n+1}^{(k)}+\sum_j\left[\sum_i\left(\frac{\partial\Phi_{n+1}^{m\ (k)}}{\partial\boldsymbol{V}_{\boldsymbol{i}}^{\boldsymbol{j}}}:\boldsymbol{\delta V}_{\boldsymbol{i}\ n+1}^{\boldsymbol{j}\ (k)}\right)\right] \tag{E.52}$$

In light of (E.49), this is written:

$$\begin{aligned}\delta\Phi^{m\,(k)}_{n+1} &= -\frac{\partial\Phi^{m\,(k)}_{n+1}}{\partial\boldsymbol{\sigma}} : \boldsymbol{C}^{(k)}_{n+1} : \sum_{j}(\delta p^{j\,(k)}_{n+1}\boldsymbol{K}^{\boldsymbol{j}\,(k)}_{n+1}) + \\ &\qquad + \sum_{j}\left[\delta p^{j\,(k)}_{n+1}\sum_{i}\left(\frac{\partial\Phi^{m\,(k)}_{n+1}}{\partial\boldsymbol{V}^{\boldsymbol{j}}_{\boldsymbol{i}}} : \boldsymbol{\Lambda}^{\boldsymbol{j}\,(k)}_{\boldsymbol{i}\,n+1}\right)\right] \Leftrightarrow\end{aligned}$$

$$\delta\Phi^{m\,(k)}_{n+1} = \sum_{j}\left\{\delta p^{j\,(k)}_{n+1}\left[-\frac{\partial\Phi^{m\,(k)}_{n+1}}{\partial\boldsymbol{\sigma}} : \boldsymbol{C}^{(k)}_{n+1} : \boldsymbol{K}^{\boldsymbol{j}\,(k)}_{n+1} + \sum_{i}\left(\frac{\partial\Phi^{m\,(k)}_{n+1}}{\partial\boldsymbol{V}^{\boldsymbol{j}}_{\boldsymbol{i}}} : \boldsymbol{\Lambda}^{\boldsymbol{j}\,(k)}_{\boldsymbol{i}\,n+1}\right)\right]\right\} \tag{E.53}$$

The equation (E.50) will then yield:

$$-\Phi^{m\,(k)}_{n+1} = \sum_{j}\left\{\delta p^{j\,(k)}_{n+1}\left[-\frac{\partial\Phi^{m\,(k)}_{n+1}}{\partial\boldsymbol{\sigma}} : \boldsymbol{C}^{(k)}_{n+1} : \boldsymbol{K}^{\boldsymbol{j}\,(k)}_{n+1} + \sum_{i}\left(\frac{\partial\Phi^{m\,(k)}_{n+1}}{\partial\boldsymbol{V}^{\boldsymbol{j}}_{\boldsymbol{i}}} : \boldsymbol{\Lambda}^{\boldsymbol{j}\,(k)}_{\boldsymbol{i}\,n+1}\right)\right]\right\} \tag{E.54}$$

Each of the equations out of the set of (E.54) corresponds to each of the mechanisms m. There are as many equations in (E.54) as the total number of m (N_m) and therefore the total number of p^m. A set of linear equations of $\{\delta p^{j\,(k)}_{n+1}\}$ is recognized in the form of:

$$\boldsymbol{B}^{(k)}_{n+1}\{\delta p^{j\,(k)}_{n+1}\} = -\{\Phi^{m\,(k)}_{n+1}\} \tag{E.55}$$

$\boldsymbol{B}^{(k)}_{n+1}$ is a $N_m \times N_m$ matrix, the components of which are found by:

$$B^{m\,(k)}_{j\,n+1} = B_{mj}{}^{(k)}_{n+1} = -\frac{\partial\Phi^{m\,(k)}_{n+1}}{\partial\boldsymbol{\sigma}} : \boldsymbol{C}^{(k)}_{n+1} : \boldsymbol{K}^{\boldsymbol{j}\,(k)}_{n+1} + \sum_{i}\left(\frac{\partial\Phi^{m\,(k)}_{n+1}}{\partial\boldsymbol{V}^{\boldsymbol{j}}_{\boldsymbol{i}}} : \boldsymbol{\Lambda}^{\boldsymbol{j}\,(k)}_{\boldsymbol{i}\,n+1}\right) \tag{E.56}$$

From (E.55), the set of $\delta p^{j\,(k)}_{n+1}$ is found by:

$$\{\delta p^{j\,(k)}_{n+1}\} = -(\boldsymbol{B}^{(k)}_{n+1})^{-1}\{\Phi^{m\,(k)}_{n+1}\} \tag{E.57}$$

At the end of every iteration the values of the set of $\{\boldsymbol{V}^{\boldsymbol{m}}_{\boldsymbol{i}}\}$ and the rest of the internal variables.

Deployment of the Fischer-Burmeister method

In subsection 5.2.3, the Fischer-Burmeister technique is used in the iterative process:

$$\delta p^{j(k)} = -\sum^{j} \left[(B^{f(k)}_{mj})^{-1} F^{m(k)} \right] \tag{E.58}$$

where

$$-F^{m(k)} = \left[\frac{\Phi^{m(k)}}{\sqrt{(\Phi^{m(k)})^2+(dp^{m(k)})^2}} + 1 \right] \delta\Phi^{m(k)} + \left[\frac{dp^{m(k)}}{\sqrt{(\Phi^{m(k)})^2+(dp^{m(k)})^2}} - 1 \right] \delta p^{m(k)} \tag{E.59}$$

According to equations (E.59) and (E.55), the components of the matrix $\boldsymbol{B^f}$ are found as:

$$B^{f(k)}_{mj} = \sum^{j} \left\{ B^{(k)}_{mj} \left[\frac{\Phi^{m(k)}}{\sqrt{(\Phi^{m(k)})^2+(dp^{m(k)})^2}} + 1 \right] + I_{mj} \left[\frac{dp^{m(k)}}{\sqrt{(\Phi^{m(k)})^2+(dp^{m(k)})^2}} - 1 \right] \right\} \tag{E.60}$$

Thermomechanical tangent moduli estimation

During an arbitrary thermomechanical path, the mechanical and thermal tangent moduli need to be calculated at the end of every loading step. Again, the additive decomposition of strains and their respective rates is taken in mind:

$$\boldsymbol{d\varepsilon} = \boldsymbol{d\varepsilon^{el}} + \boldsymbol{d\varepsilon^{th}} + \sum_{j} \boldsymbol{d\varepsilon^{j}} \tag{E.61}$$

where the sum denoted by $\sum_{j}$ refers only to the mechanisms m that are activated in the current step. j may take the values F, R or re. Given that these moduli examine the tangent behavior between two consecutive steps, the symbol d denotes the difference in the value of the variables between those steps.

The previous equation gives:

$$\boldsymbol{d\varepsilon} = \boldsymbol{d}(\boldsymbol{S} : \boldsymbol{\sigma}) + \boldsymbol{d}(\boldsymbol{\alpha}\Delta T) + \sum_j (dp^j \boldsymbol{\Lambda}_{\varepsilon}^{\boldsymbol{j}}) \Leftrightarrow$$

$$\boldsymbol{d\sigma} = \boldsymbol{C} : \left[\boldsymbol{d\varepsilon} - \sum_j \left(dp^j \boldsymbol{K}^{\boldsymbol{j}}\right) - \boldsymbol{\alpha} dT\right] \tag{E.62}$$

where

$$\boldsymbol{K}^{\boldsymbol{j}} = \frac{\partial \boldsymbol{S}}{\partial p^j} : \boldsymbol{\sigma} + \frac{\partial \boldsymbol{\alpha}}{\partial p^j}\Delta T + \boldsymbol{\Lambda}_{\varepsilon}^{\boldsymbol{j}}$$

For all different mechanisms m, it is also assumed: $d\Phi^m = 0$. But:

$$d\Phi^m = \frac{\partial \Phi^m}{\partial \boldsymbol{\sigma}} : \boldsymbol{d\sigma} + \frac{\partial \Phi^m}{\partial T} dT + \sum_j \left[\sum_i \left(\frac{\partial \Phi^m}{\partial \boldsymbol{V}_{\boldsymbol{i}}^{\boldsymbol{j}}} : \boldsymbol{d}\boldsymbol{V}_{\boldsymbol{i}}^{\boldsymbol{j}}\right)\right] \tag{E.63}$$

In light of (E.39), this is written:

$$d\Phi^m = \frac{\partial \Phi^m}{\partial \boldsymbol{\sigma}} : \boldsymbol{d\sigma} + \frac{\partial \Phi^m}{\partial T} dT + \sum_j \left[dp^j \sum_i \left(\frac{\partial \Phi^m}{\partial \boldsymbol{V}_{\boldsymbol{i}}^{\boldsymbol{j}}} : \boldsymbol{\Lambda}_{\boldsymbol{i}}^{\boldsymbol{j}}\right)\right] \tag{E.64}$$

Substituting with the expression of $\boldsymbol{d\sigma}$ from (E.62), it is found:

$$\begin{aligned} d\Phi^m = & \frac{\partial \Phi^m}{\partial \boldsymbol{\sigma}} : \boldsymbol{C} : \left[\boldsymbol{d\varepsilon} - \sum_j \left(dp^j \boldsymbol{K}^{\boldsymbol{j}}\right) - \boldsymbol{\alpha} dT\right] + \frac{\partial \Phi^m}{\partial T} dT + \\ & + \sum_j \left[dp^j \sum_i \left(\frac{\partial \Phi^m}{\partial \boldsymbol{V}_{\boldsymbol{i}}^{\boldsymbol{j}}} : \boldsymbol{\Lambda}_{\boldsymbol{i}}^{\boldsymbol{j}}\right)\right] \end{aligned} \tag{E.65}$$

and, given the null increment of the Φ^m functions:

$$\begin{aligned}&\frac{\partial\Phi^m}{\partial\boldsymbol{\sigma}}:\boldsymbol{C}:\boldsymbol{d\varepsilon}+\left(\frac{\partial\Phi^m}{\partial T}-\frac{\partial\Phi^m}{\partial\boldsymbol{\sigma}}:\boldsymbol{C}:\boldsymbol{\alpha}\right)dT+\\&+\sum_j\left\{dp^j\left[\sum_i\left(\frac{\partial\Phi^m}{\partial\boldsymbol{V_i^j}}:\boldsymbol{\Lambda_i^j}\right)-\frac{\partial\Phi^m}{\partial\boldsymbol{\sigma}}:\boldsymbol{C}:\boldsymbol{K^j}\right]\right\}=0\end{aligned}\tag{E.66}$$

There are as many equations in (E.66) as the total number of m (N_m) that are activated for the current step and therefore the total number of p^m.A set of linear equations of the vector$\{dp^j\}$ is recognized in the form of:

$$\hat{\boldsymbol{B}}\{dp^j\}=\left\{-\frac{\partial\Phi^m}{\partial\boldsymbol{\sigma}}:\boldsymbol{C}:\boldsymbol{d\varepsilon}-\left(\frac{\partial\Phi^m}{\partial T}-\frac{\partial\Phi^m}{\partial\boldsymbol{\sigma}}:\boldsymbol{C}:\boldsymbol{\alpha}\right)dT\right\}\tag{E.67}$$

where: $\hat{\boldsymbol{B}}$ is a $N_m\times N_m$ matrix, the components $\hat{B}_{mj}$ of which are found by:

$$\hat{B}_{mj}=\sum_i\left(\frac{\partial\Phi^m}{\partial\boldsymbol{V_i^j}}:\boldsymbol{\Lambda_i^j}\right)-\frac{\partial\Phi^m}{\partial\boldsymbol{\sigma}}:\boldsymbol{C}:\boldsymbol{K^j}\tag{E.68}$$

Following (E.67),

$$\{dp^j\}=\hat{\boldsymbol{B}}^{\boldsymbol{-1}}\left\{-\frac{\partial\Phi^m}{\partial\boldsymbol{\sigma}}:\boldsymbol{C}:\boldsymbol{d\varepsilon}-\left(\frac{\partial\Phi^m}{\partial T}-\frac{\partial\Phi^m}{\partial\boldsymbol{\sigma}}:\boldsymbol{C}:\boldsymbol{\alpha}\right)dT\right\}$$

or

$$dp^j=-\sum_m\left(\hat{B}_{mj}^{-1}\frac{\partial\Phi^m}{\partial\boldsymbol{\sigma}}:\boldsymbol{C}\right):\boldsymbol{d\varepsilon}-\sum_m\left[\hat{B}_{mj}^{-1}\left(\frac{\partial\Phi^m}{\partial T}-\frac{\partial\Phi^m}{\partial\boldsymbol{\sigma}}:\boldsymbol{C}:\boldsymbol{\alpha}\right)\right]dT\tag{E.69}$$

Here, the following notations are defined:

$$P_T^j=\sum_m\left[\hat{B}_{mj}^{-1}\left(\frac{\partial\Phi^m}{\partial T}-\frac{\partial\Phi^m}{\partial\boldsymbol{\sigma}}:\boldsymbol{C}:\boldsymbol{\alpha}\right)\right]\tag{E.70}$$

and

$$\boldsymbol{P}_{\varepsilon}^{\boldsymbol{j}} = \sum_{m} \left(\hat{B}_{mj}^{-1} \frac{\partial \Phi^{m}}{\partial \boldsymbol{\sigma}} : \boldsymbol{C} \right) \tag{E.71}$$

Given the major symmetry $C_{uvst} = C_{stuv}$ of the elastic stiffness tensor, the latter is now:

$$\boldsymbol{P}_{\varepsilon}^{\boldsymbol{j}} = \boldsymbol{C} : \sum_{m} \left(\hat{B}_{mj}^{-1} \frac{\partial \Phi^{m}}{\partial \boldsymbol{\sigma}} \right) \tag{E.72}$$

Thus, the equation (E.69) is now updated:

$$dp^{j} = -\boldsymbol{P}_{\varepsilon}^{\boldsymbol{j}} : \boldsymbol{d\varepsilon} - P_{T}^{j} dT \tag{E.73}$$

Substituting this expression for dp^j in (E.62), it is deduced:

$$\boldsymbol{d\sigma} = \left\{ \boldsymbol{C} : \left[\boldsymbol{I}^{(4)} + \sum_{j} (\boldsymbol{K}^{\boldsymbol{j}} \otimes \boldsymbol{P}_{\varepsilon}^{\boldsymbol{j}}) \right] \right\} : \boldsymbol{d\varepsilon} + \left\{ \boldsymbol{C} : \left[\sum_{j} (P_{T}^{j} \boldsymbol{K}^{\boldsymbol{j}}) - \boldsymbol{\alpha} \right] \right\} dT \tag{E.74}$$

Here, the desired tangent moduli become evident. The mechanical tangent modulus is:

$$\boldsymbol{L} = \boldsymbol{C} : \left[\boldsymbol{I}^{(4)} + \sum_{j} (\boldsymbol{K}^{\boldsymbol{j}} \otimes \boldsymbol{P}_{\varepsilon}^{\boldsymbol{j}}) \right] \tag{E.75}$$

and the thermal tangent modulus:

$$\boldsymbol{\Theta} = \boldsymbol{C} : \left[\sum_{j} (P_{T}^{j} \boldsymbol{K}^{\boldsymbol{j}}) - \boldsymbol{\alpha} \right] \tag{E.76}$$

Thermomechanical coupling

The local form of the first law of thermodynamics is written:

$$\dot{u} = r - \nabla \cdot \boldsymbol{q} + \boldsymbol{\sigma} : \dot{\boldsymbol{\varepsilon}} = \dot{Q} + \boldsymbol{\sigma} : \dot{\boldsymbol{\varepsilon}} \tag{E.77}$$

Here, u is the internal energy, r is the power of the internally generated heat, $\boldsymbol{q}$ is the thermal flux and Q is the total heat exchange due to both internal heat sources and conduction. On the other hand, the Gibbs free energy is given as:

$$G = u - \boldsymbol{\sigma} : \boldsymbol{\varepsilon} - sT \tag{E.78}$$

Its rate form:

$$\dot{u} = \dot{G} + (\dot{\overline{\boldsymbol{\sigma} : \boldsymbol{\varepsilon}}}) + (\dot{\overline{sT}}) \tag{E.79}$$

is replaced into (E.77) to give:

$$\dot{G} + \dot{\boldsymbol{\sigma}} : \boldsymbol{\varepsilon} + \dot{s}T + s\dot{T} = \dot{Q} \tag{E.80}$$

Applying the chain rule to derive the rate of the Gibbs free energy potential, it is found:

$$\dot{G} = \frac{\partial G}{\partial \boldsymbol{\sigma}} : \dot{\boldsymbol{\sigma}} + \frac{\partial G}{\partial T}\dot{T} + \sum_j \left[\sum_i \left(\frac{\partial G}{\partial \boldsymbol{V}_{\boldsymbol{i}}^{\boldsymbol{j}}} : \dot{\boldsymbol{V}}_{\boldsymbol{i}}^{\boldsymbol{j}} \right) \right] \tag{E.81}$$

Recalling the basic equations (4.41) and (4.42), as well as (E.39) and (E.40), this rate is now:

$$\dot{G} = -\boldsymbol{\varepsilon} : \dot{\boldsymbol{\sigma}} - s\dot{T} - \sum_j \left[\dot{p}^j \sum_i \left(\boldsymbol{A}_{\boldsymbol{i}}^{\boldsymbol{j}} \boldsymbol{:} \, \boldsymbol{\Lambda}_{\boldsymbol{i}}^{\boldsymbol{j}} \right) \right] \tag{E.82}$$

Giving the definition:

$$\pi^j = \sum_i (\boldsymbol{A}_{\boldsymbol{i}}^{\boldsymbol{j}} : \boldsymbol{\Lambda}_{\boldsymbol{i}}^{\boldsymbol{j}}) \tag{E.83}$$

the equation (E.80) is now:

$$\dot{s}T = \sum_j (\pi^j \dot{p}^j) + \dot{Q} \tag{E.84}$$

in which $\dot{s}$ is found from (4.41):

$$\begin{aligned} \dot{s} =& \frac{\partial s}{\partial \boldsymbol{\sigma}} : \dot{\boldsymbol{\sigma}} + \frac{\partial s}{\partial T}\dot{T} + \sum_j \left(\frac{\partial s}{\partial p^j} \dot{p}^j \right) = \\ &= \dot{\boldsymbol{\sigma}} : \boldsymbol{\alpha} + C_v \frac{\dot{T}}{T} + \sum_j \left\{ \dot{p}^j \left[\frac{\partial s_o}{\partial p^j} + \boldsymbol{\sigma} : \frac{\partial \boldsymbol{\alpha}}{\partial p^j} + \frac{\partial C_v}{\partial p^j} \ln \left(\frac{T}{T_o} \right) \right] \right\} \end{aligned} \tag{E.85}$$

Thus, from (E.84):

$$C_v\dot{T} = \sum_j \left\{ \dot{p}^j \left[\pi^j - \left[\frac{\partial s_o}{\partial p^j} + \boldsymbol{\sigma} : \frac{\partial \boldsymbol{\alpha}}{\partial p^j} + \frac{\partial C_v}{\partial p^j} \ln\left(\frac{T}{T_o}\right) \right] T \right] \right\} - \dot{\boldsymbol{\sigma}} : \boldsymbol{\alpha} \cdot T + \dot{Q} \tag{E.86}$$

The following notation is adopted:

$$\pi_T^j = \pi^j - \left[\frac{\partial s_o}{\partial p^j} + \boldsymbol{\sigma} : \frac{\partial \boldsymbol{\alpha}}{\partial p^j} + \frac{\partial C_v}{\partial p^j} \ln\left(\frac{T}{T_o}\right) \right] T \tag{E.87}$$

The known forms of $\dot{p}^j$ and $\dot{\boldsymbol{\sigma}}$ from (E.73) and (E.74) are also substituted into (E.86) to acquire:

$$C_v\dot{T} - \dot{Q} = - \left[\sum_j \left(\pi_T^j \boldsymbol{P}_\varepsilon^{\boldsymbol{j}} \right) + \boldsymbol{L} : \boldsymbol{\alpha} \cdot T \right] : \dot{\boldsymbol{\varepsilon}} - \left[\sum_j \left(\pi_T^j P_T^j \right) + \boldsymbol{\Theta} : \boldsymbol{\alpha} \cdot T \right] \dot{T} \tag{E.88}$$

The last equation states that the volumetric heat generation per unit time is not equal to the total heat exchange. The difference between these two quantities arises by effect of mechanical work, as it appears in the right-hand part of the equation. The part of dissipation linked to mechanical reaction of the material, such as the one found in (4.47), is also found in this part.

The quantities

$$D_{,\varepsilon} = - \left[\sum_j \left(\pi_T^j \boldsymbol{P}_\varepsilon^{\boldsymbol{j}} \right) + \boldsymbol{L} : \boldsymbol{\alpha} \cdot T \right] \tag{E.89}$$

and

$$D_{,T} = - \left[\sum_j \left(\pi_T^j P_T^j \right) + \boldsymbol{\Theta} : \boldsymbol{\alpha} \cdot T \right] \tag{E.90}$$

track the linear relation of the power of the heat generated through thermomechanical coupling with the differentials of strain and temperature.

APPENDIX E

Implementation of thermomechanical effects with Abaqus

During the n loop, a Finite Element Analysis suite, such as Abaqus, performs the task of balancing the influence of thermal fluxes with thermal energy rates. In (E.88), the first law of thermodynamics is expressed in terms of the rate difference between the rise (or reduction) of the thermal energy linked to specific heat and the heat sources. This energy rate is denoted by the variable r^{pl}:

$$r^{pl} = C_v \dot{T} - \dot{Q} = \boldsymbol{D}_{,\varepsilon} : \dot{\boldsymbol{\varepsilon}} + D_{,T} \dot{T} \tag{E.91}$$

In order to approximate the balance of thermal contributions produced by mechanical working with external thermal boundary conditions and all the temperature-dependent variables, Abaqus requires the quantities $\boldsymbol{d}^{\boldsymbol{r}}_{\boldsymbol{\varepsilon}}$ and d^r_T used in the equation

$$dr^{pl} = \boldsymbol{d}^{\boldsymbol{r}}_{\boldsymbol{\varepsilon}} : \boldsymbol{d\varepsilon} + d^r_T dT \tag{E.92}$$

To this end, we start with the expression from (E.86):

$$r^{pl} = C_v \dot{T} - \dot{Q} = \sum_j \left\{ \left[\pi^j - \left[\frac{\partial s_o}{\partial p^j} + \boldsymbol{\sigma} : \frac{\partial \boldsymbol{\alpha}}{\partial p^j} + \frac{\partial C_v}{\partial p^j} \ln \left(\frac{T}{T_o} \right) \right] T \right] \dot{p}^j \right\} - \dot{\boldsymbol{\sigma}} : \boldsymbol{\alpha} \cdot T \tag{E.93}$$

The following definition is given:

$$\bar{\pi}^j = \left[\frac{\partial s_o}{\partial p^j} + \boldsymbol{\sigma} : \frac{\partial \boldsymbol{\alpha}}{\partial p^j} + \frac{\partial C_v}{\partial p^j} \ln \left(\frac{T}{T_o} \right) \right] T \tag{E.94}$$

The differential dr^{pl} is approximated:

$$dr^{pl} = d \left\{ \sum_j \left[\left(\pi^j - \bar{\pi}^j \right) \dot{p}^j \right] - \dot{\boldsymbol{\sigma}} : \boldsymbol{\alpha} \cdot T \right\} \tag{E.95}$$

where the rate variables are substituted with the finite differences of the n loop:

$$dr^{pl} = d \left\{ \sum_j \left(\left(\pi^j - \bar{\pi}^j \right) \frac{\Delta p^j}{\Delta t} \right) - \frac{\boldsymbol{\Delta\sigma}}{\Delta t} : \boldsymbol{\alpha} \cdot T \right\} \tag{E.96}$$

This differential operation yields:

$$\begin{aligned} dr^{pl} &= d\left\{\sum_j \left[\left(\pi^j - \bar{\pi}^j\right)\frac{\Delta p^j}{\Delta t}\right] - \frac{\boldsymbol{\Delta\sigma}}{\Delta t} : \boldsymbol{\alpha} \cdot T\right\} = \\ &= \frac{1}{\Delta t}\left\{\sum_j \left[\left(d\pi^j - d\bar{\pi}^j\right)\Delta p^j + \left(\pi^j - \bar{\pi}^j\right)dp^j\right] - \left(\boldsymbol{d\sigma} : \boldsymbol{\alpha} \cdot T + \boldsymbol{\Delta\sigma} : \boldsymbol{d\alpha} \cdot T + \boldsymbol{\Delta\sigma} : \boldsymbol{\alpha} \cdot dT\right)\right\} \end{aligned} \tag{E.97}$$

where Δt is the time increment corresponding to step n.

According to convex cutting plane considerations, the various differentials appearing in the last equation are:

$$d\pi^j = d\sum_i \left(\boldsymbol{A_i^j} : \boldsymbol{\Lambda_i^j}\right) = \sum_i \left(\boldsymbol{dA_i^j} : \boldsymbol{\Lambda_i^j}\right) \tag{E.98}$$

Here,

$$\begin{aligned} \boldsymbol{dA_i^j} &= \frac{\partial \boldsymbol{A_i^j}}{\partial \boldsymbol{\sigma}} : \boldsymbol{d\sigma} + \frac{\partial \boldsymbol{A_i^j}}{\partial T}dT + \sum_g \left[\sum_f \left(\frac{\partial \boldsymbol{A_i^j}}{\partial \boldsymbol{V_f^g}} : \boldsymbol{dV_f^g}\right)\right] = \\ &= \frac{\partial \boldsymbol{A_i^j}}{\partial \boldsymbol{\sigma}} : \boldsymbol{d\sigma} + \frac{\partial \boldsymbol{A_i^j}}{\partial T}dT + \sum_g \left[dp^g \left(\sum_f \frac{\partial \boldsymbol{A_i^j}}{\partial \boldsymbol{V_f^g}} : \boldsymbol{\Lambda_f^g}\right)\right] \end{aligned} \tag{E.99}$$

The indices j and g give reference to strain mechanisms, while the indices i and f refer to model variables associated to the strain mechanism denoted by j and g respectively.

Replacing the finding of (E.99) in (E.98) yields:

$$d\pi^j = \sum_i \left\{\boldsymbol{\Lambda_i^j} : \left[\frac{\partial \boldsymbol{A_i^j}}{\partial \boldsymbol{\sigma}} : \boldsymbol{d\sigma} + \frac{\partial \boldsymbol{A_i^j}}{\partial T}dT + \sum_g \left[dp^g \sum_f \left(\frac{\partial \boldsymbol{A_i^j}}{\partial \boldsymbol{V_f^g}} : \boldsymbol{\Lambda_f^g}\right)\right]\right]\right\} \tag{E.100}$$

or

$$d\pi^j = \sum_i \left[\boldsymbol{\Lambda_i^j} : \left(\frac{\partial \boldsymbol{A_i^j}}{\partial \boldsymbol{\sigma}} : \boldsymbol{d\sigma} + \frac{\partial \boldsymbol{A_i^j}}{\partial T}dT\right)\right] + \sum_g \left(\Gamma_g^j dp^g\right) \tag{E.101}$$

Here, for the sake of simplicity, new variables Γ_g^j are defined to satisfy the equality:

$$\sum_g \Gamma^j_g dp^g = \sum_i \left\{ \boldsymbol{\Lambda}^{\boldsymbol{j}}_{\boldsymbol{i}} : \sum_g \left[dp^g \sum_f \left(\frac{\partial \boldsymbol{A}^{\boldsymbol{j}}_{\boldsymbol{i}}}{\partial \boldsymbol{V}^{\boldsymbol{g}}_{\boldsymbol{f}}} : \boldsymbol{\Lambda}^{\boldsymbol{g}}_{\boldsymbol{f}} \right) \right] \right\} \tag{E.102}$$

It is shown that:

$$\Gamma^j_g = \sum_i \left[\boldsymbol{\Lambda}^{\boldsymbol{j}}_{\boldsymbol{i}} : \sum_f \left(\frac{\partial \boldsymbol{A}^{\boldsymbol{j}}_{\boldsymbol{i}}}{\partial \boldsymbol{V}^{\boldsymbol{g}}_{\boldsymbol{f}}} : \boldsymbol{\Lambda}^{\boldsymbol{g}}_{\boldsymbol{f}} \right) \right] \tag{E.103}$$

Back in equation (E.97), the differential $d\bar{\pi}^j$is written:

$$d\bar{\pi}^j = \frac{\partial \bar{\pi}^j}{\partial \boldsymbol{\sigma}} : \boldsymbol{d\sigma} + \frac{\partial \bar{\pi}^j}{\partial T} dT = T \frac{\partial \boldsymbol{\alpha}}{\partial p^j} : \boldsymbol{d\sigma} + \frac{\partial C_v}{\partial p^j} dT + \frac{\bar{\pi}^j}{T} dT \tag{E.104}$$

and the differential $\boldsymbol{d\alpha}$ is approximated in a linear fashion, ignoring higher order terms:

$$\boldsymbol{d\alpha} = \sum_j \left(\frac{\partial \boldsymbol{\alpha}}{\partial p^j} dp^j \right) \tag{E.105}$$

Thus, (E.97) is rewritten:

$$dr^{pl} = \frac{1}{\Delta t} \left(\bar{\boldsymbol{d}}^{\boldsymbol{r}}_{\boldsymbol{\sigma}} : \boldsymbol{d\sigma} + \bar{d}^r_T dT + D_s \right) \tag{E.106}$$

where, according to equations (E.101), (E.103), (E.104) and (E.105),

$$\bar{\boldsymbol{d}}^{\boldsymbol{r}}_{\boldsymbol{\sigma}} = \sum_j \left\{ \Delta p^j \left[\sum_i \left(\frac{\partial \boldsymbol{A}^{\boldsymbol{j}}_{\boldsymbol{i}}}{\partial \boldsymbol{\sigma}} : \boldsymbol{\Lambda}^{\boldsymbol{j}}_{\boldsymbol{i}} \right) - T \frac{\partial \boldsymbol{\alpha}}{\partial p^j} \right] \right\} - \boldsymbol{\alpha} \cdot T \tag{E.107}$$

$$\bar{d}^r_T = \sum_j \left\{ \Delta p^j \left[\sum_i \left(\frac{\partial \boldsymbol{A}^{\boldsymbol{j}}_{\boldsymbol{i}}}{\partial T} : \boldsymbol{\Lambda}^{\boldsymbol{j}}_{\boldsymbol{i}} \right) - \frac{\partial C_v}{\partial p^j} - \frac{\bar{\pi}^j}{T} \right] \right\} - \boldsymbol{\Delta\sigma} : \boldsymbol{\alpha} \tag{E.108}$$

and

$$D_s = \sum_j \left\{ \Delta p^j \sum_g \left(\Gamma^j_g dp^g \right) + (\pi^j - \bar{\pi}^j) dp^j \right\} - \boldsymbol{\Delta\sigma} : \sum_j \left(\frac{\partial \boldsymbol{\alpha}}{\partial p^j} dp^j \right) .T \quad \text{(E.109)}$$

The quantity D_s can be written as an expression of a single common cofactor dp^j:

$$\begin{aligned} D_s &= \sum_j \left[\sum_g \left(\Delta p^j \Gamma^j_g dp^g \right) \right] + \sum_j \left[(\pi^j - \bar{\pi}^j) dp^j \right] - \sum_j \left(T \boldsymbol{\Delta\sigma} : \frac{\partial \boldsymbol{\alpha}}{\partial p^j} dp^j \right) \\ &= \sum_j \left\{ dp^j \left[\sum_g \left(\Delta p^g \Gamma^g_j \right) + \pi^j - \bar{\pi}^j - \boldsymbol{\Delta\sigma} : \frac{\partial \boldsymbol{\alpha}}{\partial p^j} T \right] \right\} \end{aligned} \quad \text{(E.110)}$$

The variables $\bar{d}^r_j$ are introduced as such:

$$\bar{d}^r_j = \sum_g \left(\Delta p^g \Gamma^g_j \right) + \pi^j - \bar{\pi}^j - \boldsymbol{\Delta\sigma} : \frac{\partial \boldsymbol{\alpha}}{\partial p^j} T \quad \text{(E.111)}$$

In light of (E.110) and (E.111), equation (E.106) is now:

$$dr^{pl} = \frac{1}{\Delta t} \left[\bar{\boldsymbol{d}}^{\boldsymbol{r}}_{\boldsymbol{\sigma}} : \boldsymbol{d\sigma} + \bar{d}^r_T dT + \sum_j \left(\bar{d}^r_j dp^j \right) \right] \quad \text{(E.112)}$$

Here, replacing the expressions of dp^j and $\boldsymbol{d\sigma}$ with the help of equations (E.73) and (E.74) respectively, it is found that:

$$dr^{pl} = \frac{1}{\Delta t} \left\{ \bar{\boldsymbol{d}}^{\boldsymbol{r}}_{\boldsymbol{\sigma}} : (\boldsymbol{L} : \boldsymbol{d\varepsilon} + \boldsymbol{\Theta} : dT) + \bar{d}^r_T dT + \sum_j \left[\bar{d}^r_j (-\boldsymbol{P}^{\boldsymbol{j}}_{\boldsymbol{\varepsilon}} : \boldsymbol{d\varepsilon} - P^j_T dT) \right] \right\} \quad \text{(E.113)}$$

Recalling the general form of (E.92), it is evident that:

$$\boldsymbol{d}^r_{\boldsymbol{\varepsilon}} = \frac{1}{\Delta t}\left[\bar{\boldsymbol{d}}^r_{\boldsymbol{\sigma}} : \boldsymbol{L} - \sum_j \left(\bar{d}^r_j \boldsymbol{P}^j_{\boldsymbol{\varepsilon}}\right)\right] \tag{E.114}$$

and

$$d^r_T = \frac{1}{\Delta t}\left[\bar{\boldsymbol{d}}^r_{\boldsymbol{\sigma}} : \boldsymbol{\Theta} + \bar{d}^r_T - \sum_j \left(\bar{d}^r_j P^j_T\right)\right] \tag{E.115}$$

References

D. J. Hartl and D.C. Lagoudas. Constitutive modeling and structural analysis considering simultaneous phase transformation and plastic yield in shape memory alloys. *Smart Materials and Structures*, 18(10):104017, oct 2009. ISSN 0964-1726. doi: 10.1088/0964-1726/18/10/104017. E-2

MODÉLISATION DU COMPORTEMENT MULTIAXIAL CYCLIQUE DES ALLIAGES À MÉMOIRE DE FORME

RESUME : De nouvelles approches phénoménologiques sur la modélisation du comportement des AMFs sont nécessaires pour tenir en compte de leur réponse complexe sous chargement multiaxial. L'effet de l'anisotropie induit une dépendance de leur comportement inélastique à la direction du chargement pour des cas superélastiques. La réorientation martensitique affecte drastiquement la réponse du matériau sous chargement non-proportionnel. La charge répétitive modifie aussi certaines propriétés du matériau. L'objectif de cette étude est de proposer un nouveau modèle constitutif thermodynamique robuste pour les AMFs, focalisé surtout sur des compositions NiTi équiatomiques pour capter la transformation martensitique anisotrope et la réorientation des variantes martensitiques, toujours en considérant le fort couplage thermomécanique. Une nouvelle approche mathématique est introduite pour capter l'anisotropie de contraintes et de l'évolution des déformations inélastiques lors de la transformation directe, causée par les conditions de mise en forme des structures en AMFs. Cette méthode est évaluée en employant des courbes contraintes-déformations résultant de chargements proportionnels simulés par un modèle micromécanique. Un modèle phénoménologique fortement couplé, qui considère surtout la réorientation martensitique, est développé sur SMART+, une plate-forme numérique en C++, et évalué en exécutant des simulations numériques d'expériences non-proportionnelles déjà existantes. Des structures complexes sont également simulées en employant la Méthode des Éléments Finis. Une partie de ce travail concerne aussi l'étude expérimentale des effets du chargement cyclique sur l'évolution des déformations résiduelles et le seuil de transformation des alliages NiTi sous sollicitation uniaxiale et biaxiale.

Mots clés : modèle phénoménologique, réorientation martensitique, couplage thermomécanique, anisotropie, conditions de chargement complexes, comportement cyclique, chargements non-proportionnels.

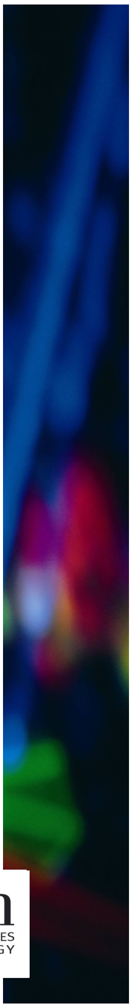

CYCLIC MULTIAXIAL BEHAVIOR MODELING OF SHAPE MEMORY ALLOYS

ABSTRACT : New phenomenological approaches in modeling the behavior of SMAs are needed to account for their complex response under multiaxial loading. The effect of anisotropy induces a dependence of their inelastic behavior to the direction of the loading for superelastic cases. Martensitic reorientation affects drastically material response under non-proportional loading. Repeated loading also alters certain material properties. The goal of this study is to propose a new robust thermodynamic constitutive model for SMAs with focus on equiatomic NiTi compositions to capture anisotropic martensitic transformation and reorientation of martensitic variants, always taking in mind the strong thermomechanical coupling. A new mathematical approach is introduced to account for the anisotropy of stresses and the evolution of inelastic strains during forward transformation caused by the forming conditions of SMA structures. This method is evaluated by utilizing stress-strain curves resulting from proportional loading simulated with a micromechanical model. A phenomenological thermodynamic model considering especially martensitic reorientation and exhibiting the strong thermomechanical coupling is developed. It is implemented on SMART+, a numerical platform in C++, and evaluated by simulating existing non-proportional experiments. Complex structures are also simulated using Finite Element Analysis. A part of this work also concerns the experimental study of the effects of cyclic loading to the evolution of residual strain and transformation threshold of NiTi under uniaxial and biaxial testing.

Keywords : phenomenological model, martensitic reorientation, thermomechanical coupling, anisotropy, complex loading conditions, cyclic behavior, non-proportional paths.